Sediment-hosted Zn-Pb-Ag mineralization in the Red Dog district, Alaska, USA: pre-ore environments and mineralizing processes

by

Merilie A. Reynolds

A thesis submitted in partial fulfillment of the requirements for the degree of

Doctor of Philosophy

Department of Earth and Atmospheric Sciences
University of Alberta

© Merilie A. Reynolds, 2019

Abstract

Sediment-hosted massive sulfide (SHMS) deposits are an important source of global zinc resources, and the Red Dog Pb-Zn-Ag district in Alaska (USA) contains giant deposits of this type. The existing model for ore formation at Red Dog involves early diagenetic replacement of sediment deposited in a restricted basin with stratified suboxic bottom waters. We present new observations of trace fossils *Schaubcylindrichnus* ichnospecies (isp.) and *Chondrites* isp. in several Red Dog deposits. The presence of the trace fossils, the size of the largest burrows, and the pervasiveness of the ichnofabric indicate that at least some intervals of the host sediment were deposited in an oxygenated middle to outer shelf environment. To reconcile these data with those from previous regional sedimentological and lithogeochemical studies, we propose a new model whereby the ore-hosting sediment was deposited in a shelfal setting in which redox conditions were affected by a fluctuating oxygen minimum zone. The strong spatial correlation between bioturbation and Red Dog SHMS deposits suggests that the presence of trace fossils may have played an important role in controlling the flow of ore-forming fluids by increasing host sediment permeability.

The Anarraaq area of the Red Dog district contains a barren barite body with as much as 1 Gt of barite and a sulfide deposit with an inferred resource of 19.4 Mt at 14.4% Zn, 4.2% Pb, and 73.4 ppm Ag. Rhenium-osmium isochron ages of organic-rich mudstone overlying the sulfide deposit (339.1 ± 8.3 Ma), pre-ore diagenetic pyrite in the sulfide deposit (333.0 ± 7.4 Ma), and hydrothermal pyrite (334.4 ± 5.3 Ma) are all within uncertainty of each other and of the Re-Os isochron age of the Main deposit in the Red Dog Mine Area (338.3 ± 5.8 Ma; Morelli et al., 2004). This indicates that hydrothermal mineralization was broadly synchronous on a regional scale and that mineralization was approximately coincident with sedimentation.

We present an updated stratigraphic, structural, and paragenetic framework for the Anarraaq area based on detailed logging, thin-section microscopy, and the construction of two cross sections. Importantly, this work reveals that Anarraaq contains *three* discrete intervals of abundant pre-ore barite, carbonate, and pyrite in the organic-rich mudstone of the Mississippian Kuna

Formation (Ikalukrok unit). One of these intervals – the Anarraaq barite body – is barren; the other two were later overprinted by Zn-Pb-Ag mineralization and comprise the Anarraaq sulfide deposit. Textural observations indicate that the carbonate and pre-ore pyrite are diagenetic (not sedimentary and hydrothermal, respectively, as previously interpreted) and their spatial relationship to barite (previously interpreted to form at a cold methane seep) suggest that all three minerals precipitated in association with methane-related diagenetic processes.

In situ isotopic data (secondary ion mass spectrometry; SIMS) from barite ($\delta^{18}O$ and $\delta^{34}S$), pyrite and marcasite ($\delta^{34}S$) in the Anarraaq area indicate that much of the pre-ore barite formed in the very shallow subsurface where rates of bacterial sulfate reduction (BSR) were high and produced relatively small fractionations and minor reservoir effects. At the same time, BSR also took place farther below the seafloor where the dissolution of barite in methanic pore waters provided a secondary source of sulfate. The fractionation produced during this process was also small. In both settings, BSR was likely coupled to the anaerobic oxidation of methane (i.e., sulfate-driven anaerobic oxidation of methane); carbonate and pyrite are common byproducts of this process. The introduction of hydrothermal fluids generated zones of high porosity and permeability as they dissolved diagenetic carbonate. Hydrothermal pyrite and marcasite in the Anarraaq sulfide deposit display a wide range of $\delta^{34}S$ values with local small-scale spatial-temporal heterogeneity. This may reflect 1) mixing between two reservoirs of diagenetic (biogenic) bisulfide with distinct S isotopic compositions or 2) bacterial, and possibly other types of sulfate reduction of a single reservoir of hydrothermal sulfate under conditions of highly variable sulfate and reductant availability. Overall, microbial activity and methane played important and complex roles in the formation of high-grade Zn-Pb-Ag ore in the Anarraaq sulfide deposit. We suspect that methane-related alteration of host strata may have been a crucial pre-condition for the emplacement of all SHMS mineralization in the Red Dog district.

Preface

The concept of this PhD project was developed by Dr. Sarah A. Gleeson and Teck Resources Limited. Core logging, sample collection, and access to historic exploration data were made possible by the generous assistance of many members of the Teck exploration team at Red Dog. Though I conducted most of the core logging and sample collection for this project, many people contributed including Dr. Sarah A. Gleeson, Betsy A. Friedlander, and James McCusker.

Chapter 2 was published in *Geology* as Reynolds, M.A., Gingras, M.K., Gleeson, S.A., and Stemler, J.U., 2015, More than a trace of oxygen: Ichnological constraints on the formation of the giant Zn-Pb-Ag ± Ba deposits, Red Dog district, Alaska: *Geology*, v. 43, no. 10, p. 867–870. Core logging and core and outcrop sampling was conducted by M.A.R. Sample preparation and imaging was carried out by M.A.R. All authors contributed to project design, discussion of results and their implications, as well as preparation of the manuscript. M.A.R. wrote the initial manuscript and oversaw each stage of revision.

Chapter 3 will be submitted to *Economic Geology* as Reynolds, M.A., Gleeson, S.A., Creaser, R.A., Friedlander, B.A., Haywood, J, Hnatyshin, D., McCusker, J., Waldron, J.W.F., The impact of diagenetic processes on sediment-hosted massive sulfide ore distribution: Geochronological, stratigraphic, textural, and petrographic relationships between silica, barite and sulfides in the Anarraaq Zn-Pb-Ag deposit, Red Dog District, Alaska. Core logging and sampling was conducted by M.A.R., S.A.G., B.A.F., and J.M. Cross section construction and interpretation was carried out by M.A.R., B.A.F., J.M., and J.H. Petrography and imaging was carried out by M.A.R. Further sample preparation and Re-Os geochronology was conducted by M.A.R., D.H., and R.A.C. All authors contributed to project design, discussion of results and their implications, as well as preparation of the manuscript. M.A.R. wrote the initial manuscript and will oversee every stage of revision.

Chapter 4 will be submitted to *Economic Geology* as Reynolds, M.A., Gleeson, S.A., Stern, R.A., Sulfur cycling, an important process in the formation of the Anarraaq barite body and Zn-Pb-Ag deposit, Red Dog district, Alaska: a SIMS study of barite ($\delta^{34}S$ and $\delta^{18}O$), pyrite and marcasite ($\delta^{34}S$). Core logging and sampling was conducted by M.A.R. and S.A.G. Thin-section petrography was carried out by M.A.R. Further sample preparation, imaging, and secondary ion mass spectrometry was conducted by M.A.R. and R.A.S. All authors contributed to project design, discussion of results and their implications, as well as preparation of the manuscript. M.A.R. wrote the initial manuscript and will oversee every stage of revision.

The ideas presented here are my own, although they have developed over time through discussions with co-authors. All the writing and figures presented here are my own, as are any errors or omissions.

Acknowledgements

This thesis is brought to you by Tim Horton's small steeped tea (two milks).

Jokes aside, this thesis has been made possible by a huge amount of support and encouragement from more people than I can mention here.

Many thanks to my primary supervisor, Sarah Gleeson, for inviting me to work with you on such a fabulous ore deposit for my PhD. What a gift! Thank you for your patience and enthusiasm, and for encouraging me to look for the strengths that may be hidden within the parts of myself that I think of as faulty. A special thanks to the other U of A faculty members who adopted me formally (Rob Creaser) and informally (Nick Harris, Pilar Lecumberri-Sanchez, Matt Steele-MacInnis, and John Waldron) after Sarah's relocation to Germany.

Funding for this work was provided by Teck Resources Limited and a Collaborative Research and Development grant from the Natural Sciences and Engineering Research Council of Canada (awarded to S.A.G. and Robert A. Creaser). Additional support was provided through a Vanier Scholarship, a University of Alberta President's Doctoral Prize of Distinction, and a University of Alberta Doctoral Recruitment Scholarship. Generous travel grants from the SEG Foundation and the SGA supported my travel to present my research at two SEG conferences and a Goldschmidt conference, respectively.

Thanks to everyone at Teck who helped with the logistics of my visits to Red Dog Mine in northwestern Alaska and to the corporate office in Vancouver. It has been a great pleasure to be a part of a safe, spirited, and science-focused exploration team. Thanks to all of you who attended one of my presentations or read one of my reports, and especially those of you who have taken the time to engage me in discussion about Red Dog-related geology.

Special thanks to the real heroes of the EAS department: Shyra Craig, Igor Jakab, and Mark Labbe. Martin Von Dollen, I feel so fortunate that my tenure in EAS overlapped with yours. Here's to quality thin-sections and green papaya salad! Thanks to Mark Simms in the Crustal Re-Os Geochronology Laboratory and Katie Nichols in the Canadian Centre for Isotopic Microanalysis for all your help with sample preparation. Thanks to Marylin Huff for her work maintaining the reflected light microscopes and help trouble-shooting any problems. Thanks to Diane Caird for her work in the XRD lab and to Erin Walton for the use the micro-Raman at MacEwan.

Thanks to Andy Dufrane for letting me use Iolite in his lab and for being more curious about what I was doing with it than anyone else; to Andrew Locock for his excellent operation of the electron microprobe and badassery in all things mineralogic; and to Murray Gingras for teaching me about trace fossils and how to go about make a nice figure of plates. Thanks to Rich-

ard Stern for providing a high-quality SIMS facility. Long Li, thank you for a very long discussions about S isotopes. Thanks to Danny Hnatyshin for showing me the ropes in Re-Os geochronology and for your dogged determination to get some usable data from my samples.

Tom Chacko, thank you for the gentle and attentive style with which you administered guidance as the Associate Chair for graduate studies. (But I want you to know that I am disappointed / still waiting for you to give an Atlas talk. Come on! What is your excuse now that you are no longer grad chair?)

Thanks to the folks in the Inorganic and Isotope Geochemistry section at the Helmholtz Centre GFZ in Potsdam for making me feel welcome, especially Julia Fechner who brought me soup when I was sick. Marcus Oelze, it was a pleasure to work with you in the laser ablation lab.

Thanks to Balz Kamber and Cora McKenna in the Geochemistry Laboratories of Trinity College Dublin. Balz, writing the ARIS manuscript with you was an important experience for me because of the way I felt like we were genuine collaborators; thank you for that.

Additional scientific discussions and camaraderie were provided by Kurt Borth, Kevin Byrne, Hilary Corlett, Janina Czas, Lauren Davies, Kan Li, Joe Magnall, Phil Rieger, Devon Smith, Morgan Snyder, Michelle Speta, Shawna White, Faye Wyatt, and many others.

Thanks to my family and non-PhD-related friends for not asking ‘When will you be finished?’ very often and for putting up with a sorry deficiency of communication. And finally, a big thank you to Tyler. I only agreed to marry you, if you were willing to move to Edmonton with me so I could do this PhD. But in retrospect, I probably should have been of the mindset that I would only agree to do this PhD, if you were willing to marry me and move to Edmonton. I am so lucky it worked out like it has. Thanks for being the best listener, for keeping food in the fridge and on the table, and for being open to adventure. Chapter 6 is the best part of this thesis!

Table of Contents

List of Figures

List of Tables

Chapter 1: Introduction

Understanding the evolution of ocean chemistry and reduction-oxidation (redox) conditions through geologic time is crucial to the investigation of important topics such as paleoclimate, atmospheric oxygenation, and the evolution of life. In particular, periods of widespread ocean anoxia have long been of special interest because of their connection to mass extinction events, deposition of petroleum source rocks, the global sulfur cycle, and numerous other natural phenomena. A link between global ocean anoxic events and the occurrence of lead-zinc ± silver deposits hosted in organic-rich mudstone was first identified by Turner (1992) and basin restriction and anoxia have remained central components of related deposit models (e.g., Blevings et al., 2013; Goodfellow and Lydon, 2007; Slack et al., 2015).

The classic genetic model for these types of deposits is the sedimentary exhalative (SEDEX) model (summarized in Goodfellow and Lydon, 2007; Fig. 1.1). The SEDEX model involves metalliferous basinal brines traveling up extensional faults and "exhaling" into the euxinic (anoxic, H_2S-rich) bottom waters of a marine basin with a restricted, stratified water column. Base metal sulfides precipitate in the water column and are then deposited synsedimentarily with organic-rich mudstone. Key deposit characteristic associated with this genetic interpretation include dark-colored, fine-grained, organic-rich host strata; interlaminated sulfides; and strongly positive $\delta^{34}S$ values in sulfide minerals.

Dark colored, fine-grained, organic-rich mudstones were conventionally interpreted to be the standard product of sediment deposition in deep, low energy and oxygen-poor environments (Aplin and Macquaker 2011); restricted basins with stratified water columns, such as the Black Sea, were long considered to be the best modern analogue for ocean anoxia in Earth's history (Lyons et al., 2009). However, more recent studies reveal that many black shales contain subtle sedimentary structures and mineralogical heterogeneity that indicate deposition took place in more varied settings (e.g., Schieber, 2003; Schieber and Riciputi, 2004; Macquaker et al., 2007). In modern oceans, the bulk of marine carbon burial takes place on continental shelves (i.e., at < 200 m water depth) rather that in deeper water, even though the shelves account for only around 5% of the global seafloor area (Dunne et al., 2007). Continental margins that are the site of upwelling of nutrient-rich water are associated with particularly high rates of biogenic productivity and water column deoxygenation (e.g., Hammersley et al., 2007; Kuypers et al., 2005). These open-marine oxygen minimum zones (OMZs) have received increasing attention as a potentially a more appropriate analogue for ocean anoxia in the geological past (e.g., Zhang et al., 2016; Hammarlund et al., 2017; Guilbaud et al., 2018; Scholz et al., 2018).

In the SEDEX model, laminated sulfides are a product of long-lived basin euxinia where reduced S in the water column serves to trap metals. However, Leach et al. (2005) pointed out that laminated sulfide textures could also be produced by preferential replacement of laminated

host strata. More recent work indicates that the redox state of the ocean can be far more dynamic in space and time than previously believed (Poulton and Canfield, 2011, and references therein). For example, März et al. (2008) showed that fluctuations between euxinic (anoxic, H_2S-rich) and ferruginous (anoxic, Fe^{2+}-rich) conditions can take place over as little as 20ky. In the cases where sulfide precipitation did take place in the water column, the requisite euxinic conditions could have formed on a local rather than global scale (Leach et al., 2010). Furthermore, the free H_2S required for sub-seafloor replacement-style mineralization can develop in the pore waters of marine sediments as they become isolated from the overlying water column such that the bottom water redox conditions may be irrelevant to replacement-style mineralization (Leach et al., 2010; Gleeson et al., 2013). Magnall et al. (2018) showed that host strata of the Tom and Jason deposits (Selwyn basin, Yukon) were dominantly ferruginous, not euxinic. Magnall et al. (2016) cautioned that basin restriction could impose mass balance limitations on S availability that would be problematic for precipitation of massive amounts of sulfide minerals.

Sulfide minerals with positive $\delta^{34}S$ values are characteristic of SEDEX deposits (Lyons et al., 2006). The positive $\delta^{34}S$ values are linked to basin restriction and the development of Rayleigh-type reservoir effects in a system closed to sulfate (i.e., at the basin scale; Goodfellow and Jonasson, 1984). Several workers have challenged this interpretation in recent years. Magnall et al. (2016) and Johnson et al. (2018) showed that diagenetic pyrite with a positive $\delta^{34}S$ signature in strata hosting SEDEX-style mineralization is the product of sulfate reduction coupled to the anaerobic oxidation of methane operating below the sediment surface. Sangster (2018) suggested that more positive $\delta^{34}S$ values in the HYC deposit could be controlled by a reduction in the size of fractionation (controlled by changes in the conditions of reduction) produced during sulfate reduction (instead of an evolution of the composition of the sulfate reservoir over time).

In light of this evolution in thinking, I re-investigate the genesis of Zn-Pb mineralization hosted in organic-rich mudstones in the Red Dog Pb-Zn-Ag district in northwestern Alaska. Although the term SEDEX continues to be used in some informal contexts as a catch-all label for Zn-Pb mineralization associated with organic-rich mudstone, many workers prefer more descriptive names. In this contribution, we use the term sediment-hosted massive sulfide (SHMS) to refer to Zn-Pb sulfide deposits hosted in organic-rich, clastic-dominated strata.

1.1 Red Dog Pb-Zn-Ag District

The Red Dog Pb-Zn-Ag district is located in northwestern Alaska (Fig. 1.2) and contains one of the world's largest operating zinc mines (www.teck.com) as well as a number of unmined deposits and prospects (Blevings et al. 2013). Red Dog is located in the fold-thrust belt of the mid-Jurassic to Cretaceous Brookian orogeny and the district geology is characterized by extensive thrusting, folding, and low-grade metamorphism (De Vera et al., 2004). These

structural complications can obscure the original geometry of the ore deposits and the context of the surrounding host sediment.

Mineralization occurs within the Carboniferous Kuna Formation, which comprises variably siliceous black mudstones and shales, lesser calcareous interbeds and, locally, black chert and massive to nodular barite horizons (Slack et al., 2004a; Dumoulin et al., 2004; Fig. 1.3) . Sedimentological and microfossil data observed in unaltered Kuna Formation indicate that sediment deposition took place in variably distal slope settings (Dumoulin et al. 2004). The calcareous component of Kuna Formation strata was delivered to the slope by turbidites or other types of mass flows (Dumoulin et al. 2004). The presence of abundant radiolarians (Dumoulin et al., 2004; Kelley et al., 2004a), high concentrations of organic carbon (locally > 8 wt. % TOC; Slack et al., 2004b), and phosphorites in coeval strata (Dumoulin et al., 2011) suggest that upwelling played an important role in the regional depositional regime (Dumoulin et al. 2004; Dumoulin et al. 2011). Bulk rock geochemical data of samples of unmineralized Kuna Formation have been interpreted to indicate anoxic, denitrifying bottom water conditions formed in a restricted basin (Slack, et al. 2004b).

The Anarraaq deposit was a covered target discovered in 1999 as a result of drilling of a gravity anomaly (Kelley, et al., 2004a). Relatively little scientific research has been done on the deposit since its discovery (Kelley et al., 2004a and minor attention in some other publications of the same volume; Schardt et al., 2008). A number of characteristics of Anarraaq are similar to the Mine Area deposits, which have been studied in more detail. However, Anarraaq is distinct in that the ore zone occurs stratigraphically separated from a discrete barite horizon. In this respect, the paragenetic relationships appear to be somewhat simplified and may allow new insights into the processes that resulted in sulfide deposition.

Barite, pyrite, quartz, and carbonate minerals are commonly associated with SHMS deposits in the Red Dog district. Although these minerals are not of any economic value, they are the focus of considerable interest because of their spatial relationship to Zn-Pb mineralization. In terms of production, the occurrence of barite, pyrite, and quartz all have important implications for the geometallurgical properties of ore. For example, barite-rich ore is ‘soft’ and relatively easy to crush whereas quartz-rich ore is much more difficult to process. From an exploration standpoint, barite produces a gravity anomaly that has been a useful tool for the discovery of deeply-buried Zn-Pb mineralization such as the Anarraaq deposit (Kelley et al., 2004a). Despite the recognition of the importance of these non-economic minerals, the underlying genetic controls on their relationship to Zn-Pb mineralization are less well understood.

Cooke et al. (2000) proposed that baritic SHMS deposits form from reduced hydrothermal fluids (that transport barium in addition to base metals) whereas non-baritic deposits form from oxidized hydrothermal fluids. Other workers suggest that barite may have

been formed by a different fluid than the ore-forming fluid (e.g., Leach et al., 2005; Magnall et al., 2016) and this is the preferred model at Red Dog (Blevings et al., 2013). There, barite is thought to form at seafloor vents where fluid rich in methane and barium encounter seawater sulfate in the water column or shallow subsurface (Johnson et al., 2004; Ayuso et al., 2004; Johnson et al., 2009). Barite occurs within the Mine Area deposits, where it is replaced by and intergrown with ore-stage sulfides (Kelley et al., 2004b; Johnson et al., 2004). In these deposits, thermogenic reductive dissolution of barite may have provided an important source of reduced sulfur for ore-stage mineralization in the Mine Area deposits (Kelley et al., 2004b). In the Anarraaq area, as much as 1 Gt of barite occurs in the Ikalukrok unit but it is stratigraphically separated from the Anarraaq sulfide deposit (Kelley et al., 2004a) and in other places barite occurs independent of any known Zn-Pb mineralization (Johnson et al., 2004). It remains unclear what factors control the spatial relationship (or lack thereof) between barite and Zn-Pb mineralization.

Pyrite is abundant and widespread in the Red Dog District. It is a common component in ore zones (Kelley et al., 2004a; Kelley et al., 2004b) but also occurs in barren Ikalukrok mudstone (Slack et al., 2004b). In the Anarraaq deposit, the low-grade part of the deposit is characterized by massive pyrite (Kelley et al., 2004a); this pyrite it treated as distal alteration halo associated with hydrothermal mineralization (Schardt et al., 2008). In other prospects, massive amounts of pyrite occur with almost no Zn-Pb mineralization (James Stemler, pers. comm.).

Quartz and carbonate are both important sedimentary components of the Ikalukrok unit. Biogenic cherts and highly biosiliceous mudstones may have acted as a regional trap for hydrothermal fluids (Slack et al., 2004b). Slack et al. (2004a) interpreted silicification within Red Dog ore zones to be genetically linked Zn-Pb mineralization but Leach et al. (Leach et al. 2004) interpreted it to have been introduced much later during the Brookian orogeny. (Kelley, et al., 2004a) interpreted the Anarraaq sulfide deposit to have formed by replacing sedimentary carbonate debrite; the local abundance of carbonate may have been an important control on the high grade Zn-Pb mineralization of the Anarraaq sulfide deposit. Yet in the Mine Area deposits, there is no conclusive evidence that carbonate replacement was an important genetic process (Kelley et al., 2004b).

Rhenium-osmium dating of ore-stage pyrite in the Main deposit yielded an isochron age of 338.3±5.8 Ma (Morelli et al., 2004), which is synchronous (within error) of the relatively loosely constrained biostratigraphic age range of the upper Kuna formation (Meramecian to early Chesterian; Dumoulin et al., 2004). Textural evidence suggests that most sulfide precipitation took place via replacement after host sediment deposition (Kelley et al., 2004a; Kelley et al., 2004b; Blevings et al., 2013). No other SHMS deposits in the Red Dog district have been dated;

little is known about the duration of the Zn-Pb mineralization on the district scale. Furthermore, the relationship between ore formation and early diagenetic processes remains unclear.

The source of the metals in the Red Dog deposits is unknown. Based on a Pb isotope study of sulfide minerals in various deposits, Ayuso et al., (2004) suggested that Red Dog base metals were leached from clastic rocks in older stratigraphy. The initial osmium ratio ($^{187}Os/^{188}Os$) calculated from Re-Os age of ore-stage pyrite indicates that fluids were sourced from a crustal reservoir no older than ~410 Ma but is also permissive of a mantle source (Morelli et al., 2004). In a more recent interpretation of initial osmium ratios of variably metalliferous samples of the Ikalukrok unit, Slack et al. (2012) suggested that the Red Dog mineralizing fluids were strongly influenced by a component derived from leaching of mafic igneous rocks.

Based on sulfur isotope data from the Mine Area deposits, Kelley et al. (2004b) interpreted sulfide ore to incorporate a mix of reduced sulfur produced by bacteriogenic sulfate reduction and thermogenic sulfate reduction. In the Mine Area deposits, the contribution of biogenic bisulfide was relatively minor and it accumulated in pore waters prior to the main phases of Zn-Pb mineralization as seawater sulfate was reduced (Kelley et al., 2004b). Thermogenic bisulfide was produced during the main ore-stage via reduction of seawater or pore water sulfate, or the reductive dissolution of barite (Kelley et al., 2004b). This interpretation differs significantly from the classic SEDEX model in which strongly positive $\delta^{34}S$ values are interpreted to be a product of Rayleigh-type reservoir effects in a restricted basin with depleted sulfate concentrations (Goodfellow and Jonasson, 1984; Goodfellow, 2007).

Johnson et al. (2004) speculated that in non-baritic Red Dog deposits, bacterial sulfate reduction coupled to the anaerobic oxidation of methane (SD-AOM) might make an important contribution to the supply of reduced sulfur. Then recently, Magnall et al. (2016) and Johnson et al. (2018) showed that SD-AOM was an important process during the diagenesis of strata hosting several SHMS deposits in the Selwyn basin (Yukon). However, the idea has not been explored in any further detail at Red Dog.

1.2 Research questions

In this thesis, I investigate several questions that are fundamental to understanding the genesis of SHMS mineralization in the Red Dog district:

- **A.** What was the environment of deposition of the strata hosting Zn-Pb mineralization in the Red Dog district?
- **B.** What are the genetic relationships among barite, pyrite, carbonate, quartz, and Zn-Pb mineralization in the Anarraaq area?
- **C.** What is the age of ore emplacement in the Anarraaq deposit? How does it compare with the age of host sediment deposition and with the age of ore emplacement elsewhere in the Red Dog district?

D. What were the source(s) of sulfur and the mechanism(s) of sulfate reduction involved in the formation of the Anarraaq sulfide deposit?

These questions are addressed in three chapters.

In **Chapter 2**, we present new observations of trace fossils that are preserved in several Red Dog ore zones and related zones rich in barite and quartz. These data are especially important because sedimentological features are rarely preserved within the ore zones; most previous work has focused on sedimentological and bulk rock geochemical data collected from un-mineralized host strata outside the ore zones. The dataset in this chapter offers some important new insights into the environment of deposition of host sediment (**Question A**).

In **Chapter 3**, we present a pair of cross-sections through the Anarraaq sulfide deposit and barite body that were constructed based on observations from new drill core, an extensive re-logging campaign, and data from historic drill core logs. These sections provide a stratigraphic and structural framework for the Anarraaq barite body and sulfide deposit. Detailed petrographic observations at a variety of scales (e.g., hand sample, thin-section microscopy) were used to create a mineral paragenesis and the distribution of key paragenetic phases are plotted on the sections. This work clarifies much about the relationships among barite, pyrite, carbonate, quartz, and Zn-Pb mineralization (**Question B**). Re-Os isochron ages are reported for pre-ore and hydrothermal pyrite in the Anarraaq sulfide deposit and the organic-rich mudstone immediately overlying the deposit host. These data constrain the absolute timing of sediment deposition and sulfide mineralization at Anarraaq and whether it was contemporaneous with mineralization in the Main deposit in the Mine Area (**Question C**).

In **Chapter 4**, we present in situ isotopic data for barite ($\delta^{34}S$ and $\delta^{18}O$), pyrite, and marcasite ($\delta^{34}S$) from the Anarraaq barite body and sulfide deposit. These data complement the detailed petrographic data presented in Chapter 3 by allowing a more in-depth investigation of the geochemical processes that produced the textures described in Chapter 3 (**Question B**). The S and O isotopic data reveal important new insights into sulfur cycling during host sediment deposition, early diagenesis, and hydrothermal mineralization (**Question D**).

Taken together, this work significantly advances our understanding of how SHMS deposits formed in the Red Dog district. The economic importance of these deposits – the Red Dog district contains one of the world's largest producing zinc mines (www.teck.com) and SHMS deposits contain the majority of the western world's zinc resources (Goodfellow and Lydon 2007) – makes understanding how they formed particularly important. A deposit model is the foundation of any exploration program; this thesis contributes to ongoing efforts to discover new Zn and Pb resources around the world.

1.3 References

Aplin, A.C., and Macquaker, J.H.S., 2011, Mudstone diversity: Origin and implications for source, seal, and reservoir properties in petroleum systems: AAPG Bulletin, v. 95, p. 2031–2059, doi: 10.1306/03281110162.

Ayuso, R A et al. 2004. "Origin of the Red Dog Zn-Pb-Ag Deposits, Brooks Range, Alaska: Evidence from Regional Pb and Sr Isotope Sources." *Economic Geology* 99: 1533–34.

Blevings, S., Kraft, J., Stemler, J., and Krolak, T., 2013, An overview of the structure, stratigraphy, and Zn-Pb-Ag deposits of the Red Dog District, northwestern Alaska, *in* Colpron, M., et al., eds., Tectonics, metallogeny, and discovery: The North American Cordillera and similar accretionary settings: Society of Economic Geologists Special Publication 17, p. 361–387.

Cooke, D., Bull, S., Large, R., and McGoldrick, P., 2000, The importance of oxidized brines for the formation of Australian Proterozoic stratiform sediment-hosted Pb-Zn (Sedex) deposits: Economic Geology, v. 95, p. 1–18, http://171.67.121.50/content/95/1/1.short (accessed March 2014).

De Vera, J, KR McClay, and AR King. 2004. "Structure of the Red Dog District, Western Brooks Range, Alaska." Economic Geology 99: 1415–34.

Dumoulin, J.A., Harris, A.G., Blome, C.D., and Young, L.E., 2004, Depositional settings, correlation, and age of Carboniferous rocks in the western Brooks Range, Alaska: Economic Geology and the Bulletin of the Society of Economic Geologists, v. 99, p. 1355–1384, doi:10.2113 /gsecongeo .99.7.1355.

Dumoulin, J.A., Slack, J.F., Whalen, M.T., and Harris, A.G., 2011, Depositional setting and geochemistry of phosphorites and metalliferous black shales in the Carboniferous–Permian Lisburne Group, northern Alaska, *in* Dumoulin, J.A. and Galloway, J.P. eds., USGS Professional Paper 1776-C, p. 1–64,

Dunne, J.P., Sarmiento, J.L., and Gnanadesikan, A., 2007, A synthesis of global particle export from the surface ocean and cycling through the ocean interior and on the seafloor: Global Biogeochemical Cycles, v. 21, p. 1–16, doi: 10.1029/2006GB002907.

Goodfellow, W.D., and Jonasson, I.R., 1984, Ocean stagnation and ventilation defined by Delta-S-34 secular trends in pyrite and barite, Selwyn basin, Yukon: Geology, v. 12, p. 583–586.

Goodfellow, W.D., 2007, Base metal metallogeny of the Selwyn Basin, Canada, *in* Goodfellow, W., ed., Mineral deposits of Canada: A synthesis of major deposit-types, district metallogeny, the evolution of geological provinces, and exploration methods: Geological Association of Canada, Mineral Deposits Division, Special Publication 5, p. 553–579.

Goodfellow, W.D., and Lydon, J.W., 2007, Sedimentary exhalative (SEDEX) deposits, *in*

Goodfellow, W.D. ed., Mineral deposits of Canada, Geological Association of Canada, p. 163–183.

Hamersley, M.R., Lavik, G., Woebken, D., Rattray, J.E., Lam, P., Hopmans, E.C., Damste, J.S.S., Kruger, S., Graco, M., Gutierrez, D., and Kuypers, M.M.M., 2007, Anaerobic ammonium oxidation in the Peruvian oxygen minimum zone: Limnology and Oceanography, v. 52, p. 923–933.

Hammarlund, E.U., Gaines, R.R., Prokopenko, M.G., Qi, C., Hou, X.-G., and Canfield, D.E., 2017, Early Cambrian oxygen minimum zone-like conditions at Chengjiang: Earth and Planetary Science Letters, v. 475, p. 160–168, doi: https://doi.org/10.1016/j.epsl.2017.06.054.

Johnson, C.A., Kelley, K.D., and Leach, D.L., 2004, Sulfur and oxygen isotopes in barite deposits of the western Brooks Range, Alaska, and implications for the origin of the Red Dog massive sulfide deposits: Economic Geology and the Bulletin of the Society of Economic Geologists, v. 99, p. 1435–1448, doi:10.2113 /gsecongeo .99.7 .1435.

Johnson, C.A., Emsbo, P., Poole, F.G., and Rye, R.O., 2009, Sulfur- and oxygen-isotopes in sediment-hosted stratiform barite deposits: Geochimica et Cosmochimica Acta, v. 73, p. 133–147, doi: 10.1016/j.gca.2008.10.011.

Johnson, C.A., Slack, J.F., Dumoulin, J.A., Kelley, K.D., and Falck, H., 2018, Sulfur isotopes of host strata for Howards Pass (Yukon-Northwest Territories) Zn-Pb deposits implicate anaerobic oxidation of methane, not basin stagnation: Geology, v. 46, p. 619–622, doi: 10.1130/G40274.1.

Kelley, K.D., Dumoulin, J.A., and Jennings, S., 2004a, The Anarraaq Zn-Pb-Ag and barite deposit, northern Alaska: Evidence for replacement of carbonate by barite and sulfides: Economic Geology and the Bulletin of the Society of Economic Geologists, v. 99, p. 1577–1591, doi: 10.2113 /gsecongeo .99.7.1577.

Kelley, K.D., Leach, D.L., Johnson, C.A., Clark, J.L., Fayek, M., Slack, J.F., Anderson, V.M., Ayuso, R.A., and Ridley, W.I., 2004b, Textural, compositional, and sulfur isotope variations of sulfide minerals in the Red Dog Zn-Pb-Ag deposits, Brooks Range, Alaska: Implications for ore formation: Economic Geology and the Bulletin of the Society of Economic Geologists, v. 99, p. 1509–1532, doi:10.2113 /gsecongeo .99 .7 .1509.

Kuypers, M.M.M., Lavik, G., Woebken, D., Schmid, M., Fuchs, B.M., Amann, R., Jørgensen, B.B., and Jetten, M.S.M., 2005, Massive nitrogen loss from the Benguela upwelling system through anaerobic ammonium oxidation.: Proceedings of the National Academy of Sciences of the United States of America, v. 102, p. 6478–83, doi: 10.1073/pnas.0502088102.

Leach, D.L., Marsh, E., Emsbo, P., Rombach, C.S., Kelley, K.D., and Anthony, M., 2004, Nature

of hydrothermal fluids at the shale-hosted Red Dog Zn-Pb-Ag deposits, Brooks range, Alaska: Economic Geology, v. 99, p. 1449–1480.

Leach, D.L., Sangster, D., Kelley, K.D., Large, R.R., Garven, G., and Allen, C.R., 2005, Sediment-hosted lead-zinc deposits: a global perspective, *in* Hedenquist, J.W., Thompson, J.F.H., Goldfarb, R.J., and Richards, J.P. eds., 100th Anniversary Volume, Society of Economic Geologists, p. 561–607.

Leach, D.L., Bradley, D.C., Huston, D., Pisarevsky, S.A., Taylor, R.D., and Gardoll, S.J., 2010, Sediment-hosted lead-zinc deposits in Earth history: Economic Geology and the Bulletin of the Society of Economic Geologists, v. 105, p. 593–625, doi:10.2113/gsecongeo.105.3.593.

Lyons, T.W., Anbar, A.D., Severmann, S., Scott, C., and Gill, B.C., 2009, Tracking Euxinia in the Ancient Ocean: A Multiproxy Perspective and Proterozoic Case Study: Annual Review of Earth and Planetary Sciences, v. 37, p. 507–534, doi: 10.1146/annurev.earth.36.031207.124233.

Lyons, T.W., Gellatly, A.M., McGoldrick, P.J., and Kah, L.C., 2006, Proterozoic sedimentary exhalative (SEDEX) deposits and links to evolving ocean chemistry, *in* Kesler, S.E. and Ohmoto, H. eds., Evolution of Early Earth's Atmosphere, Hydrosphere, and Biosphere—Constraints from Ore Deposits, v. Geological, p. 169–184, doi: 10.1130/2006.1198(10).

Macquaker, J.H.S., Taylor, K.G., and Gawthorpe, R.L., 2007, High-Resolution Facies Analyses of Mudstones: Implications for Paleoenvironmental and Sequence Stratigraphic Interpretations of Offshore Ancient Mud-Dominated Successions: Journal of Sedimentary Research, v. 77, p. 324–339, doi: 10.2110/jsr.2007.029.

Magnall, J.M., Gleeson, S.A., Poulton, S.W., Gordon, G.W., and Paradis, S., 2018, Links between seawater paleoredox and the formation of sediment-hosted massive sulphide (SHMS) deposits — Fe speciation and Mo isotope constraints from Late Devonian mudstones: Chemical Geology, v. 490, p. 45–60, doi: 10.1016/j.chemgeo.2018.05.005.

Magnall, J.M., Gleeson, S.A., Stern, R.A., Newton, R.J., Poulton, S.W., and Paradis, S., 2016, Open system sulphate reduction in a diagenetic environment – isotopic analysis of barite ($\delta^{34}S$ and $\delta^{18}O$) and pyrite ($\delta^{34}S$) from the Tom and Jason Late Devonian Zn-Pb-Ba deposits, Selwyn Basin, Canada: Geochimica et Cosmochimica Acta, doi: 10.1016/j.gca.2016.02.015.

März, C., Poulton, S.W., Beckmann, B., Küster, K., Wagner, T., and Kasten, S., 2008, Redox sensitivity of P cycling during marine black shale formation: Dynamics of sulfidic and anoxic, non-sulfidic bottom waters: Geochimica et Cosmochimica Acta, v. 72, p. 3703–3717, doi: 10.1016/j.gca.2008.04.025.

Morelli, R.M., Creaser, R.A., Selby, D., Kelley, K.D., and King, A.R., 2004, Re-Os sulfide

geochronology of the Red Dog sediment-hosted Zn-Pb-Ag deposit, Brooks Range, Alaska: Economic Geology and the Bulletin of the Society of Economic Geologists, v. 99, p. 1569–1576, doi: 10.2113 /gsecongeo .99.7.1569.

Poulton, S.W., and Canfield, D.E., 2011, Ferruginous Conditions: A Dominant Feature of the Ocean through Earth's History: Elements, v. 7, p. 107–112, doi: 10.2113/gselements.7.2.107.

Sangster, D.F., 2018, Toward an integrated genetic model for vent-distal SEDEX deposits: Mineralium Deposita, v. 53, p. 509–527, doi: 10.1007/s00126-017-0755-3.

Schardt, C., Garven, G., Kelley, K.D., and Leach, D.L., 2008, Reactive flow models of the Anarraaq Zn–Pb–Ag deposit, Red Dog district, Alaska: Mineralium Deposita, v. 43, p. 735–757, doi: 10.1007/s00126-008-0193-3.

Schieber, J., 2003, Simple gifts and buried treasures—implications of finding bioturbation and erosion surfaces in black shales: The Sedimentary Record, v. 1, p. 4–8,

Schieber, J., and Riciputi, L., 2004, Pyrite ooids in Devonian black shales record intermittent sea-level drop and shallow-water conditions: Geology, v. 32, p. 305, doi: 10.1130/G20202.1.

Scholz, F., 2018, Identifying oxygen minimum zone-type biogeochemical cycling in Earth history using inorganic geochemical proxies: Earth-Science Reviews, v. 184, p. 29–45, doi: 10.1016/j.earscirev.2018.08.002.

Slack, J.F., Kelley, K.D., Anderson, V.M., Clark, J.L., and Ayuso, R. a., 2004a, Multistage Hydrothermal Silicification and Fe-Tl-As-Sb-Ge-REE Enrichment in the Red Dog Zn-Pb-Ag District, Northern Alaska: Geochemistry, Origin, and Exploration Applications: Economic Geology, v. 99, p. 1481–1508, doi: 10.2113/gsecongeo.99.7.1481.

Slack, J.F., Dumoulin, J.A., Schmidt, J.M., Young, L.E., and Rombach, C.S., 2004b, Paleozoic sedimentary rocks in the Red Dog Zn-Pb-Ag District and vicinity, western Brooks Range, Alaska: Provenance, deposition, and metallogenic significance: Economic Geology and the Bulletin of the Society of Economic Geologists, v. 99, p. 1385–1414, doi:10.2113 / gsecongeo .99 .7.1385.

Slack, J.F., Selby, D., and Dumoulin, J.A., 2012, A hydrothermal source for metals in the metalliferous black shales fo the Brooks Range, northern Alaska: geochemical and osmium isotope evidence: Geological Society of America Abstracts with Programs, v. 44, p. 600.

Slack, J.F., Selby, D., and Dumoulin, J.A., 2015, Hydrothermal, biogenic, and seawater components in metalliferous black shales of the Brooks Range, Alaska: Synsedimentary metal enrichment in a carbonate ramp setting: Economic Geology and the Bulletin of the Society of Economic Geologists, v. 110, p. 653–675, doi: 10.2113 /econgeo.110.3.653.

Turner, R.J.W., 1992, Formation of Phanerozoic stratiform sediment, hosted zinc-lead deposits:

Evidence for the critical role of ocean anoxia: Chemical Geology, v. 99, p. 165–188, doi:10.1016 /0009 -2541 (92) 90037-6.

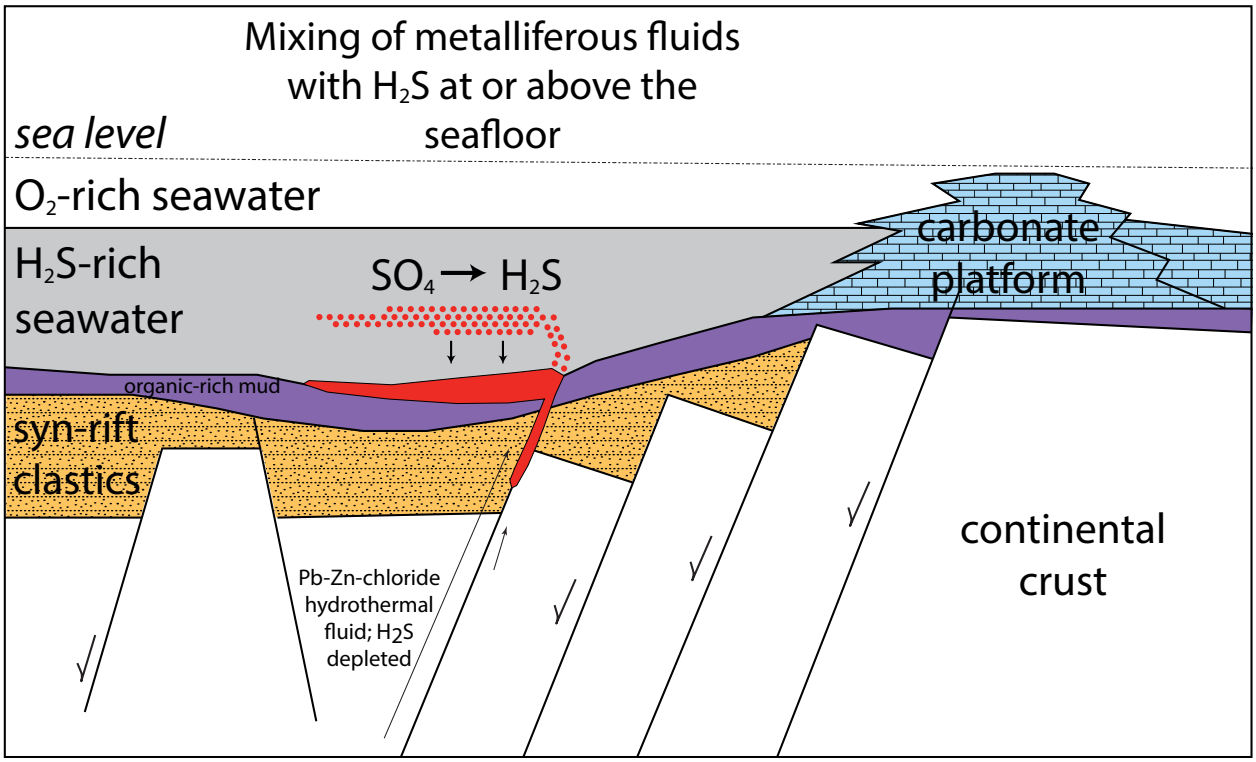

Figure 1.1: The classic model for SEDEX style mineralization. Modified after Fig. 7 in Goodfellow et al. (2007).

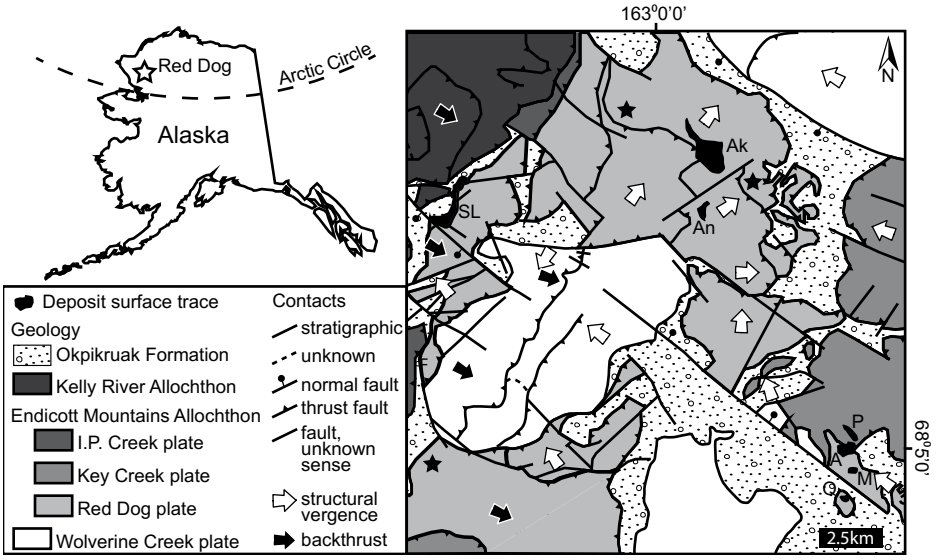

Figure 1.2: The Red Dog district is located in the Brooks fold-thrust belt of northwestern Alaska. The Mine Area includes the Main (M), Aqqaluk (A), Paalaaq (P), and Qanaiyaq (Q) deposits. Other known mineralization occurs in the Anarraaq (An), Su-Lik (SL), and Aktigiruk (Ak) deposits and several other prospects (stars). Modified after Fig. 2 in Blevings et al. (2013).

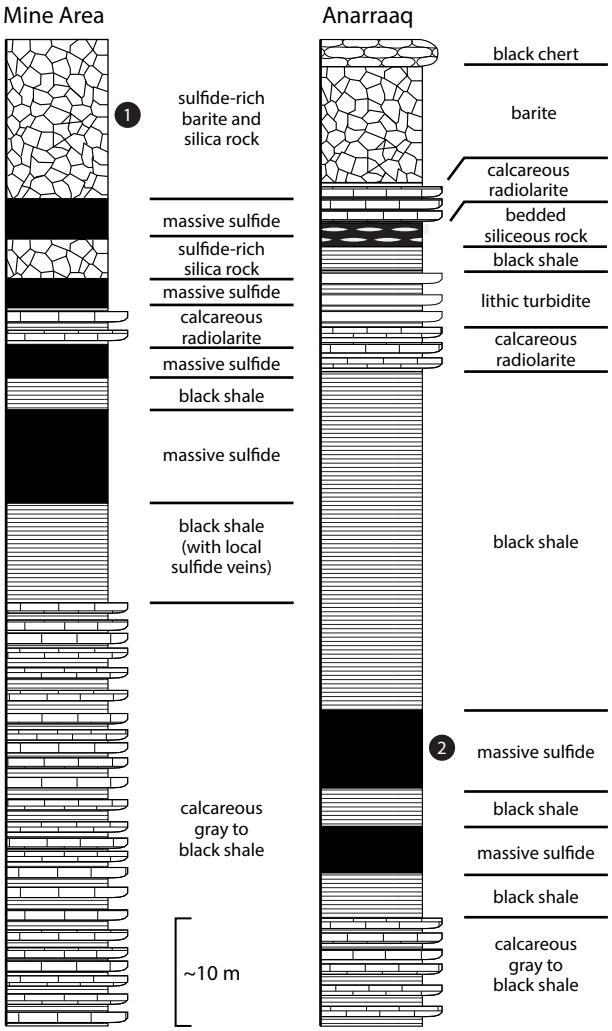

Figure 1.3: Detailed stratigraphic columns for the Kuna Formation in the Mine Area and at Anarraaq. Figure modified after Fig. 3 in Slack et al. (2004a).

Chapter 2: More than a trace of oxygen: Ichnological constraints on the formation of the giant Zn-Pb-Ag ± Ba deposits, Red Dog district, Alaska

2.1 Introduction and background

Sediment-hosted massive sulfide deposits (SHMS) are an important source of global zinc resources. The sedimentary exhalative model for these deposits (Goodfellow, 2007, and references therein) involves flow of metalliferous fluids up extensional faults and exhalation of those fluids into euxinic (anoxic, H_2S-bearing) bottom waters in a restricted marine environment. Sulfide minerals are precipitated in the water column and deposited as synsedimentary sulfide laminae. Turner (1992) linked the occurrence of sedimentary exhalative deposits and worldwide ocean anoxic events in the geologic record.

More recently, workers have noted that unequivocal evidence for exhalation is rare and the H_2S required for subseafloor sulfide formation can develop in the pore water of most marine sediments during burial and diagenesis (Leach et al., 2010). This evolution in thinking has led to the more descriptive nomenclature of SHMS deposits (e.g., Leach et al., 2010). Nevertheless, the concept of a stratified water column in a restricted basin persists as a fundamental component of the genetic models for many SHMS deposits, including those in the Red Dog district in northwestern Alaska (USA). There, although sulfide ore is now believed to be replacive, not exhalative, the idea of the restricted basin is still central to the deposit model (Fig. 2.1A; Slack et al., 2015).

The Red Dog Zn-Pb-Ag ± Ba district hosts several of the world's giant SHMS deposits. Red Dog is located in the fold-thrust belt of the Middle Jurassic to Cretaceous Brookian orogen (Fig. DR1; Blevings et al., 2013). Red Dog SHMS deposits are hosted in the upper part of the Carboniferous Kuna Formation, which comprises variably siliceous black mudstone and shale, lesser calcareous interbeds, and, locally, black chert and massive to nodular barite layers (Fig. DR2; Dumoulin et al., 2004). Sedimentological and microfossil data from regional studies of unaltered Kuna Formation strata are interpreted to indicate that sediment deposition took place in distal slope settings, the calcareous component being delivered to the slope by mass flow events (Dumoulin et al., 2004). The Kuna Formation is considered to be a distal facies of the Lisburne Group, which extends across northern Alaska and is characterized elsewhere by platformal carbonates and phosphorites (Dumoulin et al., 2014). In addition to the phosphorites, locally abundant radiolarians and high concentrations of total organic carbon are considered evidence that upwelling played an important role in the regional depositional regime (Dumoulin et al., 2014).

Bulk geochemical data from the Kuna Formation are interpreted to indicate widespread suboxic, denitrifying bottom-water conditions (Dumoulin et al., 2014). A range of Cr/V (marine

fraction) values may indicate rare transitory occurrence of slightly oxidizing conditions as well as some mixing with anoxic or sulfidic bottom waters (Dumoulin et al., 2014), but the spatial-temporal relationship between these samples and Red Dog ore zones is not clear. Slack et al. (2004, p. 1406) reported five samples enriched in MnO in relatively close proximity to known sulfide ore (but still more than 65 m stratigraphically above the Anarraaq sulfide deposit) and suggested that these samples formed in oxic depositional conditions "on topographic highs above one or more basin-scale, anoxic-oxic boundaries in the water column."

Sulfide ore in the mine area deposits has been dated as coeval, within error, of the upper Kuna Formation (Morelli et al., 2004). Most sulfide ore appears to be hosted by organic-rich mudstone of the Ikalukrok unit (a local name for the upper Kuna Formation), although few primary sedimentary textures are preserved within the mineralized zones. Exceptions include the Anarraaq deposit, where Kelley et al. (2004a) suggested that ore replaced calcareous debrites during early diagenesis, and some parts of the mine area deposits, where Kelley et al. (2004b) reported local replacement of barite by sulfide minerals. Although subseafloor replacement is accepted to have played an important role in most of the Red Dog district sulfide deposits, workers still visualize this happening below the stratified waters of a restricted basin (e.g., Slack et al., 2015).

Bioturbation is present in several Red Dog ore zones and related hydrothermally altered zones rich in barite and quartz. These trace fossils have been interpreted to be formed by vent-associated alvinellid worms (Moore et al., 1986), methane-seep fauna (Johnson et al., 2004), annelid-like organisms (Kelley et al., 2004b), and shallower water organisms transported to the slope by gravity flows (Dumoulin et al., 2004). Dumoulin et al. (2014, p. 220) mentioned that "burrowed intervals found locally in the Kuna Formation demonstrate that oxygen levels at the sediment-water interface were locally or periodically high enough to support soft-bodied infauna" and that these intervals are interpreted to be most common close to the basin margins, but they did not describe, name, or discuss these features. We present some new observations of the Red Dog trace fossils with important implications for interpreting the paleodepositional environment of sediment hosting Red Dog deposits and the model for ore formation.

2.2 Trace fossil observations

Two types of trace fossils occur in the Red Dog deposits (Fig. 2.2). Both show consistent diameter along observable lengths and circular cross sections, attesting to their biogenicity. In the best preserved samples, the intensity of bioturbation ranges from 4 to 6 on the Bioturbation Index of Taylor et al. (2003).

The smaller burrows are ~0.5 mm in diameter and have no lining (Fig. 2.2). These traces branch and crosscut each other (Figs. 2.2A and 2.2B; Fig. DR3A), have no preferred orientation, and are pervasive where the bioturbated texture is preserved. The smaller burrows are composed

of quartz in a matrix of sphalerite, pyrite, quartz, and/or barite. Rare specimens are rimmed in sphalerite (Fig. 2.2C; Fig. DR4A): these features are interpreted to be reactive boundaries between trace and matrix and not linings because the same feature is present at the perimeter of some of the larger burrow linings (Fig. DR4A).

The larger ichnofossils are 3–10 mm in internal diameter with an additional 1–2-mm-thick lining. These trace fossils are sinuous in plan form (Fig. 2.2A), do not branch or crosscut, and range from approximately bedding parallel to inclined in orientation. The larger trace fossils are sparse and characteristically form clusters of several trace fossils, commonly in association with the smaller burrows. The burrow linings are commonly composed of dark gray quartz (Figs. 2.2C and 2.2D) but are locally replaced by sulfide (Fig. 2.2C; Fig. DR4C). Burrow infill is similar to the local matrix in mineralogy and texture and can be composed of quartz, disseminated sulfides, and/or barite.

Drill core logs indicate that the larger burrows are common in intervals 40–50 m thick (locally >80 m) in the Aqqaluk and Main deposits of the mine area, although the contribution of structural thickening is unknown. Preserved bioturbated fabrics are less common in the Anarraaq deposit. There is no evidence of bioturbation in the Kuna Formation beyond the ore zones or the barite- and quartz-rich rocks in the mine area deposits.

2.3 Interpretation and discussion

The smaller of the two types of burrows has received little attention from other workers. Moore et al. (1986, p. 1714) suggested that they are "fecal pellets, algal debris, or bacterial clumps." Because the best-preserved examples are branching (Fig. 2.2B; Fig. DR3A), we reinterpret them to be the trace fossil *Chondrites* isp. *Chondrites* occurs in a wide variety of depositional settings, ranging from the innermost shelf (e.g., Hertweck et al., 2007) to basinal (e.g., Bromley and Ekdale, 1984). Penetrative (i.e., three dimensional) *Chondrites*-dominated ichnofossil assemblages (as observed in the samples from Red Dog) exemplify middle to outer shelf environments, where O_2 is reduced but not absent (MacEachern et al., 2010; Savrda, 1995; Ekdale, 1988). The pervasive bioturbation associated with the observed *Chondrites* is consistent with long-term substrate colonization and high infaunal population densities (Gingras et al., 2008).

The larger type of trace fossil has a simple sinuous morphology, unornamented lining, and is variably oriented, and is therefore best described by the ichnogenus *Schaubcylindrichnus* (Fig. DR6). Because all the samples in this study have undergone intense hydrothermal alteration and barite, quartz, and /or sulfide mineralization, we have not classified these trace fossils to the ichnospecies level. *Schaubcylindrichnus* occurs in a range of depositional environments from the lower shoreface to the shelf, but is most common in proximal inner shelf settings (Campbell et al., 2006). No fossil assemblages with

only *Chondrites* and *Schaubcylindrichnus* are reported in the literature, but the two traces commonly occur together with additional trace types in shelfal locales (Campbell et al., 2006). That additional traces are not present at Red Dog suggests either low diversity of trace makers or selective preservation of the *Chondrites* and *Schaubcylindrichnus* trace fossils.

The Red Dog ichnofossils assigned here to *Schaubcylindrichnus* were previously reported. Moore et al. (1986) interpreted them to be the product of vent-associated worms, but such worm tubes (e.g., Little et al., 1999) differ from those at Red Dog in that they do not conform to bedding, the original burrows are many times smaller than the surrounding linings, and the linings are more irregular. Johnson et al. (2004) proposed that the burrows were produced by organisms living in methane seep environments. However, the worm tubes reported in modern and fossil cold seeps are serpulidae or vestimentiferans and almost always occur in megafaunal communities of bivalves and/or gastropods (Campbell, 2006, and references therein), neither of which are present at Red Dog. Kelley et al. (2004b, p. 1517) suggested that the burrows were secreted by "annelid-like organisms" (e.g., serpulid tubes) "that lived in a variety of settings within the Kuna basin". Serpulid tubes are body fossils consisting of biogenic aragonite or calcite that possess ornamentation, coil or interweave around each other, and encrust hardgrounds or colonize softgrounds by forming a wide base (e.g., an open spiral) that prevents the tube from sinking into the mud (Jaeger, 2012). All of these traits are absent from the Red Dog traces.

The exclusive occurrence of trace fossils within the sulfide deposits at Red Dog suggests that bioturbation-enhanced sediment permeability may have had a significant control on subsurface fluid flow and the resulting distribution of ore. Enhanced sediment permeability due to bioturbation is common (Gingras et al., 1999) and has gained increasing attention in the petroleum industry because it can affect reservoir volumes and production performance (e.g., increasing bulk permeability by three orders of magnitude; Pemberton and Gingras, 2005). At Red Dog, traces rarely appear to have undergone compaction; this may indicate that hydrothermal fluids were introduced soon after sedimentation. Barite mineralization predates the introduction of ore-stage sulfide minerals and quartz (Kelley et al., 2004b), and may have locally reduced the permeability of bioturbated zones through early cementation. This could explain the presence of barite-rich, sulfide-poor zones in some deposits (e.g., Figs. 2.2A and 2.2B). An alternative explanation for the spatial correlation between bioturbation and the sulfide deposits is that barite and/or sulfide mineralization locally preserved what was initially more widespread bioturbation. However, it is difficult to impossible to determine which hypothesis is more accurate.

The presence of *Schaubcylindrichnus* and *Chondrites* suggests that at least part of the Kuna Formation hosting Red Dog SHMS deposits accumulated in bathymetries consistent with an oxygenated middle to outer shelf environment (Fig. 2.1B). That only two types of ichnofossil

are identifiable may suggest that diversity was limited. Reductions in ichnogenera diversities, reduced trace fossil abundances, decreasing burrow diameters, and decreasing depth of burrow penetration into the substrate can be the result of lowered O_2 conditions (Rhoads and Morse, 1971; Savrda and Bottjer, 1994). Although the Red Dog ichnofossil assemblage shows reduced diversity, the high trace fossil abundance, the large diameters of *Schaubcylindrichnus*, and the penetrative nature of burrowing support oxic conditions.

Although some rare geochemical evidence for oxic conditions in the Kuna Formation has been reported (Dumoulin et al., 2014; Slack et al., 2004), it does not occur in close spatial association with the Red Dog ore deposits. Dumoulin et al. (2014) and Slack et al. (2004) envisioned the Red Dog deposits forming in the deep, stratified waters of a restricted subbasin with oxygenated conditions occurring only rarely at the basin margins (Fig. 1A). Our data instead support a model whereby middle to outer shelfal sediment experienced oxygenated conditions prior to barite or sulfide mineralization. There is abundant evidence for upwelling in the form of regionally abundant radiolarians and phosphorites (Dumoulin et al., 2014); in modern continental margins where upwelling occurs, oxygen minimum zones commonly form and can fluctuate in depth on relatively short time scales (e.g., Gutiérrez et al., 2008). Such a setting could account for the interlayering of variably organic-rich mudstone with little to no bioturbation and intensely bioturbated layers as well as the variability reported in geochemical redox proxies.

2.4 Conclusions

The presence of the trace fossils *Schaubcylindrichnus* and *Chondrites* in Red Dog SHMS deposits suggests that host sediment was deposited in a middle to outer shelf environment. Despite the apparent low diversity of trace fossil types, the abundance and penetrative nature of traces and the large diameters of *Schaubcylindrichnus* indicate that host sediment was deposited under an oxygenated water column. That burrow linings and infill are replaced with barite, hydrothermal quartz, and sulfide, and lack evidence for compaction, suggests that hydrothermal fluids entered sediment soon after deposition. To reconcile these data with previous interpretations of bulk-rock geochemical data and abundant regional evidence for upwelling, we propose a new model for the Red Dog district SHMS deposits in which host sediment was deposited in a shelfal environment under fluctuating redox conditions created by an oxygen minimum zone.

2.5 Acknowledgements

This work was funded by Teck Resources Limited and by a Collaborative Research and Development grant from the Natural Sciences and Engineering Research Council of Canada. We thank the geologists active in the Red Dog district (Alaska) for technical assistance and

geological discussions and M. Hitzman, P. Gammon, and an anonymous reader for thoughtful reviews.

2.6 References

Blevings, S., Kraft, J., Stemler, J., and Krolak, T., 2013, An overview of the structure, stratigraphy, and Zn-Pb-Ag deposits of the Red Dog District, northwestern Alaska, *in* Colpron, M., et al., eds., Tectonics, metallogeny, and discovery: The North American Cordillera and similar accretionary settings: Society of Economic Geologists Special Publication 17, p. 361–387.

Bromley, R., and Ekdale, A., 1984, *Chondrites*: A trace fossil indicator of anoxia in sediments: Science, v. 224, p. 872–874, doi:10.1126 /science .224 .4651.872.

Campbell, K.A., 2006, Hydrocarbon seep and hydrothermal vent paleoenvironments and paleontology: Past developments and future research directions: Palaeogeography, Palaeoclimatology, Palaeoecology, v. 232, p. 362–407, doi: 10.1016 /j .palaeo .2005 .06.018.

Campbell, K.A., Nesbitt, E.A., and Bourgeois, J., 2006, Signatures of storms, oceanic floods and forearc tectonism in marine shelf strata of the Quinault Formation (Pliocene), Washington, USA: Sedimentology, v. 53, p. 945–969, doi: 10.1111 /j .1365 -3091 .2006 .00788.x.

Dumoulin, J.A., Harris, A.G., Blome, C.D., and Young, L.E., 2004, Depositional settings, correlation, and age of Carboniferous rocks in the western Brooks Range, Alaska: Economic Geology and the Bulletin of the Society of Economic Geologists, v. 99, p. 1355–1384, doi:10.2113 /gsecongeo .99.7.1355.

Dumoulin, J.A., Johnson, C.A., Slack, J.F., Bird, K.J., Whalen, M.T., Moore, T.E., Harris, A.G., and Sullivan, P.B.O., 2014, Carbonate margin, slope, and basin facies of the Lisburne Group (Carboniferous–Permian) in northern Alaska, *in* Verwer, K., et al., eds., Deposits, architecture, and controls of carbonate margin, slope, and basinal settings: SEPM (Society for Sedimentary Geology) Special Publication 105, p. 211–236.

Ekdale, A.A., 1988, Pitfalls of paleobathymetric interpretations based on trace fossil assemblages: Palaios, v. 3, p. 464–472, doi:10.2307/3514720.

Gingras, M.K., Pemberton, S.G., Mendoza, C.A., and Henk, F., 1999, Assessing the anisotropic permeability of Glossifungites surfaces: Petroleum Geoscience, v. 5, p. 349–357, doi:10.1144/petgeo .5 .4.349.

Gingras, M.K., Pemberton, S.G., Dashtgard, S., and Dafoe, L., 2008, How fast do marine invertebrates burrow?: Palaeogeography, Palaeoclimatology, Palaeoecology, v. 270, p. 280–286, doi:10.1016 /j .palaeo .2008 .07.015.

Goodfellow, W.D., 2007, Base metal metallogeny of the Selwyn Basin, Canada, *in* Goodfellow,

W., ed., Mineral deposits of Canada: A synthesis of major deposit-types, district metallogeny, the evolution of geological provinces, and exploration methods: Geological Association of Canada, Mineral Deposits Division, Special Publication 5, p. 553–579.

Gutiérrez, D., Enríquez, E., Purca, S., Quipúzcoa, L., Marquina, R., Flores, G., and Graco, M., 2008, Oxygenation episodes on the continental shelf of central Peru: Remote forcing and benthic ecosystem response: Progress in Oceanography, v. 79, p. 177–189, doi:10.1016/j .pocean .2008 .10.025.

Hertweck, G., Wehrmann, A., and Liebezeit, G., 2007, Bioturbation structures of polychaetes in modern shallow marine environments and their analogues to *Chondrites* group traces: Palaeogeography, Palaeoclimatology, Palaeoecology, v. 245, p. 382–389, doi:10.1016/j .palaeo .2006 .09.001.

Jaeger, M., 2012, Sabellids and serpulids (Polychaeta sedentaria) from the type Maastrichtian, the Netherlands and Belgium, *in* Jagt, J.W.M., et al., eds., Fossils of the type Maastrichtian (Part 1): Scripta Geologica Special Issue 8, p. 45–81.

Johnson, C.A., Kelley, K.D., and Leach, D.L., 2004, Sulfur and oxygen isotopes in barite deposits of the western Brooks Range, Alaska, and implications for the origin of the Red Dog massive sulfide deposits: Economic Geology and the Bulletin of the Society of Economic Geologists, v. 99, p. 1435–1448, doi:10.2113 /gsecongeo .99.7 .1435.

Kelley, K.D., Dumoulin, J.A., and Jennings, S., 2004a, The Anarraaq Zn-Pb-Ag and barite deposit, northern Alaska: Evidence for replacement of carbonate by barite and sulfides: Economic Geology and the Bulletin of the Society of Economic Geologists, v. 99, p. 1577–1591, doi: 10.2113 /gsecongeo .99.7.1577.

Kelley, K.D., Leach, D.L., Johnson, C.A., Clark, J.L., Fayek, M., Slack, J.F., Anderson, V.M., Ayuso, R.A., and Ridley, W.I., 2004b, Textural, compositional, and sulfur isotope variations of sulfide minerals in the Red Dog Zn-Pb-Ag deposits, Brooks Range, Alaska: Implications for ore formation: Economic Geology and the Bulletin of the Society of Economic Geologists, v. 99, p. 1509–1532, doi:10.2113 /gsecongeo .99 .7 .1509.

Leach, D.L., Bradley, D.C., Huston, D., Pisarevsky, S.A., Taylor, R.D., and Gardoll, S.J., 2010, Sediment-hosted lead-zinc deposits in Earth history: Economic Geology and the Bulletin of the Society of Economic Geologists, v. 105, p. 593–625, doi:10.2113/ gsecongeo.105.3.593.

Little, C.T.S., Maslennikov, V.V., Morris, N.J., and Gubanov, A.P., 1999, Two Palaeozoic hydrothermal vent communities from the southern Ural Mountains, Russia: Palaeontology, v. 42, p. 1043–1078, doi:10.1111/1475-4983.00110.

MacEachern, J.A., Pemberton, S.G., Gingras, M.K., and Bann, K.L., 2010, Ichnology and facies models, *in* James, N.P., and Dalrymple, R.W., eds., Facies models 4: St. John's,

Newfoundland, Geological Association of Canada, p. 19–58.

Moore, D.W., Young, L.E., Modene, J.S., and Plahuta, J.T., 1986, Geologic setting and genesis of the Red Dog zinc-lead-silver deposit, western Brooks Range, Alaska: Economic Geology and the Bulletin of the Society of Economic Geologists, v. 81, p. 1696–1727, doi:10.2113/gsecongeo .81 .7.1696.

Morelli, R.M., Creaser, R.A., Selby, D., Kelley, K.D., and King, A.R., 2004, Re-Os sulfide geochronology of the Red Dog sediment-hosted Zn-Pb-Ag deposit, Brooks Range, Alaska: Economic Geology and the Bulletin of the Society of Economic Geologists, v. 99, p. 1569–1576, doi: 10.2113 /gsecongeo .99.7.1569.

Pemberton, S.G., and Gingras, M.K., 2005, Classification and characterizations of biogenically enhanced permeability: American Association of Petroleum Geologists Bulletin, v. 89, p. 1493–1517, doi:10.1306/07050504121.

Rhoads, D.C., and Morse, J.W., 1971, Evolutionary and ecological significance of oxygen-deficient marine basins: Lethaia, v. 4, p. 413–428, doi: 10.1111 /j .1502 -3931 .1971. tb01864.x.

Savrda, C.E., 1995, Ichnologic applications in paleoceanographic, paleoclimatic, and sea-level studies: Palaios, v. 10, p. 565–577, doi: 10.2307/3515095.

Savrda, C.E., and Bottjer, D.J., 1994, Ichnofossils and ichnofabric in rhythmically bedded pelagic/ hemipelagic carbonates: Recognition and evaluation of benthic redox and scour cycles, *in* de Boer, L., and Smith, D.G., eds., Orbital forcing and cyclic sequences: International Association of Sedimentologists Special Publication 19, p. 195–210, doi:10.1002/9781444304039.ch15.

Slack, J.F., Dumoulin, J.A., Schmidt, J.M., Young, L.E., and Rombach, C.S., 2004, Paleozoic sedimentary rocks in the Red Dog Zn-Pb-Ag District and vicinity, western Brooks Range, Alaska: Provenance, deposition, and metallogenic significance: Economic Geology and the Bulletin of the Society of Economic Geologists, v. 99, p. 1385–1414, doi:10.2113 / gsecongeo .99 .7.1385.

Slack, J.F., Selby, D., and Dumoulin, J.A., 2015, Hydrothermal, biogenic, and seawater components in metalliferous black shales of the Brooks Range, Alaska: Synsedimentary metal enrichment in a carbonate ramp setting: Economic Geology and the Bulletin of the Society of Economic Geologists, v. 110, p. 653–675, doi: 10.2113 /econgeo.110.3.653.

Taylor, A., Goldring, R., and Gowland, S., 2003, Analysis and application of ichnofabrics: Earth-Science Reviews, v. 60, p. 227–259, doi: 10.1016/S0012 -8252 (02) 00105-8.

Turner, R.J.W., 1992, Formation of Phanerozoic stratiform sediment, hosted zinc-lead deposits: Evidence for the critical role of ocean anoxia: Chemical Geology, v. 99, p. 165–188, doi:10.1016 /0009 -2541 (92) 90037-6.

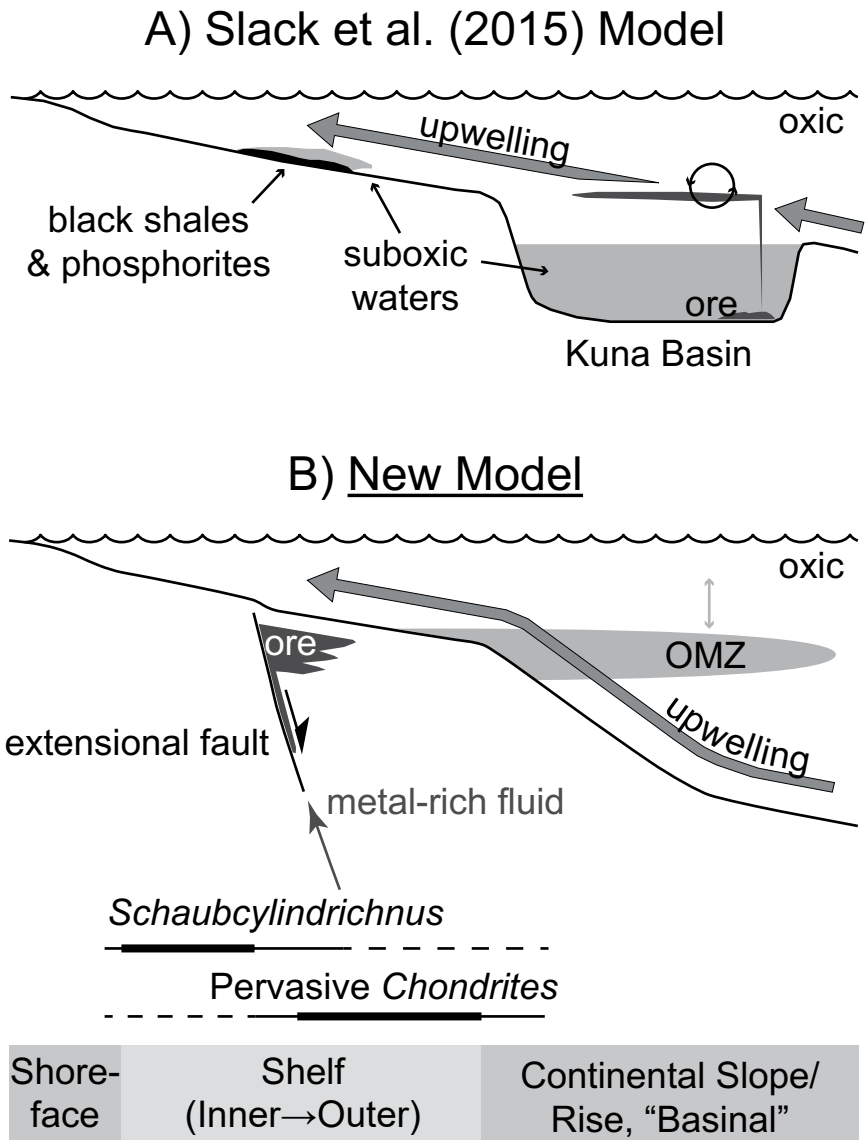

Figure 2.1: (a) The existing model for host sediment deposition in the Red Dog district, Alaska, USA (modified from Slack et al., 2015). (b) A new model that takes into account the typical depositional environments of *Schaubcylindrichnus* and pervasive *Chondrites* (thicker line indicates a more common association) and invokes a fluctuating oxygen minimum zone (OMZ) to explain variable redox conditions of host sediment. Zones of upwelling water do not necessarily crosscut the OMZ, as shown in this figure; the two zones more likely occur with some lateral offset along the shelf.

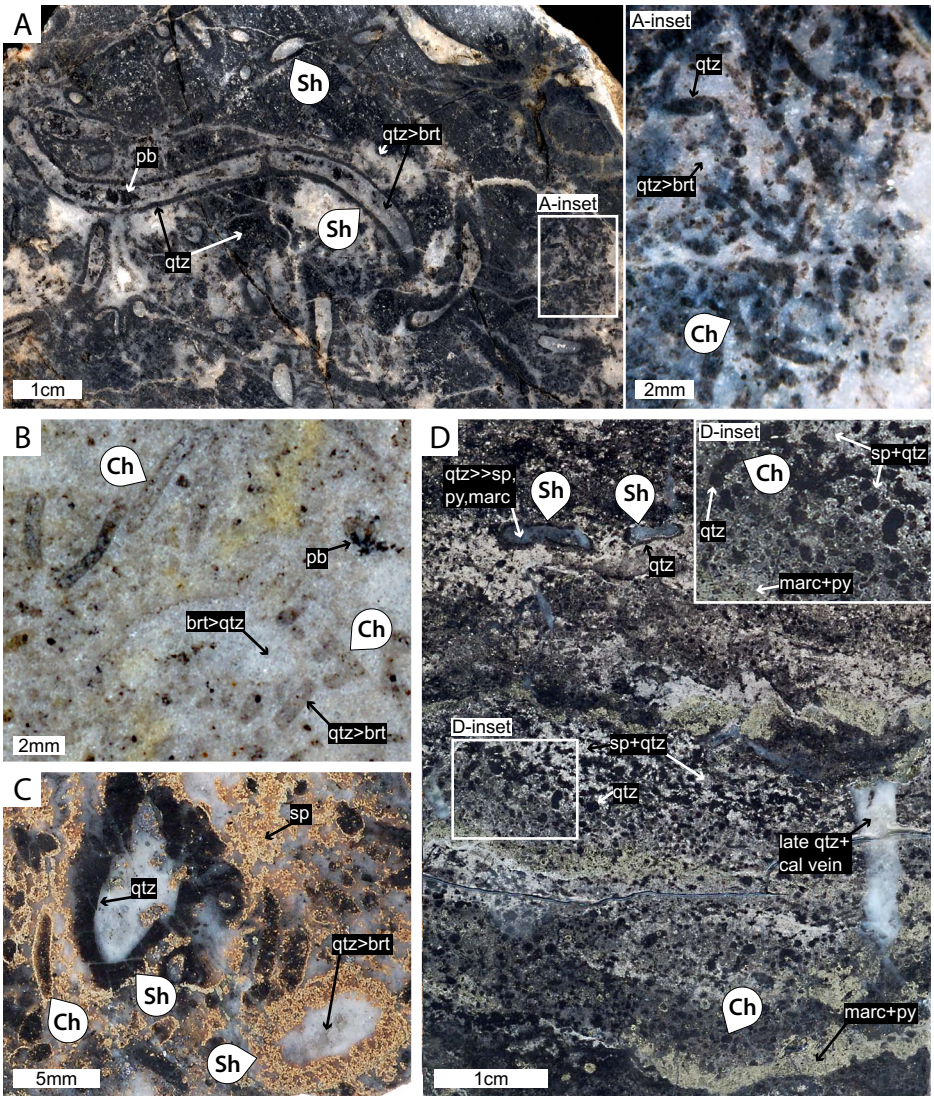

Figure 2.2: (a) Bedding-parallel polished slab from Qanaiyaq deposit (Alaska) containing abundant *Shaubcylindrichnus* (Sh) and *Chondrites* (Ch). Note branching *Chondrites* indicated in inset. Abbreviations: qtz—quartz, brt—barite, pb—pyrobitumen. (b) Bedding-parallel polished slab from Qanaiyaq containing *Chondrites*. Note branching *Chondrites* indicated at right. Yellow coloration is surficial staining. (c) Polished slab of unknown orientation from Aqqaluk sulfide deposit containing *Schaubcylindrichnus* and *Chondrites* (sp—sphalerite). (d) Polished core in depositional orientation from Anarraaq sulfide deposit containing *Schaubcylindrichnus* and *Chondrites*. Abbreviations: py—pyrite, marc—marcasite, cal—calcite. Additional samples and more detailed descriptions are provided in Figures DR3 and DR4.

Chapter 3: The impact of diagenetic processes on sediment-hosted massive sulfide ore distribution: Geochronological, stratigraphic, textural, and petrographic relationships between silica, barite and sulfides in the Anarraaq Zn-Pb-Ag deposit, Red Dog District, Alaska

3.1 Introduction

The Red Dog district in northwestern Alaska contains several world-class sediment-hosted massive sulfide (SHMS) Zn-Pb deposits (Fig. 3.1; Blevings et al., 2013). Barite and Fe sulfide (pyrite and marcasite) are common components of the Red Dog SHMS deposits. Importantly, barite produces a strong gravity anomaly that has proven to be a powerful tool in exploration of the district (Blevings et al., 2013). However, barite and Zn-Pb-Fe sulfides also occur independent of each other and Fe sulfide is the dominant component in some low-grade Zn-Pb prospects in the Red Dog district (Fig. 3.1; Kelley and Jennings, 2004; Blevings et al., 2013). The genetic controls on the varying relationships of the three components are not well understood.

Barite in the Red Dog district is thought to have formed when diagenetic fluids enriched in methane and barium vented into sulfate-bearing bottom waters or shallow pore waters (Johnson et al., 2004; Ayuso et al., 2004; Johnson et al., 2009). This type of environment is commonly referred to as a cold methane seep (Suess, 2014). Baritic cold methane seeps generally form on continental margins with abundant biogenic productivity in the overlying water column (Torres et al., 2003). There, biologically mediated barite precipitation in the water column results in relatively high concentrations of 'biogenic' barite in organic-rich, and commonly opal-rich, sediment (Bishop, 1988; Paytan et al., 1993). Degradation of organic matter during burial creates strongly reducing, methane-rich pore waters that dissolve the biogenic barite despite its low solubility (Brumsack, 1986; Torres et al., 1996). Where these fluids migrate into sulfate-bearing seawater or shallow pore waters, barite re-precipitates (Brumsack, 1986; Torres et al., 1996, 2003).

Because barium is transported in methane-bearing fluids, barite precipitation is closely linked to an important biological process, sulfate-driven anaerobic oxidation of methane (SD-AOM), which proceeds by the reaction (Eq. 1; Barnes and Goldberg, 1976; Reeburgh, 1976):

$$CH_4 + SO_4^{2-} \rightarrow HCO_3^- + HS^- + H_2O \quad \text{(Eq. 1)}$$

Sulfate-driven anaerobic oxidation of methane commonly takes place below the sediment surface in a zone called the sulfate-methane transition (SMT; Iversen and Jørgensen, 1985). There, upward diffusing methane and downward diffusing seawater sulfate are depleted by SD-AOM (Iversen and Jørgensen, 1985). Diagenetic barite precipitates just above the SMT (Dickens,

2001), where the absence of methane and the presence of sulfate result in a decrease in the solubility of barium. Sulfate-driven AOM is also associated with precipitation of diagenetic carbonate (e.g., Paull et al., 1992) and pyrite (Q. Lin et al., 2016; Z. Lin et al., 2016), and with the dissolution, migration, and reprecipitation of opaline silica (Smrzka et al., 2015).

Recent work has shown that the Tom and Jason SHMS deposits at Macmillan Pass (Magnall et al., 2016) contain pre-ore barite and pyrite formed at the SMT and that strata hosting SHMS mineralization at Howards Pass (Johnson et al., 2018) contain methane-derived diagenetic pyrite and carbonate. At Red Dog, Kelley et al. (2004a) proposed that thermogenic reductive dissolution of early barite provided an important source of S for later hydrothermal mineralization in the mine area deposits (Qanaiyaq, Main, Aqqaluk, and Paalaaq; Fig. 3.1). Furthermore, Johnson et al. (2004) recognized the link between barite precipitation and SD-AOM as a possible source of reduced sulfide (HS^-) for Zn-Pb ore formation but neither group of workers considered how methane-derived carbonate and pyrite may have altered Red Dog host sediment prior to hydrothermal mineralization. Much about the role of pre-ore diagenetic processes in the formation of Red Dog SHMS deposits remains poorly understood.

The Anarraaq area of the Red Dog district is an ideal place to investigate these relationships as it contains both a sulfide-only deposit and a barite-only body (Kelley et al., 2004b). An additional advantage to studying this area is that recent drilling campaigns offer fresh drill core. The Anarraaq sulfide deposit contains an inferred resource of 19.4 Mt at 14.4% Zn, 4.2% Pb, and 73.4 ppm Ag (Krolak et al., 2017). The overlying Anarraaq barite body contains as much as 1 Gt of barite and is separated from the sulfide deposit by 20-60 m of barren host rock (Kelley et al., 2004b). Kelley et al. (2004b) reported only rare barite in the Anarraaq sulfide deposit or in laterally equivalent strata, concluding that it was “unlikely that the sulfides replaced barite” (p. 1586). They instead interpret sulfide to have replaced carbonate debrites (Kelley et al., 2004b).

In this study, we present new petrographic data from the Anarraaq barite body and the Anarraaq sulfide deposit. The barite body is not overprinted by Zn-Pb mineralization and therefore provides insight into how methane-driven diagenetic processes (beyond simple barite precipitation) altered the host sediment. We then consider how pre-existing diagenetic phases affected the formation of the Anarraaq sulfide deposit and other giant sulfide deposits in the Red Dog district. Rhenium-osmium (Re-Os) isotope geochemistry is used to constrain the age of the Anarraaq sulfide deposit relative to host sediment, pre-ore diagenetic alteration, and other Red Dog deposits.

3.2 Geological Setting

The Red Dog district lies within the Arctic Alaska terrane, which comprises Devonian to Jurassic sedimentary rocks deposited on a passive continental margin (Moore et al., 1986,

1994). The area underwent significant shortening during the late Jurassic to Cretaceous Brookian orogeny, when the terrane collided with an intraoceanic island arc (Moore et al., 1986, 1994). District geology is characterized by extensive thrusting, folding, and very low grade metamorphism (De Vera et al., 2004) and is mapped according to a framework of tectonic packages of varying scales (Fig. 3.1; Young, 2004; Blevings et al., 2013). All known SHMS mineralization in the Red Dog district is hosted in the Red Dog thrust sheet of the Endicott Mountains allochthon (Figs. 3.1, 3.2; Blevings et al., 2013). In the Anarraaq area, structural vergence is to the northeast (Fig. 3.1; De Vera, 2005) and thrust faults are offset by steeply dipping tear faults that accommodate variable lateral displacement (Fig. 3.3; Blevings et al., 2013).

The Red Dog SHMS deposits are hosted in the Ikalukrok unit of the upper part of the Mississippian Kuna Formation. The Ikalukrok unit primarily comprises black mudstone, shale, and chert; lesser calcareous intervals (Dumoulin et al., 2004); contains local intervals of massive, laminated, and nodular barite (Johnson et al., 2004); and minor igneous intrusions (Young, 2004). Ikalukrok sediment is characterized by high concentrations of organic carbon, silicon, and phosphate, and abundant radiolarians (Slack et al., 2004a; Dumoulin et al., 2004, 2014). The Kuna Formation is the deep-water facies of the Lisburne Group and was deposited in a sediment-starved, extensional basin flanked by carbonate platforms (Young, 2004). Upwelling of nutrient-rich waters played an important role in the regional depositional regime (Dumoulin et al., 2014) and may have given rise to a fluctuating oxygen minimum zone that resulted in variable redox conditions (Reynolds et al., 2015). The calcareous component of the Ikalukrok unit is thought to originate from the erosion of adjacent carbonate platforms (Dumoulin et al., 2004) and the igneous intrusions are linked to extensional and transtensional deformation (Young, 2004).

The model for Red Dog SHMS mineralization involves a saline brine (14-19 wt. % NaCl equiv) that originated from evaporated seawater and was heated to 100-200°C as it circulated though the subsurface (Leach et al., 2004). The hydrothermal fluid scavenged metals from the fluvial-deltaic sandstones and conglomerates of the Endicott Group, which underlies the Kuna Formation (Young et al., 2004). The hydrothermal fluid flowed into the shallow subsurface via extensional faults and there replaced Ikalukrok sediment (Kelley et al., 2004a; Kelley et al., 2004b). Ore-stage pyrite in the Main deposit has been dated at 338.3 ± 5.8 Ma, which is coeval within uncertainty to the biostratigraphic age of the upper Kuna Formation (Morelli et al., 2004). In many mineralized zones, the intensity of mineralization makes it difficult or impossible to identify the original composition of the host sediment. However, barite replacement is evident in the mine area deposits (Kelley et al., 2004a) and carbonate replacement may have been an important ore-forming process at Anarraaq (Kelley et al., 2004b).

3.3 Methods

3.3.1 Petrography and sections

The petrographic observations reported in this study are drawn from the detailed re-logging of 13 drill cores along 2 sections through the Anarraaq area (Fig. 3.3), more than 500 samples of cut core, and more than 80 thin sections. Re-logging included painting cores with a dilute hydrochloric acid solution containing alizarin red S and potassium ferricyanide to allow for rapid identification of carbonate phases (Hitzman, 1999). In addition to detailed hand sample and thin-section petrographic descriptions, scanning electron microscopy (SEM) was used to characterize microscopic textural relationships, and energy dispersive spectroscopy (EDS) and Raman spectroscopy were used to confirm mineralogy. Additional lithological and textural details for drill core not re-logged in this campaign were drawn from original logs and, where available, from high resolution photographs of boxes of fresh core.

3.3.2 Whole rock geochemistry

Four sub-samples of the black shale sample 923-2123 were sent to Bureau Veritas Commodities Canada Ltd. in Vancouver, British Columbia for analysis of whole rock geochemical composition. There, samples were pulverized to 85% with a particle size less than 74 μm. For analysis of major oxides and refractory and rare earth elements, sample powders were fused with lithium metaborate/tetraborate and analyzed by X-ray fluorescence and inductively coupled plasma-mass spectrometry (ICP-MS), respectively. Concentrations of additional trace elements were determined on powders digested by aqua regia and analyzed by ICP-MS. Carbon and sulfur contents were determined by LECO analysis.

3.3.3 Re–Os sampling and analytical methods

This study used material from three intervals of drill core from Anarraaq (Fig. 3.4). Sample 923-2123 is composed of black shale with disseminated pyrite and minor quartz-calcite veinlets (Fig. S3.1A) and was located approximately 12 m above the Anarraaq sulfide deposit. The veinlets and macroscopic accumulations of pyrite were avoided during sub-sampling of the shale. Sample 1716-2520.8 is from within the Anarraaq sulfide deposit and is composed of black mudstone with diagenetic pyrite nodules (Fig. S3.1B). Although this sample contains no apparent ore-stage hydrothermal overprint, the pyrite nodules are crosscut by minor quartz veinlets. The pre-ore pyrite nodules were sub-sampled with care to exclude any quartz veinlets or mudstone. Sample 1723-2104.5 is also from within the Anarraaq sulfide deposit and is primarily composed of hydrothermal pyrite and calcite precipitated within a large vein (Fig. S3.1C). The ore-stage pyrite in this sample has two distinct textures; only the more abundant colloform pyrite was sub-sampled.

The Re-Os analyses were carried out at the Crustal Re-Os Geochronology Laboratory of

the Department of Earth and Atmospheric Sciences, University of Alberta, Canada. Each shale or pyrite sub-sample was cut from original core material using a rock saw and then polished to remove any residue left by the saw. Shale samples were then powdered in an agate mill whereas pyrite samples were manually crushed using ceramics to a size of approximately 1-5 mm and hand-picked under a stereoscope to remove any impurities. Several hundred milligrams of sample were then added to a Carius tube with a known amount of ^{185}Re and ^{190}Os spike solution and 8 mL of Cr(VI)-H_2SO_4 (for shales) or 2 mL of 10 N HCl and 6 mL 16 N HNO_3 (for pyrite). The Carius tubes were sealed and heated to 220 °C for 48 (pyrite) to 72 hours (shales) to ensure sample-spike equilibration. Additional details of the chemical procedures for sample digestion and purification of Re and Os are provided by Selby and Creaser (2003) and Hnatyshin et al. (2016).

The abundance and isotopic composition of Re and Os were determined by isotope dilution-negative thermal ionization mass spectrometry (ID-TIMS) with a ThermoScientific Triton TIMS under conditions comparable to those of Hnatyshin et al. (2016) to ensure a stable ion beam. Data were reduced according to the method of Kendall et al. (2004) whereby two-sigma uncertainties for $^{187}Re/^{188}Os$ and $^{187}Os/^{188}Os$ are determined by numerical error propagation and implementation of an error correlation (ρ) between $^{187}Re/^{188}Os$ and $^{187}Os/^{188}Os$. Blank corrections for shale data were 0.3 ± 0.1 pg for Os at a ^{187}Os-^{188}Os ratio of 0.20 ± 0.05 and 15 ± 3 pg for Re. For pyrite, the Os blank correction is 0.047 ± 0.012 pg at a ^{187}Os-^{188}Os ratio of 0.183 ± 0.056, the Re correction being 1.1 ± 0.6 pg. Age calculations of Re-Os isotope data were performed using Isoplot version 3.00 (Ludwig, 2001) and the ^{187}Re-decay constant of Smoliar et al. (1996).

3.4 Results

3.4.1 Structural setting of the Anarraaq area

The Anarraaq sulfide deposit is located around 600 m below the surface and comprises 2 discrete ore zones – the Upper Zone and the Lower Zone (Figs. 3.4, 3.5) – hosted in black Ikalukrok mudstone. The ore zones are characterized by distinctive styles of Zn-Pb mineralization (see below for more details) and are bounded by intervals of sheared mudstone that contain local fragments of ore (Fig. 3.6B). The boundaries of these shear zones are marked as faults in Figs. 3.4 and 3.5 but the magnitude of displacement along them is poorly constrained. Some ore-bearing intervals are characterized by abundant shear zones (Figs. 3.4, 3.5, 3.6A).

The Anarraaq sulfide deposit is overlain by 40 to 120 m of unmineralized Ikalukrok mudstone with local intervals of grey calcareous turbidite, black calcareous mudstone, limestone nodules, and pyrite layers and nodules (Figs. 3.4, 3.5). In core 809, a calcareous turbidite is well preserved with an interval of upward-graded bedding underlain by load structures. Calcareous

intervals containing local graded bedding occur at a similar stratigraphic level to the northeast (cores 1718, 811, 1714) but are shear-bounded with no preserved load structures. Multiple calcareous turbidite intervals occur in some cores (e.g., 1185) whereas it is completely absent from others (e.g., 806, 1713). Local shear textures also occur in black mudstone.

At least one thrust fault cuts up section through the Anarraaq barite body. Evidence for fault-related folds in the hanging wall includes changes in unit thickness and bedding oriented at a low angle to the core axis. Additional structural complications may be responsible for other unexplained inconsistencies in stratigraphic thickness of the massive and nodular barite units.

3.4.2 Barite body

Kelley et al. (2004b) provide an excellent descriptive overview of the Anarraaq barite body that is consistent with our observations. In brief, the barite body comprises an upper interval of nodular barite in black chert and siliceous mudstone underlain by laminated to massive barite (Figs. 3.4, 3.5). The lower part of the massive barite is locally calcareous, as are rare nodules in the upper interval. The barite body is underlain by black mudstone with the uppermost 10-20 m containing interbeds of chert and calcareous radiolarite. We note that in several drill cores, an interval of bedded to nodular pyrite (≤ 6 m thick) also occurs just below the massive barite (Figs. 3.4, 3.5). In this study, we present observations from a detailed petrographic study that provides some new insight into the paragenesis of barite, calcite, quartz, and pyrite.

Barite that appears to be laminated on the hand sample scale, comprises microscopic disseminated to patchy barite in dark brown, siliceous mudstone or, more commonly, light brown chert (Fig. 3.7). Chert contains abundant organic-rich clasts that are visually indistinguishable from typical Ikalukrok mudstone (Fig. 3.7C). These organic-rich clasts vary in size and shape but commonly occur as elongate stringers (Fig. 3.7A, B, F) which give the rock its ‘laminated’ texture in hand sample. The contact between the mudstone clasts and the surrounding light brown chert is variably sharp or gradational (Fig. 3.7C). Locally, the ‘laminated’ fabric of the barite is crosscut by zones of barite depletion (Fig. 3.7B). Boundaries of crystals in disseminated and patchy barite are everywhere highly irregular (Fig. 3.7G).

Massive barite comprises microcrystalline barite with local disseminated siliceous inclusions (Fig. 3.7F-G). Larger clasts or patches of chert or mudstone are absent from massive barite. The contact between laminated and massive barite is variably sharp, highly irregular, or crosscutting remnant mudstone laminae (Figs. 3.7A-B, 3.8A-B).

Laminated or massive barite is locally calcareous (Fig. 3.8). In addition to patchy irregularly shaped barite disseminations, euhedral barite laths are also commonly associated with calcite (Fig. 3.8C-G). Both barite textures can occur within tens of microns of each other, cemented by calcite (Fig. 3.8D, F-G). The boundaries between calcareous and non-calcareous

barite is irregular and crosscut remnant sedimentary laminae (Fig. 3.8A-B). Although there is a drastic reduction in calcite concentration over a distance of <1 mm (Fig. 3.8E), rare large calcite crystals (300 x 500 μm) occur at least 1 cm beyond this boundary within the massive barite (Fig. 3.8B). These calcite crystals appear to have precipitated with euhedral barite as the surrounding massive barite was dissolved (Fig. 3.8F).

Within the calcareous barite and roughly parallel to the contact with non-calcareous barite is an irregular zone characterized by abundant quartz and depleted barite (Fig. 3.8B, E). Barite is less abundant within the quartz and is highly irregular in shape (Fig. 3.8D-E); the barite appears to have experienced dissolution and remobilization prior to quartz cementation. Veinlets with similar quartz-barite textures occur throughout most of the calcareous zone in this sample (Fig. 3.8C-D) but the highest concentrations of quartz occur near the contact with non-calcareous barite (Fig. 3.8B, E).

Coarse, crystalline barite veins are ubiquitous in the Anarraaq barite body (Figs. 3.7B, 3.8B). In some places, these veins are clearly associated with a local increase in the concentration of disseminated barite in the surrounding host rock (Fig. 3.7C-D). Barite veins commonly contain patches of pyrobitumen (Figs. 3.7B, 3.8B) cementing euhedral barite crystals and rare calcite.

Pyrite locally underlying the massive barite interval comprises abundant framboids and spheroids, which are overgrown by a later generation of massive fine-crystalline pyrite (Fig. 3.9). Abundant siliceous skeletal material is preserved in the massive pyrite (Fig. 3.9B-C). In one place, layers of essentially intact radiolarians are observed (Fig. 3.9C). A minor later generation of euhedral pyrite is associated with crosscutting quartz veinlets.

3.4.3 Sulfide deposit

The Anarraaq sulfide deposit is divided into two ore zones and although they share many characteristics, they are thrust bounded and have distinctly different sphalerite textures. The sphalerite in each zone is also distinguished by its Fe content and trace element geochemistry (Kelley et al., 2004b; Smith, 2017). We discuss the main textural characteristics and mineralogy of each zone here.

3.4.3.1 Lower Zone

Pre-ore components – The Anarraaq sulfide deposit is hosted in a variably siliceous, organic-rich mudstone. This organic-rich mudstone contains several phases that pre-date ore-stage mineralization including barite, pyrite, quartz, and lesser marcasite and apatite (Fig. 3.10). Pre-ore barite occurs most commonly as grey nodules, irregular patches, and layers within the mudstone (Fig. 3.11A). Microscopic textures within these features can contain coalescing crystal laths but amorphous masses are more common (Fig. 3.11B-D). Where crystal laths

are present, they can be difficult to identify in hand sample because of the small crystal size (locally > 1 cm in length but generally ≤200 μm) and the near ubiquitous replacement by quartz, sulfide minerals, and lesser pyrobitumen or calcite (Figs. 3.11, 3.12A-C). Despite pervasive replacement, rare remnant barite has been detected by EDS on the electron microprobe (Fig. 3.12B). It is unclear if quartz replacement of barite pre-dates sphalerite (Fig. 3.11). Rare apatite laths hundreds of microns in length are also observed in mudstone.

Iron sulfide occurs as disseminations in mudstone and as macroscopic layers, laminae, and nodules (Fig. 3.13A-B). In hand sample, early Fe sulfides are very finely crystalline and relatively dull in luster compared with later pyrite phases. Nodules can be several millimeters to 10 cm in diameter and range in shape from rounded to sub-angular, tabular to irregular. Layers are commonly 1 cm or less in thickness. Contacts between Fe sulfide features and mudstone are variably planar and sharp or irregular, wavy, and slightly gradational contacts. Iron sulfide nodules and layers locally coalesce such that up to a meter of core may be massive Fe sulfide. The dominant Fe sulfide is pyrite, which occurs as framboids (Fig. 3.13G) or spheroids (Figs. 3.12C, 3.13D-F), euhedrons that locally overgrow framboids (Fig. 13G), and fine crystalline masses (Figs. 3.12C, 13D-G) locally intergrown with slightly coarser crystalline marcasite. A distinctive characteristic of the early Fe sulfide phases is the presence of abundant siliceous inclusions, many of which are clearly biogenic in origin. The best-preserved microfossils are Spumullarian radiolarians (Fig. 3.13E-F) and the morphology of less complete skeletal fragments is mostly consistent with this identification.

Main ore-stage mineralization – The main ore-stage assemblage is dominated by marcasite, pyrite, sphalerite, quartz, galena, and minor pyrobitumen (Fig. 3.10). Ore-stage pyrite and marcasite display a wide variety of textures that are generally more coarsely crystalline (Fig. 3.12D) than pre-ore Fe sulfide and they do not contain siliceous skeletal material. Some ore-stage marcasite crystals have been partially replaced by ore-stage pyrite (Fig. 3.12D). The Fe sulfide is commonly intermixed with sphalerite at a very fine scale (e.g., Fig. 3.12A-C) but it also occurs as macroscopic veins, cavity rims (e.g., Fig. 3.14A), vein rims, and rare stalactites. Ore-stage Fe sulfide predates some sphalerite and vice versa, commonly within the same hand sample.

Sphalerite in the Lower Zone is highly variable in color and intracrystalline color zonation is ubiquitous (Figs. 3.11C, F-G; 3.14B; 3.15B). Even sphalerite in a distal part of the Lower Zone which is apparently homogenous in color in hand sample (Fig. 3.13B) shows evidence of color zonation in thin-section (Fig. 3.13C). Sphalerite occurs as veins (Figs. 3.11A, 3.15), disseminations in mudstone (Figs. 3.14B-C, G-H, 3.15), pseudomorphs after barite (Figs. 3.11, 3.12A-C), and in complex hydrothermal breccias (Figs. 3.14A-C, 3.12A, F).

Sphalerite veins crosscut mudstone and pre-ore Fe sulfide and barite features (Figs. 3.11A, 3.15A). Veins are locally associated with disseminated sphalerite in mudstone, which

can be so intense that it obscures the host lithology (Fig. 3.15; note local zones of intense disseminated sphalerite mineralization in Fig. 3.15A). Sphalerite preferentially replaces barite over the surrounding mudstone (Fig. 3.11A-B) and sphalerite crystals grow inwards from the edge of pseudomorphs after barite (Fig. 3.11F). Where sphalerite is in contact with quartz, the quartz can have a corroded texture (Fig. 3.14I).

The most intensely mineralized parts of the deposit are characterized by hydrothermal breccias. Some of these are almost completely composed of sulfides (Fig. 3.12A). More commonly, hydrothermal breccias contain a complex mixture of sulfides, quartz, mudstone, and pre-ore Fe sulfide (the wall rock in Fig. 3.14A, see also 3.14B-C, G-H; most of Fig. 3.12F). In some places, hydrothermal breccias are stratiform, bounded by intervals of apparently undisturbed mudstone and pre-ore Fe sulfide layers (Fig. 3.12F).

Some hydrothermal breccias contain irregularly shaped cavities up to 10 cm across that are filled with layered or laminated 'internal' sediment. Internal sediment is predominantly composed of microcrystalline and euhedral quartz with lesser organic material (including local pyrobitumen), Fe sulfides, and sphalerite (Fig. 3.14A, D-F, I). Microcrystalline quartz predates euhedral quartz (Figs. 3.14A) and both phases are intergrown with sphalerite. In hand sample, siliceous internal sediment can be very dark grey to black and can easily be mistaken for Ikalukrok mudstone (Fig. 3.12F-G). Multiple cavities over several meters contain identical internal stratigraphic sequences, suggesting interconnection at the time of internal sedimentation.

Galena rarely occurs outside the zones of most intense zinc mineralization. In some places, galena and sphalerite appear to be coeval at the hand sample scale. However, thin sections reveal that galena is relatively late and clearly out of equilibrium with sphalerite and Fe sulfide phases (Fig. 3.12E). Locally, galena is intergrown with rhombic dolomite crystals (Fig. 3.12E) or anhedral, inclusion-rich quartz.

Late ore-stage alteration – Calcite with minor quartz and pyrobitumen constitute the late ore-stage alteration. Coarse euhedral calcite crystals deform internal sediment laminae within cavities (Fig. 3.12F-G). Calcite and quartz occur as cement in cavities above internal sediment and in breccias with clasts of ore-stage sulfides (Fig. 3.12A). Quartz and calcite occur as veins, which are locally rimmed with ore-stage sulfides (Fig. 3.11A), and generally crosscuts all earlier phases (Figs. 3.12F, 3.13A-C). Pyrobitumen cements space between calcite crystals (Fig. 3.13A). Cubic pyrite commonly occurs at the edges of calcite and quartz veins that crosscut pre-ore Fe sulfide (Fig. 3.13D). Rare local dolomite and barite also occur with late ore-stage calcite.

3.4.3.2 Upper Zone

The mineralogy, paragenetic relationships, and some textures of the Upper Zone are similar to those of the Lower Zone (Figs. 3.10). Only the differences are noted here.

Pre-ore components – In the Upper Zone, pre-ore barite is rarely preserved as identifiable,

silicified laths and nodules (Figs. 3.16A-C, 3.17F). Pre-ore pyrite nodules are generally smaller in diameter (<1 cm) than in the Lower Zone and at least some of these form by replacing (silicified) barite nodules (Fig. 3.16A). On a microscopic scale, pre-ore pyrite consists of coalescing colloform features (Fig. 3.17G) but also contains abundant siliceous microfossils as in the Lower Zone. Rare pyrite layers are composed of tightly-packed pyrite framboids and euhedra.

Main ore-stage mineralization – The most evident difference between the Lower and Upper Zones is the nature of the sphalerite. Upper Zone sphalerite is uniformly pale tan in hand sample (Figs. 3.16A, 3.17A) and displays no color zonation at the microscopic scale. Upper Zone sphalerite is almost everywhere intimately associated with quartz. In most places, very fine sphalerite is disseminated in microcrystalline quartz (Figs. 3.16B-C) but rare euhedral quartz crystals contain sphalerite inclusions (Fig. 3.17B-C, K) and are locally cemented by sphalerite (Fig. 3.17B-C). A continuum of microcrystalline to euhedral quartz-sphalerite textures can occur within a single sample.

Locally, sphalerite, quartz, and ore-stage Fe sulfide preferentially replace barite over the surrounding mudstone (Fig. 3.16B-C). Elsewhere, angular clasts of mudstone cemented by quartz-sphalerite do occur (Fig. 3.17J) but irregular and gradational boundaries between mudstone and quartz-sphalerite domains are more common (Fig. 3.17A, D-E, J). Many intervals centimeters to meters in thickness are so intensely mineralized that it is impossible to discern the original host lithology (e.g., the right end of Fig. 3.16A). These intervals locally appear to be stratabound (Fig. 3.16A). Sphalerite also occurs as laminae in mudstone (Fig. 3.16A) with rare crosscutting feeder veinlets; at the microscopic scale laminated sphalerite is disseminated (Figs. 3.16D-E). Sphalerite has a close spatial relationship with pyrobitumen (Fig. 3.16F). Overall, veins of main ore-stage phases are much less common relative to the Lower Zone.

Ore-stage pyrite and marcasite overlap sphalerite precipitation and have a similar range of textures as in the Lower Zone. In general, ore-stage Fe sulfide is less coarse crystalline, and no stalactites have been observed. Galena postdates sphalerite (Fig. 3.17G) but also forms subhedral crystals up to several millimeters across in mudstone (Fig. 3.16A). At least some crystalline galena replaces siliceous and organic-poor nodules, which may have originally been composed of barite. Galena is locally associated with apatite.

3.4.3.3 Deposit-scale distribution of paragenetic phases

Pre-ore components – Pre-ore textures in the Lower Zone are best preserved in the three cores in the northwestern half of the longitudinal section (cores 1723, 1716, and 1712; Fig. 3.18A) where overprinting by ore-stage mineralization is less intense. These cores show the same general pre-ore upward sequence of (from lowest to highest):

1. Less abundant (<20%) pre-ore Fe sulfide layers and nodules in black mudstone.

2. Abundant (>20 %) pre-ore Fe sulfide layers and nodules in black mudstone.
3. Poorly preserved host rock with local intervals or clasts of black mudstone and pre-ore Fe sulfide layers and nodules.
4. Silicified barite in black mudstone with lesser disseminated pre-ore Fe sulfide.

Although mineralization becomes more intense in the southeastern part of the longitudinal section (Fig. 3.18B), rare evidence for barite occurs at a consistent stratigraphic level in cores 1714 and 923 (Fig. 3.18A). In the cross-section, intervals of silicified barite in black mudstone occur only in cores 1713 and 1717 (Fig. 3.19A). An additional sample of possible laminated (silicified) barite occurs at the base of core 1717 (Fig. 3.19A).

The Upper Zone is smaller and less laterally extensive. Much of the Upper Zone is characterized by poorly preserved host rock with local intervals or clasts of black mudstone and pre-ore Fe sulfide nodules. As in the Lower Zone, the interval of poorly preserved host rock is underlain by black mudstone with abundant Fe sulfide layers. In the Upper Zone, this interval also contains laminae of an unknown composition that have been preferentially replaced by sphalerite. Unequivocal preservation of barite textures is relatively rare and occurs in the middle to upper part of the ore zone. Rare layers of tightly packed pyrite framboids, spheroids, or euhedrons with minor overgrowth textures are observed at both the top and bottom of the main ore zone (Figs. 3.18A, 3.19A).

Ore-stage mineralization – In the Lower Zone, the mineralization decreases in intensity from southeast to northwest (Figs. 3.18B, 3.19B). In the southeast, ore-stage sulfides completely replace the host rock. Common textures in the southeast include multiple generations of sphalerite, abundant ruby red and brown sphalerite, abundant galena, hydrothermal breccias, and local cavities with internal sediment. In the northwest, the uppermost part of the Lower Zone is characterized by hydrothermal veining and preferential replacement of barite; the middle to upper part shows intervals of complete host rock replacement; and the base is characterized by hydrothermal veining and local crackle and mosaic breccias cemented with hydrothermal minerals. Main ore-stage minerals in the northwest are relatively rare (especially galena); late stage hydrothermal minerals (especially calcite) are dominant. Although sphalerite in the northwestern part of the deposit can be pale tan in color, it can be distinguished from Upper Zone sphalerite by the intercrystallite color zonation observed on a microscopic scale.

In the Upper Zone, there is not a clear geographical trend of increasing intensity of base-metal mineralization, although the thickest interval of high-grade ore is in the southwesternmost drill core 809 (Fig. 3.5B). The main ore body is characterized by an interval of intense replacement with local preservation of black mudstone and pre-ore pyrite. This zone is underlain by an interval of ‘laminated’ sphalerite with local ore-stage veining.

3.4.4 Whole rock geochemistry

Whole rock geochemical analysis of subsamples of shale sample 923-2123 were carried out to assess what type of alteration may have taken place after deposition; results can be found in Tab. S3.1 (archived online). With between 75-80 wt. % SiO_2, the black shale is more siliceous than the average black mudstone (Gromet et al., 1984; Taylor and McLennan, 1995) but typical for the Ikalukrok (Slack et al., 2004a). The two subsamples analyzed for total organic carbon (TOC) contain 4.20 and 2.53 wt. % TOC, which are within the range expected for Kuna Formation shales (Slack et al., 2004a). The concentration of trace metals such as Zn (387-788 ppm), Cu (73.7-97.9 ppm), Ag (1.58-2.51 ppm), Tl (1.28-2.71 ppm), and As (3.4-8.3 ppm) are consistent with 'non-metalliferous' Ikalukrok shale as it is defined by Slack et al. (2015).

3.4.5 Rhenium-osmium geochronology

Detailed results from Re-Os analyses of shale and pyrite samples are reported in Table 1. The shale contains the highest concentrations of Re and Os (19.4-40.5 ppb and 888-1709 ppt, respectively) and pre-ore pyrite has the lowest concentrations (0.47-1.30 ppb and 16.57-29.35 ppt). Ore-stage pyrite contains intermediate values of Re (2.86-4.80 ppb) and Os (22.30-28.96 ppt). The ore-stage pyrite is the most radiogenic with $^{187}Os/^{188}Os$ of 6.79-12.00; shale and pre-ore pyrite samples are characterized by $^{187}Os/^{188}Os$ of less than 2.

Regression of seven shale analyses yields an age of 339.1 ± 8.3 Ma (MSWD = 19) with an initial Os ratio of 0.375 ± 0.019 (Fig. 3.20A). Six analyses from pre-ore pyrite produce a very similar isochron with an age of 333.0 ± 7.4 Ma (MSWD = 1.08) and an initial Os ratio of 0.432 ± 0.025 (Fig. 3.20A). Results from three ore-stage pyrite analyses are reported and although these are not sufficient to build a meaningful isochron, the data points lie very close to the pre-ore pyrite isochron. Regression of all pyrite analyses together yields an age of 334.4 ± 5.3 Ma (MSWD = 3.7) and initial Os ratio of 0.422 ± 0.081 (Fig. 3.20B), similar, within the resolution of the analytical results, to the pre-ore only regression. Furthermore, all pyrite analyses from this study lie very close to the isochron reported by Morelli et al. (2004) for ore-stage pyrite from the Main deposit. When the analyses from both studies are regressed together, they yield an age of 336.0 ± 3.9 Ma (MSWD = 29) with an initial Os ratio of 0.34 ± 0.11 (Fig. 3.20C), which is within the uncertainty of the results of Morelli et al. (2004; 338.3 ± 5.8 Ma, initial Os of 0.20 ± 0.21) and of this study.

3.5 Discussion

3.5.1 Diagenetic and hydrothermal processes

3.5.1.1 Anarraaq barite body

The Anarraaq barite body formed when diagenetic fluid bearing methane and barium

vented into sulfate-bearing pore water or bottom waters above the sediment surface (Johnson et al., 2004). Although previous work on Red Dog barite occurrences has focused almost entirely on the conditions of barite precipitation, there are other important geochemical processes associated with methane-driven diagenesis that should be considered. Methane reacts with sulfate in an important biological process, sulfate-driven anaerobic oxidation of methane (SD-AOM), which proceeds by the equation 1 (Barnes and Goldberg, 1976; Reeburgh, 1976). This reaction is mediated by a consortium of sulfate-reducing bacteria and syntrophic anaerobic methanotropic archea (Hoehler et al., 1994; Knittel and Boetius, 2009).

Sulfate-driven AOM can take place in the water column or below the sediment surface, and in the latter case the reaction zone is referred to as the sulfate-methane transition (SMT; Fig. 3.21). In this scenario, barite re-precipitates just above the SMT where pore water methane is depleted, and dissolved barium encounters seawater sulfate in the pore waters (Dickens, 2001). The location of the SMT relative to the seafloor is primarily controlled by the upward flux of methane, the seawater sulfate concentration, and the rate of sedimentation (Jørgensen et al., 2004; Arning et al., 2015). As the location of the SMT changes relative to existing diagenetic barite, barite may undergo repeated cycles of dissolution and re-precipitation (Snyder et al., 2007).

The SMT is also commonly associated with pyrite enrichment that is manifested by clusters of framboids with secondary pyrite overgrowths (Q. Lin et al., 2016; Z. Lin et al., 2016). Bisulfide (HS^-) produced during SD-AOM reacts with iron, to produce pyrite. Some dissolved iron originates locally within SMT sediment, but excess HS^- can also accumulate and diffuse beyond the SMT. Stratiform pyrite has been observed to form below the SMT where excess HS^- encounters upwards-diffusing dissolved Fe^{2+} sourced from deeper sediment (Jørgensen et al., 2004).

The bicarbonate (HCO_3^-) produced by SD-AOM results in an increase in pH and in some cases, carbonate precipitation (e.g., Paull et al., 1992). The increase in alkalinity can also cause dissolution and mobilization of biogenic silica from the SMT to the lower pH fringes where it re-precipitates as a cement or by replacing methane-derived carbonate (Smrzka et al., 2015). If the ratio of barium to methane in the fluid is relatively high, barite precipitation can out-compete SD-AOM for sulfate and suppress carbonate precipitation (Aloisi et al., 2004).

It is within this context that we discuss the new petrographic data from the Anarraaq barite body. Kelley at al. (2004b) interpreted the Anarraaq barite body to have formed by replacing calcareous debrite. There is abundant textural evidence indicating that barite precipitated below the sediment surface, including variable preservation of sedimentary fabrics with contacts that are discordant to sedimentary fabrics (Fig. 3.7A-B), and veins that appear to be feeders for disseminated barite (Fig. 3.7D). However, the petrographic data in this study

indicate that calcite in the barite body is authigenic: it crosscuts sedimentary laminae and postdates at least some barite (Fig. 3.8B). Furthermore, calcite precipitation is closely linked to barite dissolution-reprecipitation (Fig. 3.8F-G) and silicon migration (Fig. 3.8B-E). These characteristics are consistent with what is expected at a SMT. We interpret the boundary of calcareous barite in Fig. 3.8 to be an alteration front which records a pH gradient that formed in response to SD-AOM producing bicarbonate (Fig. 3.21).

Where layered to nodular pyrite is associated with Zn-Pb mineralization, it is commonly interpreted to be hydrothermal (Kelley et al., 2004b) and in some places synsedimentary in origin (Blevings et al., 2013). Framboids can form within the water column (e.g., Wilkin et al., 1996) but the abundance and clustered nature of framboids in the strata underlying the Anarraaq barite body (Fig. 3.9C) is characteristic of framboids formed below the sediment surface at modern SMTs (Q. Lin et al., 2016). The pyrite overgrowths are certainly secondary and are not dissimilar to overgrowths reported in modern SMT sediment (Q. Lin et al., 2016; Z. Lin et al., 2016). The Anarraaq barite body is not overprinted by Zn-Pb mineralization, so it seems unlikely that Pyrite 1-3 are hydrothermal.

The deposit-scale stratigraphic relationship between barite, carbonate, and pyrite is consistent with precipitation at a SMT where SD-AOM was focused near the basal (calcareous) part of the massive barite for a prolonged period. Interestingly, evidence for diagenetic barite dissolution is nearly ubiquitous in the Anarraaq barite body: the irregular shape of disseminated barite crystals (e.g., Fig. 3.7G) indicates that pore waters must have been out of equilibrium with barite. This includes the upper non-calcareous massive barite and the rarely calcareous barite nodules. Although barite is extremely insoluble under oxidizing conditions, it is known to dissolve under reducing conditions, especially in the presence of sulfate-reducing bacteria (McCready and Krouse, 1980). Methane is a powerful reductant and we interpret the sub-vertical zones of barite depletion in Fig. 3.7B to be pathways along which the movement of methane-rich fluids was focused.

3.5.1.2 Anarraaq sulfide deposit – pre-ore components

The pre-ore host rock components in the Anarraaq sulfide deposit have some striking similarities – compositional, textural, and stratigraphic relationships – to the Anarraaq barite body. Barite and layered to nodular pyrite occur in both the Upper Zone and Lower Zone, and pre-ore pyrite textures include framboids and overgrowths with well-preserved radiolarian skeletal material. Although no pre-ore carbonate is preserved in the sulfide deposit, Kelley et al. (2004b) suggested that hydrothermal breccias were formed by large-scale dissolution of carbonate. If carbonate was a component of the ‘poorly preserved host’ rock type (Fig. 3.18A), then the deposit scale pre-ore stratigraphy of the Lower Zone is consistent with a SMT located within the strata for a prolonged period. The pre-ore stratigraphy is less well defined in the Upper

Zone but pre-ore pyrite does appear to be the dominant component at the base of the zone, as would be expected at a SMT. Therefore, we propose that each sulfide zone has overprinted a pre-existing SMT.

Almost no barite remains in the sulfide deposit: it has all been dissolved and replaced with quartz or sulfide minerals. Previous workers suggested that silicification in Red Dog ore zones was primarily associated with ore-stage mineralization (Slack et al., 2004b) or with the much younger Brookian orogeny (Leach et al., 2004). We have presented clear evidence for the presence of hydrothermal quartz (e.g., Figs. 3.14, 3.17). However, we also presented new textural evidence that shows that barite dissolution (Figs. 3.7, 3.8) and silicon migration (Fig. 3.8b) were important pre-ore processes associated with methane-driven diagenesis in the Anarraaq barite body. It follows that dissolution and silicification of barite in the Anarraaq sulfide deposit may have pre-dated ore-stage mineralization, although additional hydrothermal silicification cannot be ruled out. The idea that barite dissolution was primarily driven by diagenetic fluid prior to the introduction of ore-stage mineralization is compatible with the assertion of Leach et al. (2004) that hydrothermal fluids were oxic and sulfate-bearing and, thus, could not dissolve barite.

3.5.2 Original distribution of Anarraaq pre-ore barite-carbonate-pyrite occurrences

The amount of offset on the faults overlying each ore zone in the Anarraaq sulfide deposit is poorly constrained. If minimal displacement has taken place on these faults, the present-day configuration of the Lower Zone, Upper Zone, and the barite body would reflect the original stratigraphic relationship of the three paleo-SMTs and hydrothermal overprints. If significant offset has taken place, each ore zone and the barite body may represent repeated Ikalukrok strata that formed laterally to each other and were later structurally superimposed. Because shear zones contain local fragments of ore (Fig. 3.6), deformation must have taken place after hydrothermal mineralization, most likely in the Brookian orogeny during the Mesozoic Era.

One argument for the scenario in which the three paleo-SMTs formed in the present-day configuration is the seemingly low probability that Brookian faulting would have resulted in the near-perfect vertical alignment of the three zones. Also consistent with formation in the present-day configuration is the more complete dissolution of barite in the Anarraaq sulfide deposit relative to the barite body: more deeply buried sediment would have passed more time in the methanic redox zone and experienced more barite dissolution. The exceptionally large amount of barite in the barite body could be due in part to recycling of barium from the underlying SMTs. In this scenario, the contrasting styles of mineralization in the two ore zones could be controlled by variation in the depth below the sediment surface or the composition of the host sediment, or by formation via two discrete pulses of hydrothermal fluid with different chemistries.

It seems unlikely, however, that depth below the sediment surface could be responsible for such an abrupt change in style of mineralization: the vertical distance between Upper and

Lower Zone styles of mineralization is locally less than 3 m (e.g., core 923). Given the poor preservation of the host rock, it is difficult to assess what effect host sediment composition may have had on style of mineralization. If two pulses of chemically distinct hydrothermal fluid were involved, we might expect to see some overprinting textures, but none have been observed. Displacement on faults could explain how contrasting styles of mineralization occur in such close spatial association without any overprinting textures.

Low-angle faults appear to cut both up and down section in the inferred direction of transport (see Figs. 3.5, 3.19A), indicating that Brookian deformation was more complex than the simple stacking of horses in a duplex system as suggested by De Vera et al. (2013). Several explanations are possible. First, the lenticular nature of the ore zones and barite body may have generated significant dips at the time of formation due to differential compaction, causing thrust faults to locally cut down section. Second, the direction of tectonic transport may not have been parallel to the cross-section shown in Fig. 3.5, and the ramps shown in the section may therefore be lateral or oblique ramps, rather than frontal ramps as implied by the vergence directions shown by Blevings et al. (2013). Third, out-of-sequence thrusts may have occurred during Brookian deformation, possibly due to the laterally heterogeneous mechanical properties of the ore bodies. More work is required to resolve this issue.

We note that the pre-ore baritic strata of the Lower Zone correlate well among cores 1723, 1716, 1712, 1717, and 1713, with a trend of gradual thickening towards the most intensely mineralized part of the deposit (Figs. 3.18A, 3.19A). In contrast to this trend, cores 1714 and 808 show a thinning or absence of pre-ore barite and a dramatic thinning in the overall thickness of the Lower Zone (Fig. 3.19A). This may reflect the original geometry of pre-ore barite or later structural modification. Although the main thickness of the Upper Zone occurs in the northwestern part of the sulfide deposit, intervals of Upper Zone style mineralization further to the northeast are characterized by pervasive shearing that clearly postdates mineralization (e.g., core 1185; Fig. 3.6). Although this geometry could be partly inherited from a heterogeneous original distribution of mineralized units, the evidence for deformation strongly suggests that fragments of Upper Zone material were transported along a fault. The discontinuity of turbidite strata across the cross-section (Fig. 3.5) and the common shear textures in the unmineralized Ikalukrok mudstone overlying the Upper Zone could also be an indication of significant tectonic modification. Therefore, we consider that there is strong evidence that the original geometry of the ore bodies was modified by Brookian deformation.

3.5.3 Timing of diagenesis and hydrothermal activity

The Re-Os isochron ages for the black shale just above the Anarraaq sulfide deposit (339.1 ± 8.3 Ma) and the pre-ore pyrite from within the Anarraaq sulfide deposit (333.0 ± 7.4 Ma) are within error of the Re-Os isochron age of ore-stage pyrite in the Main deposit in the

Mine Area (338.3 ± 5.8 Ma; Morelli et al., 2004). Although the three data points for ore-stage pyrite at Anarraaq are not sufficient to create a meaningful isochron, the fact that they plot very close to the pre-ore pyrite isochron suggests that the ore-stage Re-Os systematics are not grossly different from the pre-ore stage pyrite. Overall, the data are consistent with contemporaneous Zn-Pb mineralization at Anarraaq and the Main deposit.

Although there is some ambiguity about the stratigraphic relationship between the Anarraaq sulfide deposit and the overlying non-mineralized sediment, the overlapping Re-Os isotopic ages are compatible with the idea that sediment deposition and ore formation were relatively close in age. As in the Main deposit, the textural evidence at Anarraaq indicates that Zn-Pb mineralization was replacive but the absolute timescale of replacement cannot be resolved with the current Re-Os isochron ages.

The transformation of opal A to opal CT plays an important role in cementation during sediment diagenesis in biosiliceous mudstone. Temperature is one of several factors that controls this transformation, which usually takes place between 25 and 50°C (Davies and Ireland, 2011). Fluid inclusion microthermometry of sphalerite from the Main and Aqqaluk deposits suggests that the hydrothermal fluid was between 110 and 180 °C during ore-stage mineralization (Leach et al., 2004); it is possible that hydrothermal fluids locally accelerated the process of cementation in the host strata. Notwithstanding this complication, we note that the presence of sphalerite veins (Figs. 3.11A, 3.15A) and angular mudstone clasts (Figs. 3.14B, 3.17J) cemented in sphalerite indicate some degree of sediment lithification had taken place prior to the onset of ore formation. The locally disseminated nature of sphalerite in mudstone (Figs. 3.15, 3.17D-E) suggests that some porosity was still present at the time of the earliest mineralization; alternatively, this porosity may have been generated by hydrothermal dissolution. In the Lower Zone, the colloform sphalerite pseudomorphs after barite indicate open space growth (e.g., Fig. 3.11F) and we interpret the barite crystals (or more likely, carbonate or opaline Si pseudomorphs formed as a result of methane-related diagenesis) to have been completely dissolved by hydrothermal fluid prior to sphalerite precipitation. For this to be possible, the mudstone surrounding the barite crystal must have been well-lithified to prevent collapse into the open space of the dissolved crystal. The relative rarity of veining and angular mudstone clasts in the Upper Zone, in combination with the presence of irregular and gradational boundaries between mudstone and quartz-sphalerite domains (Fig. 3.17A, D-E, J), suggests that Upper Zone sediment may have been less completely cemented than the Lower Zone at the time of Zn-Pb mineralization.

3.5.4 Initial Os composition

The global marine Os record is not well constrained during the Carboniferous but there are several published Re-Os isochrons for Late Devonian shales in Western Canada and one

for a Lower-Middle Pennsylvanian shale in the Eastern United States (Fig. 3.22). These data indicate that marine $^{187}Os/^{188}Os$ was between 0.37 to 0.64 in the late Devonian (~360 Ma; Creaser et al., 2002; Selby and Creaser, 2003, 2005) and no higher than 0.72 in the Lower to Middle Pennsylvanian (323 ± 7.8 Ma; Geboy et al., 2015). The initial $^{187}Os/^{188}Os$ value for the Anarraaq shale isochron is broadly consistent with these data and may be representative of global marine Os composition.

Slack et al. (2015) proposed that Middle Mississippian (~335 Ma) marine $^{187}Os/^{188}Os$ was much higher (~1.08) and that Ikalukrok shales with lower initial $^{187}Os/^{188}Os$ record the local/intermittent influence of a metalliferous hydrothermal fluid venting into the seawater. This interpretation is based on single sample analyses and calculated initial $^{187}Os/^{188}Os$ values rather than full isochrons, which makes it more difficult to assess the effects of possible post-depositional disturbance of the Re-Os system. To increase the global marine $^{187}Os/^{188}Os$ composition by more than 0.5 in 20-30 Myr would require a large increase in radiogenic Os input via continental weathering; that is, an increase that is on par with or more extreme than what has been observed in more recent geologic history during the rise of the Himalayan mountains (Peucker-Ehrenbrink and Ravizza, 2000; Turekian and Pegram, 1997). The marine $^{87}Sr/^{86}Sr$ ratio is a proxy for global rates of continental weathering that is relatively well constrained over Earth history (Burke et al., 1982; Veizer et al., 1999). Mississippian marine $^{87}Sr/^{86}Sr$ was equal to or lower than Late Devonian values (Denison et al., 1994). It therefore seems unlikely that Mississippian global marine $^{187}Os/^{188}Os$ would have been significantly higher than Late Devonian values, although we cannot rule out local effects, especially if Ikalukrok mudstone was deposited in a restricted basin. Furthermore, the shale sample analyzed for Re-Os in this study has relatively low concentrations of the trace metals that Slack et al. (2015) expected to correlate with the influence of a synsedimentary hydrothermal component (387-788 ppm Zn, 73.7-97.9 ppm Cu, 1.58-2.51 ppm Ag, 1.28-2.71 ppm Tl, and 3.4-8.8 ppm As; Tab. S3.1). We suggest that the variability in calculated initial $^{187}Os/^{188}Os$ values reported by Slack et al. (2015) is more likely controlled by post-depositional disturbance of the Re-Os system or the local contribution of a more radiogenic clastic component.

The initial $^{187}Os/^{188}Os$ value of the Anarraaq pre-ore pyrite isochron is only slightly higher than that of the shale. We interpret pre-ore pyrite to have formed at a SMT during early diagenesis upon mixing of pore waters originally derived from Mississippian seawater. The similar initial $^{187}Os/^{188}Os$ values of pre-ore pyrite and shale are consistent with this interpretation.

The initial $^{187}Os/^{188}Os$ values reported in this study are within error of the value reported by Morelli et al. (2004) for ore-stage pyrite in the Main deposit (0.2 ± 0.21; Fig. 3.22). However, our results are more precise and overlap only the highest part of the 2σ confidence range of Morelli et al. (2004). Because of the large uncertainty on the initial $^{187}Os/^{188}Os$ value, Morelli

et al. (2004) considered both mantle and relatively young (<410 Ma) crustal reservoirs as possible sources of Os in the hydrothermal fluid. In view of the similarity between the initial $^{187}Os/^{188}Os$ of the shale isochron and the ore-stage pyrite (regressed with pre-ore pyrite) at Anarraaq, influence from a mantle Os reservoir on the hydrothermal fluids composition is not required. In fact, the data from this study are compatible with the model of Leach et al. (2004), whereby hydrothermal fluids formed from a basinal brine evolved from evaporated seawater of Mississippian or Devonian age that circulated through the Devonian Endicott Group sedimentary rocks.

3.5.5 Implications for the genesis of and exploration for SHMS deposits

Evidence for early barite overprinted by zinc mineralization has been reported in the Main, Aqqaluk, Paalaaq, and Qanaiyaq deposits in the mine area (Blevings et al., 2013; Kelley et al., 2004a). As the Anarraaq sulfide deposit illustrates, barite can be poorly preserved and very difficult to identify: the deposit was discovered in 1999 (Kelley et al., 2004b) but only in this study do we recognize that barite was a significant component of the host rock. Furthermore, the massive, patchy, and disseminated textures that characterize much of the Anarraaq barite body are not unique to barite; if these textures were to be completely replaced by other minerals, it would be impossible to identify the precursor as barite. So although several additional base metal deposits and prospects in the Red Dog district (e.g., Aktigiruk, Su Lik) reportedly contain no barite (Blevings et al., 2013), it is possible that barite was present initially but was then later replaced by various diagenetic and hydrothermal minerals. Furthermore, we have suggested that pre-ore pyrite and carbonate are products of SD-AOM and are genetically linked to barite formation. Therefore, the presence of authigenic carbonate or laminated pyrite even in the absence of barite may be treated as evidence of similar diagenetic conditions at a SMT. It is possible that all Red Dog sulfide deposits overprint former SMTs.

As we have discussed, barium from dissolved barite is likely to reprecipitate in younger strata (Brumsack, 1986; Torres et al., 1996, 2003). In the Anarraaq barite body, we have proposed that much of the barium in the nodular barite interval is recycled from the underlying interval of massive barite. Barite is also reported in the younger Siksikpuk and Otuk formations in the Red Dog plate (Young, 2004); we suggest that a relative local abundance of barite in these strata may reflect the presence of large barite accumulations in the underlying Ikalukrok unit. In combination with detailed structural reconstructions, this approach may prove a useful exploration tool for identifying prospective host rocks. It remains unclear what contribution hydrothermal fluids may have made to barite dissolution and therefore, if barium concentrations of younger strata might reflect a more direct relationship with local hydrothermal activity.

In the distal northwestern part of the Anarraaq deposit Lower Zone, zinc mineralization is most intense in the upper part of the deposit where we interpret pre-ore barite and carbonate

to have been present (Figs. 3.18B, 3.23). It follows that the formation of barite and methane-derived carbonate and their subsequent dissolution was an important prerequisite for creating a porous and permeable host rock. We would also expect methane and excess bisulfide (HS^-) to be present in an SMT, both of which could serve as a highly effective trap for hydrothermal metals. The size, mineralogy, and pore water composition of a paleo-SMT may have played a key role in determining the ultimate size and grade of the overprinting base metal deposit.

Johnson et al. (2004) speculated that SD-AOM may have been the key chemical pathway for producing bisulfide for massive sulfide deposits at Red Dog, especially in deposits like Anarraaq where little to no diagenetic barite had been identified. However, they did not link the SD-AOM process to precipitation of authigenic pyrite and carbonate. The recognition that SD-AOM was an important pre-ore diagenetic process at Anarraaq (Johnson et al., 2004; this study) is consistent with recent findings in other SHMS districts in the Canadian cordillera. Magnall et al. (2016) interpreted SHMS mineralization in the Tom and Jason deposits of Macmillan Pass (Yukon) to overprint pre-ore barite and pyrite that formed at the SMT. Johnson et al. (2018) found that diagenetic pyrite and carbonate in the host strata of SHMS mineralization at Howards Pass (Yukon–Northwest Territories) was also influenced by SD-AOM. All of these SHMS deposits, including those at Red Dog, are hosted in organic-rich sediment deposited on continental margins where upwelling of nutrient-rich deep ocean water resulted in abundant biogenic productivity in the water column (Dumoulin et al., 2014; Magnall et al., 2015; Slack et al., 2017; Magnall et al., 2018). At Howards Pass, Johnson et al. (2018) linked an increase in sedimentary carbon content to an increase in production of biogenic methane and influence of SD-AOM on diagenesis.

At Red Dog, the spatial coincidence between barite ± carbonate ± pyrite SMT accumulations and overprinting Zn-Pb deposits suggests a link between the mechanisms which control the location of each. One possibility is that early diagenetic and later hydrothermal fluids used similar pathways to flow into the shallow subsurface. Diagenesis of biosiliceous mudstones such as the Ikalukrok has been linked with the development of non-tectonic, intraformational faulting and pore fluid expulsion (Cartwright, 1994; Volpi et al., 2003; Davies et al., 2008) and this could have been the mechanism that controlled the location of large-scale SMT diagenesis. Hydrothermal fluids are thought to have flowed up tectonic extensional faults (Moore et al., 1986); perhaps these faults exploited pre-existing faults or zones of weakness that served as flow pathways for diagenetic fluids bearing methane and barium. This scenario would be consistent with the occurrence of some barite bodies that were not overprinted by hydrothermal fluids, as occur at Red Dog.

Two additional important implications emerge from distinguishing pre-ore diagenetic phases from hydrothermal mineralization. The first relates to the sub-classification system of

Cooke et al. (2000) in which stratiform sediment-hosted Zn-Pb deposits are formed by either oxidized or reduced hydrothermal fluids. In this scheme, barite is a distinctive feature of the class of deposits formed from reduced fluids. However, if barite pre-dates hydrothermal mineralization as we suggest in this study, its occurrence would be independent of the composition of the hydrothermal fluid and is instead controlled by the pre-ore diagenetic history of the host sediment. Notably, methane-derived carbonate (with no barite) is known to accumulate in marine strata in a variety of other tectono-sedimentary settings (Suess, 2014). Perhaps variability in the source (and composition) of methane-bearing fluid might explain some of the differences observed among SHMS deposits. Another alternative is that secular changes in ocean chemistry have affected the way Ba is (or is not) sequestered in zones of high water-column biological productivity.

The second important implication concerns exploration for SHMS deposits. Here, we have suggested that the dominant sulfide component of the northwestern, lower grade part of the Anarraaq sulfide deposit is pre-ore pyrite linked to methane-related diagenesis. Previous workers (Kelley et al., 2004b; Schardt et al., 2008) have considered this zone to represent a hydrothermal pyrite halo. Instead, we consider the distal hydrothermal signature in this part of the deposit to be characterized by relatively minor ore-stage Fe sulfide and sphalerite with abundant late ore-stage calcite-quartz ± pyrobitumen veins (Fig. 3.13A-B). We would expect the geochemical characteristics of the pre-ore pyrite to represent the diagenetic environment prior to hydrothermal mineralization; it would not necessarily provide vectors towards high-grade ore except in that it indicates prospective host strata. Furthermore, pre-ore barite creates gravity anomalies which may not directly relate to the presence of Zn-Pb mineralization.

In summary, understanding the mechanisms of formation of hydrothermal ore deposits that form in the shallow subsurface of marine sediment requires an understanding of key diagenetic processes. At Red Dog, pre-ore diagenetic processes created physical and chemical traps for later Zn-Pb mineralization. These processes must be considered when developing an exploration program and extra care must be taken to distinguish pre-ore and ore components during the interpretation of sedimentological, geochemical, and geophysical data.

3.6 Conclusions

The Re-Os isochron ages of Ikalukrok shale, pre-ore diagenetic pyrite, and hydrothermal pyrite (isochron constructed in combination with pre-ore data) at Anarraaq are all within error of the Re-Os isochron age of the Main deposit in the Mine Area (Morelli et al., 2004). This indicates that the hydrothermal event was synchronous on a regional scale. The initial Os composition of the Anarraaq isochrons is consistent with expected values for Devonian and Mississippian seawater; it is unlikely that a mantle source had a significant influence on hydrothermal fluids.

The Anarraaq area contains 3 successions of pre-ore baritic, calcareous, and pyritic strata interpreted to be paleo-SMTs. Two of these are overprinted by hydrothermal mineralization and comprise the Upper Zone and Lower Zone in the Anarraaq sulfide deposit. The third paleo-SMT – the Anarraaq barite body – was not overprinted. It is possible that the vertically stacked paleo-SMTs remain in their approximate depositional position; this would indicate that SD-AOM was focused at 3 different stratigraphic intervals during 3 different time periods. However, it cannot be ruled out that the paleo-SMTs formed laterally to each other and were structurally superimposed during the late Jurassic to Cretaceous Brookian orogeny, long after local overprinting by hydrothermal fluids.

In the Anarraaq sulfide deposit, methane-related diagenetic processes played a key role in the formation of high-grade SHMS mineralization. Sulfate-driven AOM resulted in the precipitation of authigenic carbonate and subsequent dissolution by acidic hydrothermal fluids created large volumes of space for sulfide precipitation. The cycle of barite precipitation and dissolution linked to the upward migration of an SMT over time may have introduced additional porosity and permeability to the host sediment prior to hydrothermal mineralization. Furthermore, pore water methane and/ or the bisulfide produced by SD-AOM could have served as a potent trap for metals transported by hydrothermal fluids.

Barite; pyrite layers, laminae, and nodules; textures suggestive of carbonate replacement; or some combination of these are reported in all known Red Dog deposits and prospects. This suggests that development of a SMT was a vital pre-condition for SHMS mineralization in the Red Dog district. This idea is consistent with recent reports that SD-AOM was an important pre-ore diagenetic process in sediments hosting SHMS deposits in Howard's Pass and MacMillan Pass. We propose that the size, mineralogy, and pore water composition of paleo-SMTs may have played a key role in determining the ultimate size, grade, and metallurgical characteristics of overprinting SHMS deposits.

3.7 Acknowledgements

This work was funded by Teck Resources Limited and by a Collaborative Research and Development grant and a Vanier Canada Graduate Scholarship from the Natural Sciences and Engineering Research Council of Canada. Special thanks to Pilar Lecumberri-Sanchez and Morgan Snyder at the University of Alberta, and the geologists active in the Red Dog district (Alaska) for technical assistance and geological discussions.

3.8 References

Arning, E.T., Gaucher, E.C., van Berk, W., and Schulz, H.M., 2015, Hydrogeochemical models locating sulfate-methane transition zone in marine sediments overlying black shales: A new tool to locate biogenic methane? Marine and Petroleum Geology, v. 59, p. 563–574,

doi: 10.1016/j.marpetgeo.2014.10.004.

Ayuso, R.A., Kelley, K.D., Leach, D.L., Young, L.E., Slack, J.F., Wandlass, G., Lyon, A.M., and Dillingham, J.L., 2004, Origin of the Red Dog Zn-Pb-Ag deposits, Brooks Range, Alaska: Evidence from regional Pb and Sr isotope sources: Economic Geology, v. 99, p. 1533–1554, www.intl-econgeol.geoscienceworld.org/content/99/7/1533.short.

Barnes, R.O., and Goldberg, E.D., 1976, Methane production and consumption in anoxic marine sediments: Geology, v. May, p. 297–300, doi: 10.1130/0091-7613(1976)42.0.CO;2.

Bishop, J.K.B., 1988, The barite-opal-organic carbon association in oceanic particulate matter: Nature, v. 332, p. 341–343, doi: 10.1038/332341a0.

Blevings, S., Kraft, J., Stemler, J., and Krolak, T., 2013, An overview of the structure, stratigraphy, and Zn-Pb-Ag deposits of the Red Dog District, Northwestern Alaska, in Colpron, M., et al., eds., Tectonics, metallogeny, and discovery: The North American Cordillera and similar accretionary settings: Society of Economic Geologists Special Publication 17, p. 361–387.

Brumsack, H.J., 1986, The inorganic geochemistry of Cretaceous black shales (DSDP Leg 41) in comparison to modern upwelling sediments from the Gulf of California, in Summerhayes, C.P. et al., eds., North Atlantic Palaeoceanogrphy: Geological Society Special Publications, v. 21, p. 447–462, doi: 10.1144/GSL.SP.1986.021.01.30.

Burke, W.H., Denison, R.E., Hetherington, E.A., Koepnick, R.B., Nelson, H.F., and Otto, J.B., 1982, Variation of seawater Sr87-Sr86throughout Phanerozoic time.: Geology, v. 10, p. 516–519, doi: 10.1130/0091-7613(1982)10<516:VOSSTP>2.0.CO.

Cartwright, J.A., 1994, Episodic basin-wide fluid expulsion from geopressured shale sequences in the North Sea Basin: Geology, v. 22, p. 447–450, doi: 10.1130/0091-7613(1994)022<0447:EBWFEF>2.3.CO;2.

Cooke, D., Bull, S., Large, R., and McGoldrick, P., 2000, The importance of oxidized brines for the formation of Australian Proterozoic stratiform sediment-hosted Pb-Zn (Sedex) deposits: Economic Geology, v. 95, p. 1–18, http://171.67.121.50/content/95/1/1.short.

Creaser, R., Papanastassiou, D., and Wasserburg, G., 1991, Negative thermal ion mass spectrometry of osmium, rhenium and iridium: Geochimica et Cosmochimica Acta, v. 55, p. 397–401, www.sciencedirect.com/science/article/pii/0016703791904277.

Creaser, R.A., Sannigrahi, P., Chacko, T., and Selby, D., 2002, Further evaluation of the Re-Os geochronometer in organic-rich sedimentary rocks: A test of hydrocarbon maturation effects in the Exshaw Formation, Western Canada Sedimentary Basin: Geochimica et Cosmochimica Acta, v. 66, p. 3441–3452, doi: 10.1016/S0016-7037(02)00939-0.

Davies, R.J., Goulty, N.R., and Meadows, D., 2008, Fluid flow due to the advance of basin-scale silica reaction zones: Bulletin of the Geological Society of America, v. 120, p. 195–206,

doi: 10.1130/B26099.1.

Davies, R.J., and Ireland, M.T., 2011, Initiation and propagation of polygonal fault arrays by thermally triggered volume reduction reactions in siliceous sediment: Marine Geology, v. 289, p. 150–158, doi: 10.1016/j.margeo.2011.05.005.

Denison, R.E., Koepnick, R.B., Burke, W.H., Hetherington, E.A., and Fletcher, A., 1994, Construction of the Mississippian, Pennsylvanian and Permian seawater 87Sr/86Sr curve: Chemical Geology: Isotope Geoscience Section, v. 112, p. 145–167.

Dickens, G.R., 2001, Sulphate profiles and barium fronts in sediments on the Blake Ridge: present and past methane fluxes through a large gas hydrate resevoir: Geochimica et Cosmochimica Acta, v. 65, p. 529–543.

Dumoulin, J., Harris, A.G., Blome, C.D., and Young, L.E., 2004, Depositional settings, correlation, and age of Carboniferous rocks in the western Brooks Range, Alaska: Economic Geology, v. 99, p. 1355–1384, www.intl-econgeol.geoscienceworld.org/content/99/7/1355.short.

Dumoulin, J.A., Johnson, C.A., Slack, J.F., Bird, K.J., Whalen, M.T., Moore, T.E., Harris, A.G., and Sullivan, P.B.O., 2014, Carbonate margin, slope, and basin facies of the Lisburne Group (Carboniferous-Permian) in northern Alaska, in Verwer, K., Playton, T., and Harris, P. eds., Special Publication 105, SEPM, v. 105, p. 211–236, doi: 10.2110/sepmsp.105.02.

Geboy, N.J., Tripathy, G.R., Ruppert, L.F., Eble, C.F., Blake, B.M., Hannah, J.L., and Stein, H.J., 2015, Re-Os age for the Lower-Middle Pennsylvanian Boundary and comparison with associated palynoflora: International Journal of Coal Geology, v. 140, p. 23–30, doi: 10.1016/j.coal.2015.01.002.

Gromet, L.P., Haskin, L.A., Korotev, R.L., and Dymek, R.F., 1984, The “North American shale composite”: Its compilation, major and trace element characteristics: Geochimica et Cosmochimica Acta, v. 48, p. 2469–2482, doi: 10.1016/0016-7037(84)90298-9.

Hitzman, M.W., 1999, Routine staining of drill core to determine carbonate mineralogy and distinguish carbonate alteration textures: Mineralium Deposita, 34(8), p. 794–798.

Hnatyshin, D., Kontak, D.J., Turner, E.C., Creaser, R.A., Morden, R., and Stern, R.A., 2016, Geochronologic (ReOs) and fluid-chemical constraints on the formation of the Mesoproterozoic-hosted Nanisivik ZnPb deposit, Nunavut, Canada: Evidence for early diagenetic, low-temperature conditions of formation: Ore Geology Reviews, v. 79, p. 189–217, doi: 10.1016/j.oregeorev.2016.05.017.

Hoehler, T.M., Alperin, M.J., Albert, D.B., and Martens, C.S., 1994, Field and laboratory studies of methane oxidation in an anoxic marine sediment: Evidence for a methanogen-sulfate reducer consortium: Global Biogeochemical Cycles, v. 8, p. 451–463, doi:

10.1029/94GB01800.

Iversen, N., and Jørgensen, B.B., 1985, Anaerobic methane oxidation rates at the sulphate-methane transition in marine sediments from Kattegat and Skagerrak (Denmark): Limnology and Oceanography, v. 30, p. 944–955.

Johnson, C.A., Emsbo, P., Poole, F.G., and Rye, R.O., 2009, Sulfur- and oxygen-isotopes in sediment-hosted stratiform barite deposits: Geochimica et Cosmochimica Acta, v. 73, p. 133–147, doi: 10.1016/j.gca.2008.10.011.

Johnson, C.A., Kelley, K.D., and Leach, D.L., 2004, Sulfur and oxygen isotopes in barite deposits of the western Brooks Range, Alaska, and implications for the origin of the Red Dog massive sulfide deposits: Economic Geology, v. 99, p. 1435–1448, gsecongeo.highwire.org/content/99/7/1435.short.

Johnson, C.A., Slack, J.F., Dumoulin, J.A., Kelley, K.D., and Falck, H., 2018, Sulfur isotopes of host strata for Howards Pass (Yukon-Northwest Territories) Zn-Pb deposits implicate anaerobic oxidation of methane, not basin stagnation: Geology, v. 46, p. 619–622, doi: 10.1130/G40274.1.

Jørgensen, B.B., Böttcher, M.E., Lüschen, H., Neretin, L.N., and Volkov, I.I., 2004, Anaerobic methane oxidation and a deep H2S sink generate isotopically heavy sulfides in Black Sea sediments: Geochimica et Cosmochimica Acta, v. 68, p. 2095–2118, doi: 10.1016/j.gca.2003.07.017.

Kelley, K.D., Dumoulin, J.A., and Jennings, S., 2004b, The Anarraaq Zn-Pb-Ag and Barite Deposit, Northern Alaska: Evidence for Replacement of Carbonate by Barite and Sulfides: Economic Geology, v. 99, p. 1577–1591, doi: 10.2113/gsecongeo.99.7.1577.

Kelley, K.D., and Jennings, S., 2004, A special issue devoted to barite and Zn-Pb-Ag deposits in the Red Dog district, Western Brooks Range, Northern Alaska: Economic Geology, v. 99, p. 1267–1280, econgeol.geoscienceworld.org/content/99/7/1267.short.

Kelley, K.D., Leach, D.L., Johnson, C.A., Clark, J.L., Fayek, M., Slack, J.F., Anderson, V.M., Ayuso, R.A., and Ridley, W.I., 2004a, Textural, compositional, and sulfur isotope variations of sulfide minerals in the Red Dog Zn-Pb-Ag deposits, Brooks Range, Alaska: Implications for Ore Formation: Economic Geology, v. 99, p. 1509–1532, doi: 10.2113/gsecongeo.99.7.1509.

Kendall, B., Creaser, R.A., Ross, G.M., and Selby, D., 2004, Constraints on the timing of Marinoan “Snowball Earth” glaciation by 187Re-187Os dating of a Neoproterozoic, post-glacial black shale in Western Canada: Earth and Planetary Science Letters, v. 222, p. 729–740.

Knittel, K., and Boetius, A., 2009, Anaerobic Oxidation of Methane: Progress with an Unknown Process: Annual review of microbiology, 63, p. 311-334, doi:10.1146/annurev.

micro.61.080706.093130.

Krolak, T., Palmer, K., Lacouture, B., Paley, N., 2017, NI 43-101 Technical Report for Red Dog Mine, Alaska, USA, 143 p.

Lash, G.G., 2015, Pyritization induced by anaerobic oxidation of methane (AOM) - An example from the upper devonian shale succession, western New York, USA: Marine and Petroleum Geology, v. 68, p. 520–535, doi: 10.1016/j.marpetgeo.2015.10.002.

Leach, D.L., Marsh, E., Emsbo, P., Rombach, C.S., Kelley, K.D., and Anthony, M., 2004, Nature of hydrothermal fluids at the shale-hosted Red Dog Zn-Pb-Ag deposits, Brooks range, Alaska: Economic Geology, v. 99, p. 1449–1480, 171.67.121.50/content/99/7/1449.short.

Lin, Z., Sun, X., Peckmann, J., Lu, Y., Xu, L., Strauss, H., Zhou, H., Gong, J., Lu, H., and Teichert, B.M.A., 2016, How sulfate-driven anaerobic oxidation of methane affects the sulfur isotopic composition of pyrite: A SIMS study from the South China Sea: Chemical Geology, v. 440, p. 26–41, doi: dx.doi.org/10.1016/j.chemgeo.2016.07.007.

Lin, Q., Wang, J., Algeo, T.J., Sun, F., and Lin, R., 2016, Enhanced framboidal pyrite formation related to anaerobic oxidation of methane in the sulfate-methane transition zone of the northern South China Sea: Marine Geology, v. 379, p. 100–108.

Ludwig, K., 2001, Isoplot 3.00, a geochronologic toolkit for Microsoft Excel. Special Publication, 4: Berkeley Geochronological Center.

Magnall, J.M., Gleeson, S.A., and Paradis, S., 2015, The importance of siliceous radiolarian-bearing mudstones in the formation of sediment-hosted Zn-Pb ?? Ba mineralization in the Selwyn Basin, Yukon, Canada: Economic Geology, v. 110, p. 2139–2146.

Magnall, J.M., Gleeson, S.A., Poulton, S.W., Gordon, G.W., and Paradis, S., 2018, Links between seawater paleoredox and the formation of sediment-hosted massive sulphide (SHMS) deposits — Fe speciation and Mo isotope constraints from Late Devonian mudstones: Chemical Geology, v. 490, p. 45–60, doi: 10.1016/j.chemgeo.2018.05.005.

Magnall, J.M., Gleeson, S.A., Stern, R.A., Newton, R.J., Poulton, S.W., and Paradis, S., 2016, Open system sulphate reduction in a diagenetic environment – isotopic analysis of barite ($\delta^{34}S$ and $\delta^{18}O$) and pyrite ($\delta^{34}S$) from the Tom and Jason Late Devonian Zn-Pb-Ba deposits, Selwyn Basin, Canada: Geochimica et Cosmochimica Acta, doi: 10.1016/j.gca.2016.02.015.

McCready, R.G.L. and Krouse, H.R., 1980, Sulfur isotope fractionation by Desulfovibrio vulgaris during metabolism of BaSO4: Geomicrobiology Journal, v. 2, no.1, pp.55-62.

Moore, T.E., Wallace, W., Bird, K., Karl, S., Mull, C., and Dillon, J., 1994, Geology of northern Alaska, in Plafker, G. and Berg, H. eds., The geology of Alaska, Geological Society of America, p. 49–140.

Moore, D.W., Young, L.E., Modene, J.S., and Plahuta, J.T., 1986, Geologic setting and genesis of

the Red Dog zinc-lead-silver deposit, western Brooks Range, Alaska: Economic Geology, v. 81, p. 1696–1727, doi: 10.2113/gsecongeo.81.7.1696.

Morelli, R.M., Creaser, R.A., Selby, D., Kelley, K.D., and King, A.R., 2004, Re-Os sulfide geochronology of the Red Dog sediment-hosted Zn-Pb-Ag deposit, Brooks Range, Alaska: Economic Geology, v. 99, p. 1569–1576, gsecongeo.highwire.org/content/99/7/1569.short.

Paull, C.K., Chanton, J.P., Neumann, A.C., Coston, J.A., Martens, C.S., and Showers, W., 1992, Indicators of Methane-Derived Carbonates and Chemosynthetic Organic Carbon Deposits: Examples from the Florida Escarpment: Palaios, v. 7, p. 361–375, doi: 10.2307/3514822.

Paytan, A., Kastner, M., Martin, E.E., MacDougall, J.D., and Herbert, T., 1993, Marine barite as a monitor of seawater strontium isotope composition: Nature, v. 366, p. 445–449, doi: 10.1038/366445a0.

Peucker-Ehrenbrink, B., and Ravizza, G., 2000, The marine osmium isotope record: Terra Nova, v. 12, p. 205–219, doi: 10.1046/j.1365-3121.2000.00295.x.

Reeburgh, W.S., 1976, Methane consumption in Cariaco Trench waters and sediments: Earth and Planetary Science Letters, v. 28, p. 337–344, doi: 10.1016/0012-821X(76)90195-3.

Reynolds, M.A., Gingras, M.K., Gleeson, S.A., and Stemler, J.U., 2015, More than a trace of oxygen: Ichnological constraints on the formation of the giant Zn-Pb-Ag ± Ba deposits, Red Dog district, Alaska: Geology, v. 43, doi: 10.1130/G36954.1.

Schardt, C., Garven, G., Kelley, K.D., and Leach, D.L., 2008, Reactive flow models of the Anarraaq Zn–Pb–Ag deposit, Red Dog district, Alaska: Mineralium Deposita, v. 43, p. 735–757, doi: 10.1007/s00126-008-0193-3.

Selby, D., and Creaser, R.A., 2005, Direct radiometric dating of the Devonian-Mississippian time-scale boundary using the Re-Os black shale geochronometer: Geology, v. 33, p. 545–548, doi: 10.1130/G21324.1.

Selby, D., and Creaser, R. a., 2003, Re–Os geochronology of organic rich sediments: an evaluation of organic matter analysis methods: Chemical Geology, v. 200, p. 225–240, doi: 10.1016/S0009-2541(03)00199-2.

Slack, J.F., Dumoulin, J.A., Schmidt, J.M., Young, L.E., and Rombach, C.S., 2004a, Paleozoic sedimentary rocks in the Red Dog Zn-Pb-Ag District and vicinity, western Brooks Range, Alaska: Provenance, deposition, and metallogenic significance: Economic Geology, v. 99, p. 1385–1414, 171.67.121.50/content/99/7/1385.short.

Slack, J.F., Falck, H., Kelley, K.D., and Xue, G.G., 2017, Geochemistry of host rocks in the Howards Pass district, Yukon-Northwest Territories, Canada: implications for sedimentary environments of Zn-Pb and phosphate mineralization: Mineralium Deposita,

v. 52, p. 565–593.

Slack, J.F., Kelley, K.D., Anderson, V.M., Clark, J.L., and Ayuso, R. a., 2004b, Multistage Hydrothermal Silicification and Fe-Tl-As-Sb-Ge-REE Enrichment in the Red Dog Zn-Pb-Ag District, Northern Alaska: Geochemistry, Origin, and Exploration Applications: Economic Geology, v. 99, p. 1481–1508, doi: 10.2113/gsecongeo.99.7.1481.

Slack, J.F., Selby, D., and Dumoulin, J.A., 2015, Hydrothermal, Biogenic, and Seawater Components in Metalliferous Black Shales of the Brooks Range, Alaska: Synsedimentary Metal Enrichment in a Carbonate Ramp Setting: Economic Geology, v. 110, p. 653–675, doi: 10.2113/econgeo.110.3.653.

Smith, D., 2017, Lithophile and chalcophile elements in sphalerite from the Anarraaq sediment-hosted Zn-Pb-Ag deposit, Red Dog district, Alaska (master's thesis): University of Alberta, Edmonton, Alberta.

Smoliar, M.I., Walker, R.J., and Morgan, J.W., 1996, Re-Os Ages of Group IIA, IIIA, IVA, and IVB Iron Meteorites: Science, v. 271, p. 1099–1102.

Smrzka, D., Kraemer, S.M., Zwicker, J., Birgel, D., Fischer, D., Kasten, S., Goedert, J.L., and Peckmann, J., 2015, Constraining silica diagenesis in methane-seep deposits: Palaeogeography, Palaeoclimatology, Palaeoecology, v. 420, p. 13–26, doi: 10.1016/j.palaeo.2014.12.007.

Snyder, G.T., Dickens, G.R., and Castellini, D.G., 2007, Labile barite contents and dissolved barium concentrations on Blake Ridge : New perspectives on barium cycling above gas hydrate systems: v. 95, p. 48–65, doi: 10.1016/j.gexplo.2007.06.001.

Suess, E., 2014, Marine cold seeps and their manifestations: geological control, biogeochemical criteria and environmental conditions: International Journal of Earth Sciences, v. 103, p. 1889–1916, doi: 10.1007/s00531-014-1010-0.

Taylor, S.R., and McLennan, S.M., 1995, The geochemical evolution of the continental crust: Reviews of Geophysics, v. 33, p. 241, doi: 10.1029/95RG00262.

Torres, M.E., Bohrmann, G., Dubé, T.E., and Poole, F.G., 2003, Formation of modern and Paleozoic stratiform barite at cold methane seeps on continental margins: Geology, v. 31, p. 897, doi: 10.1130/G19652.1.

Torres, M.E., Brumsack, H.J., Bohrmann, G., and Emeis, K.C., 1996, Barite fronts in continental margin sediments: A new look at barium remobilization in the zone of sulfate reduction and formation of heavy barites in diagenetic fronts: Chemical Geology, v. 127, p. 125–139, doi: 10.1016/0009-2541(95)00090-9.

Turekian, K.K., and Pegram, W.J., 1997, Os Isotope Record in a Cenozoic Deep-Sea Core: Its Relation to Global Tectonics and Climate, in Tectonic Uplift and Climate Change, p. 383–397, doi: 10.1007/978-1-4615-5935-1_17.

Veizer, J., Ala, D., Azmy, K., Bruckschen, P., Buhl, D., Bruhn, F., Garden, G.A.F., Diener, A., Ebneth, S., Godderis, Y., Jasper, T., Korte, C., Pawellek, F., Podlaha, O.G., et al., 1999, 87Sr/86Sr, δ13C and δ18O evolution of Phanerozoic seawater: Chemical Geology, v. 161, p. 59–88, doi: 10.1016/S0009-2541(99)00081-9.

De Vera, J., 2005, Structure of the Red Dog District, Western Brooks Range, Alaska: University of London, 633 p., http://www.arlis.org/docs/vol1/D/773627462.pdf.

De Vera, J., McClay, K., and King, A., 2004, Structure of the Red Dog District, Western Brooks Range, Alaska: Economic Geology, v. 99, p. 1415–1434, http://econgeol.geoscienceworld.org/content/99/7/1415.short.

Volpi, V., Camerlenghi, a, Hillenbrand, C.-D., Rebescon, M., and Ivaldiz, R., 2003, Effects of biogenic silica on sediment compaction and slope stability on the Pacificmargin of the Antarctic Peninsula: Basin Research, v. 15, p. 339–363, doi: 10.1046/j.1365-2117.2003.00210.x.

Wilkin, R.T., Barnes, H.L., and Brantley, S.L., 1996, The size distribution of framboidal pyrite in modern sediments : An indicator of redox conditions: v. 60, p. 3897–3912.

Young, L.E., 2004, A Geologic Framework for Mineralization in the Western Brooks Range, Alaska: Economic Geology, v. 99, p. 1281–1306, doi: 10.2113/gsecongeo.99.7.1281.

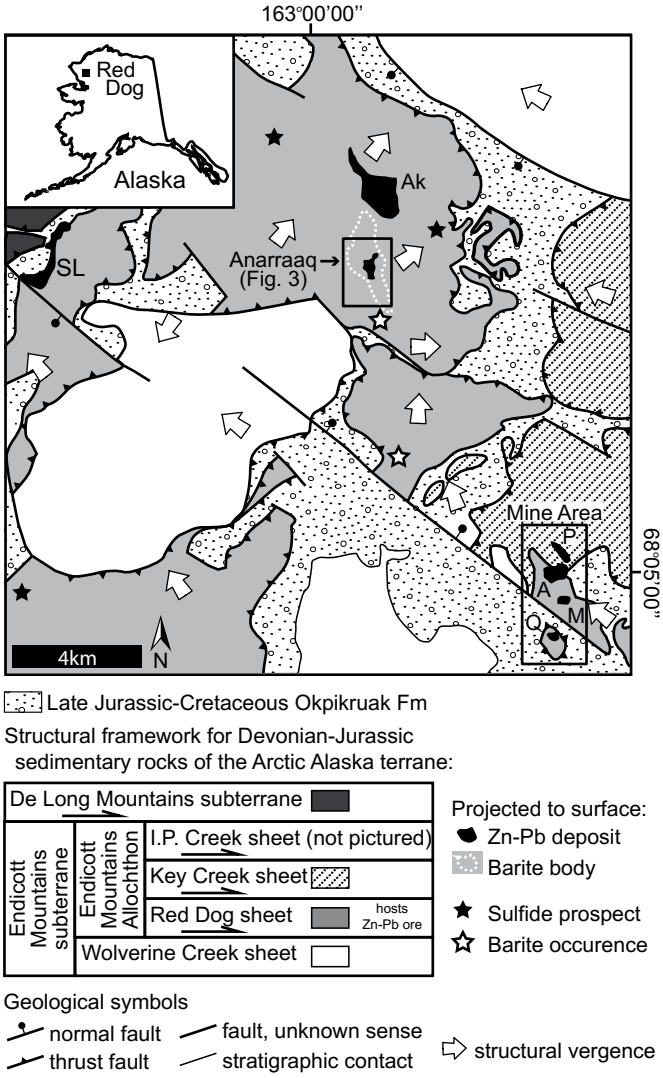

Figure 3.1: Regional map of the Red Dog district. Modified after Figs. 2, 3, and 14 in Blevings et al. (2013). Mine area deposits include Main (M), Aqqaluk (A), Paalaaq (P), and Qaanaaq (Q). Other deposits include Anarraaq, Aktigiruk (Ak), and Su Lik (SL). Several additional prospects and barite occurrences are also highlighted. Thrust sheets have been referred to as 'plates' in previous publications; we use 'thrust sheets' or 'sheets' in this contribution to avoid confusion with plates in the tectonic sense.

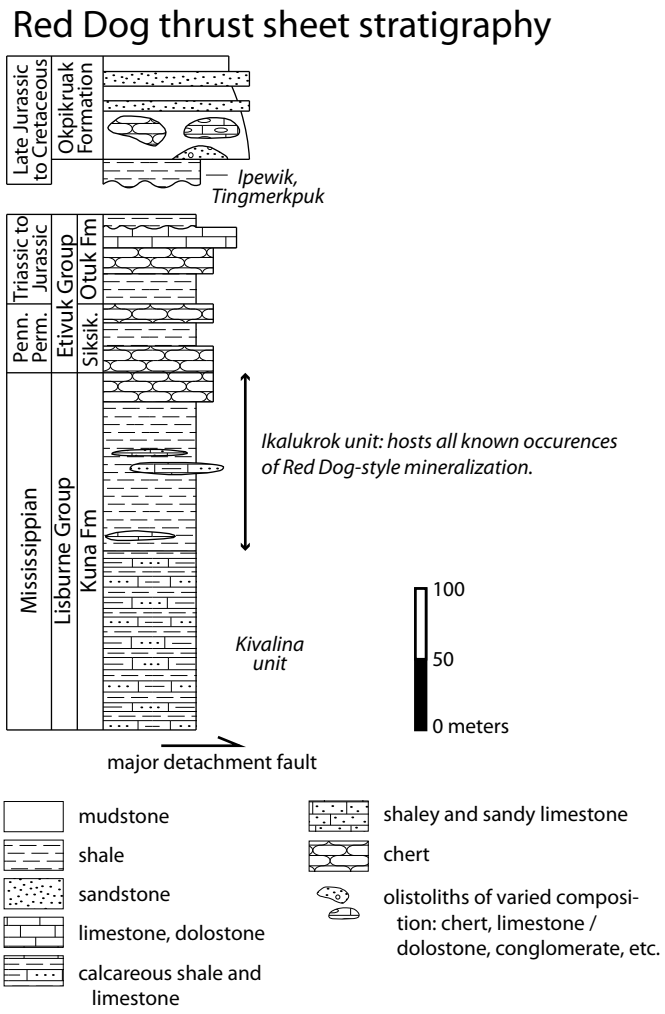

Figure 3.2: Generalized stratigraphy of the Red Dog thrust sheet, which hosts all known SHMS mineralization in the Red Dog district. Modified after Fig. 4 in Blevings et al. (2013).

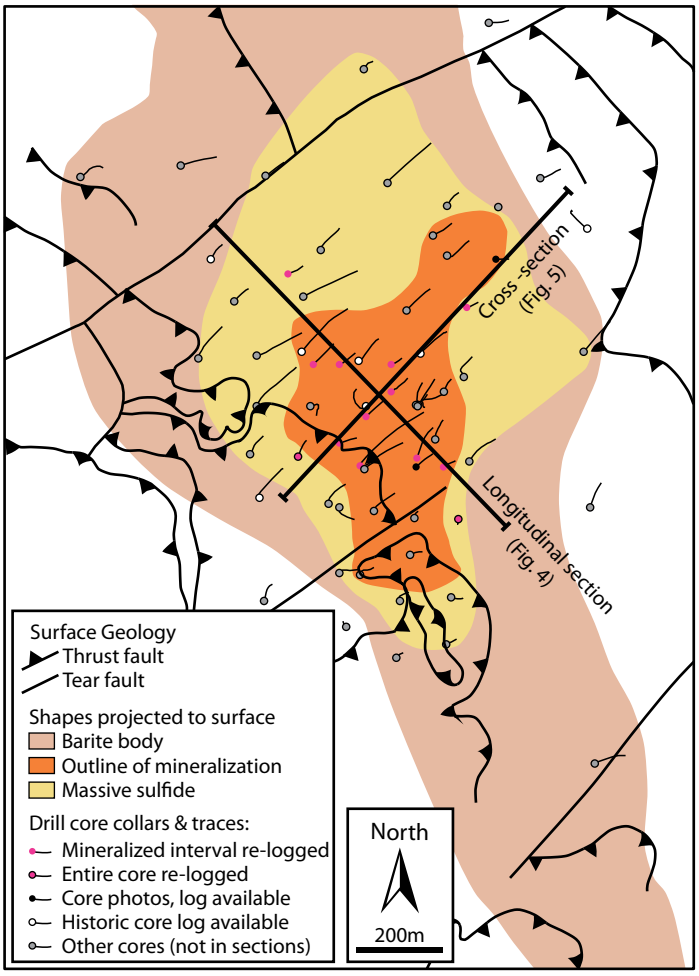

Figure 3.3: Plan map of the Anarraaq area. Modified after Fig. 14 in Blevings et al. (2013).

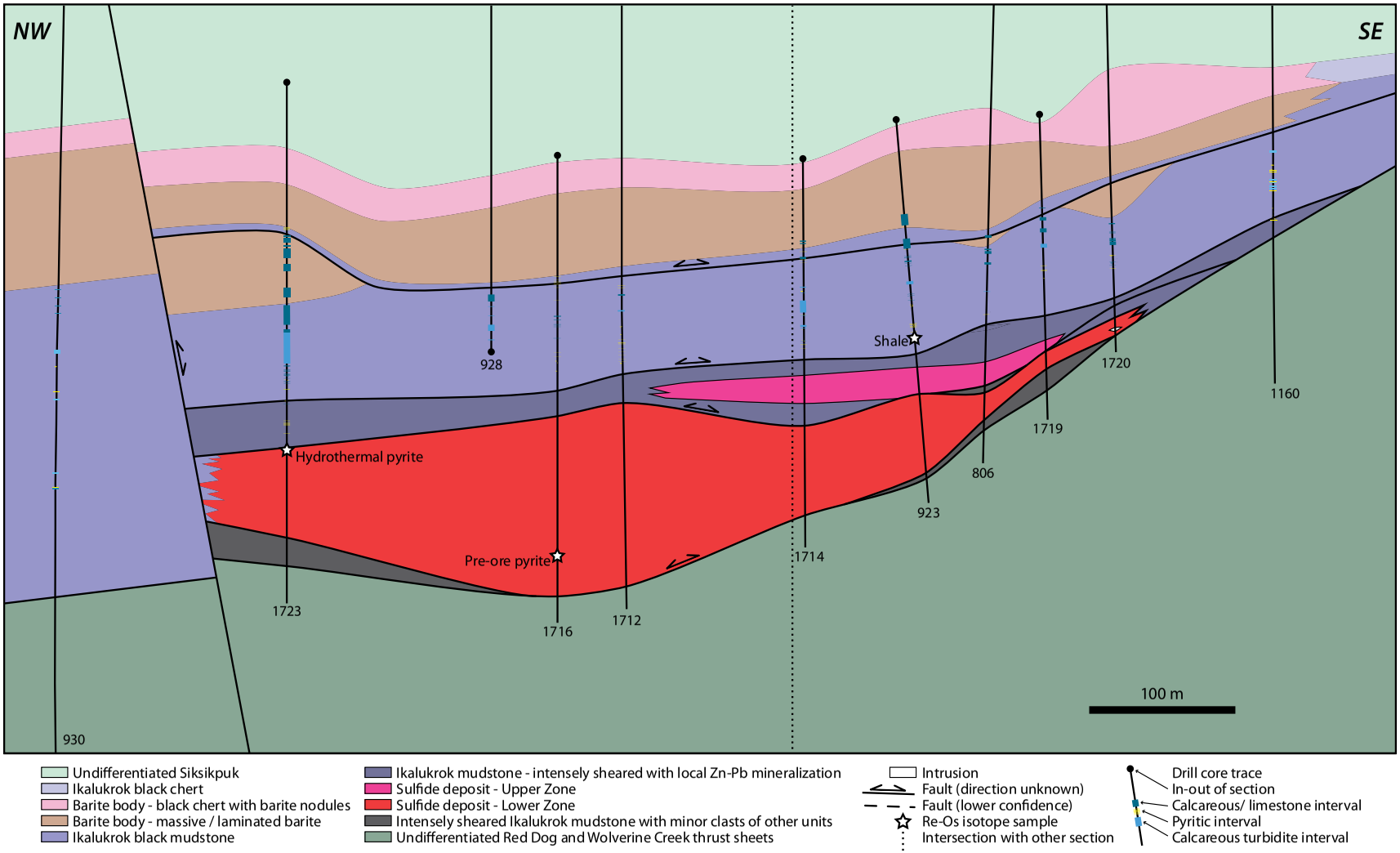

Figure 3.4 Longitudinal section through the central part of the Anarraaq sulfide deposit. Section is oriented perpendicular to the direction of transport during Brookian shortening.

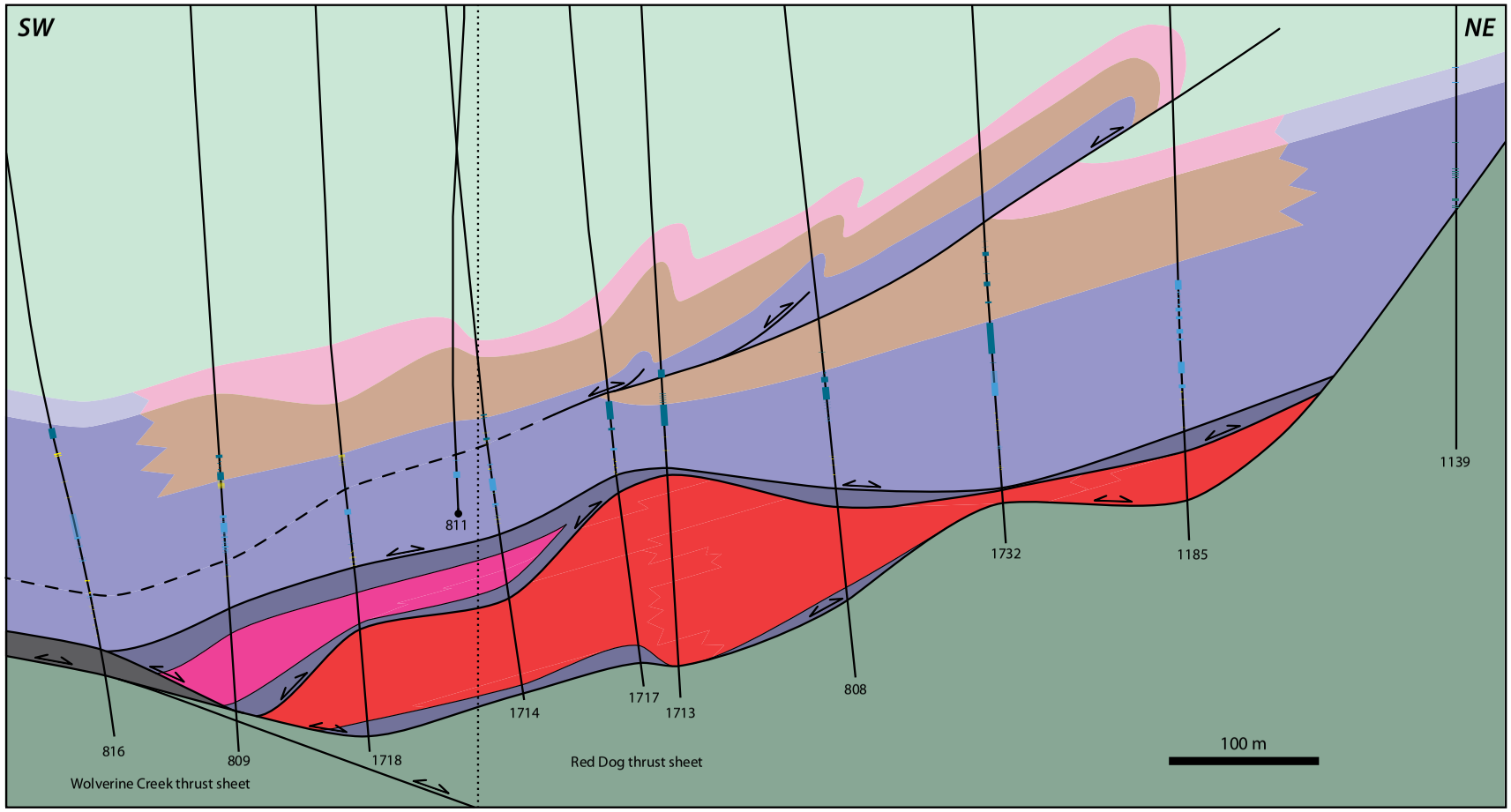

Figure 3.5: Cross-section through the central part of the Anarraaq sulfide deposit. Section is oriented parallel to the direction of transport during Brookian shortening. See Fig. 3.4 for legend.

Abbreviations: Mdst – mudstone, Py – pyrite, Qz – quartz, Sp – sphalerite.

Figure 3.6: Selected petrographic images from the Anarraaq sulfide deposit. (a) Core 1185 between 2007 and 2017 ft deep – whole core, up is to the upper left corner. This interval of the Upper Zone is characterized by abundant shear zones (underlined by red lines). (b) Sample 923-2240.9 – cut core in approximate depositional orientation. Sheared mudstone from the top of the Upper Zone contains deformed fragments of sphalerite and pyrite.

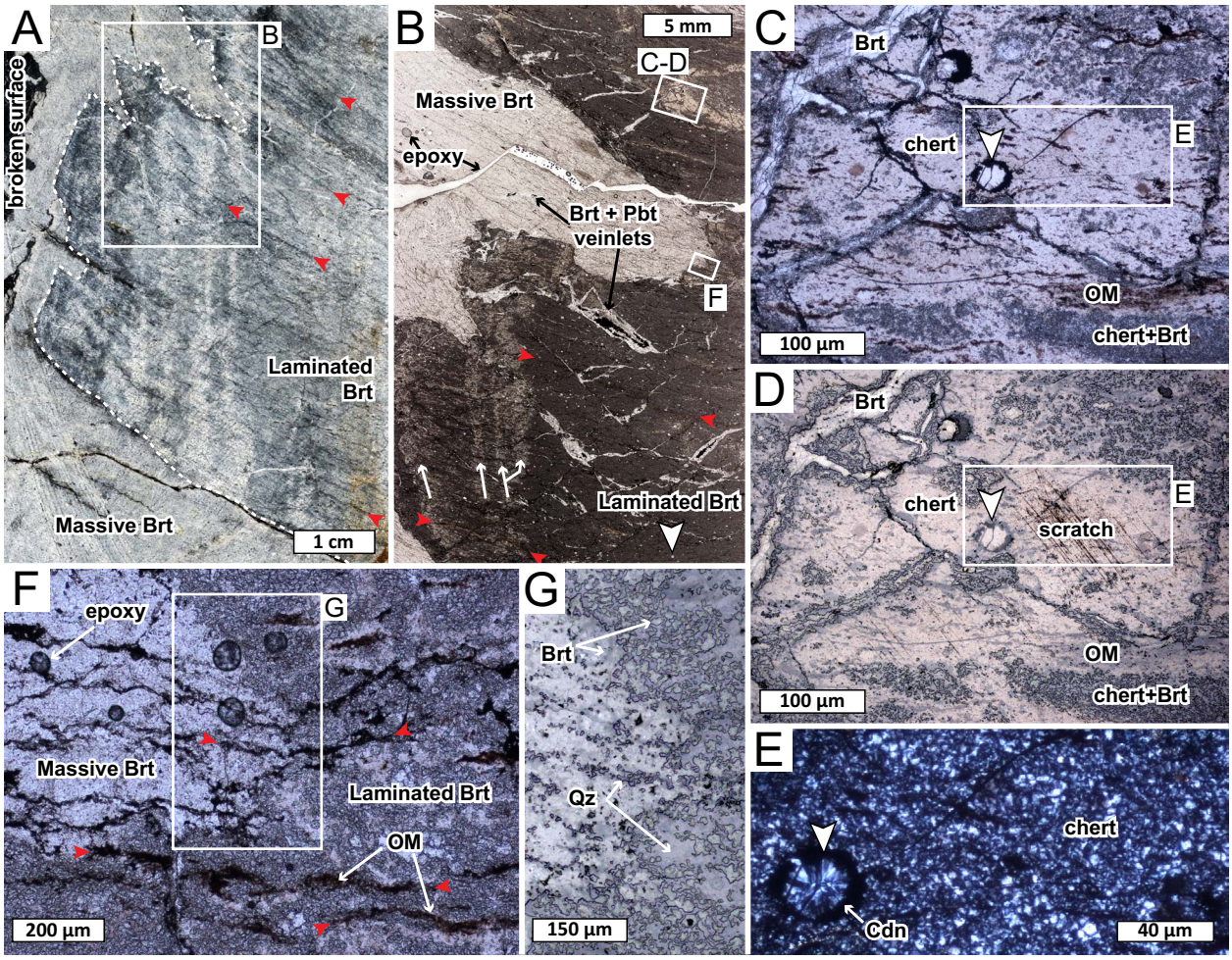

Figure 3.7: Selected petrographic images from the Anarraaq barite body. (a) Sample 809-1893.2 – cut core in approximate depositional orientation. The contact between laminated and massive barite is very irregular and is discordant to remnant mudstone laminae. (b) Approximate inset area in a – thin section in plane-polarized light. Thin section was made from the other side of cut sample. Light-colored vertical features (white arrows) are depleted in barite; reducing fluids were focused here. Coarser crystalline barite ± pyrobitumen veinlets occur in both massive and laminated barite. (c) Inset area in b – thin section in plane-polarized light. Light brown chert with local clasts/ patches of enriched organic material. (d) Same as in c but in reflected light. Note how barite veinlets are associated with disseminated barite in chert. (e) Inset area in c-d – thin section in cross-polarized light. Radiolarian is preserved as chalcedony; chert is microcrystalline. (f) Inset area in b – thin section in plane-polarized light. Contact between laminated and massive barite. The laminated texture is composed of disseminated barite in chert with discontinuous organic rich laminae. (g) Inset area in f – thin section in reflected light. Disseminated barite crystals are highly irregular in shape.

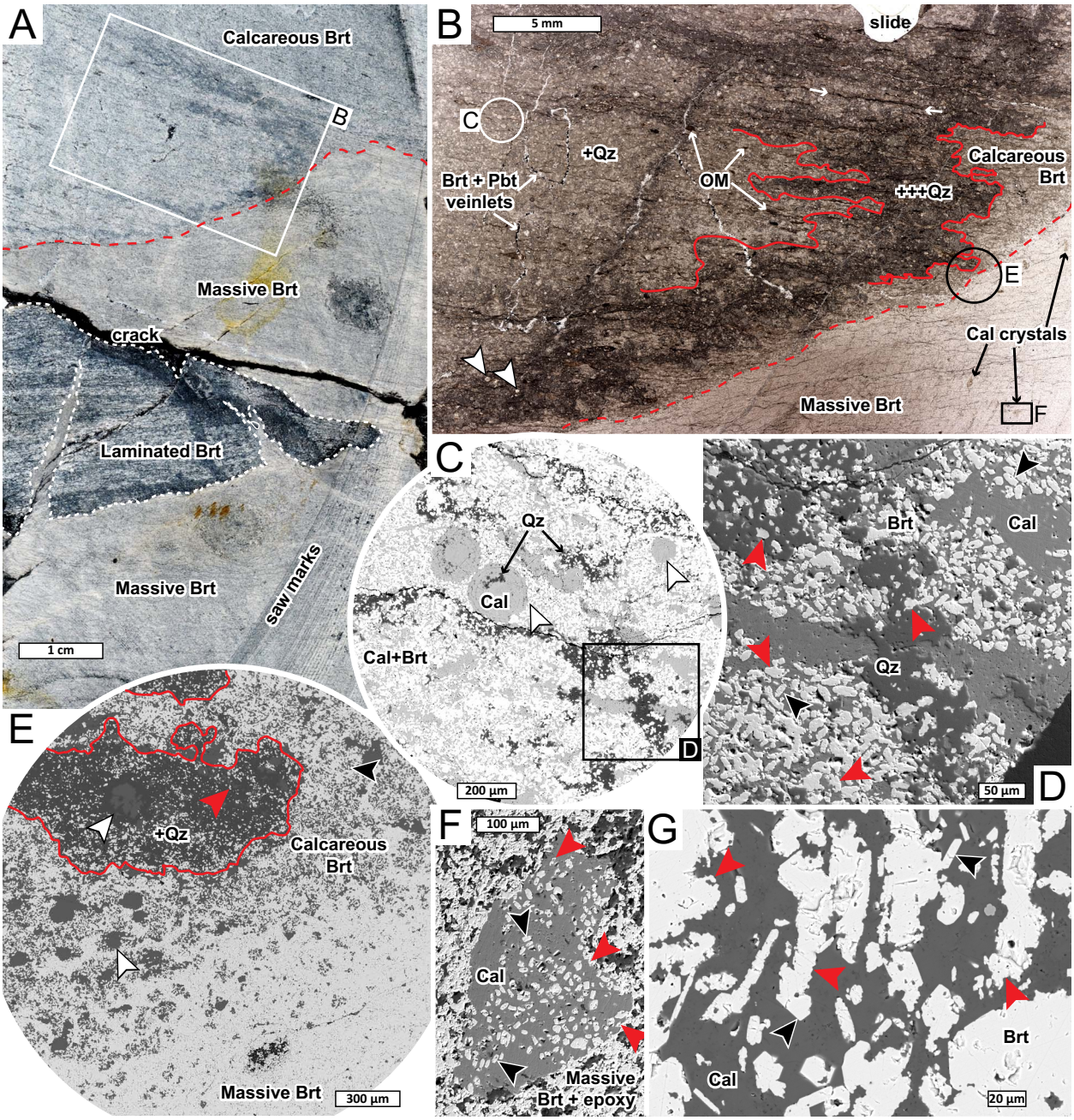

Figure 3.8: Selected petrographic images from the Anarraaq barite body. (a) Sample 809-1913.1 – hand sample in approximate depositional orientation. The contact between massive and laminated barite is highly irregular and crosscuts laminated fabric. The contact of calcareous barite is also irregular. (b) Inset area in a – thin section in plane-polarized light. The transition between calcareous and non-calcareous barite is associated with a quartz alteration front. Both boundaries are discordant to remnant mudstone laminae. (c) Inset area in b – backscattered electron image.

Quartz occurs as veinlets and is associated with calcite and barite depletion. (d) Inset area in c – SEM image. Barite is relatively abundant in calcite and occurs as irregularly shaped and euhedral crystals. Barite is less abundant in quartz and occurs only as highly irregularly-shaped crystals. (e) Inset area in b – backscattered electron image. Closeup of contact between calcareous and non-calcareous barite. Addition of quartz is associated with removal of calcite and barite. The addition of calcite is somewhat gradational. (f) Inset area in b – SEM image. Euhedral calcite crystal in massive barite contains abundant euhedral and rare irregularly shaped barite crystals. (g) Calcareous barite nodule in sample 809-1739.8 – backscattered electron image. Barite and calcite display both out-of-equilibrium and equilibrium textures.

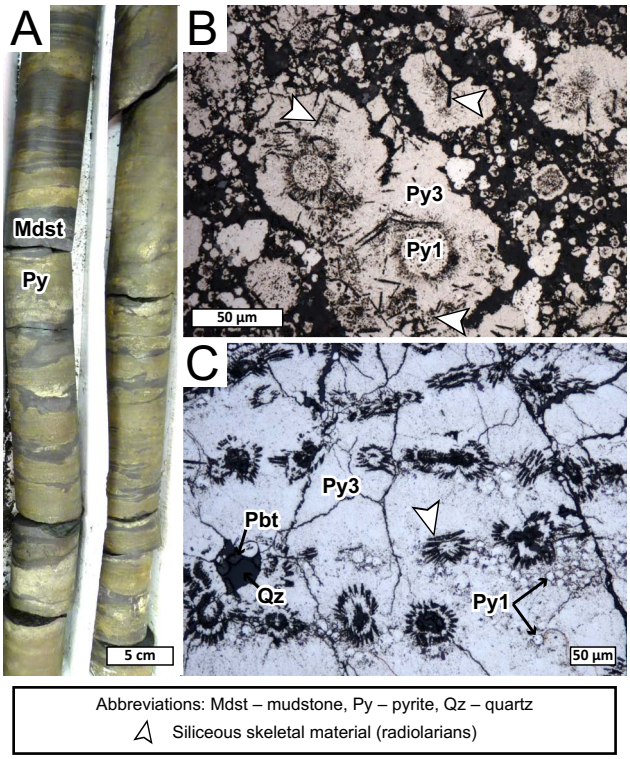

Figure 3.9: Selected petrographic images from the interval of mudstone with abundant layered and nodular pyrite, underlying the Anarraaq barite body. (a) Core 809 between 1972 and 1976 ft deep – whole core in approximate depositional orientation. (b) Sample 809-1980.3 – thin section in reflected light. Pyrite framboids (Py1) overgrown by massive pyrite (Py3), which contains siliceous radiolarian skeletal material, in siliceous mudstone. (c) Sample 809-1971.8 – thin section in reflected light. Massive pyrite (Py3) overgrowing local clusters of pyrite spheroids (Py1) and preserving radiolarian skeletons.

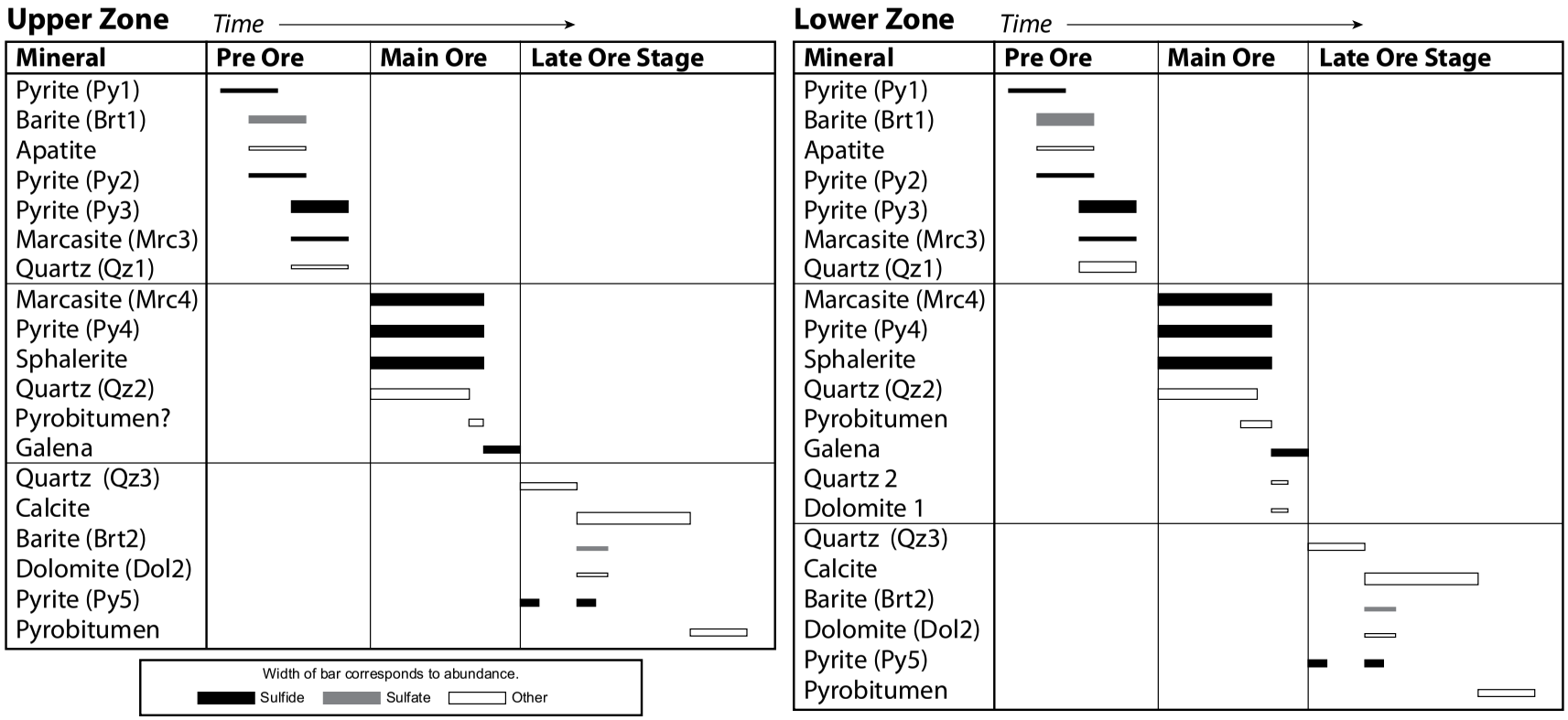

Figure 3.10: Paragenetic chart for the Upper and Lower Zones in the Anarraaq sulfide deposit.

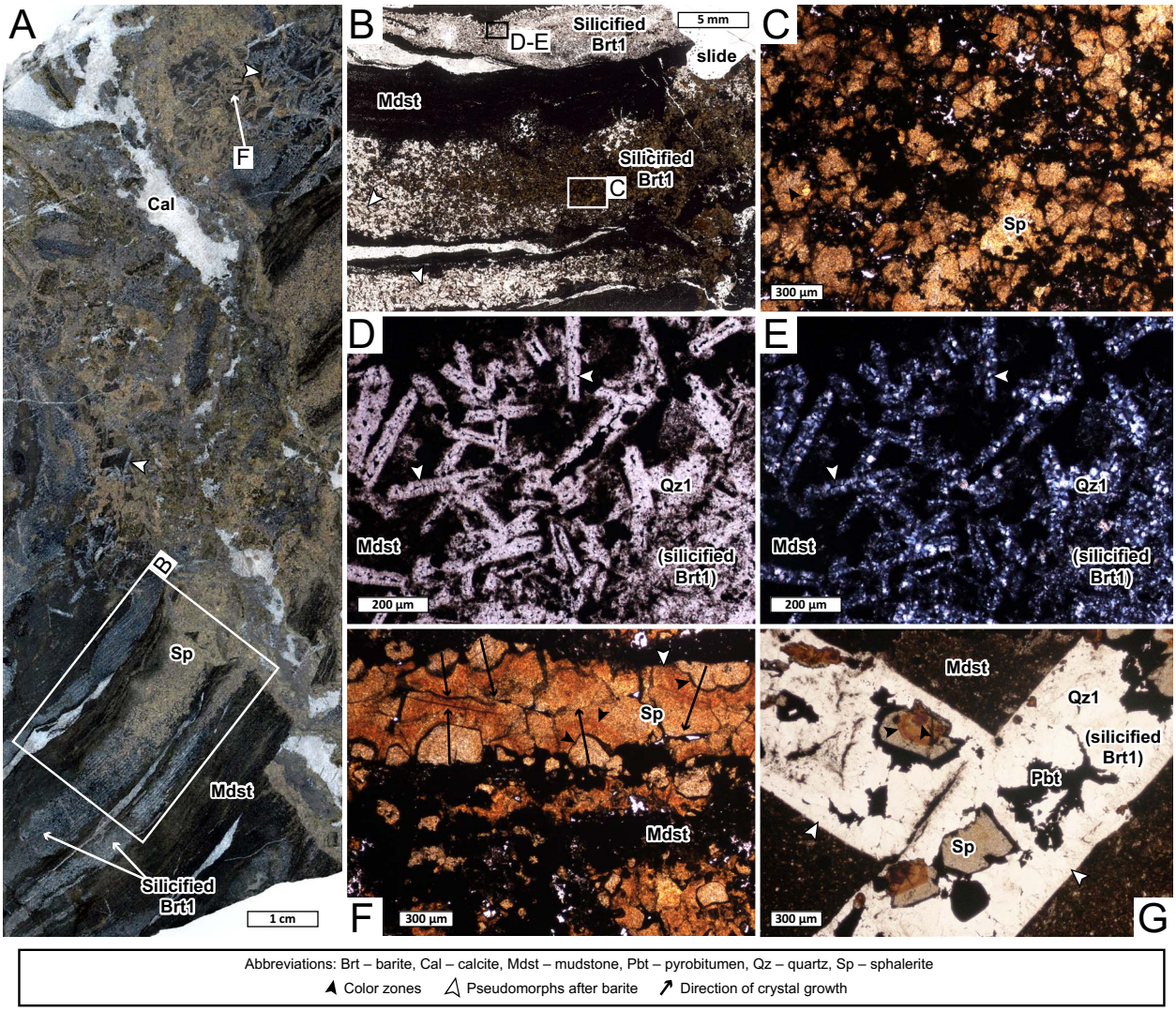

Figure 3.11: Selected petrographic images from the Anarraaq sulfide deposit Lower Zone. (a) Core 1717-2317 – hand sample in approximate depositional orientation. Ore-stage vein crosscuts interbedded mudstone and silicified barite. Silicified barite is preferentially replaced by sphalerite near the crosscutting vein. (b) Inset area in a – thin-section in plane polarized light. (c) Inset area in b – thin-section in plane polarized light. Note local color zonation and that no evidence of pre-ore barite is preserved. (d-e) Inset area in b – thin-section in plane polarized and cross polarized light. Coalescing barite laths are replaced by microcrystalline quartz. (f) Approximate location noted in a – thin-section in plane polarized light. Sphalerite pseudomorph after barite. Color zones indicate that barite was completed dissolved prior to sphalerite nucleation at the edge of the former barite crystal and inward growth. (g) Sample 1717-2252.5 – thin-section in plane polarized light. Quartz pseudomorph after barite appears to have experienced local dissolution followed by sphalerite crystal growth and cementation in pyrobitumen.

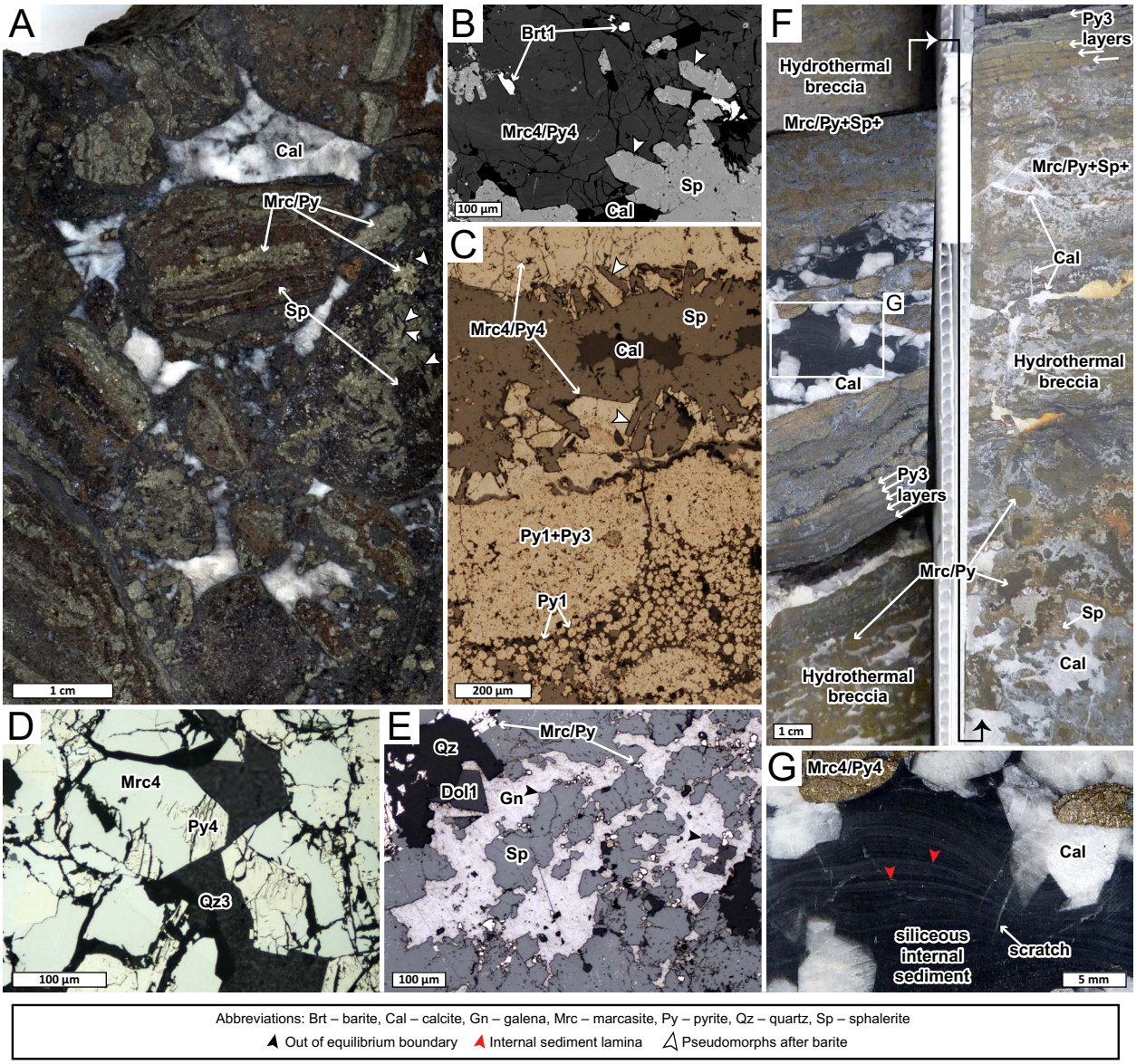

Figure 3.12: Selected petrographic images from the Anarraaq sulfide deposit Lower Zone. (a) Sample 923-2251.2 – cut core in approximate depositional orientation. Hydrothermal breccia comprised of massive sulfide clasts cemented in calcite. Note rare sphalerite pseudomorphs. (b) Back scattered electron and (c) reflected light images from the sample in a. Remnant barite and an most sphalerite pseudomorphs after barite are rare, very fine crystalline, and difficult to identify. Fe sulfide in this sample comprises early framboids (Py1) overgrown by massive fine crystalline pyrite (Py3) and abundant coarser crystalline Fe sulfide (Py4, Mrc4). (d) Core 923-2376.6 – thin-section in reflected light. Pyrite has partially replaced euhedral marcasite crystal. Note the overall complexity of pyrite-marcasite textures. (e) Core 923-2385.3 – thin-section in reflected light. Euhedral dolomite is intergrown with galena. Galena is extremely out of equilibrium with earlier sphalerite. (f) Sample 1716-2347 – cut core in approximate depositional orientation.

Although much of sample is a chaotic hydrothermal breccia, short intervals of apparently undisturbed pre-ore pyrite layers (Py3) layers are also preserved. (g) Inset area in f – cut core. Internal sediment laminae are deformed by euhedral calcite crystals. Note the similarity between internal sediment (which is hydrothermal in origin) and Ikalukrok mudstone.

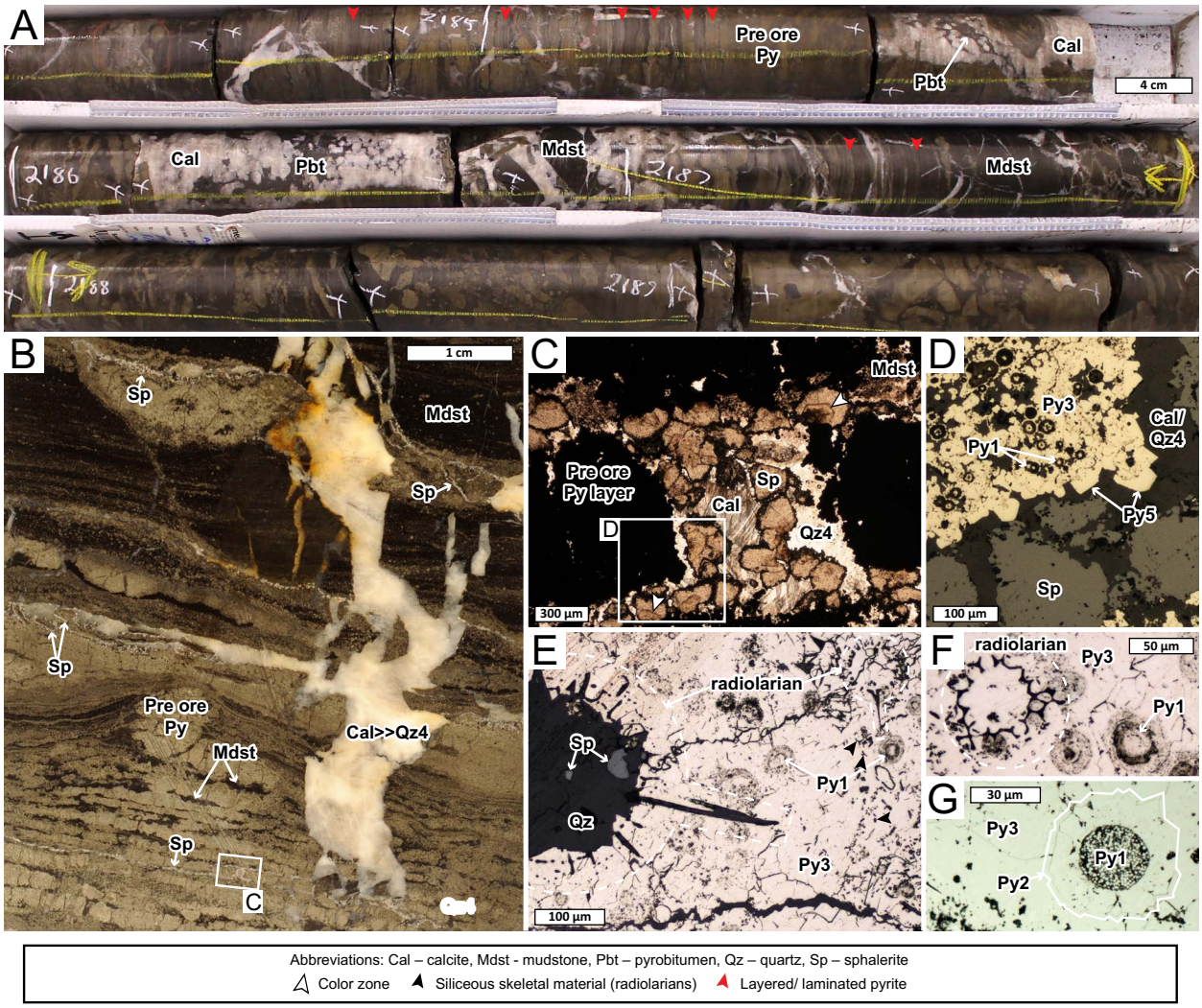

Figure 3.13: Selected petrographic images from the Anarraaq sulfide deposit Lower Zone. (a) Core 1723 between 2184 and 2190 ft deep – whole core, up is to the upper left corner. Pre-ore pyrite in Ikalukrok mudstone crosscut by ore-stage calcite-quartz-pyrobitumen veins. (b) Sample 1723-2197.6 – cut core in approximate depositional orientation. Pre-ore pyrite in mudstone crosscut by sphalerite veinlets and late ore-stage calcite-quartz. (c) Inset area in b – thin-section in plane polarized light. Although sphalerite is light tan and homogenous in hand sample, zoning is observed in thin section. (d) Inset area in c – thin-section in reflected light. Pre-ore pyrite layer is composed of spheroids (Py1) and massive overgrowths (Py3) and rimmed with cubic pyrite (Py5) where in contact with quartz-calcite vein. (e-f) Sample 1713-2352.5 – thin-section in reflected light. Pre-ore pyrite layers comprise pyrite spheroids (Py1), massive overgrowths (Py3), and radiolarian skeletal material. (g) Sample 923-2404.8 – thin-section in reflected light. Pyrite framboids (Py1) are locally overgrown by euhedral pyrite (Py3).

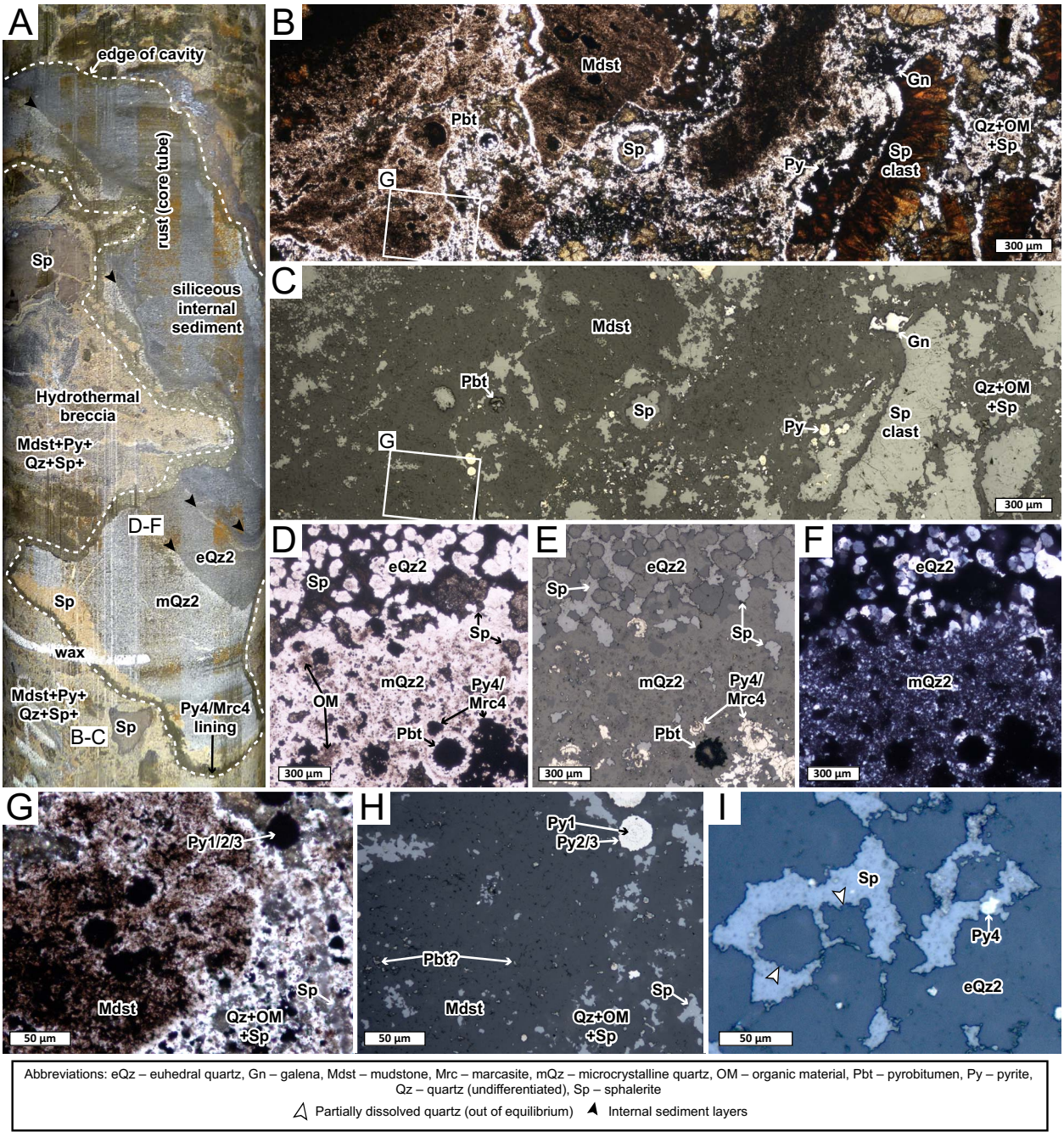

Figure 3.14: Selected petrographic images from the Anarraaq sulfide deposit Lower Zone. (a) Sample 1713-2495 – whole core in approximate depositional orientation. Hydrothermal breccia contains a cavity filled with internal sediment. (b-c) Approximate location indicated in a – thin-section in plane polarized and reflected light, respectively. Clasts of mudstone and sphalerite are cemented by a mixture of quartz, organic material, and sphalerite. (d-f) Approximate location indicated in a – thin-section in plane polarized, reflected, and cross polarized light, respectively. Internal sediment is composed of quartz (microcrystalline, mQz2, and later euhedral, eQz2),

organic material, and ore-stage sulfides. Sub-rounded pyrobitumen occurrence is interpreted to have been a hydrocarbon bubble during mineralization. (g-h) Inset area in b-c – thin-section in plane polarized and reflected light. The transition from mudstone clast to cement is somewhat gradational. (i) Close up of euhedral quartz 'sediment' (eQz2) from sample in a – thin-section in reflected light. Euhedral quartz (eQz2) was partially dissolved before cemented in sphalerite.

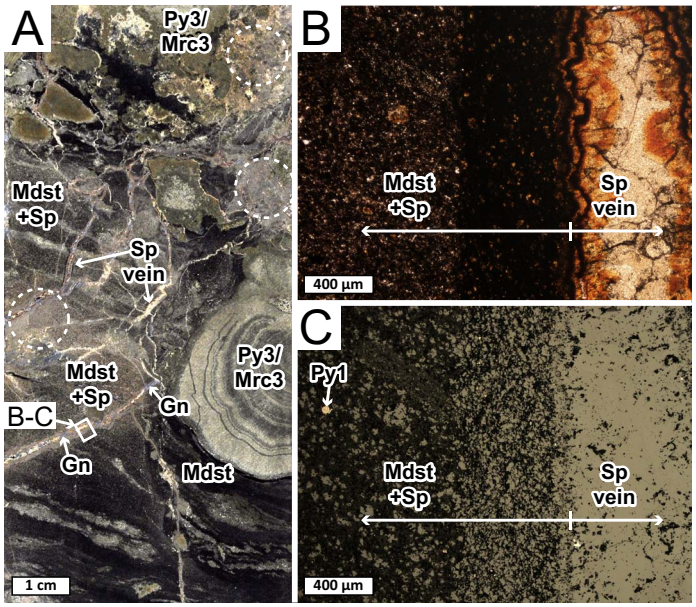

Figure 3.15: Selected petrographic images from the Anarraaq sulfide deposit Lower Zone. (a) Sample 1713-2536 – cut core in approximate depositional orientation. Ikalukrok mudstone and pre-ore Fe sulfide (Py3/Mrc3) are overprinted with disseminated sphalerite and sphalerite-galena veins. Dashed line circles highlight areas where host rock would be difficult to identify without the rest of the sample for context. (b-c) Inset in a – thin-section in plane polarized and reflected light images, respectively. Sphalerite vein has alteration selvedge of intense sphalerite replacement of mudstone. Disseminated sphalerite farther left may be exploiting pore space that was open at the time of mineralization.

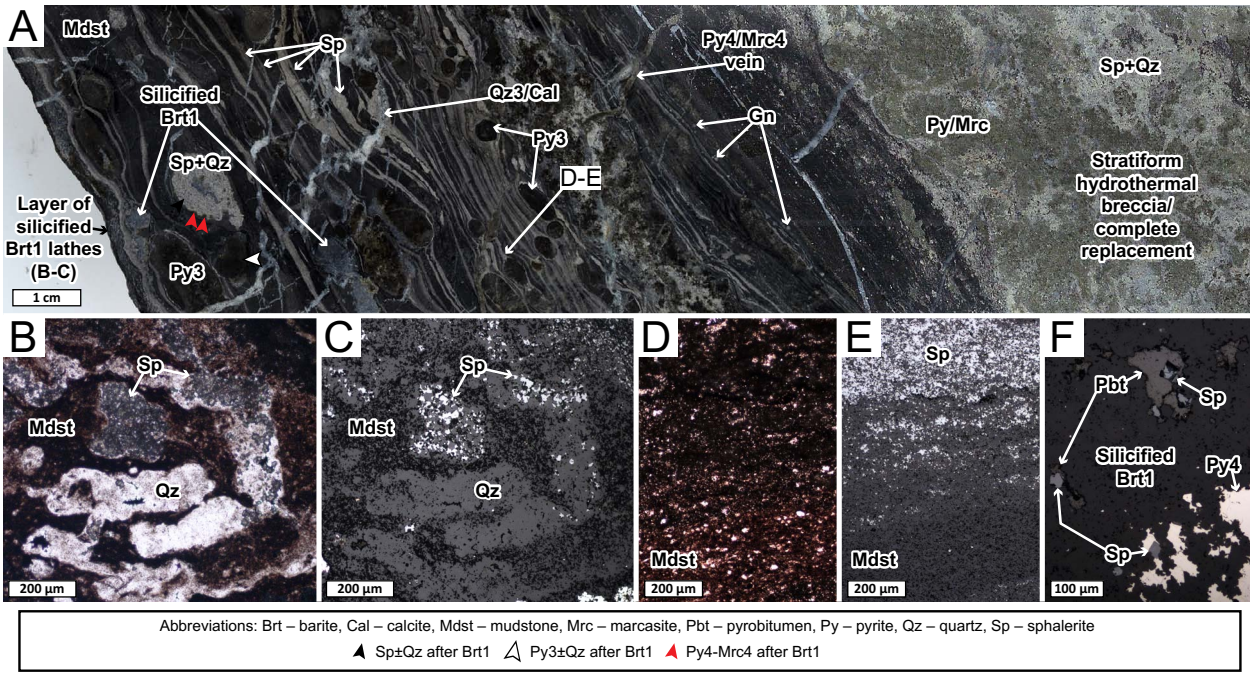

Figure 3.16: Selected petrographic images from the Anarraaq sulfide deposit Upper Zone. (a) Sample 1719-2154 – cut core, up section is to the left. On the left, laminated sphalerite in Ikaluk-rok mudstone. Silicified barite laths locally coalesce to form nodules, which are locally replaced by Fe sulfide and sphalerite. Relatively large galena subhedrons are indicated. On the right, an interval of chaotic hydrothermal breccia appears to be strataform. (b-c) Approximate location indicated in a – thin-section in plane polarized and reflected light images, respectively. Typical Lower Zone sphalerite texture is very fine crystalline and disseminated in quartz. Sphalerite preferentially replaces silicified barite. (d-e) Approximate location indicated in a – thin-section in plane polarized and reflected light images, respectively. Although laminated sphalerite appears to have sharp boundaries in hand sample, thin-section shows the contact with mudstone to be gradational. (f) From silicified barite nodule in a – thin-section in reflected light image. Sphalerite and pyrobitumen have a close spatial relationship, similar to in the Lower Zone (Fig. 3.11G).

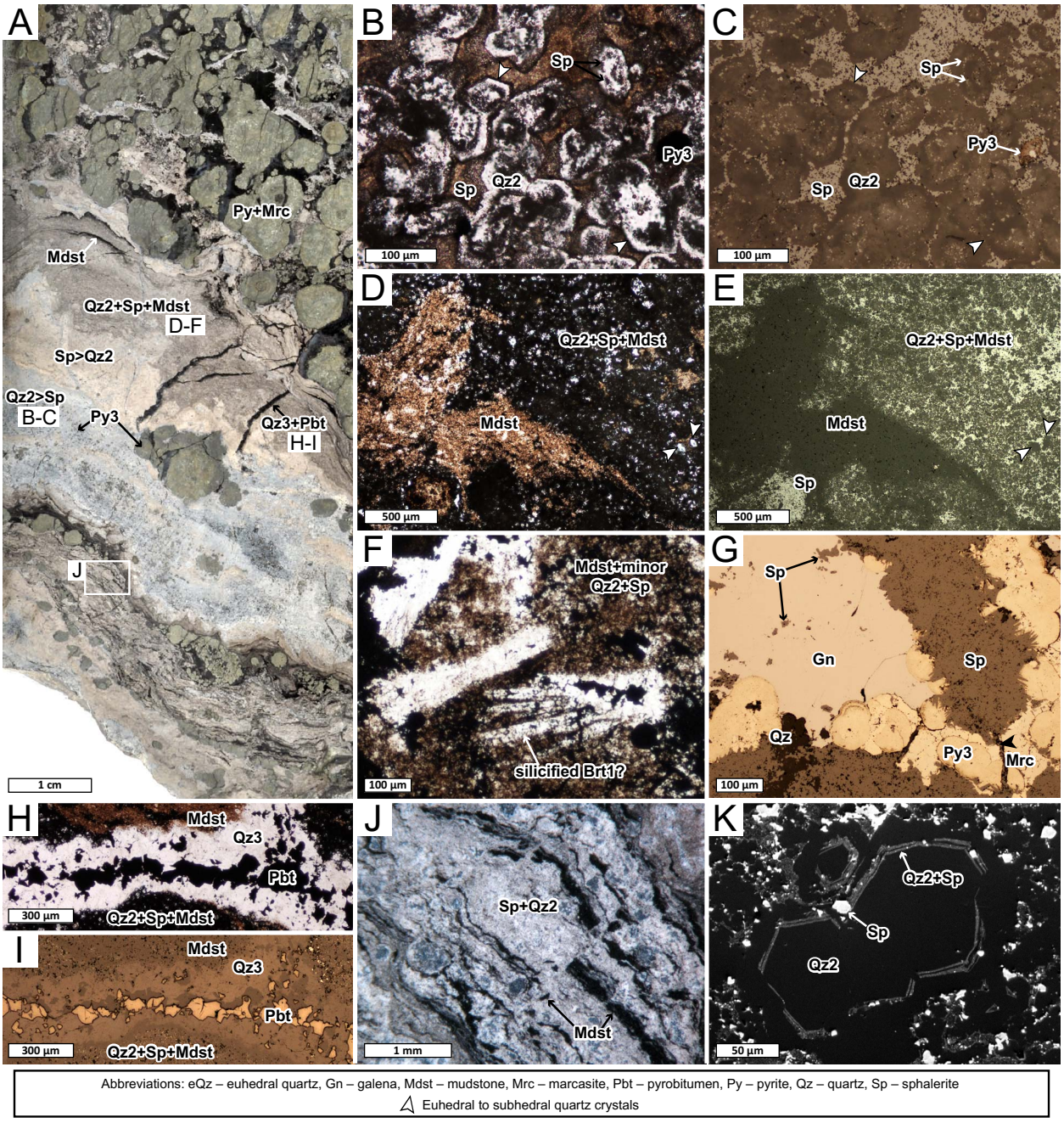

Figure 3.17: Selected petrographic images from the Anarraaq sulfide deposit Upper Zone. (a) Sample 809-2332.7 – cut core in approximate depositional orientation. (b-c) Approximate location indicated in a – thin-section in plane polarized and reflected light images, respectively. Euhedral quartz crystals (Qz2) with sphalerite inclusions, cemented with sphalerite. (d-e) Approximate location indicated in a – thin-section in plane polarized and reflected light images, respectively. Quartz and sphalerite replace mudstone. Local quartz euhedrons indicate this is likely the same phase of quartz in b-c. (f) Approximate location indicated in a – thin-section in plane

polarized image. Possible quartz pseudomorphs after barite laths. (g) From a – thin-section in reflected light. Galena is late and out of equilibrium with sphalerite (note highly irregularly shaped sphalerite islands in galena). Sample also contains pre-ore colloform pyrite (Py3) and marcasite, which are crosscut by sphalerite. (h-i) Approximate location indicated in a – thin-section in plane polarized and reflected light images, respectively. Late quartz-pyrobitumen veinlet. (j) Inset in a – cut core. Sphalerite-quartz cements mudstone clasts. (k) Sample 923-2202.3 – back scattered electron image. Sphalerite occurs along growth zone in euhedral quartz.

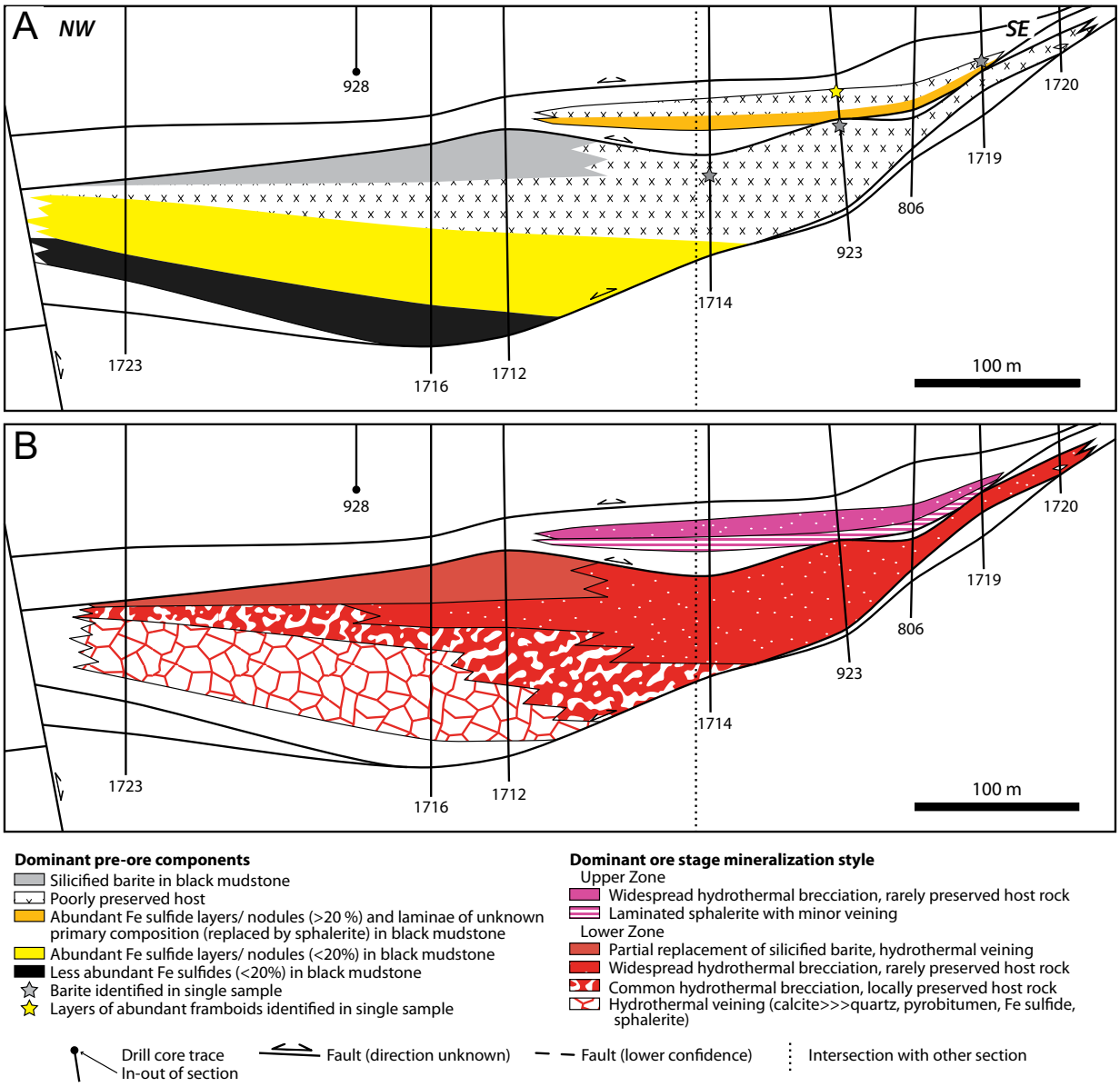

Figure 3.18: Close up of the longitudinal section of the Anarraaq sulfide deposit in Fig. 3.4 showing the spatial distribution of (a) pre-ore components and (b) ore-stage mineralization styles.

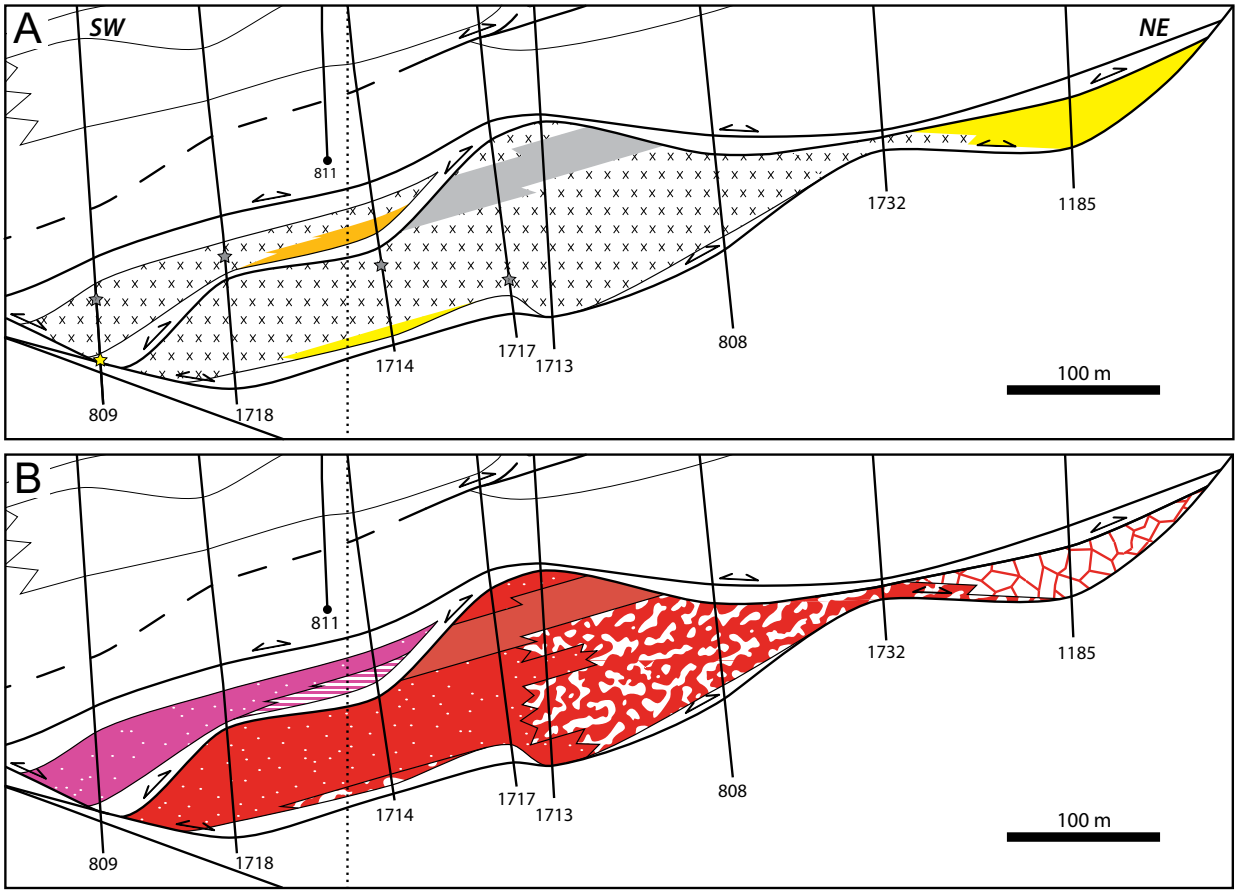

Figure 3.19: Close up of the cross-section of the Anarraaq sulfide deposit in Fig. 3.5 showing the spatial distribution of (a) pre-ore components and (b) ore-stage mineralization styles. See Fig. 3.18 for legend.

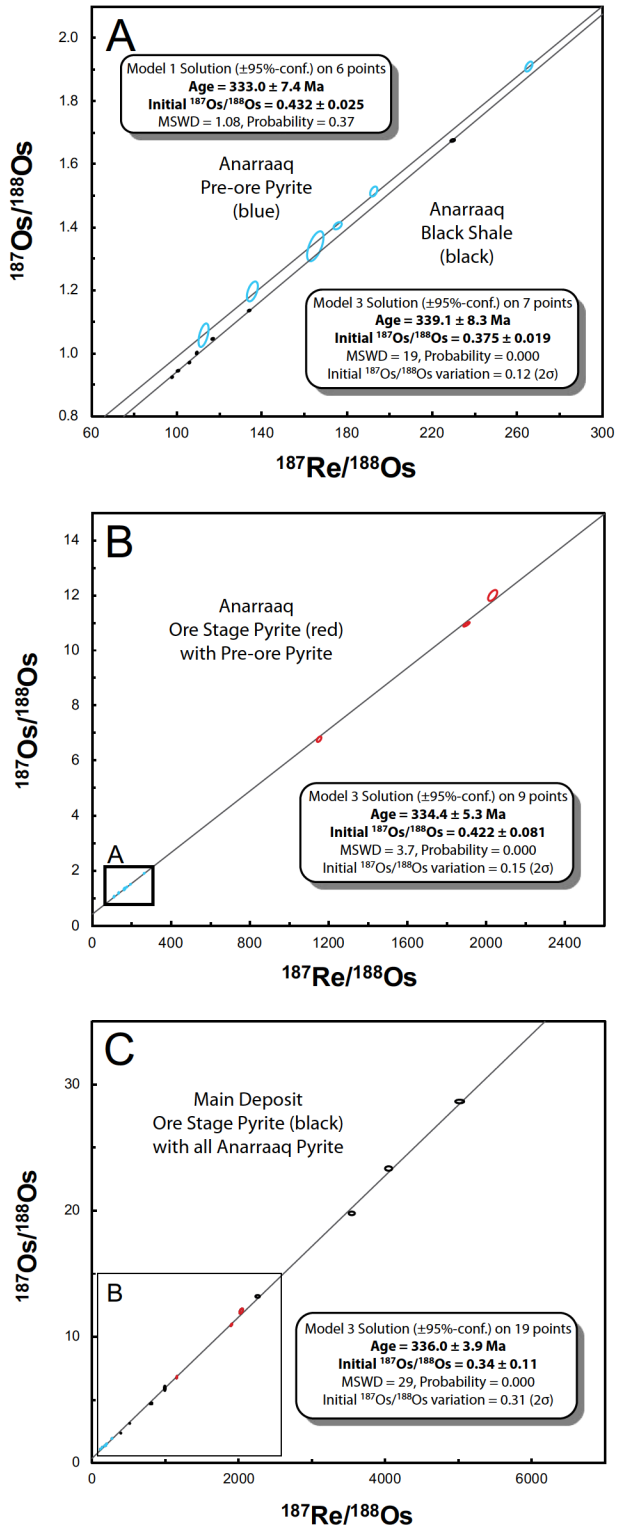

Figure 3.20: Re-Os isochron diagrams for (a) pre-ore pyrite in the Anarraaq sulfide deposit and overlying mudstone, (b) pre-ore and ore-stage pyrite in the Anarraaq sulfide deposit, and (c) ore-stage pyrite from the Anarraaq and Main deposits. Data from the Main deposit is from Morelli et al. (2004).

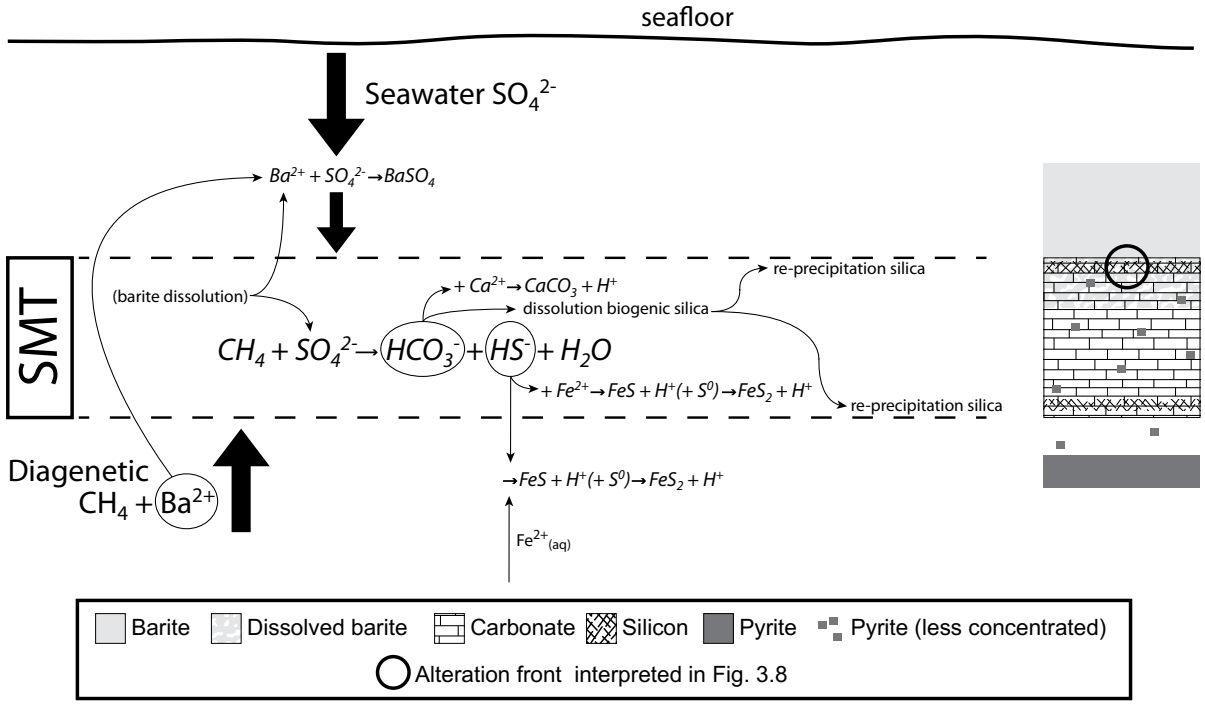

Figure 3.21: An overview of the chemical reactions and mineral precipitates associated with sulfate-driven anaerobic oxidation of methane (SD-AOM) at a sulfate methane transition (SMT). Modified after Fig. 14 in Lash et al. (2015).

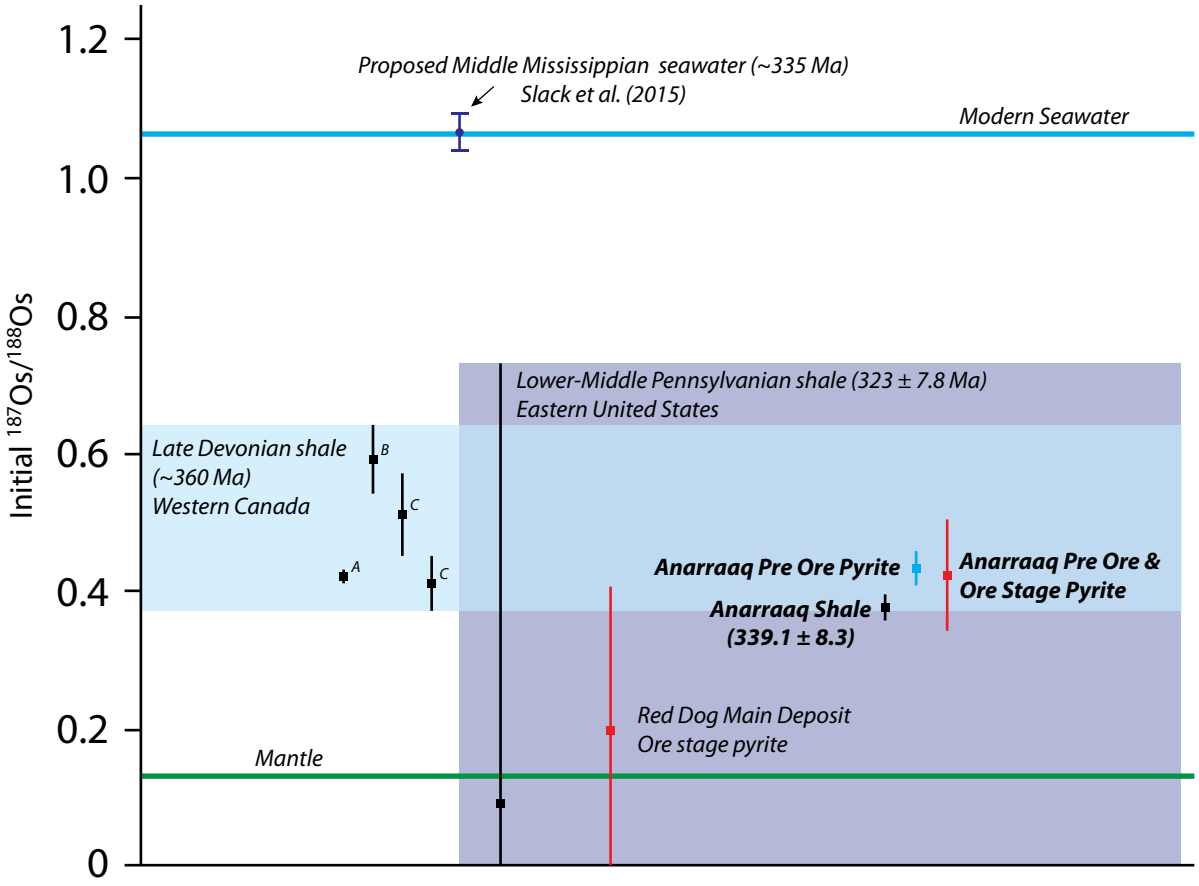

Figure 3.22: Initial Os isotopic composition ($^{187}Os/^{188}Os$) of pre-ore and ore-stage pyrite from the Anarraaq sulfide deposit and overlying Ikalukrok shale. Also plotted are data from ore-stage pyrite in the Red Dog Main deposit (Morelli et al., 2004); several Late Devonian shales (A: Selby and Creaser, 2005; B: Creaser et al., 2002; C: Selby and Creaser, 2003); and a Lower-Middle Pennsylvanian shale (Geboy et al., 2015). The Os compositions of modern seawater and the mantle reservoirs are from Peuckler-Ehrenbrink and Ravizza (2000).

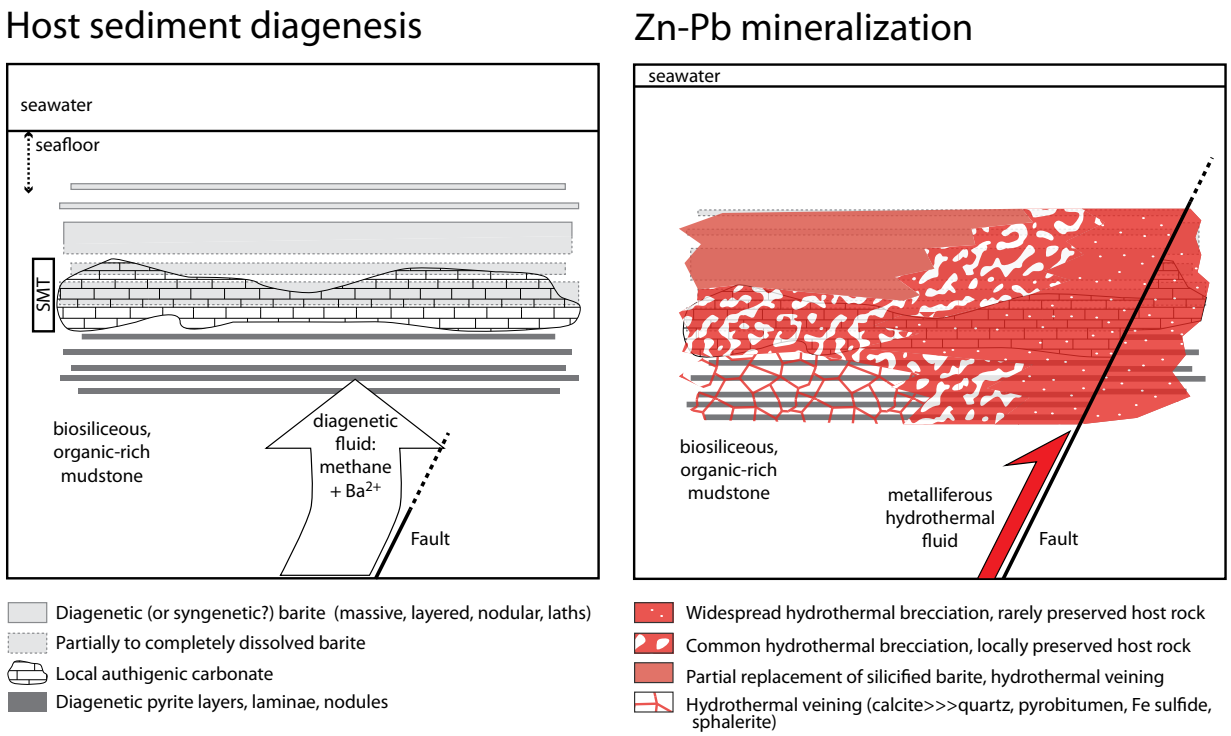

Figure 3.23: Deposit model for the Anarraaq sulfide deposit Upper and Lower Zones. A methane and barite rich diagenetic fluid interacts with seawater sulfide to form some combination of barite, carbonate, and pyrite. Dissolution of barite may increase porosity and permeability of sediment over time. Metalliferous hydrothermal fluid flows into the shallow subsurface where it easily dissolved carbonate and maybe even some siliceous mudstone, further increasing the porosity and permeability.

Table 3.1: Re-Os isotopic results for Anarraaq.

Re–Os results for Anarraaq

Sample Name	Sample Type	Re ppb	Os ppt	^{187}Re / ^{188}Os	± 2σ	^{187}Os / ^{188}Os	± 2σ	Rho
923-2123-A1	Shale	23.1	1253	97.98	0.3	0.925	0.002	0.4
923-2123-A2	Shale	24.4	1126	116.90	0.4	1.046	0.003	0.4
923-2123-B-2	Shale	21.8	888	133.99	0.5	1.135	0.003	0.4
923-2123-D-2	Shale	24.1	1218	105.93	0.4	0.970	0.002	0.3
923-2123-G-2	Shale	19.4	1025	100.69	0.4	0.944	0.002	0.4
923-2123-M	Shale	34.9	1709	109.48	0.4	1.001	0.002	0.3
923-2123-N	Shale	40.5	1021	229.63	0.8	1.675	0.004	0.4
1716-2520.8 A	Pyrite - pre ore (Py1-3)	1.30	28.98	265.42	1.52	1.91	0.01	0.54
1716-2520.8 Y	Pyrite - pre ore (Py1-3)	0.47	19.21	135.51	1.99	1.20	0.03	0.52
1716-2520.8 C+3	Pyrite - pre ore (Py1-3)	0.80	23.51	192.63	1.31	1.51	0.01	0.44
1716-2520.8 C+4	Pyrite - pre ore (Py1-3)	0.61	29.35	112.60	1.91	1.06	0.03	0.54
1716-2520.8 D+2	Pyrite - pre ore (Py1-3)	0.85	28.89	165.15	3.11	1.34	0.04	0.60
1716-2520.8 X	Pyrite - pre ore (Py1-3)	0.52	16.57	175.60	1.48	1.40	0.01	0.49
1723-2104.5 A-3	Pyrite - ore stage (Py4)	4.80	28.96	2034.22	17.84	12.00	0.16	0.58
1723-2104.5 D+2	Pyrite - ore stage (Py4)	4.36	26.63	1901.08	12.76	10.94	0.08	0.82
1723-2104.5 D+3	Pyrite - ore stage (Py4)	2.86	22.30	1153.74	9.03	6.79	0.08	0.58

Chapter 4: Sulfur cycling, an important process in the formation of the Anarraaq barite body and Zn-Pb-Ag deposit, Red Dog district, Alaska: a SIMS study of barite ($\delta^{34}S$ and $\delta^{18}O$), pyrite and marcasite ($\delta^{34}S$)

4.1 Introduction

Sediment-hosted massive sulfide (SHMS) deposits preserve anomalous accumulations of S in the rock record in the form of metal sulfides and, in some deposits, sulfate minerals. The Red Dog district in northwestern Alaska comprises multiple SHMS deposits (Fig. 4.1) that contain a total of around 40 Mt of S in zinc and lead sulfide minerals (Tab. 4.1 and references therein). Red Dog sulfide deposits and coeval barren strata also contain as much as an additional 275 Mt of S in barite ($BaSO_4$; Tab. 4.1; Johnson et al., 2004). Identifying the sources of S and the mechanisms of sulfate reduction is a fundamental component of understanding deposit genesis and has important implications for understanding the S cycle throughout geological time (Lyons et al., 2006; Leach et al., 2010; Farquhar et al., 2010).

Bacterial sulfate reduction (BSR) of seawater sulfate has been recognized as an important source of reduced sulfur in many sediment-hosted zinc-lead deposits (Leach et al., 2005). For example, Fallick et al. (2001) showed that more than 90 % of sulfide in the Navan Irish-type deposit was derived from BSR of seawater sulfate. Bacterial sulfate reduction is limited to low temperature environments (predominantly <60-80 °C; Machel et al., 2001) and includes the processes of organoclastic sulfate reduction (OSR) and sulfate-driven anaerobic oxidation of methane (SD-AOM). In OSR, microbes utilize organic material as an electron acceptor to reduce sulfate (Eq. 1; Canfield et al., 1991):

$$2HC_2O + SO_4^{2-} \rightarrow 2HCO_3^- + H_2S \quad \text{(Eq. 1)}$$

Where methane is present, a consortium of sulfate-reducing bacteria and syntrophic anaerobic methanotropic archea mediate SD-AOM (Eq. 2; Hoehler et al., 1994; Knittel and Boetius, 2009):

$$CH_4 + SO_4^{2-} \rightarrow HCO_3^- + HS^- + H_2O \quad \text{(Eq. 2)}$$

In marine sediment, methane is generated by the degradation of organic material in anaerobic pore waters (Reeburgh, 2007). Sulfate-driven AOM comes into play if methane diffuses into overlying sulfitic pore waters; the zone where opposing diffusive fluxes of methane and sulfate meet and SD-AOM takes place is called the sulfate-methane transition (SMT; Knittel and Boetius, 2009). Sulfate-driven AOM is a particularly important process in continental margin sediment (Egger et al, 2018) where the majority of global marine carbon burial takes place (Dunne et al., 2007). In some settings, methane escapes into marine bottom waters (e.g., Torres et al., 2003; Suess et al., 2014). These ‘methane seeps’ or ‘cold seeps’ are typically associated with advective fluid flow (e.g., along faults, etc.; Suess et al., 2014).

Organoclastic sulfate reduction and SD-AOM both produce reduced sulfide species (H_2S, HS^-) and bicarbonate (HCO_3^-), but SD-AOM generally proceeds at rates orders of magnitude faster than OSR (Aharon and Fu, 2003). For this reason, the SMT can be associated with high concentrations of bisulfide and bicarbonate and increased precipitation of 'methane-derived' diagenetic carbonate and pyrite (e.g., Jørgensen and Kasten, 2006). In some cases, methane-bearing fluids contain significant concentrations of barium (e.g., Torres et al. 2003), which precipitates as barite just above the SMT (in diffusive settings; Dickens, 2001) or in the water column or shallow subsurface (in seep settings; Aloisi et al, 2004). The stable isotope composition of these minerals provide insight into the specific conditions under which they formed (e.g., Griffith et al., 2012; Lin et al, 2016a; Antler and Pellerin et al., 2018).

In recent years, several groups of workers have recognized a link between SD-AOM and SHMS deposits. In the Red Dog district, Johnson et al. (2004, 2009) showed that baritic host strata formed at cold seeps and speculated that SD-AOM could be an important source of bisulfide (HS^-) in some of the Zn-Pb deposits. Kelley et al. (2004a) implied an additional, indirect link to SD-AOM by suggesting that thermogenic reductive dissolution of seep barite could provide an important component ore-stage bisulfide. Devonian strata in the Selwyn Basin (Canada), hosts the Tom and Jason SHMS deposits (MacMillan pass, Yukon) and regional barren barite bodies, contain barite and pyrite that formed at a SMT zone by diagenetic processes (Magnall et al., 2016a; Fernandes et al., 2017). Ordovician-Silurian strata hosting Zn-Pb mineralization at Howard's Pass (Yukon–Northwest Territories) contain methane-derived carbonate and pyrite (Johnson et al., 2018). Reynolds (Chapter 3) proposed that host strata in the Red Dog district also contains pre-ore, methane-derived carbonate and pyrite, in addition to seep barite, and that these components are overprinted by Zn-Pb mineralization in the Anarraaq sulfide deposit.

In this study, we report *in situ* isotopic data for barite ($\delta^{34}S$ and $\delta^{18}O$) and for pyrite and marcasite ($\delta^{34}S$) in the Anarraaq barite body and Anarraaq sulfide deposit (Fig. 4.1). The data are presented within the detailed petrographic, stratigraphic, and structural context for the Anarraaq area set forth by Reynolds (Chapter 3). This study focused on pyrite (and marcasite) rather than sphalerite for two reasons. First, Reynolds (Chapter 3) identified 5 generations of Fe sulfide that span from early diagenesis (pre-ore) to late hydrothermal mineralization, allowing for S source and cycling to be investigated over a broad time period. Second, there is less uncertainty associated with secondary ion mass spectrometry (SIMS) of pyrite because crystal orientation does not affect instrumental bias as it does in sphalerite (Kozdon et al., 2010).

In the barite body, our data build on the bulk mineral separate analyses of barite by Johnson et al. (2004) to investigate how the conditions of barite precipitation (and associated SD-AOM) may have changed over time and what role methane-related diagenetic processes played in the

precipitation of early pyrite. We compare these data with results from pre-ore barite and pyrite in the Anarraaq sulfide deposit to assess whether diagenetic mineral phases within the host strata formed under similar conditions. Finally, we discuss results from hydrothermal Fe sulfide phases in the sulfide deposit to address the sources of S and the nature of S cycling during Zn-Pb mineralization.

4.2 Background

4.2.1 Geologic setting

The Red Dog district contains a sequence of Devonian to Jurassic sedimentary rocks deposited on the passive continental margin of the Arctic Alaska terrane (Moore et al., 1986, 1994). Located in the fold and thrust belt of the Middle Jurassic to Cretaceous Brooks orogen, the region has undergone extensive shortening (thrusting and folding) and low grade metamorphism (De Vera et al., 2004; Blevings et al., 2013). District geology is mapped according to a framework of tectonic packages of varying scales (Fig. 4.1; Young, 2004; Blevings et al., 2013). The Red Dog thrust sheet of the Endicott Mountains allochthon contains all known SHMS mineralization in the Red Dog district (Figs. 4.1; Blevings et al., 2013).

Red Dog SHMS mineralization is hosted in the Upper Mississippian Ikalukrok unit (Kuna Formation, Lisburne Group), which primarily comprises siliceous, organic-rich mudstone deposited in shelf and slope settings at subtropical to temperate latitudes (Dumoulin, 2004; Lewchuk et al., 2004; Slack et al., 2004; Dumoulin et al, 2014; Reynolds et al., 2015). The Ikalukrok unit also contains minor black chert and calcareous interbeds; some of the calcareous strata were delivered by mass flow events from coeval platform carbonates (Dumoulin, 2004) but others may be authigenic (Reynolds, Chapter 3). The regional depositional regime was characterized by upwelling of nutrient-rich deep water and high rates of biogenic productivity in the water column (Dumoulin et al., 2014). Bottom water redox conditions fluctuated (Slack et al., 2004; Dumoulin et al., 2014; Slack et al, 2015; Reynolds et al., 2015). Local accumulations of barite in the Ikalukrok formed in cold seep settings, where fluids rich in methane and barium interacted with sulfate-bearing bottom water or pore water (Johnson et al., 2004; Ayuso et al., 2004; Johnson et al., 2009).

Red Dog SHMS deposits formed where a metalliferous hydrothermal fluid flowed into the shallow subsurface via extensional faults (Kelley et al., 2004a; Kelley et al., 2004b). Rhenium-osmium isochron ages of ore-stage pyrite in the Main and Anarraaq deposits are nearly identical to each other (338.3 ± 5.8 Ma and 334.4 ± 5.3 Ma, respectively; Morelli et al., 2004; Reynolds, Chapter 3) and within error of the Re-Os isochron age of Ikalukrok mudstone (339.1 ± 8.3 Ma; Reynolds, Chapter 3) and the biostratigraphic age of the upper Kuna Formation (Meramecian to early Chesterian; Dumoulin et al., 2004). Textural evidence indicates that although some

host sediment may have been unconsolidated at the time of ore-formation, the bulk of ore was emplaced in well-lithified and diagenetically modified strata (Kelley et al., 2004a; Reynolds et al., 2015, Chapter 3). Replacement of barite and carbonate were important processes during ore formation (Kelley et al., 2004a, 2004b; Reynolds, Chapter 3).

4.2.2 Anarraaq deposit

The samples in this study are from the Anarraaq area, which is located approximately 10 km northwest of the Mine Area (Fig. 4.1). The Anarraaq area is described in detail by Kelley et al. (2004b) and Reynolds (Chapter 3). It contains a barite body and a sulfide deposit, which are vertically separated from each other by approximately 60 m of barren Ikalukrok strata (Fig. 4.2). The Anarraaq barite body contains up to 1 Gt of barite (Kelley et al., 2004b) and the sulfide deposit contains an inferred resource of 19.4 Mt at 14.4% Zn, 4.2% Pb, and 73.4 ppm Ag (Krolak et al., 2017).

The Anarraaq barite body contains an interval of nodular barite in black chert and siliceous mudstone underlain by laminated to massive barite (Fig. 4.2; Kelley et al., 2004b; Reynolds, Chapter 3). The basal interval of the laminated to massive barite is locally calcareous and in some places is underlain by an interval of layered to laminated pyrite (Fig. 4.3; Kelley et al., 2004b; Reynolds, Chapter 3). The barite formed in a cold methane seep setting (Johnson et al., 2004; Ayuso et al., 2004; Johnson et al., 2009). Based on petrographic textures and stratigraphic relationships, Reynolds (Chapter 3) proposed that the carbonate and pyrite components formed at roughly the same time as the barite as the result of methane-related diagenesis near a SMT.

The Anarraaq sulfide deposit comprises the Upper Zone and Lower Zone (Fig. 4.2; Reynolds, Chapter 3). The style of hydrothermal mineralization is somewhat different in each zone; for example, the sphalerite color, texture, and chemistry are distinctive (Kelley et al., 2004b; Smith, 2017; Reynolds, Chapter 3). The ore zones are fault-bounded but it is not clear how much displacement may have taken place along those faults (Reynolds, Chapter 3). The host strata in each ore zone comprises Ikalukrok mudstone with pre-ore barite, carbonate, and pyrite in the same stratigraphic orientation as in the barite body (Fig. 4.4; Reynolds, Chapter 3). Reynolds (Chapter 3) proposed that each ore zone formed by overprinting sediment formed at a cold methane seep, similar to the Anarraaq barite body.

4.2.3 Mineralogy and paragenesis of S-bearing phases

The paragenetic relationships among S-bearing phases in the barite body and sulfide deposit are described in detail by Reynolds (Chapter 3) and are summarized in this section and in Fig. 4.5. The barite body contains a wide variety of microscopic barite textures including disseminations in mudstone or chert, irregular patches, microcrystalline masses, coarser crystalline veinlets, and rare barite laths (Fig. 4.6); these textures are not subdivided into distinct

paragenetic phases because of their complexity and spatial heterogeneity. Pyrite framboids and spheroids (Pyrite 1) are disseminated in the nodular barite interval, are very rare in the laminated to massive barite, and are abundant and locally form clusters in the layered to laminated pyrite (Fig. 4.7B). Locally, pyrite euhedrons (Pyrite 2) are disseminated in mudstone or occur as overgrowths on framboids and spheroids. The volumetrically most important pyrite phase in the layered to laminated pyrite interval (Pyrite 3) occurs as massive overgrowths to Pyrite 1 and 2 and contain abundant siliceous radiolarian skeletal material (Fig. 4.7A-B). A relatively late phase of cubic pyrite occurs in quartz veinlets that crosscut Pyrite 1-3 in the layered to laminated interval.

The Anarraaq sulfide deposit also contains pre-ore barite and pyrite and similar mineralogy and paragenetic relationships are observed in both ore zones. Pre-ore barite occurs as laths (Barite 1), which locally coalesce in rosettes, nodules, and layers in Ikalukrok mudstone. It is possible that additional barite textures were present but are no longer recognizable due to extensive replacement by hydrothermal mineral phases (Reynolds, Chapter 3). Pre-ore pyrite in the sulfide deposit (Pyrite 1-3; Fig. 4.7C-E) is texturally very similar to the interval of layered to laminated pyrite which underlies the barite body. In the sulfide deposit, Pyrite 3 is locally colloform (Figs. 4.7E, 8C, 8E) and associated with minor Marcasite 3.

Hydrothermal Fe sulfides (Marcasite 4 and Pyrite 4; Fig. 4.8A-E) display a wide variety of textures that are relatively coarse crystalline (up to 500 μm) and locally euhedral. At least some Pyrite 4 formed as pseudomorphs after Marcasite 4 (e.g., Fig. 4.8D). Cubic pyrite (Pyrite 5; Fig. 4.8E) and rare barite laths (Barite 2) are associated with late hydrothermal calcite-quartz veins that crosscut the Zn mineralization. As with the pre-ore components, the occurrence of hydrothermal Fe sulfide and barite phases is similar in both ore zones.

4.3 Analytical methods

Sample preparation and secondary ion mass spectrometry (SIMS) of pyrite, marcasite, and barite were carried out at the Canadian Centre for Isotopic Microanalysis (CCIM) at the University of Alberta. Regions of interest from polished thin-sections were cut or cored into 1.5 to 4 mm disks with a diamond bit. In one case, a polished rock slab was also cored. The samples (n=47) were mounted in two 25 mm diameter epoxy pucks along with pre-polished fragments of CCIM pyrite (S0302A) and barite (S0327) reference materials (RMs; for more details see Magnall et al., 2016a). All sample and reference material were located within the inner 12 mm diameter of each mount, where spatially-correlated analytical biases are minimized. The mounts were lightly polished with diamond compounds on rotary equipment, cleaned with a lab soap solution and de-ionized H_2O, and then coated with 7 nm of high-purity Au. The mounts were imaged with a Zeiss EVO MA15 scanning electron microscope operating at 20kV and 3 to 4 nA. Prior to SIMS analysis, the mounts were coated with an additional 23 nm of Au.

Sulfur and oxygen isotope ratios ($^{34}S/^{32}S$ and $^{18}O/^{16}O$, respectively) were determined using an IMS-1280 multi-collector ion microprobe and are reported in standard δ notation relative to Vienna Canyon Diablo Triolite (VCDT) for sulfur and Vienna Standard Mean Ocean Water (VSMOW) for oxygen. Oxygen isotope ratios were analyzed in barite subsequent to the S-isotope measurements, predominantly in closely-adjacent spots, but where space was limited, directly within the previous S-isotope spot. The operating conditions for SIMS analyses are summarized in Tab. 4.2 and described in some detail here. Primary beam conditions for most analyses utilized 20 keV $^{133}Cs^+$ ions focused to 10 µm diameter rastered slightly during acquisition resulting in a sampled area of ~13 x 15 µm. In a small subset of samples, a non-rastered beam was focused to 8 µm. The primary beam was rastered across an 18 x 18 µm area for 45-60 s prior to analysis to clean the surface of Au and contaminants, and implant Cs. Negative secondary ions were extracted through 10 kV to the grounded secondary column and automated tuning of the secondary ions in the Transfer section preceded each analysis. The isotopes for each element of interest (^{34}S and ^{32}S; ^{18}O and ^{16}O) were analyzed simultaneously in Faraday cups. Analyses of unknowns were interspersed with the appropriate RM in a 4:1 ratio. In the analytical session during which O isotope analyses were carried out on spots previously analyzed for S isotopic composition, the RM analyses were also set to re-analyze previous spots.

Total uncertainties for pyrite and barite average ±0.2 – 0.3 ‰ (2σ) per spot for sulfur and ±0.3 ‰ (2σ) for oxygen. These include propagation of within-spot counting errors (0.03-0.13 ‰), between-spot errors to account for geometric effects (0.1-0.35 ‰), and between-session error that accounts for uncertainty in the mean instrumental mass fractionation (IMF). The IMF was determined from the replicate analyses of the appropriate RM for each analytical session, after correction for systematic within-session drift in IMF that ranged from 0 – 0.35‰. The total uncertainty does not include the absolute uncertainty in the true composition of the RMs (Tab. 4.2). No orientation-related biases (Kozdon et al., 2010) have been found for SIMS analysis of pyrite or barite at CCIM.

Marcasite is a polymorph of pyrite (FeS_2) with an orthorhombic instead of cubic crystal structure. It is a common ore stage mineral in the Red Dog samples and 89 marcasite unknowns were analyzed as part of this study using the same conditions and procedures described above for pyrite. The S0302A pyrite RM was used as no marcasite RM was available. It should also be noted that marcasite has not been tested for crystal orientation effects on instrumental bias such as those identified in sphalerite. Kozdon et al. (2010) reported a variation of up to 3.4 ‰ between grains of sphalerite with different crystal orientations but the variation within a single grain of sphalerite (0.3 ‰) was on par with the uncertainty associated with pyrite and barite analyses in this study. Variation of a similar order of magnitude could be associated with SIMS analyses of marcasite. Despite the added uncertainty and absence of an ideal RM, we note that the overall

range of $\delta^{34}S$ values recorded in ore-stage pyrite and marcasite (Fig. 4.5D) is very similar, which provides some confidence in the general accuracy of the marcasite results. The range of $\delta^{34}S$ values recorded in marcasite is an order of magnitude larger than what might be expected for any orientation-related effects on instrumental bias. Furthermore, similar S isotopic compositional trends are commonly observed in pyrite and marcasite and some of the trends we discuss are contained within a single crystal (e.g., Fig. 4.8D) giving added confidence to the accuracy of the results relative to each other within the grain.

4.4 Results

A total of 221 *in situ* microanalyses of S isotopic composition were carried out on pyrite, 77 on marcasite, and 212 on barite. An additional 217 analyses of O isotopic composition were also carried out on barite (Tab. S4.1; archived online). All S isotopic data are plotted by phase in Fig. 4.5 and spatially coupled $\delta^{34}S$ and $\delta^{18}O$ values from barite are plotted in Fig. 4.9. All isotopic data from the Anarraaq barite body are also plotted by depth in Fig. 4.3. Representative examples of isotopic compositions within their petrographic context are shown in Figs. 4.6, 4.7, and 4.8.

4.4.1 Anarraaq barite body

The isotopic composition of barite in the Anarraaq barite body has $\delta^{34}S$ values and $\delta^{18}O$ values that range from +16.2 to +58.0 ‰ and +10.6 to +27.3 ‰, respectively, which is broadly consistent with the bulk mineral separate analyses conducted on samples from the same drill core (Fig. 4.3; Johnston et al., 2004). The lowest $\delta^{34}S$ and $\delta^{18}O$ values from this study overlap with constraints for Mississippian seawater sulfate (Claypool et al., 1980; Kampschulte and Strause, 2004), with the exception of a small number of $\delta^{18}O$ values that are slightly lower. The highest $\delta^{34}S$ and $\delta^{18}O$ values occur in the nodular barite of the uppermost Ikalukrok unit and in the overlying Siksikpuk Formation. Apart from this general trend, little to no systematic correlation is observed between barite texture and isotopic composition (e.g., Fig. 4.6G-H). Data from two samples show a positive correlation between $\delta^{34}S$ and $\delta^{18}O$ values (Fig. 4.9C-D). Linear regression analysis of data from sample 1796.3 yields a slope of 0.30 ($R^2 = 0.86$; Fig. 4.9C). Linear regression analysis of data from sample 1796.3 yields a slope of 0.47 ($R^2 = 0.70$; Fig. 4.9D).

All phases of pyrite analyzed in the layered to laminated pyrite interval fall within a relatively narrow range of positive values (+17.3 to +22.5 ‰; Fig. 4.3). In that interval, all Pyrite 1 values overlap constraints for seawater sulfate whereas some Pyrite 3 and later cubic pyrite values are slightly higher (Fig. 4.5C); no Pyrite 2 was successfully analyzed. In the laminated to massive barite interval, pyrite is very rare and none was successfully analyzed. In the nodular barite interval, Pyrite 1 preserves highly negative $\delta^{34}S$ values (-18.4 to -41.61 ‰; Figs. 4.3, 5B).

4.4.2 Anarraaq sulfide deposit

4.4.2.1 Pre-ore barite and Fe sulfide

In the Lower Zone of the Anarraaq sulfide deposit, rarely preserved Barite 1 laths have $\delta^{34}S$ and $\delta^{18}O$ values of +17.3 to +27.2 ‰ and +12.7 to +17.8 ‰, respectively. Linear regression of paired S and O isotope data for Barite 1 yields a slope of 0.56 ($R^2 = 0.64$; Fig. 4.9E). The S isotopic composition of Pyrite 1 is strongly negative (-50.4 to -24.0 ‰; Fig. 4.5D). The $\delta^{34}S$ values of Pyrite 2, Pyrite 3, and Marcasite 3 are positive (+6.8 to +20.2 ‰); of these phases, only the most positive $\delta^{34}S$ values of Pyrite 3 overlap the composition of Mississippian seawater (Claypool et al., 1980; Kampschulte and Strause, 2004).

The only pre-ore component that was analyzed in the Upper Zone of the sulfide deposit is Pyrite 3. In contrast to the positive $\delta^{34}S$ values of Pyrite 3 in the Lower Zone, Pyrite 3 in the Upper Zone is characterized by $\delta^{34}S$ values that range from -41.9 to +4.2 ‰. (Fig. 4.5E). Pyrite 3 in the Upper Zone is more commonly colloform (Figs. 4.8C, E) and the highest and lowest measured $\delta^{34}S$ values are from within less than 100 μm of each other in an area with colloform crystal zonation (Fig. 4.8C). Additional analytical spots along a transect perpendicular to zoning indicate that the $\delta^{34}S$ values of Pyrite 3 fluctuated up and down at least twice over the course of crystal growth.

4.4.2.2 Main ore stage

Ore-stage Fe sulfides (Pyrite 4 and Marcasite 4) in the Lower Zone have $\delta^{34}S$ values that range from -35.1 to +19.3 ‰, with the most positive values overlapping Mississippian seawater sulfate (Fig. 4.5D). This range is similar to the *in situ* $\delta^{34}S$ values reported for ore stage pyrite and sphalerite in the Main, Aqqaluk, and Paalaaq deposits of the Mine Area (Fig. 4.5F; Kelley et al., 2004a). In samples 923-2251.2 and 923-2292.9, the $\delta^{34}S$ values of ore stage Fe sulfide span more than 45 ‰ within a single sample. The overall range of $\delta^{34}S$ values in Marcasite 4 (-35.1 to + 19.2 ‰) and Pyrite 4 (-33.8 to +19.3 ‰) are nearly identical (Fig. 4.5D). The S isotopic composition of Marcasite 4 and Pyrite 4 in each sample is typically similar. Some Fe sulfide crystals are composed of both Marcasite 4 and Pyrite 4 and in these places, the S isotopic composition appears to be broadly independent of the mineralogy (e.g., Fig. 4.5D).

Backscattered electron imaging of ore stage Fe sulfides shows well-defined growth zoning is present locally (e.g., Fig. 4.8B). Transects of analytical spots perpendicular to growth zones reveal a large variability in S isotopic composition over time. For example, the $\delta^{34}S$ values in marcasite in Figs. 4.8A-B range from -32.1 to +15.0 ‰ (Δ 47.1 ‰). Different sections of the transect show both increasing and decreasing $\delta^{34}S$ values over time (i.e., -25.6 to -12.7 ‰ and then later +15.0 to +0.7 ‰). Despite the relatively large uncertainty associated with marcasite analyses (see methods section), the change in $\delta^{34}S$ values are an order of magnitude larger and

represent real trends in the data.

Ore stage Fe sulfide in the Upper Zone is commonly somewhat finer crystalline and less abundant, which made targeting material to analyze more of a challenge. The range of $\delta^{34}S$ values in ore stage Fe sulfide in the Anarraaq Upper Zone (-12.2 to +20.7 ‰) does not include the strongly negative values recorded in the Lower Zone (Fig. 4.5E). However, this may simply be due to the relatively small sample size (n=17 in 2 samples).

4.4.2.3 Late ore stage

The S isotopic composition of the late ore stage Pyrite 5 is similar in the Lower and Upper Zones (+11.7 to +12.4 ‰ and +9.1 to +14.5 ‰, respectively) and is slightly lower than Mississippian seawater sulfate (Fig. 4.5D-E). There is some indication that the isotopic composition of Pyrite 5 is independent from that of the earlier phase(s) of Fe sulfide it crosscuts. For example, Pyrite 5 in Fig. 4.8G has positive $\delta^{34}S$ values (+11.5 and +13.6 ‰) whereas the Pyrite 3 it crosscuts has negative values (between -12.3 and -8.7 ‰). Barite 2 was only analyzed in the Upper Zone and there the $\delta^{34}S$ and $\delta^{18}O$ values fall within a relatively narrow range (+27.9 to +28.9 ‰ and +16.9 to +18.3 ‰, respectively; Fig. 4.9E). These values are more positive than Mississippian seawater sulfate and slightly exceed the highest values measured in Barite 1 of the Lower Zone.

4.5 Discussion

4.5.1 Anarraaq barite body

4.5.1.1 Laminated to massive barite interval and underlying layered to nodular pyrite interval

The S and O isotopic composition of barite in all samples from the laminated to massive barite interval overlaps constraints for Mississippian seawater sulfate ($\delta^{34}S$ of +14 to +21 ‰ and $\delta^{18}O$ of +12.1 to +14.3 ‰). The S and O isotopic composition of Mississippian seawater sulfate is based on the composition of carbonate associated sulfate in Mississippian carbonates (Kampschulte and Strause, 2004) and the composition of Mississippian evaporites (Claypool et al., 1980), respectively. Following the example of Johnson et al. (2009), we have subtracted 3.5 ‰ from the O isotopic composition of Mississippian evaporites to account for the fractionation predicted during evaporite formation (Claypool et al., 1980); the fractionation produced in the S isotopic composition is small enough to ignore. Yet some $\delta^{18}O$ values of barite in this study are slightly lower than constraints for Mississippian seawater. This may indicate that global seawater sulfate O isotopic composition varied somewhat more that suggested by the study of Claypool et al. (1980), that the O isotope fractionation that takes place during evaporite precipitation was underestimated by Claypool et al. (1980), that the fractionation associated with barite precipitation is larger than previously suggested by Turchyn and Schrag (2006), or that another

mechanism not previously considered may be involved.

Most samples in the laminated to massive barite interval are defined by a very small range of $\delta^{34}S$ and $\delta^{18}O$ values and show almost no modification relative to constraints for Mississippian seawater sulfate (Fig. 4.3). This suggests that barite precipitated in a system open to seawater sulfate, either in the water column or just below the sediment surface where pore waters were still relatively un-modified (Griffith et al., 2012). Two laminated to massive barite samples (at depths 1796.3 and 1893.2) contain some $\delta^{34}S$ values that are significantly more positive than constraints for Mississippian seawater (i.e., >> 21 ‰) consistent with barite precipitation beneath the sediment surface in a system at least partially closed to seawater sulfate (Paytan et al., 2002). Linear regression of the data from these samples yields slopes (Fig. 4.9C-D) that are within the range of those observed in seep sediment (i.e., between 0.25 and 0.5) where methane bubbles out of the sediment into the water column and sulfate reduction is dominated by SD-AOM rather than OSR (Sivan et al., 2014; Aharon and Fu, 2000; Aharon and Fu, 2003; Rubin-Blum et al., 2014; Antler and Pellerin, 2018).

Methane seepage and barite precipitation in the water column are commonly associated with the formation of barite chimneys, communities of chemosynthetic megafauna, or microbial mats (e.g., Fu and Aharon, 1997; Torres et al., 2003). None of these features are reported in the Anarraaq barite body (Kelley et al., 2004b; Reynolds, Chapter 3). Johnson et al. (2004) suggested that the laminated barite textures may resemble growth layers in barite chimneys; however, laminated barite can also form in sub-seafloor settings (e.g. Magnall et al., 2016a; Fernandes et al., 2017). In the Anarraaq barite body, massive barite and barite veins commonly crosscut laminated textures, indicating that some barite certainly formed below the sediment surface (Reynolds, Chapter 3). In the absence of other textural evidence, we consider it likely that Anarraaq barite formed at shallow depths within the poorly consolidated sediment.

The lack of substantial reservoir effects preserved in the barite (i.e., $\delta^{34}S$ >> 30 ‰, $\delta^{18}O$ >> 16 ‰) is somewhat surprising given that the S and O composition of residual sulfate in the pore waters of modern SMT zones or methane seeps are typically highly modified (e.g., Aharon and Fu, 2003; Rubin-Blum et al., 2014; Lin et al., 2016a; Lin et al., 2016b). This is true even in seep sediment that primarily operates as an open system (e.g., Aharon and Fu, 2003). Magnall et al. (2016a) reported similar muted reservoir effects preserved in pre-ore barite in the Devonian Tom and Jason SHMS deposits (MacMillan Pass, Yukon). Magnall et al. (2016a) attributed this phenomenon to the magnitude of fractionation produced during sulfate reduction being relatively small (around 10‰) resulting in minimal modification of the residual sulfate reservoir.

The S isotopic composition of all pyrite phases in the layered to laminated pyrite unit (17.3 to 21.5 ‰) is almost identical to constraints for Mississippian seawater (14 to 21 ‰; Fig. 4.3). Since no barite is intergrown with this pyrite, we do not know the isotopic composition

of the sulfate from which the pyrite was derived. However, if it was similar to the S isotopic composition of the overlying barite (i.e., between 16.2 and 33.3 ‰), the magnitude of fractionation produced during sulfate reduction would have been around 16 ‰ or less. Therefore, the S isotopic composition of barite and pyrite are broadly consistent with a scenario in which both minerals are produced from a single reservoir of sulfate that undergoes BSR characterized by small magnitude fractionations.

Deusner et al. (2014) showed that SD-AOM produces small fractionations when methane is abundant and the rate of sulfate reduction is high. The smallest fractionation they produced in their laboratory experiments was around 20 ‰. This is broadly consistent with the minimum fractionations observed in modern natural systems (e.g., Aharon and Fu; 2003) but still somewhat higher than what is suggested by our data. Sivan et al. (2014) showed that the presence of Fe oxide enhances SD-AOM by increasing the activity of S cycling microorganisms, resulting in a 50% decrease in the magnitude of fractionation produced during sulfate reduction. So perhaps the presence of abundant Fe oxide (or other electron acceptors with large free-energy yields, such as nitrate or manganese oxide) in pore waters could have played a role in determining the S and O isotopic composition of residual pore water sulfate. One important difference between the Anarraaq barite body (and other Paleozoic barite occurrences) and many modern SMT zones and seeps is the quantity of barite present. The large concentrations of barite in Paleozoic strata () may be an indicator of some fundamental difference in paleo marine environments, or its presence may have changed the dynamics of S cycling in some more direct way, or some combination of the two.

Reynolds (Chapter 3) reported widespread barite dissolution in the Anarraaq barite body and suggested this was occurring in methanic pore waters below a SMT zone (e.g., Snyder et al., 2007). It seems plausible that in this setting, dissolution of barite may have provided a secondary supply of sulfate for BSR (i.e., *dissolved barite* BSR instead of *seawater* BSR). Because the pore waters were methanic, it is also possible barite dissolution may have been coupled to the anaerobic oxidation of methane (*dissolved barite* SD-AOM). If the rate of dissolved barite BSR was limited by the rate of barite dissolution, sulfate reduction might have been nearly quantitative and produced a very small fractionation. A similar phenomenon was reported where thermochemical reduction of sulfate (TSR) in the presence of dissolved methane was limited by the relatively slow rate of anhydrite ($CaSO_4$) dissolution: the $\delta^{34}S$ of the resulting pyrite showed little to no fractionation (Worden et al., 2000). Therefore, dissolved barite BSR offers a possible alternative explanation for why the isotopic composition of the layered to laminated pyrite is nearly identical to the composition of the stratigraphically closest barite samples (Fig. 4.3). Indeed, carbonate and layered to laminated pyrite at the base of the barite body may be a product of dissolved barite BSR rather than seawater SD-AOM at a relatively shallow SMT.

Several studies have shown that bacteria can metabolize barite under anaerobic conditions (e.g., Romer and Schwartz, 1965; Bolze et al., 1974; McCready and Krouse, 1980). McCready and Krouse (1980) showed that where bacteria metabolize barite, the rate of barite dissolution *relative* to the rate of sulfate reduction exerts an important control on the magnitude of the S isotopic fractionation produced during BSR (and also generates CO_2 which resulted in Ba carbonate formation). Such a process may have occurred at Anarraaq, however, cannot easily be recognized in the rock record.

Dissolution of barite also would have resulted in the recycling of barium at depth and in an increase in the concentration of dissolved barium up-section (Fig. 4.10B). In turn, a high barium to methane ratio would have developed in shallow pore waters, especially if methane was also being removed via dissolved barite SD-AOM at depth (Fig. 4.10B). According to Aloisi et al. (2004), a high barium to methane ratio can result in barite precipitation out-competing SD-AOM for seawater sulfate and the consequent suppression of carbonate precipitation. In this way, dissolution of barium at depth may have exerted some control on the rare occurrence of carbonate in the upper part of the Anarraaq barite body (Kelley et al., 2004b; Reynolds, Chapter 3).

4.5.1.2 Nodular barite in black chert interval

Samples from the nodular barite interval have strongly positive $\delta^{34}S$ and $\delta^{18}O$ values, with even the minimum values measured in each sample exceeding constraints on Mississippian seawater (Fig. 4.3). The isotopic composition and nodular character of the barite indicate that it formed below the sediment surface (Paytan et al., 2002). Although the coupled S and O isotopic data do not reveal how the composition of residual pore water sulfate evolved with depth beneath the seafloor, sample 1729.5 does include some values with high $\delta^{18}O$: $\delta^{34}S$ ratios (Fig. 4.9A). This suggests that the initial slope (i.e., the slope of the apparent linear phase, or SALP) may have been quite steep before flattening out to form a concave-down pattern. In general, steeper SALPs are associated with slower rates of reduction, increased reversibility of the sulfate reducing enzymatic pathway, and a relatively larger influence of an equilibrium isotope effect on O whereby oxygen atoms exchange between water and intermediate redox species of sulfur within the bacterial cell (Fritz et al., 1989; Wortmann et al, 2007; Antler et al., 2013).

Pyrite framboids (Pyrite 1) are not uncommon in samples from the nodular barite interval but only a few were analyzed by SIMS because of their disseminated nature. The $\delta^{34}S$ values are strongly negative (Fig. 4.3) and can only be explained by BSR in a system at least partially open to sulfate (e.g., Kaplan and Rittenberg, 1964; Sim, Bosak, et al., 2011). Organoclastic sulfate reduction and SD-AOM produce a similar range of magnitudes of fractionation and therefore cannot be used to distinguish the two processes (e.g., Sim et al., 2011; Deusner et al., 2014). However, the $\delta^{34}S$ values of framboids in sample 1759.3 (-35.1 to -41.6 ‰) require a minimum

fractionation of 50 ‰ relative to constraints for Mississippian seawater sulfate. In a seep setting, the magnitude of fractionation is expected to be somewhat smaller (+20 to +40 ‰; Deusner et al., 2014). Therefore, the pyrite data is permissive of a scenario in which methane is diffusion-limited and fully consumed at a SMT.

The depth of a SMT is controlled by the flux of methane, the concentration of sulfate in seawater, and the rate of sediment deposition (e.g., Arning et al., 2015), but methane seeps are typically associated with particularly high fluxes of methane (Suess, 2014). At Anarraaq, the transition from laminated-massive barite (with a relatively small range of $\delta^{34}S$ and $\delta^{18}O$ values overlapping constraints for seawater sulfate; low SALP) to nodular barite (with strongly positive $\delta^{34}S$ and $\delta^{18}O$ values, (?)high SALP, and > 50 ‰ fractionation preserved in pyrite) likely represents a significant decrease in the flux of methane. One possible explanation for this change is that the primary source of methane shifted from being advective fluid flow from a deeper reservoir of diagenetic fluid to the local methanogenesis of organic matter (Fig. 4.10C).

Barite dissolution coupled to BSR and upward barium migration could have continued during this period, although it likely would have done so at a slower rate in response to the smaller flux of methane. Carbonate and larger accumulations of pyrite are rare in the nodular barite unit (Reynolds, Chapter 3). This suggests that the ratio of barium to methane remained high and/or the SMT was migrating up through the sediment at a fairly constant rate (i.e., maintaining a constant depth relative to the seafloor).

4.5.2 Anarraaq sulfide deposit

4.5.2.1 Pre-ore barite and Fe sulfide

In the Lower Zone of the Anarraaq sulfide deposit, the S and O isotopic composition of Barite 1 is similar to barite in the laminated to massive interval of the barite body (Fig. 4.9). The size of the barite crystals (locally >1 cm; Reynolds, Chapter 3) and the fact that several $\delta^{34}S$ values exceed constraints for Mississippian seawater, are consistent with precipitation below the sediment-water interface (Paytan et al., 2002). Linear regression of the Barite 1 data yields a slope (0.56; Fig. 4.9E) that is slightly larger than the maximum slope expected in methane seep sediment (0.25 to 0.5) but much smaller than the range of SALP expected in sediment where methane is diffusion-limited and is depleted at a SMT (>2; Antler and Pellerin, 2018). Therefore, we consider that the barite in the sulfide deposit formed in a similar setting as the laminated to massive barite of the barite body.

The S isotopic composition of Pyrite 2 and Pyrite 3/ Marcasite 3 in the Lower Zone is similar to pyrite in the interval just below the barite body, although most of the $\delta^{34}S$ values from the Lower Zone are just slightly lower than constraints for Mississippian seawater sulfate (Figs. 4.5C-D). In combination with the similarities in texture and stratigraphic occurrence (Reynolds,

Chapter 3), this suggests that the pyrite precipitated under similar conditions. We suspect that much of the pre-ore pyrite in the Lower Zone formed in association with barite dissolution. Notably, the strongly negative $\delta^{34}S$ values of Pyrite 1 in the Lower Zone (-50.4 to -24.0 ‰) are very different than the positive values of Pyrite 1 in the interval just below the barite body (17.3 to 18.8 ‰). As we discuss above, negative values such as these are typical of BSR in a system open to sulfate and do not allow for a distinction between OSR and SD-AOM.

An additional conspicuous difference between the interval of pre-ore pyrite in the Lower Zone (Fig. 4.4) and the layered to laminated pyrite interval that underlies the barite body (Fig. 4.3) is that the former is much thicker, especially relative to the baritic interval. If we assume that the availability of Fe was the same in both places, the larger volume of pyrite may be the result of more barite dissolution. Consistent with this idea is the observation that almost no barite is preserved in the Anarraaq sulfide deposit whereas abundant barite remains in the barite body (Reynolds, Chapter 3).

In the Upper Zone, the strongly negative $\delta^{34}S$ values of Pyrite 3 indicate BSR must have taken place in a system open to sulfate. These data are in stark contrast to the S isotopic composition of Pyrite 3 in the barite body and in the Lower Zone of the sulfide deposit and barite dissolution coupled to BSR may not have been an important process in the Upper Zone. More data is needed to understand pre-ore S dynamics of strata hosting the Upper Zone.

4.5.2.2 Ore Stage Fe sulfide

The large range of $\delta^{34}S$ values observed in ore-stage Fe sulfides in the Anarraaq sulfide deposit is similar to the overall range of values reported in sphalerite and pyrite from the Mine Area deposits (Fig. 4.5D-F; Kelley et al., 2004a). In the Mine Area, all phases of pyrite are associated with sphalerite precipitation (Kelley et al., 2004a). The most strongly negative $\delta^{34}S$ values occur in early sulfide phases and reflect BSR of seawater sulfate or pore water sulfate during sediment diagenesis (Kelley et al., 2004a). The early sulfide phases are volumetrically minor and Kelley et al. (2004a) suggest that a limited supply of metals during this period may have allowed for some accumulation of bisulfide in pore waters. The later, volumetrically more important sulfide phases are predominantly characterized by positive $\delta^{34}S$ values, although some values as low as -27 ‰ were measured (Kelley et al., 2004a). The S isotopic composition of the later phases is interpreted to reflect mixing between a reservoir of biogenic bisulfide stored in pore waters and bisulfide produced during the ore phase by thermochemical sulfate reduction (TSR) of seawater or pore water sulfate, or the reductive dissolution of barite (Kelley et al., 2004a).

Although hydrothermal Marcasite 4 and Pyrite 4 in the Anarraaq sulfide deposit contain a similar range of $\delta^{34}S$ values as hydrothermal pyrite in the Mine Area, the paragenetic context is different. The strongly negative $\delta^{34}S$ values in Marcasite 4 and Pyrite 4 do require input from a

source of S that underwent BSR (OSR or SD-AOM) in a system at least partially open to sulfate. However, in the Lower Zone, the S composition of pre-ore Pyrite 3 suggests that any local accumulation of biogenic bisulfide that existed in pore waters prior to the onset of hydrothermal mineralization would have had a *positive* $\delta^{34}S$ value. It follows that an external source of S – biogenic bisulfide, or sulfate that subsequently underwent BSR within the ore zone – must have been introduced during ore stage mineralization.

One possibility is that bisulfide with a negative $\delta^{34}S$ signature was generated by BSR in pore waters further up-section or lateral to the ore zone and then circulated into the ore zone during hydrothermal mineralization. This is similar to the model proposed for the Irish-type deposits (e.g., Wilkinson et al., 2010). In the Irish-type deposits, mixing between the diagenetic fluid (negative $\delta^{34}S$ signature) and the hydrothermal fluid (positive $\delta^{34}S$ signature) produced a wide range of $\delta^{34}S$ values in ore-stage sulfides (Anderson et al., 1998; Caulfield et al., 1986; Wilkinson et al., 2005). This includes small-scale spatial-temporal heterogeneity of S isotopic composition (e.g., Barrie et al., 2009) that is similar to results in this study (e.g., Fig. 4.8A-B).

The hydrothermal fluid that formed the deposits in the Red Dog district is presumed to be oxic (see discussion pg. 1527 in Kelley et al., 2004a), so it seems unlikely that it would have been a source of reduced sulfide to the Anarraaq sulfide deposit. But perhaps a shallow reservoir of biogenic bisulfide (negative $\delta^{34}S$ signature) could have mixed with the bisulfide that accumulated locally within the ore zone via barite dissolution coupled to BSR (positive $\delta^{34}S$ signature) to achieve a similar result. No isotopic data is available for strata overlying the Lower or Upper Zones in the Anarraaq sulfide deposit; the overlying strata may have been structurally displaced to an unknown location (Reynolds, Chapter 3). However, if we consider the Anarraaq barite body to be an analogue for the Lower Zone host strata (Reynolds, Chapter 3), the strongly negative $\delta^{34}S$ values of Pyrite 1 in the uppermost part of the barite body (i.e., the nodular barite interval) are permissive of the development of a shallow source of bisulfide with a negative $\delta^{34}S$ signature.

Alternatively, the external source of S introduced during the ore-stage could have been hydrothermal sulfate. Based on sphalerite fluid inclusion electrolyte data, Leach et al. (2004) interpreted the hydrothermal fluid to be partially derived from evaporated seawater, so it seems plausible that it may have contained a significant amount of sulfate. Bulk extraction ion chromatography analyses of sphalerite fluid inclusions contained up to 792 ng of SO_4^{2-} (Leach et al., 2004). Mississippian and Upper Devonian evaporite deposits in the region have been identified as possible sites of formation of the hydrothermal fluid (see discussion p. 1467 in Leach et al., 2004) and the constraints on S isotopic composition of seawater sulfate in the Late Devonian (+20 to +25 ‰; John et al., 2010; Chen et al., 2013) overlap Mississippian seawater sulfate. It follows that hydrothermal fluid produced from evaporated seawater from either time

period would have a similar S isotopic composition of around +20 ‰.

If the additional reservoir of S was supplied as sulfate, open system BSR would be required to operate within the ore zone at the time of mineralization. Bacterial sulfate reduction is typically limited to low temperature environments (< 60-80 °C; Machel et al., 2001). This seems at odds with fluid inclusion microthermometry of sphalerite from the Main and Aqqaluk deposits, which indicate crystallization took place at much higher temperatures (110-180°C; Leach et al., 2004). However, the fluid inclusion data are all derived from samples of late-stage coarse-crystalline red-brown sphalerite and may not be representative of temperature conditions during earlier stages of ore formation or in more distal parts of the ore zone. Magnall et al. (2016b) showed that temperatures in the Tom and Jason SHMS deposits decreased drastically over a small stratigraphic distance – around 200 °C over just 15 m – so it seems plausible that lower temperature environments conducive to BSR may have existed at least locally during ore formation in Red Dog deposits.

An alternative explanation for the extreme spatial-temporal variability in $\delta^{34}S$ values of ore-stage Fe sulfides (e.g., Fig. 4.8A-B) is that it formed from a single source of sulfate that underwent reduction in highly variable conditions. The entire range of $\delta^{34}S$ values in ore stage Fe sulfide could have been produced by BSR with fluctuating availability of reductant and sulfate. We imagine sulfate reduction taking place in a highly dynamic environment characterized by host strata with extreme variations in porosity-permeability, ranging from very low in consolidated mudstone to very high in large dissolution cavities formed in carbonate. The supply of sulfate and reductant could have fluctuated drastically in response to removal via reduction, replenishment via successive pulses of hydrothermal fluid (sulfate) or migration through host strata (reductant), and the constraints of the local porosity-permeability on these processes. The host sediment would have contained multiple types of reductants – organic material, dissolved methane, and possibly other types of hydrocarbons – and the distribution of these components may have been heterogeneous, especially considering the variable porosity-permeability.

Along with the potential for steep temperature gradients (Magnall et al., 2016b), we consider that the reaction by which sulfate reduction proceeded may also have varied significantly over space and time to include OSR, SD-AOM, and TSR. The operation of SD-AOM may have been of particular importance as it is known to proceed at rates hundreds of times faster than OSR (Aharon and Fu, 2000) and therefore would have a greater potential for producing large volumes of bisulfide over time. The sulfate reduction reactions all produce bicarbonate, which would have acted to neutralize the acidity of the hydrothermal fluid over time. The operation of these processes within the ore zone during ore formation could explain why ore-stage marcasite underwent extensive transformation to pyrite as well as the abundance of late hydrothermal calcite veins and cement (Reynolds, Chapter 3).

4.5.3 Implications for SHMS mineralization – Red Dog and other deposits

Although previous authors recognized that BSR played some role in the formation of the Zn-Pb deposits in the Red Dog district (Kelley et al., 2004a; Johnson et al., 2004; Slack et al., 2004), our study on the Anarraaq area shows that BSR may have played a more important and complex role in the formation of the barite body and sulfide deposit. Barite dissolution coupled to BSR may produce small fractionations. Bacterial sulfate reduction under conditions of highly variable sulfate and reductant availability have the potential to produce a wide range of fractionations. This has important implications for how the S isotopic composition of sulfide minerals are interpreted; in particular, positive $\delta^{34}S$ values must be interpreted with great care.

Sulfide minerals with a wide range of $\delta^{34}S$ values are characteristic of SHMS deposits (Leach et al., 2005). Positive $\delta^{34}S$ values have been interpreted to reflect the influence of TSR (e.g., Red Dog – Kelley et al., 2004a; Howards Pass – Gadd et al., 2016) or Rayleigh-type reservoir effects where BSR takes place in a closed system (e.g., in the water column of a restricted marine basin as in the classic SEDEX model developed at Tom and Jason – Goodfellow and Jonasson, 1984). Recently, workers have begun to consider additional ways in which BSR might contribute to the positive $\delta^{34}S$ signature in SHMS deposits. Lyons et al. (2006) pointed out the SD-AOM is associated with anomalously high rates of sulfate reduction which could produce small fractionations and positive $\delta^{34}S$ values. Since then, SD-AOM has been identified as an important diagenetic process in strata hosting the Tom and Jason deposits (MacMillan Pass – Yukon; Magnall et al., 2016a) and the Howards Pass deposits (Yukon-Northwest Territories; Johnson et al., 2018). In both districts, pre-ore pyrite is characterized by positive $\delta^{34}S$ values, but it remains unclear what contribution SD-AOM might make to hydrothermal sulfide minerals. Sangster (2018) suggested that in the HYC deposit, conditions controlled by the hydrothermal fluid (i.e., temperature, nutrient supply, toxicity, and sulfate supply) affected the rate of reduction or sulfate availability such that BSR produced smaller fractionations and positive $\delta^{34}S$ values. We suggest that the dissolution of barite may serve as an additional source of isotopically heavy S in some SHMS deposits, adding to the complexity of interpreting positive $\delta^{34}S$ values in SHMS deposits. We have also expanded on the idea of Sangster (2018) in that we have proposed that dynamic conditions affecting the rate of reduction and sulfate availability might not just result in positive $\delta^{34}S$ values but highly variable $\delta^{34}S$ values.

We consider that the flux of methane through Ikalukrok sediment exerted a major control on barite precipitation and dissolution and therefore, S cycling and the generation of permeability in the subsurface. Methane-related diagenetic processes were fundamental in the physicochemical preparation of the Ikalukrok unit as a prospective host, and methane may have continued to play an important role as a reductant during ore formation. In turn, the high concentration of organic matter in the Ikalukrok unit (locally > 8 wt. % TOC; Slack et al., 2004) played a key role in

the generation of methane-rich diagenetic fluids. At Red Dog, the organic-rich content of the mudstone is associated with upwelling of nutrient-rich deep waters and high levels of biogenic productivity (Dumoulin et al., 2014). Although basin restriction, a feature of the classic genetic model for SEDEX deposit, has been implicated as playing an important role in the preservation and burial of organic matter at Red Dog (e.g., Blevings et al., 2013; Slack et al., 2015), the development of an oxygen minimum zone on an open marine continental margin is another option (Reynolds et al., 2015). Overall, this study re-emphasizes the importance and complexity of the influence of microbial activity on the formation of the giant Zn-Pb deposits of the Red Dog district and the high variability of coupled physical-chemical-biological processes in space and time in the sub-seafloor environment.

4.6 Conclusions

The isotopic composition of barite ($\delta^{34}S$ and $\delta^{18}O$) and pyrite ($\delta^{34}S$) indicates that the Anarraaq barite body formed in two phases. The laminated to massive barite interval formed when the flux of methane into the shallow subsurface was relatively high. Later, the flux of methane decreased, and barite precipitated as nodules. Little to no carbonate or pyrite is associated with barite precipitation during either phase; this might be a result of a high ratio of barium to methane suppressing the rate of SD-AOM or that the location of SMT in pore waters was continually moving in response to the deposition of new sediment, or a combination of both. As barite was buried in methanic pore waters below the SMT, it dissolved and became a secondary source of sulfate for BSR. Barite dissolution was likely coupled to the anaerobic oxidation of methane and would have been most intense at the base of the barite interval where it would have operated for a prolonged period. The accumulation over time of bicarbonate and bisulfide at this location led to the precipitation of calcite and pyrite and the dissolution of biogenic opal. Dissolved barium migrated further up-section where it would have reprecipitated.

The isotopic composition of pre-ore barite and pyrite in the Lower Zone of the Anarraaq sulfide deposit indicate host strata formed in a setting as the Anarraaq barite body. Dissolution of barite coupled to BSR was likely crucial to enhancing the receptivity of the host strata to Zn-Pb mineralization because the authigenic carbonate it produced was later dissolved by hydrothermal fluid to create zones of high porosity and permeability. Less data are available from pre-ore components of the Upper Zone but it seems that host strata may have formed under somewhat different conditions.

If a significant reservoir of pore water bisulfide existed within Lower Zone host strata prior hydrothermal mineralization, we argue that it would have formed primarily via barite dissolution coupled to BSR and had a positive $\delta^{34}S$ value. The wide range and small-scale spatial-temporal variation of $\delta^{34}S$ values observed in ore stage Fe sulfide could have formed when the local reservoir of bisulfide (positive $\delta^{34}S$) mixed with an external reservoir of bisulfide (negative $\delta^{34}S$),

possibly generated in the pore water of strata above or lateral to the ore zone. An alternative explanation is that hydrothermal sulfate was reduced within the ore zone where dynamic conditions of sulfate and reductant availability produced highly variable fractionations. Biogenic sulfate reduction must have been involved at least locally and could have included OSR and SD-AOM; TSR also could have operated locally. This study emphasizes that the role BSR plays in the formation of SHMS sulfide deposits is multi-faceted with complex isotopic expressions. The S isotopic composition of sulfide minerals in SHMS systems must be interpreted with great care.

4.7 References

Aharon, P., and Fu, B., 2000, Microbial sulfate reduction rates and sulfur and oxygen isotope fractionations at oil and gas seeps in deepwater Gulf of Mexico: Geochemica et Cosmochimica Acta, v. 64, p. 233–246.

Aharon, P., and Fu, B., 2003, Sulfur and oxygen isotopes of coeval sulfate – sulfide in pore fluids of cold seep sediments with sharp redox gradients: v. 195, p. 201–218, doi: 10.1016/S0009-2541(02)00395-9.

Aloisi, G., Wallmann, K., Bollwerk, S.M., Derkachev, A., Bohrmann, G., and Suess, E., 2004, The effect of dissolved barium on biogeochemical processes at cold seeps: Geochemica et Cosmochimica Acta, v. 68, p. 1735–1748, doi: 10.1016/j.gca.2003.10.010.

Anderson, I., Ashton, J., Boyce, A., Fallick, A., and Russell, M., 1998, Ore depositional processes in the Navan Zn-Pb deposit, Ireland: Economic Geology and the Bulletin of the Society of Economic Geologists, v. 93, p. 535–563, http://apps.webofknowledge.com.login.ezproxy.library.ualberta.ca/full_record.do?product=UA&search_mode=GeneralSearch&qid=4&SID=2Bh5WkbcADHUEhmKFjS&page=1&doc=1 (accessed August 2015).

Antler, G., and Pellerin, A., 2018, A critical look at the combined use of sulfur and oxygen isotopes to study microbial metabolisms in methane-rich environments: Frontiers in Microbiology, v. 9, p. 1–7, doi: 10.3389/fmicb.2018.00519.

Arning, E.T., Gaucher, E.C., van Berk, W., and Schulz, H.M., 2015, Hydrogeochemical models locating sulfate-methane transition zone in marine sediments overlying black shales: A new tool to locate biogenic methane? Marine and Petroleum Geology, v. 59, p. 563–574, doi: 10.1016/j.marpetgeo.2014.10.004.

Ayuso, R.A., Kelley, K.D., Leach, D.L., Young, L.E., Slack, J.F., Wandlass, G., Lyon, A.M., and Dillingham, J.L., 2004, Origin of the Red Dog Zn-Pb-Ag deposits, Brooks Range, Alaska: Evidence from regional Pb and Sr isotope sources: Economic Geology, v. 99, p. 1533–1554, http://www.intl-econgeol.geoscienceworld.org/content/99/7/1533.short.

Barrie, C., Boyce, A., a.P. Boyle, Williams, P.J., Blake, K., Wilkinson, J.J., Lowther, M., MacDermott, P., and Prior, D., 2009, On the growth of colloform textures: A case study of sphalerite from the Galmoy ore body, Ireland: v. 166, p. 563–582, doi: 10.1144/0016-

76492008-080.

Blevings, S., Kraft, J., Stemler, J., and Krolak, T., 2013, An overview of the structure, stratigraphy, and Zn-Pb-Ag deposits of the Red Dog District, Northwestern Alaska, *in* Special Publication 17, Society of Economic Geologists, p. 361–387.

Bolze, C.E., Malone, P.G., and Smith, M.J., 1974, Microbial mobilization of barite: Chemical Geology, v. 13, p. 141–143, doi: 10.1016/0009-2541(74)90006-0.

Canfield, D.E., 1991, Sulfate Reduction in Deep-Sea Sediments: American Journal of Science, v. 291, p. 177–188, http://apps.webofknowledge.com.login.ezproxy.library.ualberta.ca/full_record.do?product=UA&search_mode=GeneralSearch&qid=9&SID=1EnQhDvvGAxGIz5vebt&page=1&doc=1.

Caulfield, B., Lehuray, A., and Rye, D., 1986, A review of lead and sulphur isotope investigations of Irish sediment-hosted base metal deposits with new data from the Keel, Ballinalack, Moyvoughly and Tatestown deposits.: , p. 591–615.

Chen, D., Wang, J., Racki, G., Li, H., Wang, C., Ma, X., and Whalen, M.T., 2013, Large sulphur isotopic perturbations and oceanic changes during the Frasnian–Famennian transition of the Late Devonian: Journal of the Geological Society, v. 170, p. 465 LP-476, http://jgs.lyellcollection.org/content/170/3/465.abstract.

Claypool, G.E., Holser, W.T., Kaplan, I.R., Sakai, H., and Zak, I., 1980, The age curves of sulfur and oxygen isotopes in marine sulfate and their mutual interpretation: Chemical Geology, v. 28, p. 199–260, doi: 10.1016/0009-2541(80)90047-9.

Deusner, C., Holler, T., Arnold, G.L., Bernasconi, S.M., Formolo, M.J., and Brunner, B., 2014, Sulfur and oxygen isotope fractionation during sulfate reduction coupled to anaerobic oxidation of methane is dependent on methane concentration: Earth and Planetary Science Letters, v. 399, p. 61–73, doi: 10.1016/j.epsl.2014.04.047.

Dickens, G.R., 2001, Sulphate profiles and barium fronts in sediments on the Blake Ridge: present and past methane fluxes through a large gas hydrate resevoir: Geochimica et Cosmochimica Acta, v. 65, p. 529–543.

Dumoulin, J., Harris, A.G., Blome, C.D., and Young, L.E., 2004, Depositional settings, correlation, and age of Carboniferous rocks in the western Brooks Range, Alaska: Economic …, v. 99, p. 1355–1384, http://www.intl-econgeol.geoscienceworld.org/content/99/7/1355.short (accessed November 2012).

Dumoulin, J.A., Johnson, C.A., Slack, J.F., Bird, K.J., Whalen, M.T., Moore, T.E., Harris, A.G., and Sullivan, P.B.O., 2014, Carbonate margin, slope, and basin facies of the Lisburne Group (Carboniferous-Permian) in northern Alaska, *in* Verwer, K., Playton, T., and Harris, P. eds., Special Publication 105, SEPM, v. 105, p. 211–236, doi: 10.2110/sepmsp.105.02.

Dunne, J.P., Sarmiento, J.L., and Gnanadesikan, A., 2007, A synthesis of global particle export from the surface ocean and cycling through the ocean interior and on the seafloor: Global Biogeochemical Cycles, v. 21, p. 1–16, doi: 10.1029/2006GB002907.

Egger, M., Riedinger, N., Mogollón, J.M., and Jørgensen, B.B., 2018, Global diffusive fluxes of methane in marine sediments: Nature Geoscience, v. 11, p. 421–425, doi: 10.1038/s41561-018-0122-8.

Fallick, A., Ashton, J., and Boyce, A., 2001, Bacteria were responsible for the magnitude of the world-class hydrothermal base metal sulfide orebody at Navan, Ireland: Economic …, v. 96, p. 885–890, http://171.67.121.50/content/96/4/885.short (accessed March 2014).

Farquhar, J., Wu, N., Canfield, D.E., and Oduro, H., 2010, Connections between sulfur cycle evolution, sulfur isotopes, sediments, and base metal sulfide deposits: Economic …, v. 105, p. 509–533, http://gsecongeo.highwire.org/content/105/3/509.short.

Fernandes, N.A., Gleeson, S.A., Magnall, J.M., Creaser, R.A., Martel, E., Fischer, B.J., and Sharp, R., 2017, The origin of Late Devonian (Frasnian) stratiform and stratabound mudstone-hosted barite in the Selwyn Basin, Northwest Territories, Canada: Marine and Petroleum Geology, v. 85, p. 1–15, doi: 10.1016/j.marpetgeo.2017.04.006.

Fritz, P., Basharmal, G.M., Drimmie, R.J., Ibsen, J., and Qureshi, R.M., 1989, Oxygen isotope exchange between sulphate and water during bacterial reduction of sulphate: Chemical Geology: Isotope Geoscience Section, v. 79, p. 99–105, doi: 10.1016/0168-9622(89)90012-2.

Fu, B., and Aharon, P., 1997, Origin and Depositional Model of Barite Deposits Associated with Hydrocarbon Seeps on the Gulf of Mexico Slope Offshore Louisiana: Gulf Coast Association of Geological Societies Transactions, doi: 10.1111/j.1600-6143.2011.03972.x.

Gadd, M.G., Layton-Matthews, D., Peter, J.M., Paradis, S., and Jonasson, I.R., 2016, The world-class Howard's Pass SEDEX Zn-Pb district, Selwyn Basin, Yukon. Part II: the roles of thermochemical and bacterial sulfate reduction in metal fixation: Mineralium Deposita, doi: 10.1007/s00126-016-0672-x.

Goodfellow, W.D., and Jonasson, I.R., 1984, Ocean stagnation and ventilation defined by Delta-S-34 secular trends in pyrite and barite, Selwyn basin, Yukon: Geology, v. 12, p. 583–586.

Griffith, E.M., and Paytan, A., 2012, Barite in the ocean - occurrence, geochemistry and palaeoceanographic applications: Sedimentology, v. 59, p. 1817–1835, doi: 10.1111/j.1365-3091.2012.01327.x.

Hoehler, T.M., Alperin, M.J., Albert, D.B., and Martens, C.S., 1994, Field and laboratory studies of methane oxidation in an anoxic marine sediment: Evidence for a methanogen-

sulfate reducer consortium: Global Biogeochemical Cycles, v. 8, p. 451–463, doi: 10.1029/94GB01800.

John, E.H., Wignall, P.B., Newton, R.J., and Bottrell, S.H., 2010, δ34SCAS and δ18OCAS records during the Frasnian–Famennian (Late Devonian) transition and their bearing on mass extinction models: Chemical Geology, v. 275, p. 221–234, doi: 10.1016/J.CHEMGEO.2010.05.012.

Johnson, C.A., Emsbo, P., Poole, F.G., and Rye, R.O., 2009, Sulfur- and oxygen-isotopes in sediment-hosted stratiform barite deposits: Geochimica et Cosmochimica Acta, v. 73, p. 133–147, doi: 10.1016/j.gca.2008.10.011.

Johnson, C.A., Kelley, K.D., and Leach, D.L., 2004, Sulfur and oxygen isotopes in barite deposits of the western Brooks Range, Alaska, and implications for the origin of the Red Dog massive sulfide deposits: Economic Geology, v. 99, p. 1435–1448, http://gsecongeo.highwire.org/content/99/7/1435.short (accessed March 2014).

Johnson, C.A., Slack, J.F., Dumoulin, J.A., Kelley, K.D., and Falck, H., 2018, Sulfur isotopes of host strata for Howards Pass (Yukon-Northwest Territories) Zn-Pb deposits implicate anaerobic oxidation of methane, not basin stagnation: Geology, v. 46, p. 619–622, doi: 10.1130/G40274.1.

Jorgensen, B.B., and Kasten, S., 2006, Sulfur cycling and methane oxidation, *in* Bohrmann, G. and Torres, M.E. eds., Marine Geochemistry, p. 271–309.

Kampschulte, A., and Strauss, H., 2004, The sulfur isotopic evolution of Phanerozoic seawater based on the analysis of structurally substituted sulfate in carbonates: v. 204, p. 255–286, doi: 10.1016/j.chemgeo.2003.11.013.

Kaplan, I.R., and Rittenberg, S.C., 1964, Microbiological fractionation of sulphur isotopes: Microbiology, v. 34, p. 195–212.

Kelley, K.D., Dumoulin, J.A., and Jennings, S., 2004b, The Anarraaq Zn-Pb-Ag and Barite Deposit, Northern Alaska: Evidence for Replacement of Carbonate by Barite and Sulfides: Economic Geology, v. 99, p. 1577–1591, doi: 10.2113/gsecongeo.99.7.1577.

Kelley, K.D., Leach, D.L., Johnson, C.A., Clark, J.L., Fayek, M., Slack, J.F., Anderson, V.M., Ayuso, R.A., and Ridley, W.I., 2004a, Textural, compositional, and sulfur isotope variations of sulfide minerals in the Red Dog Zn-Pb-Ag deposits, Brooks Range, Alaska: Implications for Ore Formation: Economic Geology, v. 99, p. 1509–1532, doi: 10.2113/gsecongeo.99.7.1509.

Knittel, K., and Boetius, A., 2009, Anaerobic Oxidation of Methane : Progress with an Unknown Process:, doi: 10.1146/annurev.micro.61.080706.093130.

Kozdon, R., Kita, N.T., Huberty, J.M., Fournelle, J.H., Johnson, C. a., and Valley, J.W., 2010, In situ sulfur isotope analysis of sulfide minerals by SIMS: Precision and accuracy, with

application to thermometry of ~3.5Ga Pilbara cherts: Chemical Geology, v. 275, p. 243–253, doi: 10.1016/j.chemgeo.2010.05.015.

Krolak, T., Palmer, K., Lacouture, B., Paley, N., 2017, NI 43-101 Technical Report for Red Dog Mine, Alaska, USA, 143 p.

Leach, D.L., Bradley, D.C., Huston, D., Pisarevsky, S.A., Taylor, R.D., and Gardoll, S.J., 2010, Sediment-hosted lead-zinc deposits in Earth history: Economic Geology, v. 105, p. 593–625, http://171.67.121.50/content/105/3/593.short (accessed March 2014).

Leach, D.L., Marsh, E., Emsbo, P., Rombach, C.S., Kelley, K.D., and Anthony, M., 2004, Nature of hydrothermal fluids at the shale-hosted Red Dog Zn-Pb-Ag deposits, Brooks range, Alaska: Economic Geology, v. 99, p. 1449–1480, http://171.67.121.50/content/99/7/1449.short (accessed November 2012).

Leach, D.L., Sangster, D., Kelley, K.D., Large, R.R., Garven, G., and Allen, C.R., 2005, Sediment-hosted lead-zinc deposits: a global perspective, *in* Hedenquist, J.W., Thompson, J.F.H., Goldfarb, R.J., and Richards, J.P. eds., 100th Anniversary Volume, Society of Economic Geologists, p. 561–607, http://eprints.utas.edu.au/6268/ (accessed March 2014).

Lewchuk, M.T., Leach, D.L., Kelley, K.D., and Symons, D.T.A., 2004, Paleomagnetism of the Red Dog Zn-Pb massive sulfide deposit in Northern Alaska: Economic Geology, v. 99, p. 1555–1567.

Lin, Z., Sun, X., Peckmann, J., Lu, Y., Xu, L., Strauss, H., Zhou, H., Gong, J., Lu, H., and Teichert, B.M.A., 2016, How sulfate-driven anaerobic oxidation of methane affects the sulfur isotopic composition of pyrite: A SIMS study from the South China Sea: Chemical Geology, v. 440, p. 26–41, doi: http://dx.doi.org/10.1016/j.chemgeo.2016.07.007.

Lin, Q., Wang, J., Algeo, T.J., Sun, F., and Lin, R., 2016, Enhanced framboidal pyrite formation related to anaerobic oxidation of methane in the sulfate-methane transition zone of the northern South China Sea: Marine Geology, v. 379, p. 100–108.

Lyons, T.W., Gellatly, A.M., McGoldrick, P.J., and Kah, L.C., 2006, Proterozoic sedimentary exhalative (SEDEX) deposits and links to evolving ocean chemistry, *in* Kesler, S.E. and Ohmoto, H. eds., Evolution of Early Earth's Atmosphere, Hydrosphere, and Biosphere—Constraints from Ore Deposits, v. Geological, p. 169–184, doi: 10.1130/2006.1198(10).

Machel, H.G., 2001, Bacterial and thermochemical sulfate reduction in diagenetic settings - old and new insights: v. 140, p. 143–175.

Magnall, J.M., Gleeson, S.A., Blamey, N.J.F., Paradis, S., and Luo, Y., 2016b, The thermal and chemical evolution of hydrothermal vent fluids in shale hosted massive sulphide (SHMS) systems from the MacMillan Pass district (Yukon, Canada): Geochemica et Cosmochimica Acta, v. 193, p. 251–273.

Magnall, J.M., Gleeson, S.A., Stern, R.A., Newton, R.J., Poulton, S.W., and Paradis, S., 2016a, Open system sulphate reduction in a diagenetic environment – isotopic analysis of barite ($\delta^{34}S$ and $\delta^{18}O$) and pyrite ($\delta^{34}S$) from the Tom and Jason Late Devonian Zn-Pb-Ba deposits, Selwyn Basin, Canada: Geochimica et Cosmochimica Acta, doi: 10.1016/j.gca.2016.02.015.

McCready, R.G.L., and Krouse, H.R., 1980, Sulfur isotope fractionation by desulfovibrio vulgaris during metabolism of baso4: Geomicrobiology Journal, v. 2, p. 55–62, doi: 10.1080/01490458009377750.

Moore, T.E., Wallace, W., Bird, K., Karl, S., Mull, C., and Dillon, J., 1994, Geology of northern Alaska, *in* Plafker, G. and Berg, H. eds., The geology of Alaska, Geological Society of America, p. 49–140.

Moore, D.W., Young, L.E., Modene, J.S., and Plahuta, J.T., 1986, Geologic setting and genesis of the Red Dog zinc-lead-silver deposit, western Brooks Range, Alaska: Economic Geology, v. 81, p. 1696–1727, doi: 10.2113/gsecongeo.81.7.1696.

Morelli, R.M., Creaser, R.A., Selby, D., Kelley, K.D., and King, A.R., 2004, Re-Os sulfide geochronology of the Red Dog sediment-hosted Zn-Pb-Ag deposit, Brooks Range, Alaska: Economic Geology, v. 99, p. 1569–1576, http://gsecongeo.highwire.org/content/99/7/1569.short (accessed March 2014).

Paytan, A., Mearon, S., Cobb, K., and Kastner, M., 2002, Origin of marine barite deposits : Sr and S isotope characterization: Geology, v. 30, p. 747–750.

Reeburgh, W.S., 2007, Oceanic Methane Biogeochemistry: Chemical Reviews, v. 107, p. 486–513, doi: 10.1021/cr050362v.

Reynolds, M.A., Gingras, M.K., Gleeson, S.A., and Stemler, J.U., 2015, More than a trace of oxygen: Ichnological constraints on the formation of the giant Zn-Pb-Ag ± Ba deposits, Red Dog district, Alaska: Geology, v. 43, doi: 10.1130/G36954.1.

Romer, R., and Schwartz, W., 1965, Geomikrobiologische untersuchungen V. Verwertung von sulfatmineralien und schwermetall-toleranz bei desulfurizierern: Z Allg Mikrobiol, v. 5, p. 122–135.

Rubin-Blum, M., Antler, G., Turchyn, A. V., Tsadok, R., Goodman-Tchernov, B.N., Shemesh, E., Austin, J.A., Coleman, D.F., Makovsky, Y., Sivan, O., and Tchernov, D., 2014, Hydrocarbon-related microbial processes in the deep sediments of the Eastern Mediterranean Levantine Basin: FEMS Microbiology Ecology, v. 87, p. 780–796, doi: 10.1111/1574-6941.12264.

Sangster, D.F., 2018, Toward an integrated genetic model for vent-distal SEDEX deposits: Mineralium Deposita, v. 53, p. 509–527, doi: 10.1007/s00126-017-0755-3.

Scott, K.C., Bergen, R.D., Gow, N.N., and Roscoe, W.E., 2010, Preliminary assessment of the

Lik Project, northwestern Alaska, U.S.A.: Toronto, Canada, Scott Wilson Roscoe Postle Associates Inc., NI 43-101 report, 138 p.

Sim, M.S., Bosak, T., and Ono, S., 2011, Large sulfur isotope fractionatoin does not require disproportionation: Science, v. 333, p. 74–77.

Sivan, O., Antler, G., Turchyn, A. V., Marlow, J.J., and Orphan, V.J., 2014, Iron oxides stimulate sulfate-driven anaerobic methane oxidation in seeps: Proceedings of the National Academy of Sciences, v. 111, p. E4139–E4147, doi: 10.1073/pnas.1412269111.

Slack, J.F., Dumoulin, J.A., Schmidt, J.M., Young, L.E., and Rombach, C.S., 2004, Paleozoic sedimentary rocks in the Red Dog Zn-Pb-Ag District and vicinity, western Brooks Range, Alaska: Provenance, deposition, and metallogenic significance: Economic Geology, v. 99, p. 1385–1414, http://171.67.121.50/content/99/7/1385.short.

Slack, J.F., Selby, D., and Dumoulin, J.A., 2015, Hydrothermal, Biogenic, and Seawater Components in Metalliferous Black Shales of the Brooks Range, Alaska: Synsedimentary Metal Enrichment in a Carbonate Ramp Setting: Economic Geology, v. 110, p. 653–675, doi: 10.2113/econgeo.110.3.653.

Smith, D., 2017, Lithophile and Chalcophile Elements in Sphalerite from the Anarraaq Sediment-Hosted Zn-Pb- Ag Deposit, Red Dog District, Alaska: University of Alberta, 117 p.

Snyder, G.T., Dickens, G.R., and Castellini, D.G., 2007, Labile barite contents and dissolved barium concentrations on Blake Ridge : New perspectives on barium cycling above gas hydrate systems: v. 95, p. 48–65, doi: 10.1016/j.gexplo.2007.06.001.

Suess, E., 2014, Marine cold seeps and their manifestations: geological control, biogeochemical criteria and environmental conditions: International Journal of Earth Sciences, v. 103, p. 1889–1916, doi: 10.1007/s00531-014-1010-0.

Teck Resources Limited, 2017, Annual Information Form:, https://www.teck.com/media/2017-Annual-Information-Form.pdf.

Torres, M.E., Bohrmann, G., Dubé, T.E., and Poole, F.G., 2003, Formation of modern and Paleozoic stratiform barite at cold methane seeps on continental margins: Geology, v. 31, p. 897, doi: 10.1130/G19652.1.

Turchyn, A. V, and Schrag, D.P., 2006, Cenozoic evolution of the sulfur cycle : Insight from oxygen isotopes in marine sulfate: Earth and Planetary Science Letters, v. 241, p. 763–779, doi: 10.1016/j.epsl.2005.11.007.

De Vera, J., McClay, K., and King, A., 2004, Structure of the Red Dog District, Western Brooks Range, Alaska: Economic Geology, v. 99, p. 1415–1434, http://econgeol.geoscienceworld.org/content/99/7/1415.short (accessed November 2012).

Wilkinson, J.J., Eyre, S.L., and Boyce, A.J., 2005, Ore-Forming Processes in Irish-Type

Carbonate-Hosted Zn-Pb Deposits: Evidencefrom Mineralogy, Chemistry, and Isotopic Composition of Sulfides at the Lisheen Mine: Economic Geology, v. 100, p. 63–86, doi: 10.2113/100.1.0063.

Worden, R.H., Smalley, P.C., and Cross, M.M., 2000, The Influence of Rock Fabric and Mineralogy on Thermochemical Sulfate Reduction: Khuff Formation, Abu Dhabi: Journal of Sedimentary Research, v. 70, p. 1210–1221.

Young, L.E., 2004, A Geologic Framework for Mineralization in the Western Brooks Range, Alaska: Economic Geology, v. 99, p. 1281–1306, doi: 10.2113/gsecongeo.99.7.1281.

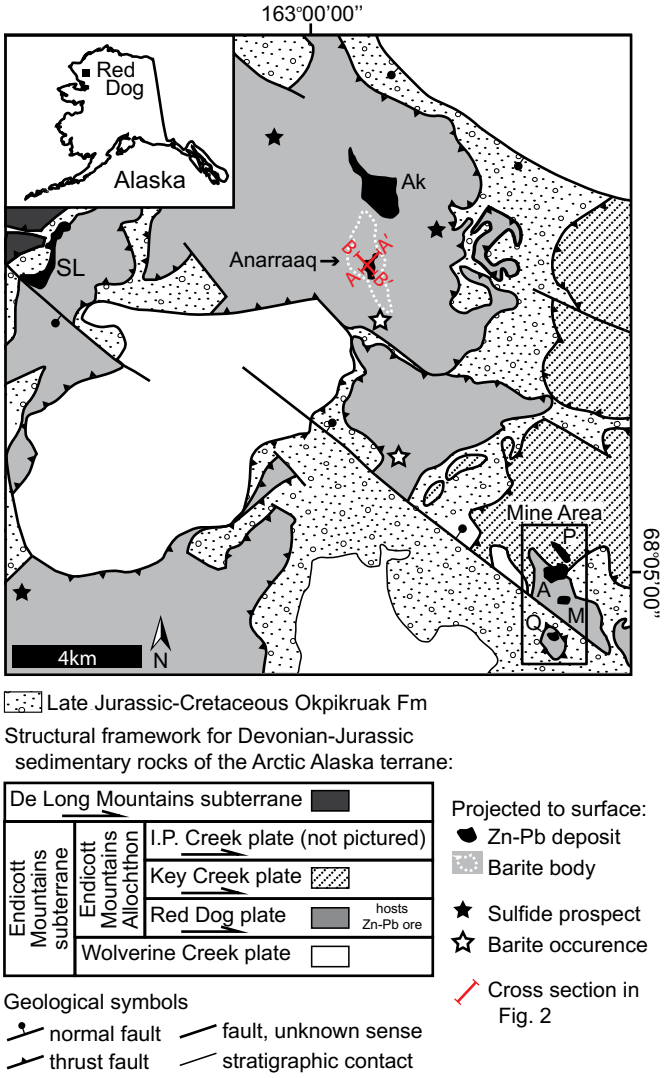

Figure 4.1: Regional map of the Red Dog district. The Mine Area deposits are Main (M), Aqqaluk (A), Paalaaq (P), and Qaanaaq (Q). Other deposits include Anarraaq, Aktigiruk (Ak), and Su Lik (SL). Several additional prospects and barite occurrences are also highlighted. Modified after Fig. 1 in Reynolds (Chapter 3).

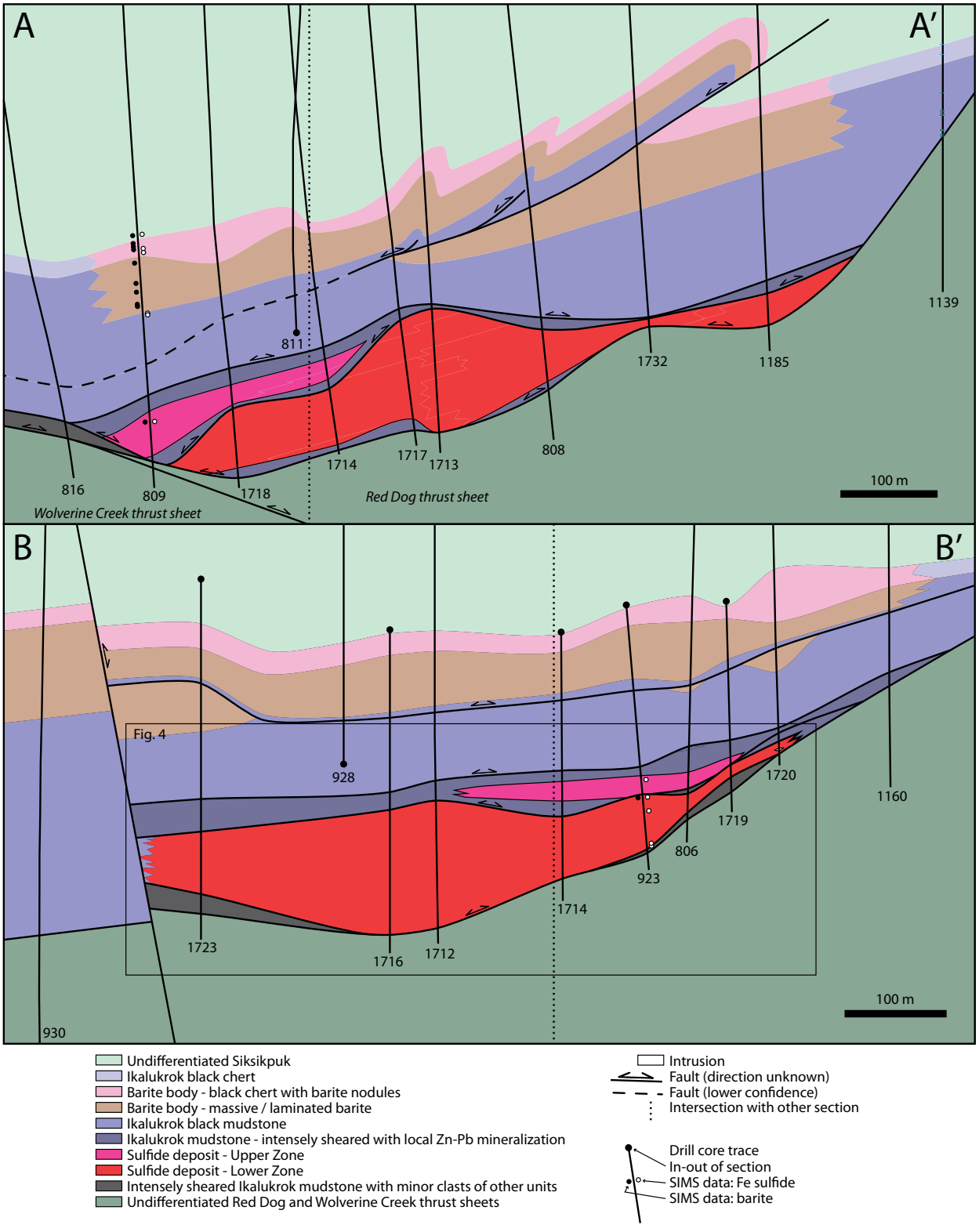

Figure 4.2: Cross-sections through the Anarraaq barite body and sulfide deposit show the locations of samples in which barite and Fe sulfide (pyrite and marcasite) were analyzed by SIMS. Modified from Figs. 4-5 in Reynolds (Chapter 3).

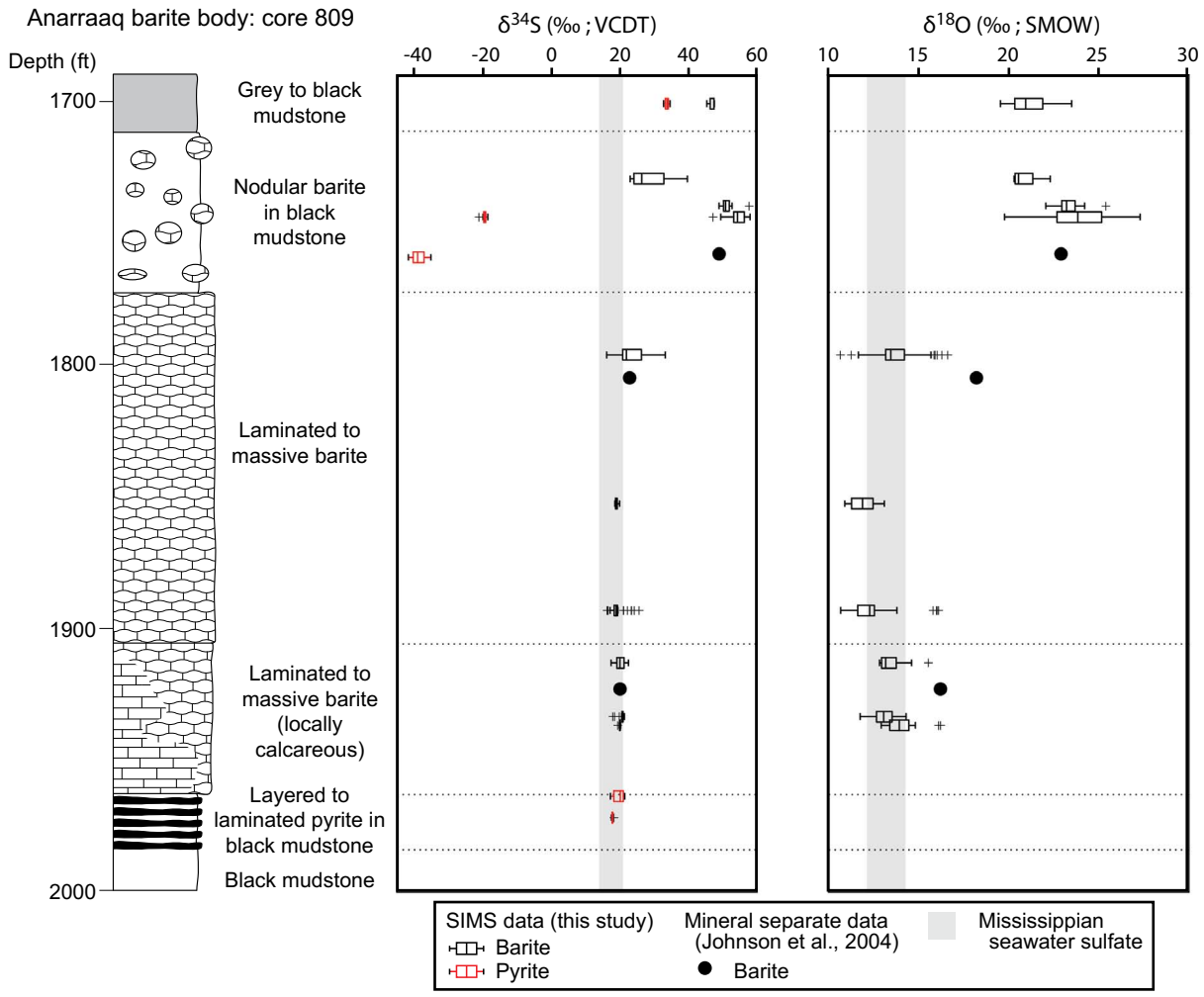

Figure 4.3: Sulfur and oxygen isotopic compositional data from drill core 809 in the Anarraaq barite body. Constraints for Mississippian seawater sulfate are from Kampschulte and Strauss (2004) and Claypool et al. (1980).

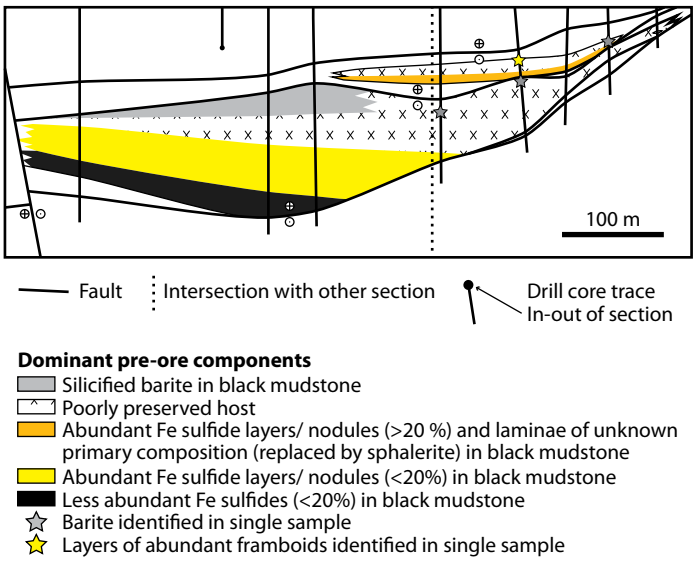

Figure 4.4: Inset from Fig. 4.2B. The mineralogy and distribution of pre-ore components in the Anarraaq sulfide deposit is similar to the Anarraaq barite body. 'Poorly preserved' interval is interpreted to contain carbonate. Modified from Fig. 3.17 in Reynolds (Chapter 3).

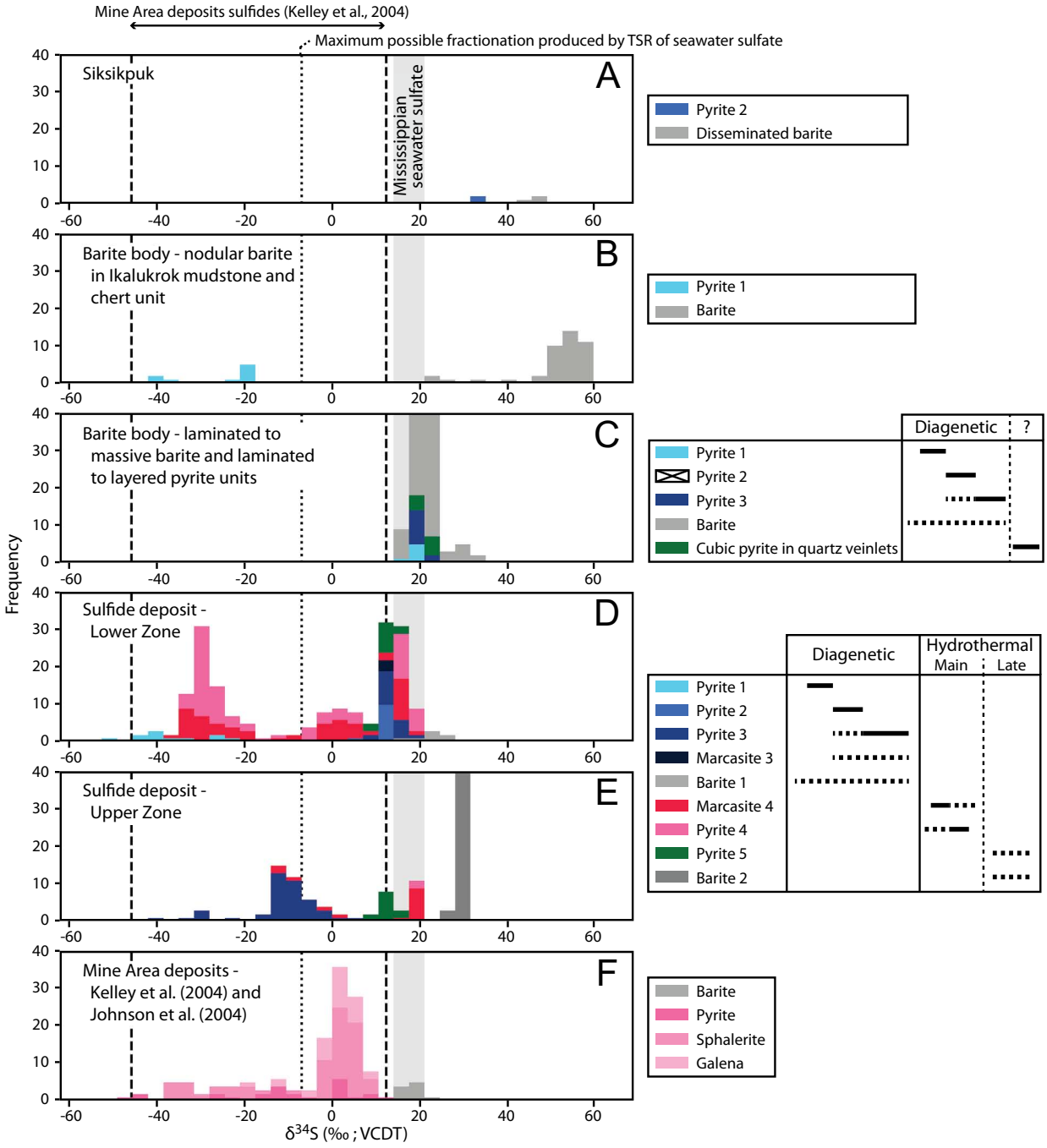

Figure 4.5: (a-e) Histograms of all *in situ* S isotopic data for Anarraaq barite, pyrite, and marcasite, organized by stratigraphic occurrence. Where enough information is available, the paragenetic relationship among S-bearing phases is summarized to the right of the histograms. (f) All S isotopic data for Mine Area deposits pyrite, sphalerite, and galena (*in situ* analyses; Kelley, Leach, et al., 2004) and barite (bulk mineral separate analyses; Johnson et al., 2004). Constraints on the S isotopic composition of seawater sulfate are from Kampschulte and Strauss (2004). The maximum fractionation that could be produced by TSR (~21 ‰; Watanabe et al., 2009; Oduro et

al., 2011) is shown relative to the minimum constraint for the S isotopic composition of seawater sulfate. Pyrite 1 – framboidal or spheroidal; Pyrite 2 – euhedral; Pyrite 3 – massive overgrowths to Pyrite 1 and 2 containing abundant siliceous radiolarian skeletal material, locally colloform; Marcasite 3 – minor, associated with Pyrite 3; Pyrite-Marcasite 4 – wide variety of textures, relatively coarse crystalline, locally euhedral; Pyrite 5 – cubic, occurs where late hydrothermal calcite-quartz veins crosscut earlier pyrite phases; Barite 1 – lathes, coalescing lathes in mud-stone; Barite 2 – lathes in late hydrothermal calcite-quartz veins.

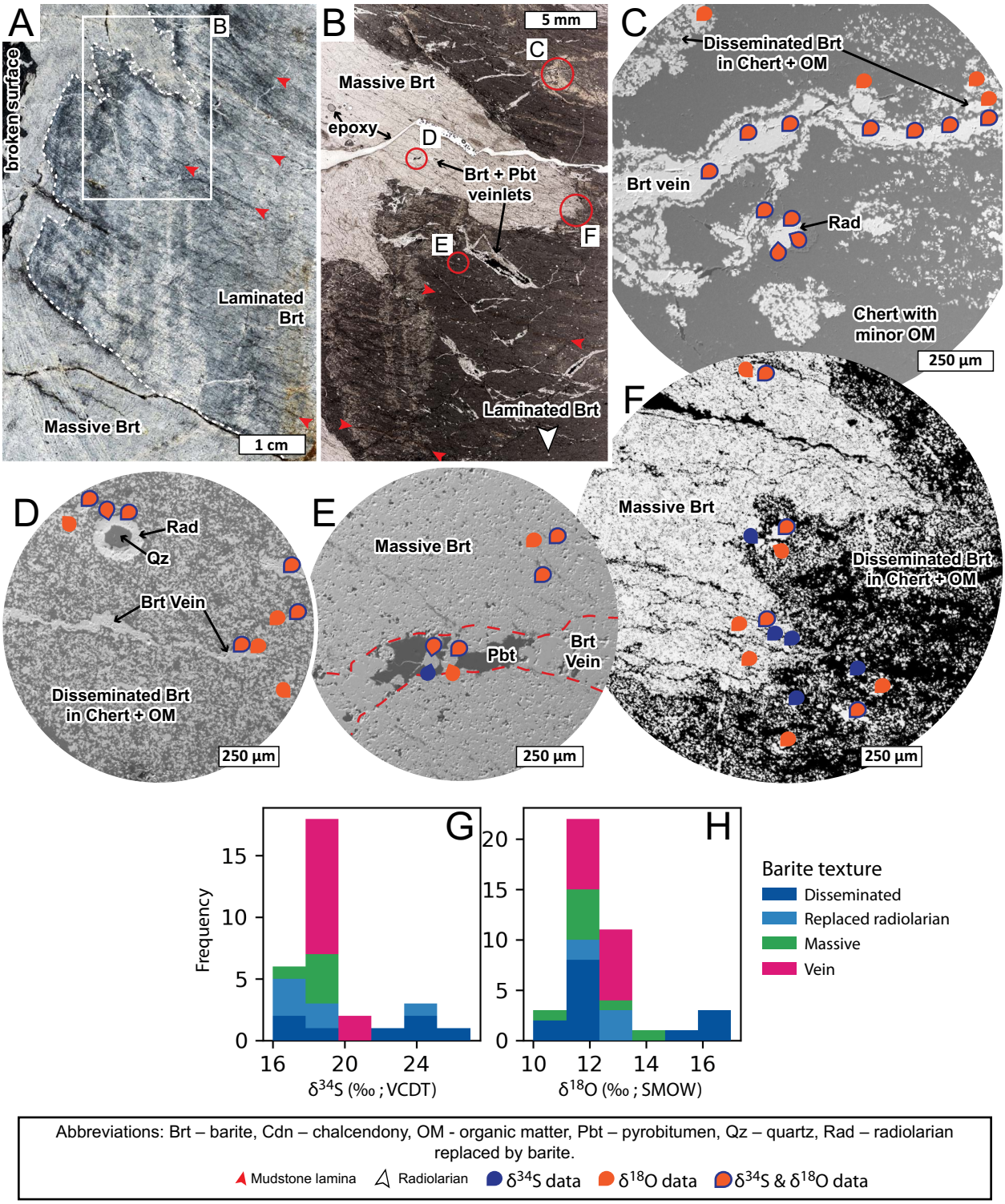

Figure 4.6: Selected petrographic images from sample 809-1893.2 in the Anarraaq barite body. (a) Cut core show laminated and massive barite textures. (b) Inset area in a – plane polarized light image. (c) Inset area in b – secondary electron image. (d) Inset area in b – secondary electron image. (e) Inset area in b – secondary electron image. Barite vein (outlined with red dashed

line) is composed of relatively coarse crystalline barite, including euhedral grains cemented by pyrobitumen. (f) Inset area in b – backscattered electron image. (g) S isotopic data collected from this sample. (h) O isotopic data collected from this image.

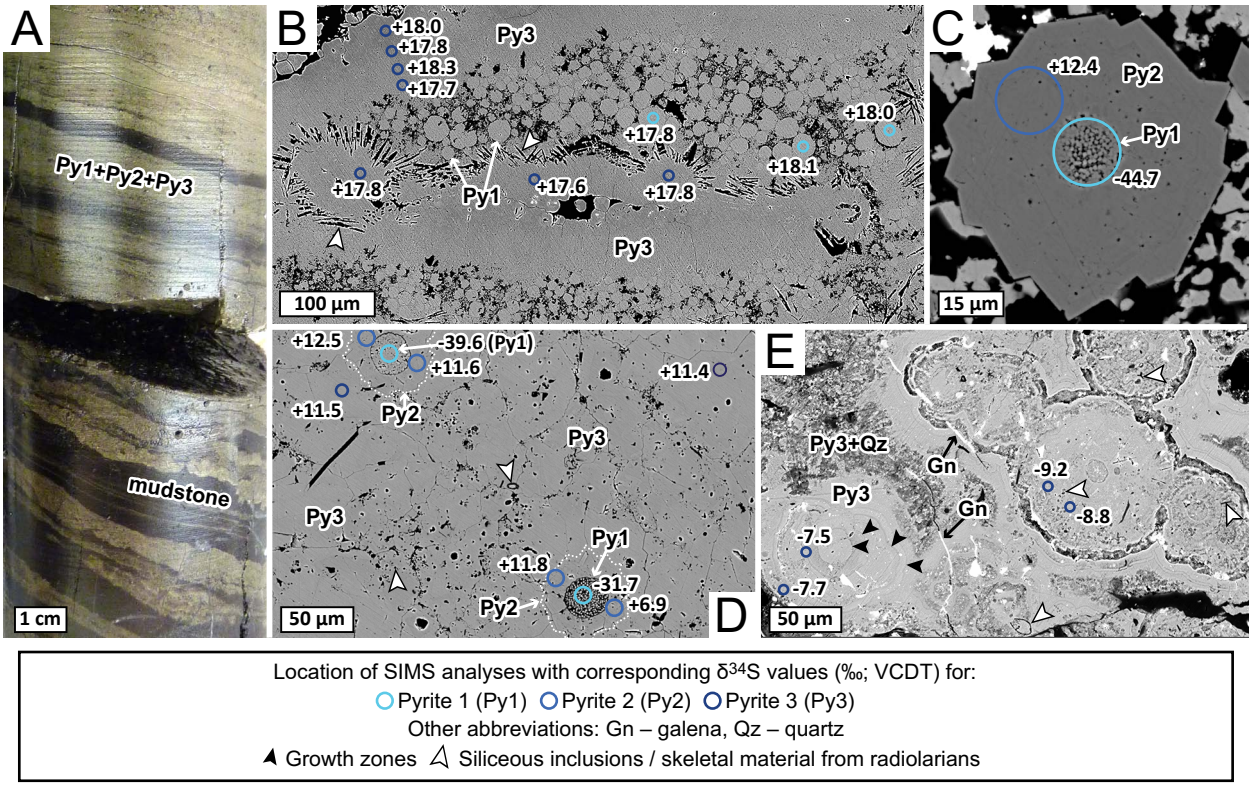

Location of SIMS analyses with corresponding $\delta^{34}S$ values (‰; VCDT) for:
Pyrite 1 (Py1) Pyrite 2 (Py2) Pyrite 3 (Py3)
Other abbreviations: Gn – galena, Qz – quartz
Growth zones Siliceous inclusions / skeletal material from radiolarians

Figure 4.7: Selected petrographic images of pre-ore pyrite phases with results from SIMS analysis. (a) Sample 809-1963.7 – whole core. Layered to laminated pyrite with organic-rich mudstone from just below the Anarraaq barite body. (b) Same sample – BSE image. Pyrite 1 spheroids and massive Pyrite 3. Note abundant siliceous radiolarian spicules preserved in Pyrite 3. (c-d) Anarraaq Lower Zone sample 923-2404.8 – BSE images. Pyrite 1-3 from the Anarraaq Lower Zone. (e) Anarraaq Upper Zone sample 923-2204.6 – BSE image. Pyrite 3 is locally colloform but still contains abundant siliceous radiolarian skeletal fragments.

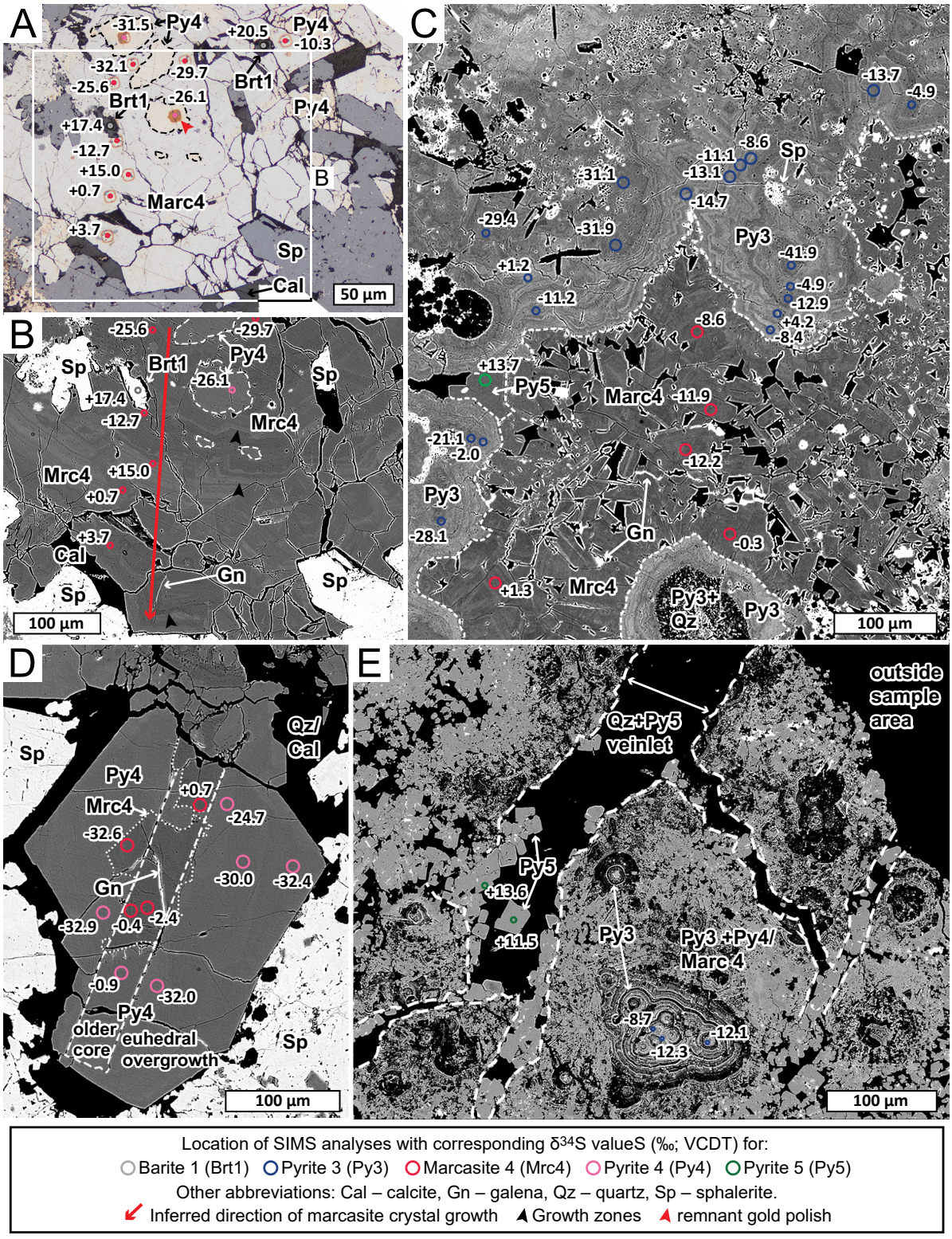

Figure 4.8: Selected petrographic images of pre-ore and hydrothermal phases with results from SIMS analysis. (a) Anarraaq Lower Zone sample 923 2251.2 – reflected light image. Several lathes are composed of Barite 1 but are replaced by sphalerite. Note the subtle difference be-

tween the color of hydrothermal Pyrite 4 (yellow) and Marcasite 4 (bluish yellow). (b) Inset area in a – BSE image. Note growth zones in Marcasite 4. (c) Anarraaq Upper Zone sample 809 2364.3 – BSE image. (d) Anarraaq Lower Zone sample 923-2292.9 – BSE image. Note the subtle difference in brightness between Pyrite 4 and Marcasite 4. The S isotopic composition of the core is independent of mineralogy; the same applies to the euhedral overgrowth. (e) Anarraaq Upper Zone sample 923 2204.6 – BSE image. Cubic Pyrite 5 occurs in quartz veinlets that cross cut mineralization.

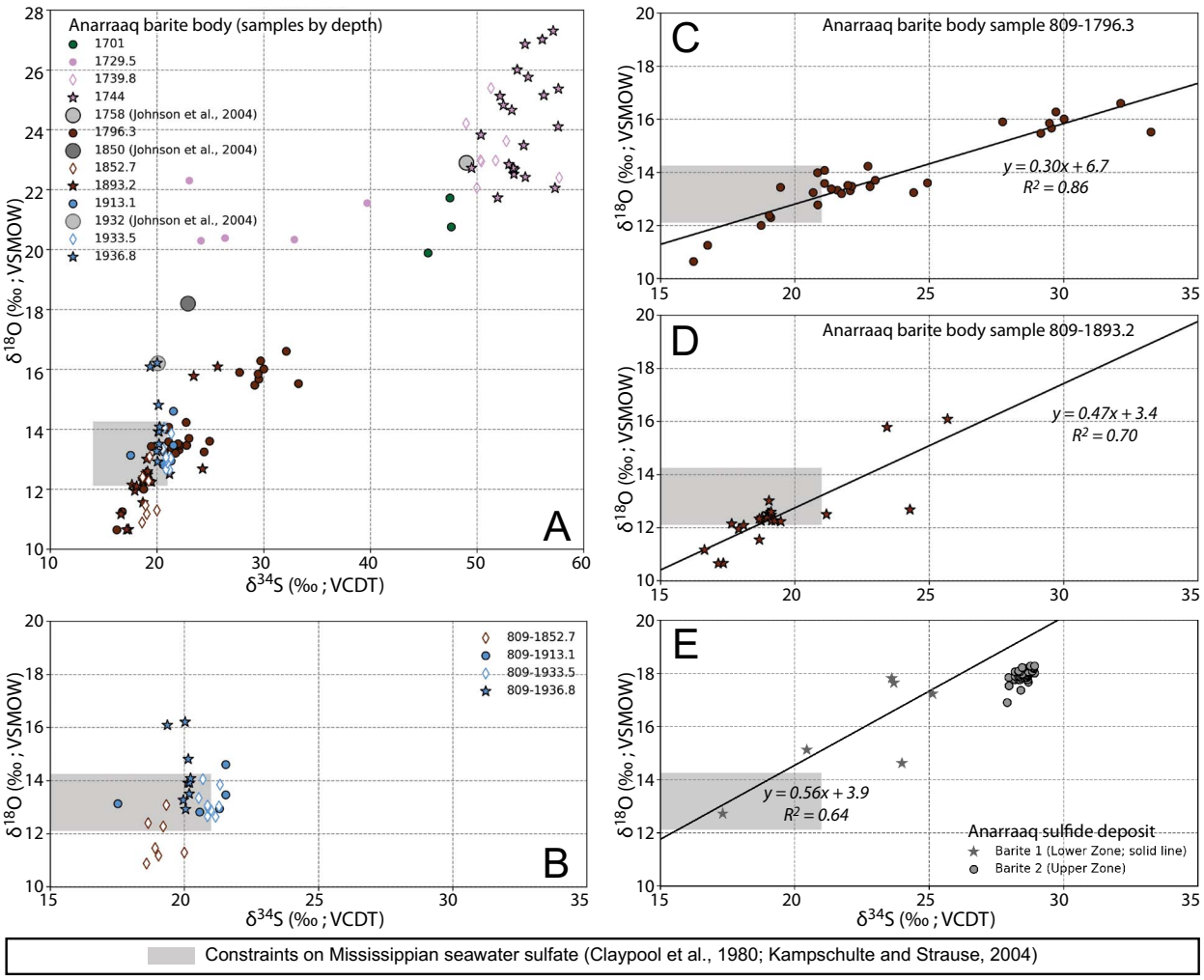

Figure 4.9: Cross plots of coupled *in situ* S and O isotopic data from the Anarraaq area. (a) Results from core 809 through the barite body are plotted by depth and are broadly similar to the mineral separate analyses of Johnson et al. (2004) from the same drill core. (b-c) Samples from the laminated to massive barite interval are re-plotted to highlight the absence (b) or presence (c-d) of a linear correlation between $\delta^{34}S$ and $\delta^{18}O$ values. (e) Results from the Anarraaq sulfide deposit.

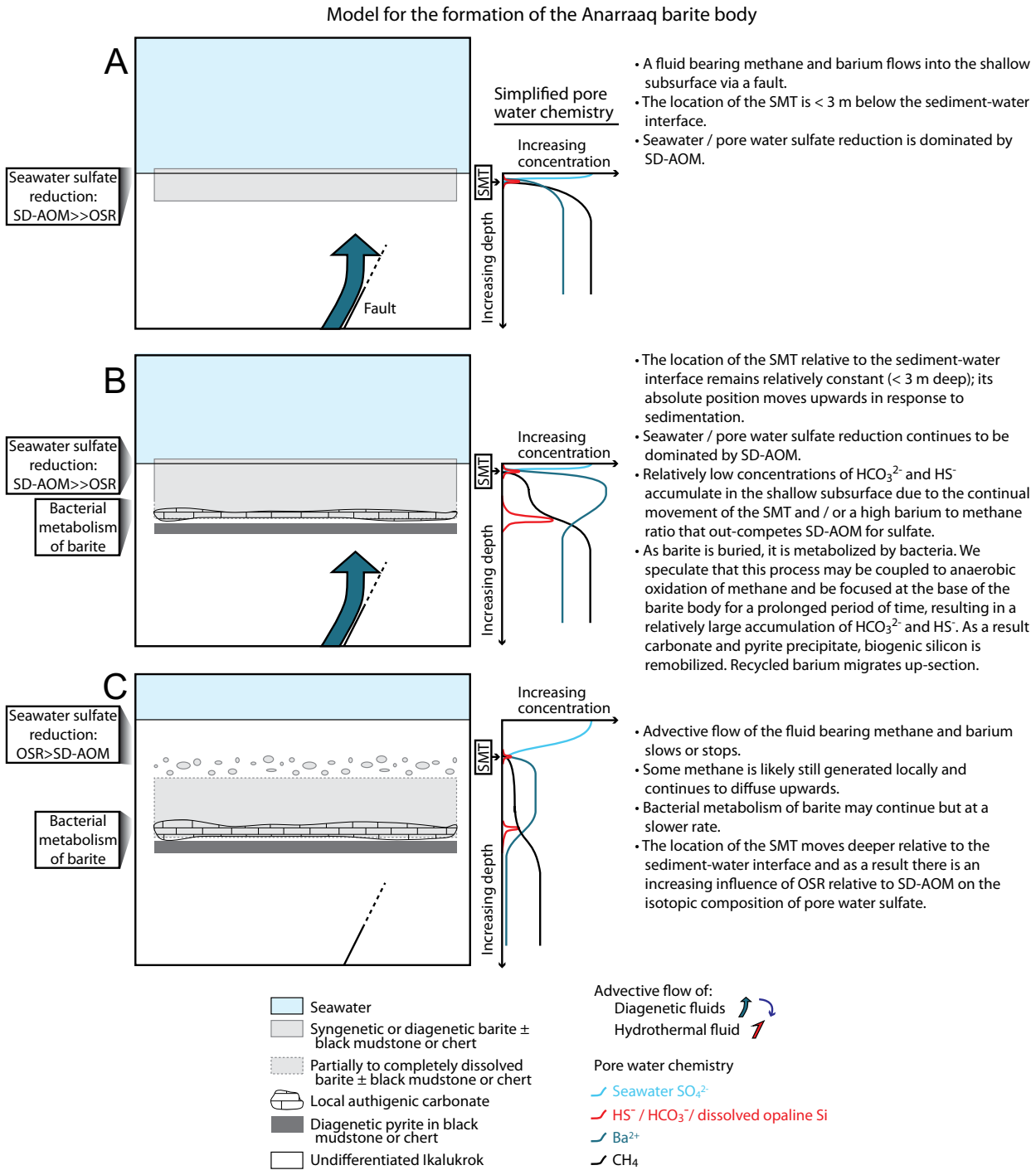

Figure 4.10: Model for the formation of the Anarraaq barite body with simplified pore water profiles showing the concentration of downward-diffusing seawater sulfate, upward-migrating methane and barium, and the local accumulation of the products of BSR (bisulfide, bicarbonate, and if the pH is high enough, dissolved opaline silicon). Profile a) shows a traditional SMT (modified after Fig. 2 in Iversen and Jørgensen, 1985, and Fig. 7 in Torres et al., 1996). Profile b) illustrates

how the bacterial metabolism of buried barite might affect pore water chemistry. Sulfate from dissolved barite is likely to be reduced immediately (possibly coupled to the anaerobic oxidation of methane), whereas the dissolved barium migrates up-section. Profile c) is similar to b) but the SMT is deeper below the seafloor.

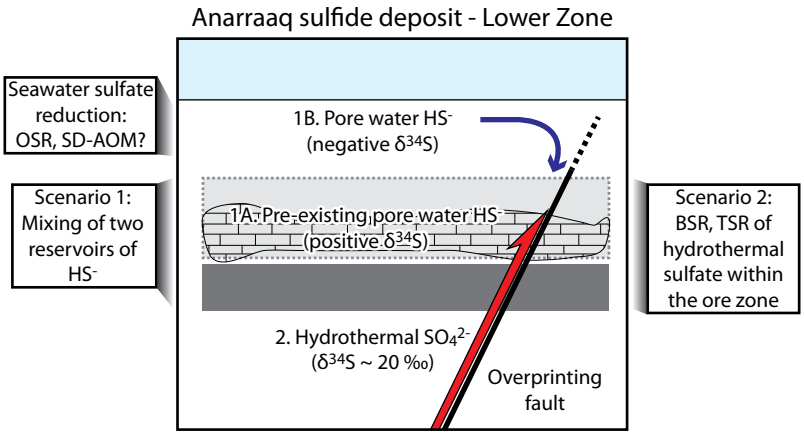

Figure 4.11: A cartoon showing the two possible scenarios for the source of reduced sulfide in the Lower Zone of the Anarraaq sulfide deposit. Hydrothermal fluids overprint host strata similar to the Anarraaq barite body in Fig. 4.13B or 4.13C. See Fig. 4.13 for legend.

	Tonnage (Mt)	Zn %	Pb %	Fe %[6]	S %[7]	Contained S (Mt)[7]
Su[1]	12.9	6.4	1.4	n.a.	3.4	0.4
Lik[2]	25.1	8.3	2.7	n.a.	4.5	1.1
Red Dog Past Production (Mt, Zn, Pb only)[3]	78.3	19.6	5.3	7.5	19.1	15.0
Red Dog Resources (Mt, Zn, Pb only)[3]						
Indicated (Aqqaluk, Qanaiyaq, Paalaaq)[3]	16.41	7.7	2.7	7.5	12.8	2.1
Inferred (Aqqaluk, Qanaiyaq, Paalaaq, Anarraaq)[3]	26.04	13.8	4.3	7.5	16.1	4.2
Red Dog Reserves (Mt, Zn, Pb only)[3]						
Probable (Aqqaluk, Qanaiyaq)[3]	50.89	15	4.2	7.5	16.7	8.5
Aktigiruq (Mt, Zn, Pb only)[4]	80	12	4	n.a.	6.5	5.2
				Subtotal for S in sulfide minerals:		**36.5**
Anarraaq barite body estimate[5]	1000				13.74	137.4
Red Dog district barite estimate (other)[5]	1000				13.74	137.4
					Subtotal for S in barite:	**274.8**
					Total:	**311.3**

Table 4.1: The total contained S contained in the Red Dog area sulfide deposits and barite occurrences has been estimated using a combination of publicly available past production, reserve and resource data (Krolak et al., 2017; Teck, 2017; Scott et al., 2010), estimates of barite contained in the district (Kelley et al., 2004b; Johnson et al., 2004); estimates of iron content in the Mine Area (Kelley et al., 2004), and reports that pyrite is relatively more abundant in the Anarraaq sulfide deposit (Kelley et al., 2004b; Blevings et al., 2013). No iron data or estimates are available for Su, Lik or Aktigiruq. Sulfur (%) is calculated based on mineral stoichiometry and the assumption that that all Zn occurs in sphalerite, Pb in galena, and Fe in pyrite.

[1.] Values for tonnage, Zn% and Pb% derived from Jennings and King (2002).

[2.] Values for tonnage, Zn% and Pb% derived from Scott et al. (2010)

[3.] Red Dog past production, reserve, and resource numbers for tonnage, Zn%, and Pb% derived from Krolak et al. (2017). Fe%, S% and S (Mt) are not derived from Krolak et al. (2017).

[4.] Aktigiruq tonnage, Zn% and Pb% represent the low range of the grade and tonnage ranges reported as an exploration target by Teck (2017).

[5.] Estimates of barite contained in Anarraaq barite body and the district are derived from Kelley et al. (2004b) and Johnson et al. (2004).

[6.] Values for Fe (%) are estimates based on information available for the Mine Area deposits in Kelley et al. (2004a) and reports that pyrite is relatively more abundant in the Anarraaq sulfide deposit (Kelley et al., 2004b; Blevings et al., 2013).

[7.] S (%) and contained S (Mt) are calculated from the Zn, Pb, Ba, Fe data.

Operating conditions for SIMS analysis on IMS-1280 multi-collector ion microprobe

	δ^{34}S-pyrite, marcasite	δ^{34}S-barite	δ^{18}O-barite
Cs probe diameter (µm)	10 (subset 8)	10	10
Acquisition raster (µm)	10 µm = 13 x 15, 8 µm = none	13 x 15	13 x 15
Beam current (nA)	1-1.5	1-1.5	1-1.5
Electron gun used	No	Yes	Yes
Implanation raster (µm)	18 x 18	18 x 18	18 x 18
Entrance slit width (µm), field apertures (mm)	122, 5 x 5	122, 5 x 5	122, 5 x 5
Field magnification	100 x	100 x	100 x
Energy slit	Fully open	Fully open	Fully open
Faraday cup detectors	$^{32}S^-$ = L'2 with 10^{10} Ω, $^{34}S^-$ = FC2 with 10^{11} Ω	$^{32}S^-$ = L'2 with 10^{10} Ω, $^{34}S^-$ = FC2 with 10^{11} Ω	$^{16}O^-$ = L'2 with 10^{10} Ω, $^{18}O^-$ = H'2 with 10^{11} Ω
Mass Resolution	2000	2000	$^{16}O^-$ = 1950, $^{18}O^-$ = 2275
Mean count rate for secondary ions detected (counts/s)	$^{32}S^-$ = 0.3 – 1.3 x 10^9, $^{34}S^-$ = 1.5 – 5.6 x 10^7	$^{32}S^-$ = 0.3 – 1.3 x 10^9, $^{34}S^-$ = 1.5 – 5.6 x 10^7	$^{16}O^-$ = 1.6 – 2.1 x 10^9, $^{18}O^-$ = 3.3 – 4.3 x 10^6
RM identity	S0302A pyrite	S0327 barite	S0327 barite
RM composition (‰)	$\delta^{34}S_{VCDT}$ = -0.2 ± 0.2	$\delta^{34}S_{VCDT}$ = +22.3 ± 0.5	$\delta^{18}O_{VSMOW}$ = +11.0 ± 0.5
Peak counding time (s)	50	50	50
Instrumental mass fractionation (‰)	?	?	3.6-4.9
Standard deviation of RM analyses (‰)	0.03 – 0.13	0.03 – 0.13	0.11 – 0.13
Within-session IMF drift (‰)	0-0.35	0-0.35	0.3
Typical ± 2σ of unknowns (‰)	0.2 – 0.3	0.2 – 0.3	0.3

Table 4.2: Operating conditions for SIMS analysis on IMS-1280 multi-collector ion microprobe.

Chapter 5: Conclusion

In this thesis, I investigate several fundamental questions about the formation of SHMS mineralization in the Red Dog district. This chapter is a summary of how the work presented in chapters 2-4 advances the genetic model for SHMS mineralization in the Red Dog district and what implications this has for SHMS deposits elsewhere in the world. This chapter also includes several suggestions for future research directions.

In Chapter 2, we present observations of trace fossils that indicate that at least some of the strata hosting SHMS deposits in the Red Dog district formed in an oxygenated middle to outer shelf setting. This interpretation contradicts previous regional sedimentological and lithogeochemical studies that indicate host sediment deposition took place under primarily anoxic, denitrifying conditions (Slack et al., 2004; Dumoulin et al., 2014). To reconcile our data with previous work, we suggest that host strata was deposited in a shelfal setting where redox conditions fluctuated in response to an expanding and contracting oxygen minimum zone. This idea represents a significant departure from the long-held view that strata hosting SHMS mineralization in the Red Dog district was deposited in a restricted basin with a stratified water column (e.g. Blevings et al., 2013; Slack et al., 2015), a concept rooted in the classic SEDEX model (Goodfellow and Lydon, 2007). Chapter 2 complements recent work by Magnall et al. (2016a; 2016b; 2018), Slack et al. (2017), and Johnson et al. (2018) in the Selwyn basin, all of which de-emphasize the influence of basin restriction during SHMS host sediment deposition.

In Chapter 3, we show that the Anarraaq area contains three discrete intervals of pre-ore barite, carbonate, and pyrite hosted in the organic-rich mudstone of the Ikalukrok unit. One of these intervals – the Anarraaq barite body – is barren and pre-ore barite, carbonate, and pyrite must have formed independent of hydrothermal mineralization. Textures preserved in the barite body reveal that carbonate is not a sedimentary debrite but instead a phase of alteration that is closely associated with barite dissolution and quartz precipitation. The other two barite-carbonate-pyrite intervals have been overprinted by Zn-Pb mineralization and make up the Upper and Lower ore zones in the Anarraaq sulfide deposit. This is the first time barite has been recognized as a significant component of this deposit. The massive pyrite that characterizes the low-grade part of the deposit is not a distal style of hydrothermal alteration but rather better-preserved host strata. We propose that each barite-carbonate-pyrite interval is the product of methane-related diagenetic processes at a sulfate-methane transition (SMT) zone, which may be a crucial prerequisite for the emplacement of high-grade SHMS ore in the Red Dog district.

Also in Chapter 3, we present rhenium-osmium isochron ages for organic-rich mudstone of the Ikalukrok unit (339.1 ± 8.3 Ma), pre-ore diagenetic pyrite (333.0 ± 7.4 Ma), and hydrothermal pyrite (334.4 ± 5.3 Ma). These ages are all within uncertainty of each other and with ore-stage pyrite at the Main deposit in the Mine Area (338.3 ± 5.8 Ma; Morelli et al., 2004).

This suggests that Zn-Pb mineralization was broadly synchronous across the Red Dog district.

In Chapter 4 we use *in situ* S and O isotopic data to investigate in more detail the idea that pre-ore barite and pyrite formed at a SMT. Our data show that barite in the Anarraaq barite body formed during two phases. First, laminated to massive barite formed during a relatively high flux of methane through the Ikalukrok sediment. Later, the flux of methane decreased; nodular barite formed during this period. Although barite precipitation during both phases was likely associated with sulfate-driven anaerobic oxidation of methane (SD-AOM), little to no coeval carbonate or pyrite precipitation took place. At the same time, BSR took place in deeper, methanic pore waters where the source of sulfate was dissolved barite. This process was likely most intense at the base of the laminated to massive barite interval and was responsible for the precipitation of massive pyrite and calcite. The S and O isotopic data available for pre-ore barite and pyrite in the Anarraaq sulfide deposit suggests that barite dissolution coupled to BSR was also an important process in Lower Zone host strata; the diagenetic conditions may have been somewhat different for Upper Zone host strata.

The S isotopic composition of hydrothermal pyrite in the Anarraaq sulfide deposit is characterized by wide range of $\delta^{34}S$ values and small-scale spatial-temporal heterogeneity. This could be the product of mixing between a local reservoir of biogenic bisulfide produced via barite dissolution coupled to BSR (positive $\delta^{34}S$ values) and an external reservoir of biogenic bisulfide produced via seawater BSR (negative $\delta^{34}S$ values) in lateral or younger strata. Alternatively, reduction of hydrothermal sulfate within the ore zone under highly variable conditions may have produced a wide variety $\delta^{34}S$ values. Overall, Chapter 4 emphasizes the importance and complexity of the role microbial activity played in the formation of the giant Zn-Pb deposits of the Red Dog district. The flux of methane through host sediment was fundamental to the physicochemical preparation of the Ikalukrok unit as a prospective host, and methane may have continued to play an important role as a reductant during ore formation.

5.1 Future research directions

Although this thesis has significantly advanced the understanding of how SHMS deposits form in the Red Dog district, many questions remain unanswered. One specific outstanding question from Chapter 4 is whether the diagenetic calcite at the base of the Anarraaq barite body (which we interpret to be the product of barite dissolution coupled to BSR) is derived from biogenic methane through the process of SD-AOM. This could be tested by analyzing the C isotopic composition of the calcite (e.g., Johnson et al., 2018). We further speculate in Chapter 4 that biogenic methane could have continued to play an important role as a reductant during ore formation; the C isotopic composition of late hydrothermal calcite may offer some insight into this idea as well.

The detailed paragenetic relationships described in Chapter 3 provide an excellent

starting point for further investigation of the conditions during ore emplacement and the likely mechanisms of ore precipitation. Microthermometry (Roedder, 1984), crush-leach (Banks and Yardley, 1992; Leach et al., 2004), and LA-ICP-MS (Heinrich et al., 2003; Pettke et al., 2012; Hammerli et al., 2013) analysis of fluid inclusions; mineral stability diagrams (Wood, 1998); and the application of modelling programs such as Geochemist's Workbench (Bethke, 2008) have potential to provide new insights in this area.

The cross-sections in Chapter 3 emphasize the importance of understanding the stratigraphy and structural geology of the Ikalukrok unit, which hosts all known Zn-Pb mineralization in the Red Dog district. Ore deposits are commonly associated with much larger alteration halos and understanding the textural, mineralogical, or geochemical patterns associated with these halos can be a powerful tool for predicting the occurrence of economic mineralization. However, the application of such tools is predicated on the assumption that the present-day position of ore deposits relative to the surrounding non-mineralized rocks is the same as at the time of deposit emplacement. If this is not the case (and it may not be at Anarraaq), a careful structural reconstruction is imperative before any meaningful investigation of potential alteration halos can be carried out.

Deformation features are difficult or impossible to recognize in the Ikalukrok by visual inspection because of its dark, fine-grained, homogenous appearance. Geophysical methods such as seismic surveys may offer some insight into internal deformation of the unit. Perhaps even more useful might be the development of a detailed chemostratigraphic framework for the Ikalukrok unit based on bulk rock major and minor element chemistry, minerology, S isotopic composition of the pyrite fraction (e.g., Canfield et al., 1986; Magnall et al., 2016a), C isotopic composition of the calcareous components (e.g., Johnson et al., 2018), S and O of any barite, or some combination. Preliminary bulk geochemical data (not included in this thesis) suggests that geochemically distinct subunits exist; if these subunits can be correlated on the district scale, this may allow for structural complications within the Ikalukrok to be unraveled. Furthermore, the isotopic geochemistry would allow an assessment of how methane-related diagenetic alteration influenced barren Ikalukrok sediment over time at a district scale. These data could be combined with other geochemical proxies for depositional conditions for a more complete picture the depositional environment.

We suggest in Chapter 3 that all deposits in the Red Dog district may overprint host sediment that underwent extensive methane-related diagenetic alteration. If this is true, the distribution of pre-ore barite ± carbonate ± pyrite Ikalukrok strata in the Red Dog district defines the distribution of prospective host strata. Understanding the controls on the occurrence of these strata would be a powerful exploration tool. We speculate that pre-ore barite-carbonate-pyrite strata are local features that formed in association with advective flow of diagenetic fluid. Do

these intervals have a more extensive, cryptic geochemical signature that could be used to vector towards them? Do they occur in a specific stratigraphic interval within the Ikalukrok? Are there synsedimentary deformational features associated with these intervals, perhaps occurring with a predictable distribution, that are recognizable in the Ikalukrok?

Finally, it would be interesting to explore the new ideas about deposit genesis presented in this thesis in the context of other districts containing SHMS mineralization. Is methane-derived carbonate (and/ or pyrite) an important component of host sediment in other SHMS districts? Particularly intriguing are the the mineralogical, textural, and geochemical similarities between the Anarraaq deposit and the Irish-type deposits(Kelley et al., 2004; Reynolds, Chapter 3-4). Could methane-related geochemical processes have played an important role in the formation of the Irish-type deposits? Is dissolution of barite an important digenetic (or hydrothermal) process in any other SHMS deposits? And what role does it play in S cycling and controlling the S isotopic composition of sulfide minerals?

5.2 Full list of references

Banks, D. A., and Yardley, B. W. D., 1992, Crush-leach analysis of fluid inclusions in small natural and synthetic samples: Geochimica et Cosmochimica Acta, v. 56, p. 245–248.

Bethke, C. M., 2008, Geochemical and Biogeochemical Reaction Modeling: New York, Cambridge University Press, 564 p.

Blevings, S., Kraft, J., Stemler, J., and Krolak, T., 2013, An overview of the structure, stratigraphy, and Zn-Pb-Ag deposits of the Red Dog District, Northwestern Alaska, in Special Publication 17: Society of Economic Geologists, p. 361–387.

Canfield, D. E., Raiswell, R., Westrich, J. T., Reaves, C. M., and Berner, R. A., 1986, The use of chromium reduction in the analysis of reduced inorganic sulfur in sediments and shales: Chemical Geology, v. 54, p. 149–155.

Dumoulin, J. A., Johnson, C. A., Slack, J. F., Bird, K. J., Whalen, M. T., Moore, T. E., Harris, A. G., and Sullivan, P. B. O., 2014, Carbonate margin, slope, and basin facies of the Lisburne Group (Carboniferous-Permian) in northern Alaska, in Verwer, K., Playton, T., and Harris, P. eds., Special Publication 105: SEPM, p. 211–236.

Goodfellow, W. D., and Lydon, J. W., 2007, Sedimentary exhalative (SEDEX) deposits, in Goodfellow, W. D. ed., Mineral deposits of Canada: Geological Association of Canada, p. 163–183.

Hammerli, J., Rusk, B., Spandler, C., Emsbo, P., and Oliver, N. H. S., 2013, In situ quantification of Br and Cl in minerals and fluid inclusions by LA-ICP-MS: A powerful tool to identify fluid sources: Chemical Geology, v. 337–338, p. 75–87.

Heinrich, C. A., Pettke, T., Halter, W. E., Aigner-Torres, M., Audétat, A., Günther, D., Hattendorf, B., Bleiner, D., Guillong, M., and Horn, I., 2003, Quantitative multi-element analysis of

minerals, fluid and melt inclusions by laser-ablation inductively-coupled-plasma mass-spectrometry: Geochimica et Cosmochimica Acta, v. 67, p. 3473–3497.

Johnson, C. A., Slack, J. F., Dumoulin, J. A., Kelley, K. D., and Falck, H., 2018, Sulfur isotopes of host strata for Howards Pass (Yukon-Northwest Territories) Zn-Pb deposits implicate anaerobic oxidation of methane, not basin stagnation: Geology, v. 46, p. 619–622.

Kelley, K. D., Dumoulin, J. A., and Jennings, S., 2004, The Anarraaq Zn-Pb-Ag and Barite Deposit, Northern Alaska: Evidence for Replacement of Carbonate by Barite and Sulfides: Economic Geology, v. 99, p. 1577–1591.

Leach, D. L., Marsh, E., Emsbo, P., Rombach, C. S., Kelley, K. D., and Anthony, M., 2004, Nature of hydrothermal fluids at the shale-hosted Red Dog Zn-Pb-Ag deposits, Brooks range, Alaska: Economic Geology, v. 99, p. 1449–1480.

Magnall, J. M., Gleeson, S. A., Stern, R. A., Newton, R. J., Poulton, S. W., and Paradis, S., 2016a, Open system sulphate reduction in a diagenetic environment – isotopic analysis of barite ($\delta^{34}S$ and $\delta^{18}O$) and pyrite ($\delta^{34}S$) from the Tom and Jason Late Devonian Zn-Pb-Ba deposits, Selwyn Basin, Canada: Geochimica et Cosmochimica Acta.

Magnall, J. M., Gleeson, S. A., Blamey, N. J. F., Paradis, S., and Luo, Y., 2016b, The thermal and chemical evolution of hydrothermal vent fluids in shale hosted massive sulphide (SHMS) systems from the MacMillan Pass district (Yukon, Canada): Geochemica et Cosmochimica Acta, v. 193, p. 251–273.

Magnall, J. M., Gleeson, S. A., Poulton, S. W., Gordon, G. W., and Paradis, S., 2018, Links between seawater paleoredox and the formation of sediment-hosted massive sulphide (SHMS) deposits — Fe speciation and Mo isotope constraints from Late Devonian mudstones: Chemical Geology, v. 490, p. 45–60.

Morelli, R. M., Creaser, R. A., Selby, D., Kelley, K. D., and King, A. R., 2004, Re-Os sulfide geochronology of the Red Dog sediment-hosted Zn-Pb-Ag deposit, Brooks Range, Alaska: Economic Geology, v. 99, p. 1569–1576.

Pettke, T., Oberli, F., Audétat, A., Guillong, M., Simon, A. C., Hanley, J. J., and Klemm, L. M., 2012, Recent developments in element concentration and isotope ratio analysis of individual fluid inclusions by laser ablation single and multiple collector ICP-MS: Ore Geology Reviews, v. 44, p. 10–38.

Roedder, E., 1984, Fluid Inclusions: Reviews in Mineralogy, v. 12, p. 1–646.

Slack, J. F., Dumoulin, J. A., Schmidt, J. M., Young, L. E., and Rombach, C. S., 2004, Paleozoic sedimentary rocks in the Red Dog Zn-Pb-Ag District and vicinity, western Brooks Range, Alaska: Provenance, deposition, and metallogenic significance: Economic Geology, v. 99, p. 1385–1414.

Slack, J. F., Selby, D., and Dumoulin, J. A., 2015, Hydrothermal, Biogenic, and Seawater

Components in Metalliferous Black Shales of the Brooks Range, Alaska: Synsedimentary Metal Enrichment in a Carbonate Ramp Setting: Economic Geology, v. 110, p. 653–675.

Slack, J. F., Falck, H., Kelley, K. D., and Xue, G. G., 2017, Geochemistry of host rocks in the Howards Pass district, Yukon-Northwest Territories, Canada: implications for sedimentary environments of Zn-Pb and phosphate mineralization: Mineralium Deposita, v. 52, p. 565–593.

Wood, S. A., 1998, Calculation of activity-activity and log fo2-pH diagrams: Techniques in hydrothermal ore deposits geology: Reviews in Economic Geology, v. 10, p. 81–96.

Full reference list

Aharon, P., and Fu, B., 2000, Microbial sulfate reduction rates and sulfur and oxygen isotope fractionations at oil and gas seeps in deepwater Gulf of Mexico: Geochemica et Cosmochimica Acta, v. 64, p. 233–246.

Aharon, P., and Fu, B., 2003, Sulfur and oxygen isotopes of coeval sulfate – sulfide in pore fluids of cold seep sediments with sharp redox gradients: v. 195, p. 201–218, doi: 10.1016/S0009-2541(02)00395-9.

Aloisi, G., Wallmann, K., Bollwerk, S.M., Derkachev, A., Bohrmann, G., and Suess, E., 2004, The effect of dissolved barium on biogeochemical processes at cold seeps: Geochemica et Cosmochimica Acta, v. 68, p. 1735–1748, doi: 10.1016/j.gca.2003.10.010.

Anderson, I., Ashton, J., Boyce, A., Fallick, A., and Russell, M., 1998, Ore depositional processes in the Navan Zn-Pb deposit, Ireland: Economic Geology and the Bulletin of the Society of Economic Geologists, v. 93, p. 535–563.

Antler, G., and Pellerin, A., 2018, A critical look at the combined use of sulfur and oxygen isotopes to study microbial metabolisms in methane-rich environments: Frontiers in Microbiology, v. 9, p. 1–7, doi: 10.3389/fmicb.2018.00519.

Aplin, A.C., and Macquaker, J.H.S., 2011, Mudstone diversity: Origin and implications for source, seal, and reservoir properties in petroleum systems: AAPG Bulletin, v. 95, p. 2031–2059, doi: 10.1306/03281110162.

Arning, E.T., Gaucher, E.C., van Berk, W., and Schulz, H.M., 2015, Hydrogeochemical models locating sulfate-methane transition zone in marine sediments overlying black shales: A new tool to locate biogenic methane? Marine and Petroleum Geology, v. 59, p. 563–574, doi: 10.1016/j.marpetgeo.2014.10.004.

Ayuso, R.A., Kelley, K.D., Leach, D.L., Young, L.E., Slack, J.F., Wandlass, G., Lyon, A.M., and Dillingham, J.L., 2004, Origin of the Red Dog Zn-Pb-Ag deposits, Brooks Range, Alaska: Evidence from regional Pb and Sr isotope sources: Economic Geology, v. 99, p. 1533–1554, http://www.intl-econgeol.geoscienceworld.org/content/99/7/1533.short.

Banks, D. A., and Yardley, B. W. D., 1992, Crush-leach analysis of fluid inclusions in small natural and synthetic samples: Geochimica et Cosmochimica Acta, v. 56, p. 245–248.

Barnes, R.O., and Goldberg, E.D., 1976, Methane production and consumption in anoxic marine sediments: Geology, v. May, p. 297–300, doi: 10.1130/0091-7613(1976)42.0.CO;2.

Barrie, C., Boyce, A., a.P. Boyle, Williams, P.J., Blake, K., Wilkinson, J.J., Lowther, M., MacDermott, P., and Prior, D., 2009, On the growth of colloform textures: A case study of sphalerite from the Galmoy ore body, Ireland: v. 166, p. 563–582, doi: 10.1144/0016-76492008-080.

Bethke, C. M., 2008, Geochemical and Biogeochemical Reaction Modeling: New York,

Cambridge University Press, 564 p.
Bishop, J.K.B., 1988, The barite-opal-organic carbon association in oceanic particulate matter: Nature, v. 332, p. 341–343, doi: 10.1038/332341a0.
Blevings, S., Kraft, J., Stemler, J., and Krolak, T., 2013, An overview of the structure, stratigraphy, and Zn-Pb-Ag deposits of the Red Dog District, northwestern Alaska, in Colpron, M., et al., eds., Tectonics, metallogeny, and discovery: The North American Cordillera and similar accretionary settings: Society of Economic Geologists Special Publication 17, p. 361–387.
Bolze, C.E., Malone, P.G., and Smith, M.J., 1974, Microbial mobilization of barite: Chemical Geology, v. 13, p. 141–143, doi: 10.1016/0009-2541(74)90006-0.
Bromley, R., and Ekdale, A., 1984, Chondrites: A trace fossil indicator of anoxia in sediments: Science, v. 224, p. 872–874, doi:10.1126 /science .224 .4651.872.
Brumsack, H.J., 1986, The inorganic geochemistry of Cretaceous black shales (DSDP Leg 41) in comparison to modern upwelling sediments from the Gulf of California, in Summerhayes, C.P. et al., eds., North Atlantic Palaeoceanogrphy: Geological Society Special Publications, v. 21, p. 447–462, doi: 10.1144/GSL.SP.1986.021.01.30.
Burke, W.H., Denison, R.E., Hetherington, E.A., Koepnick, R.B., Nelson, H.F., and Otto, J.B., 1982, Variation of seawater Sr87-Sr86throughout Phanerozoic time.: Geology, v. 10, p. 516–519, doi: 10.1130/0091-7613(1982)10<516:VOSSTP>2.0.CO.
Campbell, K.A., 2006, Hydrocarbon seep and hydrothermal vent paleoenvironments and paleontology: Past developments and future research directions: Palaeogeography, Palaeoclimatology, Palaeoecology, v. 232, p. 362–407, doi: 10.1016 /j .palaeo .2005 .06.018.
Campbell, K.A., Nesbitt, E.A., and Bourgeois, J., 2006, Signatures of storms, oceanic floods and forearc tectonism in marine shelf strata of the Quinault Formation (Pliocene), Washington, USA: Sedimentology, v. 53, p. 945–969, doi: 10.1111 /j .1365 -3091 .2006 .00788.x.
Canfield, D. E., Raiswell, R., Westrich, J. T., Reaves, C. M., and Berner, R. A., 1986, The use of chromium reduction in the analysis of reduced inorganic sulfur in sediments and shales: Chemical Geology, v. 54, p. 149–155.
Canfield, D.E., 1991, Sulfate Reduction in Deep-Sea Sediments: American Journal of Science, v. 291, p. 177–188.
Cartwright, J.A., 1994, Episodic basin-wide fluid expulsion from geopressured shale sequences in the North Sea Basin: Geology, v. 22, p. 447–450, doi: 10.1130/0091-7613(1994)022<0447:EBWFEF>2.3.CO;2.
Caulfield, B., Lehuray, A., and Rye, D., 1986, A review of lead and sulphur isotope investigations

of Irish sediment-hosted base metal deposits with new data from the Keel, Ballinalack, Moyvoughly and Tatestown deposits.: , p. 591–615.

Chen, D., Wang, J., Racki, G., Li, H., Wang, C., Ma, X., and Whalen, M.T., 2013, Large sulphur isotopic perturbations and oceanic changes during the Frasnian–Famennian transition of the Late Devonian: Journal of the Geological Society, v. 170, p. 465 LP-476.

Claypool, G.E., Holser, W.T., Kaplan, I.R., Sakai, H., and Zak, I., 1980, The age curves of sulfur and oxygen isotopes in marine sulfate and their mutual interpretation: Chemical Geology, v. 28, p. 199–260, doi: 10.1016/0009-2541(80)90047-9.

Cooke, D., Bull, S., Large, R., and McGoldrick, P., 2000, The importance of oxidized brines for the formation of Australian Proterozoic stratiform sediment-hosted Pb-Zn (Sedex) deposits: Economic Geology, v. 95, p. 1–18.

Creaser, R., Papanastassiou, D., and Wasserburg, G., 1991, Negative thermal ion mass spectrometry of osmium, rhenium and iridium: Geochimica et Cosmochimica Acta, v. 55, p. 397–401.

Creaser, R.A., Sannigrahi, P., Chacko, T., and Selby, D., 2002, Further evaluation of the Re-Os geochronometer in organic-rich sedimentary rocks: A test of hydrocarbon maturation effects in the Exshaw Formation, Western Canada Sedimentary Basin: Geochimica et Cosmochimica Acta, v. 66, p. 3441–3452, doi: 10.1016/S0016-7037(02)00939-0.

Davies, R.J., and Ireland, M.T., 2011, Initiation and propagation of polygonal fault arrays by thermally triggered volume reduction reactions in siliceous sediment: Marine Geology, v. 289, p. 150–158, doi: 10.1016/j.margeo.2011.05.005.

Davies, R.J., Goulty, N.R., and Meadows, D., 2008, Fluid flow due to the advance of basin-scale silica reaction zones: Bulletin of the Geological Society of America, v. 120, p. 195–206, doi: 10.1130/B26099.1.

De Vera, J., 2005, Structure of the Red Dog District, Western Brooks Range, Alaska: University of London, 633 p.

De Vera, J., McClay, K., and King, A., 2004, Structure of the Red Dog District, Western Brooks Range, Alaska: Economic Geology, v. 99, p. 1415–1434.

Denison, R.E., Koepnick, R.B., Burke, W.H., Hetherington, E.A., and Fletcher, A., 1994, Construction of the Mississippian, Pennsylvanian and Permian seawater 87Sr/86Sr curve: Chemical Geology: Isotope Geoscience Section, v. 112, p. 145–167.

Deusner, C., Holler, T., Arnold, G.L., Bernasconi, S.M., Formolo, M.J., and Brunner, B., 2014, Sulfur and oxygen isotope fractionation during sulfate reduction coupled to anaerobic oxidation of methane is dependent on methane concentration: Earth and Planetary Science Letters, v. 399, p. 61–73, doi: 10.1016/j.epsl.2014.04.047.

Dickens, G.R., 2001, Sulphate profiles and barium fronts in sediments on the Blake Ridge:

present and past methane fluxes through a large gas hydrate resevoir: Geochimica et Cosmochimica Acta, v. 65, p. 529–543.

Dumoulin, J. A., Johnson, C. A., Slack, J. F., Bird, K. J., Whalen, M. T., Moore, T. E., Harris, A. G., and Sullivan, P. B. O., 2014, Carbonate margin, slope, and basin facies of the Lisburne Group (Carboniferous-Permian) in northern Alaska, in Verwer, K., Playton, T., and Harris, P. eds., Special Publication 105: SEPM, p. 211–236.

Dumoulin, J., Harris, A.G., Blome, C.D., and Young, L.E., 2004, Depositional settings, correlation, and age of Carboniferous rocks in the western Brooks Range, Alaska: Economic Geology, v. 99, p. 1355–1384.

Dumoulin, J.A., Johnson, C.A., Slack, J.F., Bird, K.J., Whalen, M.T., Moore, T.E., Harris, A.G., and Sullivan, P.B.O., 2014, Carbonate margin, slope, and basin facies of the Lisburne Group (Carboniferous–Permian) in northern Alaska, in Verwer, K., et al., eds., Deposits, architecture, and controls of carbonate margin, slope, and basinal settings: SEPM (Society for Sedimentary Geology) Special Publication 105, p. 211–236.

Dumoulin, J.A., Slack, J.F., Whalen, M.T., and Harris, A.G., 2011, Depositional setting and geochemistry of phosphorites and metalliferous black shales in the Carboniferous–Permian Lisburne Group, northern Alaska, in Dumoulin, J.A. and Galloway, J.P. eds., USGS Professional Paper 1776-C, p. 1–64,

Dunne, J.P., Sarmiento, J.L., and Gnanadesikan, A., 2007, A synthesis of global particle export from the surface ocean and cycling through the ocean interior and on the seafloor: Global Biogeochemical Cycles, v. 21, p. 1–16, doi: 10.1029/2006GB002907.

Egger, M., Riedinger, N., Mogollón, J.M., and Jørgensen, B.B., 2018, Global diffusive fluxes of methane in marine sediments: Nature Geoscience, v. 11, p. 421–425, doi: 10.1038/s41561-018-0122-8.

Ekdale, A.A., 1988, Pitfalls of paleobathymetric interpretations based on trace fossil assemblages: Palaios, v. 3, p. 464–472, doi:10.2307/3514720.

Fallick, A., Ashton, J., and Boyce, A., 2001, Bacteria were responsible for the magnitude of the world-class hydrothermal base metal sulfide orebody at Navan, Ireland: Economic …, v. 96, p. 885–890.

Farquhar, J., Wu, N., Canfield, D.E., and Oduro, H., 2010, Connections between sulfur cycle evolution, sulfur isotopes, sediments, and base metal sulfide deposits: Economic …, v. 105, p. 509–533.

Fernandes, N.A., Gleeson, S.A., Magnall, J.M., Creaser, R.A., Martel, E., Fischer, B.J., and Sharp, R., 2017, The origin of Late Devonian (Frasnian) stratiform and stratabound mudstone-hosted barite in the Selwyn Basin, Northwest Territories, Canada: Marine and Petroleum Geology, v. 85, p. 1–15, doi: 10.1016/j.marpetgeo.2017.04.006.

Fritz, P., Basharmal, G.M., Drimmie, R.J., Ibsen, J., and Qureshi, R.M., 1989, Oxygen isotope exchange between sulphate and water during bacterial reduction of sulphate: Chemical Geology: Isotope Geoscience Section, v. 79, p. 99–105, doi: 10.1016/0168-9622(89)90012-2.

Fu, B., and Aharon, P., 1997, Origin and Depositional Model of Barite Deposits Associated with Hydrocarbon Seeps on the Gulf of Mexico Slope Offshore Louisiana: Gulf Coast Association of Geological Societies Transactions, doi: 10.1111/j.1600-6143.2011.03972.x.

Gadd, M.G., Layton-Matthews, D., Peter, J.M., Paradis, S., and Jonasson, I.R., 2016, The world-class Howard's Pass SEDEX Zn-Pb district, Selwyn Basin, Yukon. Part II: the roles of thermochemical and bacterial sulfate reduction in metal fixation: Mineralium Deposita, doi: 10.1007/s00126-016-0672-x.

Geboy, N.J., Tripathy, G.R., Ruppert, L.F., Eble, C.F., Blake, B.M., Hannah, J.L., and Stein, H.J., 2015, Re-Os age for the Lower-Middle Pennsylvanian Boundary and comparison with associated palynoflora: International Journal of Coal Geology, v. 140, p. 23–30, doi: 10.1016/j.coal.2015.01.002.

Gingras, M.K., Pemberton, S.G., Dashtgard, S., and Dafoe, L., 2008, How fast do marine invertebrates burrow?: Palaeogeography, Palaeoclimatology, Palaeoecology, v. 270, p. 280–286, doi:10.1016 /j .palaeo .2008 .07.015.

Gingras, M.K., Pemberton, S.G., Mendoza, C.A., and Henk, F., 1999, Assessing the anisotropic permeability of Glossifungites surfaces: Petroleum Geoscience, v. 5, p. 349–357, doi:10.1144/petgeo .5 .4.349.

Goodfellow, W. D., and Lydon, J. W., 2007, Sedimentary exhalative (SEDEX) deposits, in Goodfellow, W. D. ed., Mineral deposits of Canada: Geological Association of Canada, p. 163–183.

Goodfellow, W.D., 2007, Base metal metallogeny of the Selwyn Basin, Canada, in Goodfellow, W., ed., Mineral deposits of Canada: A synthesis of major deposit-types, district metallogeny, the evolution of geological provinces, and exploration methods: Geological Association of Canada, Mineral Deposits Division, Special Publication 5, p. 553–579.

Goodfellow, W.D., and Jonasson, I.R., 1984, Ocean stagnation and ventilation defined by Delta-S-34 secular trends in pyrite and barite, Selwyn basin, Yukon: Geology, v. 12, p. 583–586.

Griffith, E.M., and Paytan, A., 2012, Barite in the ocean - occurrence, geochemistry and palaeoceanographic applications: Sedimentology, v. 59, p. 1817–1835, doi: 10.1111/j.1365-3091.2012.01327.x.

Gromet, L.P., Haskin, L.A., Korotev, R.L., and Dymek, R.F., 1984, The "North American shale

composite": Its compilation, major and trace element characteristics: Geochimica et Cosmochimica Acta, v. 48, p. 2469–2482, doi: 10.1016/0016-7037(84)90298-9.

Gutiérrez, D., Enríquez, E., Purca, S., Quipúzcoa, L., Marquina, R., Flores, G., and Graco, M., 2008, Oxygenation episodes on the continental shelf of central Peru: Remote forcing and benthic ecosystem response: Progress in Oceanography, v. 79, p. 177–189, doi:10.1016/j .pocean .2008 .10.025.

Hamersley, M.R., Lavik, G., Woebken, D., Rattray, J.E., Lam, P., Hopmans, E.C., Damste, J.S.S., Kruger, S., Graco, M., Gutierrez, D., and Kuypers, M.M.M., 2007, Anaerobic ammonium oxidation in the Peruvian oxygen minimum zone: Limnology and Oceanography, v. 52, p. 923–933.

Hammarlund, E.U., Gaines, R.R., Prokopenko, M.G., Qi, C., Hou, X.-G., and Canfield, D.E., 2017, Early Cambrian oxygen minimum zone-like conditions at Chengjiang: Earth and Planetary Science Letters, v. 475, p. 160–168, doi: 10.1016/j.epsl.2017.06.054.

Hammerli, J., Rusk, B., Spandler, C., Emsbo, P., and Oliver, N. H. S., 2013, In situ quantification of Br and Cl in minerals and fluid inclusions by LA-ICP-MS: A powerful tool to identify fluid sources: Chemical Geology, v. 337–338, p. 75–87.

Heinrich, C. A., Pettke, T., Halter, W. E., Aigner-Torres, M., Audétat, A., Günther, D., Hattendorf, B., Bleiner, D., Guillong, M., and Horn, I., 2003, Quantitative multi-element analysis of minerals, fluid and melt inclusions by laser-ablation inductively-coupled-plasma mass-spectrometry: Geochimica et Cosmochimica Acta, v. 67, p. 3473–3497.

Hertweck, G., Wehrmann, A., and Liebezeit, G., 2007, Bioturbation structures of polychaetes in modern shallow marine environments and their analogues to Chondrites group traces: Palaeogeography, Palaeoclimatology, Palaeoecology, v. 245, p. 382–389, doi:10.1016/j .palaeo .2006 .09.001.

Hitzman, M.W., 1999, Routine staining of drill core to determine carbonate mineralogy and distinguish carbonate alteration textures: , p. 794–798.

Hnatyshin, D., Kontak, D.J., Turner, E.C., Creaser, R.A., Morden, R., and Stern, R.A., 2016, Geochronologic (ReOs) and fluid-chemical constraints on the formation of the Mesoproterozoic-hosted Nanisivik ZnPb deposit, Nunavut, Canada: Evidence for early diagenetic, low-temperature conditions of formation: Ore Geology Reviews, v. 79, p. 189–217, doi: 10.1016/j.oregeorev.2016.05.017.

Hoehler, T.M., Alperin, M.J., Albert, D.B., and Martens, C.S., 1994, Field and laboratory studies of methane oxidation in an anoxic marine sediment: Evidence for a methanogen-sulfate reducer consortium: Global Biogeochemical Cycles, v. 8, p. 451–463, doi: 10.1029/94GB01800.

Iversen, N., and Jørgensen, B.B., 1985, Anaerobic methane oxidation rates at the sulphate-

methane transition in marine sediments from Kattegat and Skagerrak (Denmark): Limnology and Oceanography, v. 30, p. 944–955.

Jaeger, M., 2012, Sabellids and serpulids (Polychaeta sedentaria) from the type Maastrichtian, the Netherlands and Belgium, in Jagt, J.W.M., et al., eds., Fossils of the type Maastrichtian (Part 1): Scripta Geologica Special Issue 8, p. 45–81.

John, E.H., Wignall, P.B., Newton, R.J., and Bottrell, S.H., 2010, δ34SCAS and δ18OCAS records during the Frasnian–Famennian (Late Devonian) transition and their bearing on mass extinction models: Chemical Geology, v. 275, p. 221–234, doi: 10.1016/J.CHEMGEO.2010.05.012.

Johnson, C. A., Slack, J. F., Dumoulin, J. A., Kelley, K. D., and Falck, H., 2018, Sulfur isotopes of host strata for Howards Pass (Yukon-Northwest Territories) Zn-Pb deposits implicate anaerobic oxidation of methane, not basin stagnation: Geology, v. 46, p. 619–622.

Johnson, C.A., Emsbo, P., Poole, F.G., and Rye, R.O., 2009, Sulfur- and oxygen-isotopes in sediment-hosted stratiform barite deposits: Geochimica et Cosmochimica Acta, v. 73, p. 133–147, doi: 10.1016/j.gca.2008.10.011.

Johnson, C.A., Kelley, K.D., and Leach, D.L., 2004, Sulfur and oxygen isotopes in barite deposits of the western Brooks Range, Alaska, and implications for the origin of the Red Dog massive sulfide deposits: Economic Geology and the Bulletin of the Society of Economic Geologists, v. 99, p. 1435–1448, doi:10.2113 /gsecongeo .99.7 .1435.

Johnson, C.A., Slack, J.F., Dumoulin, J.A., Kelley, K.D., and Falck, H., 2018, Sulfur isotopes of host strata for Howards Pass (Yukon-Northwest Territories) Zn-Pb deposits implicate anaerobic oxidation of methane, not basin stagnation: Geology, v. 46, p. 619–622, doi: 10.1130/G40274.1.

Jorgensen, B.B., and Kasten, S., 2006, Sulfur cycling and methane oxidation, in Bohrmann, G. and Torres, M.E. eds., Marine Geochemistry, p. 271–309.

Jørgensen, B.B., Böttcher, M.E., Lüschen, H., Neretin, L.N., and Volkov, I.I., 2004, Anaerobic methane oxidation and a deep H2S sink generate isotopically heavy sulfides in Black Sea sediments: Geochimica et Cosmochimica Acta, v. 68, p. 2095–2118, doi: 10.1016/j.gca.2003.07.017.

Kampschulte, A., and Strauss, H., 2004, The sulfur isotopic evolution of Phanerozoic seawater based on the analysis of structurally substituted sulfate in carbonates: v. 204, p. 255–286, doi: 10.1016/j.chemgeo.2003.11.013.

Kaplan, I.R., and Rittenberg, S.C., 1964, Microbiological fractionation of sulphur isotopes: Microbiology, v. 34, p. 195–212.

Kelley, K.D., and Jennings, S., 2004, A special issue devoted to barite and Zn-Pb-Ag deposits in the Red Dog district, Western Brooks Range, Northern Alaska: Economic Geology, v. 99,

p. 1267–1280, http://econgeol.geoscienceworld.org/content/99/7/1267.short.

Kelley, K.D., Dumoulin, J.A., and Jennings, S., 2004, The Anarraaq Zn-Pb-Ag and barite deposit, Northern Alaska: Evidence for replacement of carbonate by barite and sulfides: Economic Geology and the Bulletin of the Society of Economic Geologists, v. 99, p. 1577–1591, doi: 10.2113 /gsecongeo .99.7.1577.

Kelley, K.D., Leach, D.L., Johnson, C.A., Clark, J.L., Fayek, M., Slack, J.F., Anderson, V.M., Ayuso, R.A., and Ridley, W.I., 2004, Textural, compositional, and sulfur isotope variations of sulfide minerals in the Red Dog Zn-Pb-Ag deposits, Brooks Range, Alaska: Implications for ore formation: Economic Geology and the Bulletin of the Society of Economic Geologists, v. 99, p. 1509–1532, doi:10.2113 /gsecongeo .99 .7 .1509.

Kendall, B., Creaser, R.A., Ross, G.M., and Selby, D., 2004, Constraints on the timing of Marinoan "Snowball Earth" glaciation by 187Re-187Os dating of a Neoproterozoic, post-glacial black shale in Western Canada: Earth and Planetary Science Letters, v. 222, p. 729–740.

Knittel, K., and Boetius, A., 2009, Anaerobic Oxidation of Methane : Progress with an Unknown Process:, doi: 10.1146/annurev.micro.61.080706.093130.

Kozdon, R., Kita, N.T., Huberty, J.M., Fournelle, J.H., Johnson, C. a., and Valley, J.W., 2010, In situ sulfur isotope analysis of sulfide minerals by SIMS: Precision and accuracy, with application to thermometry of ~3.5Ga Pilbara cherts: Chemical Geology, v. 275, p. 243–253, doi: 10.1016/j.chemgeo.2010.05.015.

Krolak, T., Palmer, K., Lacouture, B., Paley, N., 2017, NI 43-101 Technical Report for Red Dog Mine, Alaska, USA, 143 p.

Kuypers, M.M.M., Lavik, G., Woebken, D., Schmid, M., Fuchs, B.M., Amann, R., Jørgensen, B.B., and Jetten, M.S.M., 2005, Massive nitrogen loss from the Benguela upwelling system through anaerobic ammonium oxidation.: Proceedings of the National Academy of Sciences of the United States of America, v. 102, p. 6478–83, doi: 10.1073/pnas.0502088102.

Lash, G.G., 2015, Pyritization induced by anaerobic oxidation of methane (AOM) - An example from the upper devonian shale succession, western New York, USA: Marine and Petroleum Geology, v. 68, p. 520–535, doi: 10.1016/j.marpetgeo.2015.10.002.

Leach, D. L., Marsh, E., Emsbo, P., Rombach, C. S., Kelley, K. D., and Anthony, M., 2004, Nature of hydrothermal fluids at the shale-hosted Red Dog Zn-Pb-Ag deposits, Brooks range, Alaska: Economic Geology, v. 99, p. 1449–1480.

Leach, D.L., Bradley, D.C., Huston, D., Pisarevsky, S.A., Taylor, R.D., and Gardoll, S.J., 2010, Sediment-hosted lead-zinc deposits in Earth history: Economic Geology and the Bulletin of the Society of Economic Geologists, v. 105, p. 593–625, doi:10.2113/

gsecongeo.105.3.593.

Leach, D.L., Sangster, D., Kelley, K.D., Large, R.R., Garven, G., and Allen, C.R., 2005, Sediment-hosted lead-zinc deposits: a global perspective, in Hedenquist, J.W., Thompson, J.F.H., Goldfarb, R.J., and Richards, J.P. eds., 100th Anniversary Volume, Society of Economic Geologists, p. 561–607.

Lewchuk, M.T., Leach, D.L., Kelley, K.D., and Symons, D.T.A., 2004, Paleomagnetism of the Red Dog Zn-Pb massive sulfide deposit in Northern Alaska: Economic Geology, v. 99, p. 1555–1567.

Lin, Q., Wang, J., Algeo, T.J., Sun, F., and Lin, R., 2016, Enhanced framboidal pyrite formation related to anaerobic oxidation of methane in the sulfate-methane transition zone of the northern South China Sea: Marine Geology, v. 379, p. 100–108.

Lin, Z., Sun, X., Peckmann, J., Lu, Y., Xu, L., Strauss, H., Zhou, H., Gong, J., Lu, H., and Teichert, B.M.A., 2016, How sulfate-driven anaerobic oxidation of methane affects the sulfur isotopic composition of pyrite: A SIMS study from the South China Sea: Chemical Geology, v. 440, p. 26–41, doi: http://dx.doi.org/10.1016/j.chemgeo.2016.07.007.

Little, C.T.S., Maslennikov, V.V., Morris, N.J., and Gubanov, A.P., 1999, Two Palaeozoic hydrothermal vent communities from the southern Ural Mountains, Russia: Palaeontology, v. 42, p. 1043–1078, doi:10.1111/1475-4983.00110.

Ludwig, K., 2001, Isoplot 3.00, a geochronologic toolkit for Microsoft Excel. Special Publication, 4: Berkeley Geochronological Center.

Lyons, T.W., Anbar, A.D., Severmann, S., Scott, C., and Gill, B.C., 2009, Tracking Euxinia in the Ancient Ocean: A Multiproxy Perspective and Proterozoic Case Study: Annual Review of Earth and Planetary Sciences, v. 37, p. 507–534, doi: 10.1146/annurev.earth.36.031207.124233.

Lyons, T.W., Gellatly, A.M., McGoldrick, P.J., and Kah, L.C., 2006, Proterozoic sedimentary exhalative (SEDEX) deposits and links to evolving ocean chemistry, in Kesler, S.E. and Ohmoto, H. eds., Evolution of Early Earth's Atmosphere, Hydrosphere, and Biosphere—Constraints from Ore Deposits, v. Geological, p. 169–184, doi: 10.1130/2006.1198(10).

MacEachern, J.A., Pemberton, S.G., Gingras, M.K., and Bann, K.L., 2010, Ichnology and facies models, in James, N.P., and Dalrymple, R.W., eds., Facies models 4: St. John's, Newfoundland, Geological Association of Canada, p. 19–58.

Machel, H.G., 2001, Bacterial and thermochemical sulfate reduction in diagenetic settings - old and new insights: v. 140, p. 143–175.

Macquaker, J.H.S., Taylor, K.G., and Gawthorpe, R.L., 2007, High-Resolution Facies Analyses of Mudstones: Implications for Paleoenvironmental and Sequence Stratigraphic Interpretations of Offshore Ancient Mud-Dominated Successions: Journal of Sedimentary

Research, v. 77, p. 324–339, doi: 10.2110/jsr.2007.029.

Magnall, J. M., Gleeson, S. A., Blamey, N. J. F., Paradis, S., and Luo, Y., 2016, The thermal and chemical evolution of hydrothermal vent fluids in shale hosted massive sulphide (SHMS) systems from the MacMillan Pass district (Yukon, Canada): Geochemica et Cosmochimica Acta, v. 193, p. 251–273.

Magnall, J. M., Gleeson, S. A., Poulton, S. W., Gordon, G. W., and Paradis, S., 2018, Links between seawater paleoredox and the formation of sediment-hosted massive sulphide (SHMS) deposits — Fe speciation and Mo isotope constraints from Late Devonian mudstones: Chemical Geology, v. 490, p. 45–60.

Magnall, J. M., Gleeson, S. A., Stern, R. A., Newton, R. J., Poulton, S. W., and Paradis, S., 2016, Open system sulphate reduction in a diagenetic environment – isotopic analysis of barite ($\delta^{34}S$ and $\delta^{18}O$) and pyrite ($\delta^{34}S$) from the Tom and Jason Late Devonian Zn-Pb-Ba deposits, Selwyn Basin, Canada: Geochimica et Cosmochimica Acta.

Magnall, J.M., Gleeson, S.A., and Paradis, S., 2015, The importance of siliceous radiolarian-bearing mudstones in the formation of sediment-hosted Zn-Pb ?? Ba mineralization in the Selwyn Basin, Yukon, Canada: Economic Geology, v. 110, p. 2139–2146.

März, C., Poulton, S.W., Beckmann, B., Küster, K., Wagner, T., and Kasten, S., 2008, Redox sensitivity of P cycling during marine black shale formation: Dynamics of sulfidic and anoxic, non-sulfidic bottom waters: Geochimica et Cosmochimica Acta, v. 72, p. 3703–3717, doi: 10.1016/j.gca.2008.04.025.

McCready, R.G.L., and Krouse, H.R., 1980, Sulfur isotope fractionation by desulfovibrio vulgaris during metabolism of BaSO4: Geomicrobiology Journal, v. 2, p. 55–62, doi: 10.1080/01490458009377750.

Moore, D.W., Young, L.E., Modene, J.S., and Plahuta, J.T., 1986, Geologic setting and genesis of the Red Dog zinc-lead-silver deposit, western Brooks Range, Alaska: Economic Geology, v. 81, p. 1696–1727, doi: 10.2113/gsecongeo.81.7.1696.

Moore, T.E., Wallace, W., Bird, K., Karl, S., Mull, C., and Dillon, J., 1994, Geology of northern Alaska, in Plafker, G. and Berg, H. eds., The geology of Alaska, Geological Society of America, p. 49–140.

Morelli, R.M., Creaser, R.A., Selby, D., Kelley, K.D., and King, A.R., 2004, Re-Os sulfide geochronology of the Red Dog sediment-hosted Zn-Pb-Ag deposit, Brooks Range, Alaska: Economic Geology and the Bulletin of the Society of Economic Geologists, v. 99, p. 1569–1576, doi: 10.2113 /gsecongeo .99.7.1569.

Paull, C.K., Chanton, J.P., Neumann, A.C., Coston, J.A., Martens, C.S., and Showers, W., 1992, Indicators of Methane-Derived Carbonates and Chemosynthetic Organic Carbon Deposits: Examples from the Florida Escarpment: Palaios, v. 7, p. 361–375, doi:

10.2307/3514822.

Paytan, A., Kastner, M., Martin, E.E., MacDougall, J.D., and Herbert, T., 1993, Marine barite as a monitor of seawater strontium isotope composition: Nature, v. 366, p. 445–449, doi: 10.1038/366445a0.

Paytan, A., Mearon, S., Cobb, K., and Kastner, M., 2002, Origin of marine barite deposits : Sr and S isotope characterization: Geology, v. 30, p. 747–750.

Pemberton, S.G., and Gingras, M.K., 2005, Classification and characterizations of biogenically enhanced permeability: American Association of Petroleum Geologists Bulletin, v. 89, p. 1493–1517, doi:10.1306/07050504121.

Pettke, T., Oberli, F., Audétat, A., Guillong, M., Simon, A. C., Hanley, J. J., and Klemm, L. M., 2012, Recent developments in element concentration and isotope ratio analysis of individual fluid inclusions by laser ablation single and multiple collector ICP-MS: Ore Geology Reviews, v. 44, p. 10–38.

Peucker-Ehrenbrink, B., and Ravizza, G., 2000, The marine osmium isotope record: Terra Nova, v. 12, p. 205–219, doi: 10.1046/j.1365-3121.2000.00295.x.

Poulton, S.W., and Canfield, D.E., 2011, Ferruginous Conditions: A Dominant Feature of the Ocean through Earth's History: Elements, v. 7, p. 107–112, doi: 10.2113/gselements.7.2.107.

Reeburgh, W.S., 1976, Methane consumption in Cariaco Trench waters and sediments: Earth and Planetary Science Letters, v. 28, p. 337–344, doi: 10.1016/0012-821X(76)90195-3.

Reeburgh, W.S., 2007, Oceanic Methane Biogeochemistry: Chemical Reviews, v. 107, p. 486–513, doi: 10.1021/cr050362v.

Reynolds, M.A., Gingras, M.K., Gleeson, S.A., and Stemler, J.U., 2015, More than a trace of oxygen: Ichnological constraints on the formation of the giant Zn-Pb-Ag ± Ba deposits, Red Dog district, Alaska: Geology, v. 43, doi: 10.1130/G36954.1.

Rhoads, D.C., and Morse, J.W., 1971, Evolutionary and ecological significance of oxygen-deficient marine basins: Lethaia, v. 4, p. 413–428, doi: 10.1111 /j .1502 -3931 .1971. tb01864.x.

Roedder, E., 1984, Fluid Inclusions: Reviews in Mineralogy, v. 12, p. 1–646.

Romer, R., and Schwartz, W., 1965, Geomikrobiologische untersuchungen V. Verwertung von sulfatmineralien und schwermetall-toleranz bei desulfurizierern: Z Allg Mikrobiol, v. 5, p. 122–135.

Rubin-Blum, M., Antler, G., Turchyn, A. V., Tsadok, R., Goodman-Tchernov, B.N., Shemesh, E., Austin, J.A., Coleman, D.F., Makovsky, Y., Sivan, O., and Tchernov, D., 2014, Hydrocarbon-related microbial processes in the deep sediments of the Eastern Mediterranean Levantine Basin: FEMS Microbiology Ecology, v. 87, p. 780–796, doi:

10.1111/1574-6941.12264.
Sangster, D.F., 2018, Toward an integrated genetic model for vent-distal SEDEX deposits: Mineralium Deposita, v. 53, p. 509–527, doi: 10.1007/s00126-017-0755-3.
Savrda, C.E., 1995, Ichnologic applications in paleoceanographic, paleoclimatic, and sea-level studies: Palaios, v. 10, p. 565–577, doi: 10.2307/3515095.
Savrda, C.E., and Bottjer, D.J., 1994, Ichnofossils and ichnofabric in rhythmically bedded pelagic/ hemipelagic carbonates: Recognition and evaluation of benthic redox and scour cycles, in de Boer, L., and Smith, D.G., eds., Orbital forcing and cyclic sequences: International Association of Sedimentologists Special Publication 19, p. 195–210, doi:10.1002/9781444304039.ch15.
Schardt, C., Garven, G., Kelley, K.D., and Leach, D.L., 2008, Reactive flow models of the Anarraaq Zn–Pb–Ag deposit, Red Dog district, Alaska: Mineralium Deposita, v. 43, p. 735–757, doi: 10.1007/s00126-008-0193-3.
Schieber, J., 2003, Simple gifts and buried treasures—implications of finding bioturbation and erosion surfaces in black shales: The Sedimentary Record, v. 1, p. 4–8,
Schieber, J., and Riciputi, L., 2004, Pyrite ooids in Devonian black shales record intermittent sea-level drop and shallow-water conditions: Geology, v. 32, p. 305, doi: 10.1130/G20202.1.
Scholz, F., 2018, Identifying oxygen minimum zone-type biogeochemical cycling in Earth history using inorganic geochemical proxies: Earth-Science Reviews, v. 184, p. 29–45, doi: 10.1016/j.earscirev.2018.08.002.
Selby, D., and Creaser, R. A., 2003, Re–Os geochronology of organic rich sediments: an evaluation of organic matter analysis methods: Chemical Geology, v. 200, p. 225–240, doi: 10.1016/S0009-2541(03)00199-2.
Selby, D., and Creaser, R.A., 2005, Direct radiometric dating of the Devonian-Mississippian time-scale boundary using the Re-Os black shale geochronometer: Geology, v. 33, p. 545–548, doi: 10.1130/G21324.1.
Sim, M.S., Bosak, T., and Ono, S., 2011, Large sulfur isotope fractionatoin does not require disproportionation: Science, v. 333, p. 74–77.
Sivan, O., Antler, G., Turchyn, A. V., Marlow, J.J., and Orphan, V.J., 2014, Iron oxides stimulate sulfate-driven anaerobic methane oxidation in seeps: Proceedings of the National Academy of Sciences, v. 111, p. E4139–E4147, doi: 10.1073/pnas.1412269111.
Slack, J. F., Dumoulin, J. A., Schmidt, J. M., Young, L. E., and Rombach, C. S., 2004, Paleozoic sedimentary rocks in the Red Dog Zn-Pb-Ag District and vicinity, western Brooks Range, Alaska: Provenance, deposition, and metallogenic significance: Economic Geology, v. 99, p. 1385–1414.
Slack, J. F., Falck, H., Kelley, K. D., and Xue, G. G., 2017, Geochemistry of host rocks in

the Howards Pass district, Yukon-Northwest Territories, Canada: implications for sedimentary environments of Zn-Pb and phosphate mineralization: Mineralium Deposita, v. 52, p. 565–593.

Slack, J. F., Selby, D., and Dumoulin, J. A., 2015, Hydrothermal, Biogenic, and Seawater Components in Metalliferous Black Shales of the Brooks Range, Alaska: Synsedimentary Metal Enrichment in a Carbonate Ramp Setting: Economic Geology, v. 110, p. 653–675.

Slack, J.F., Kelley, K.D., Anderson, V.M., Clark, J.L., and Ayuso, R. a., 2004, Multistage Hydrothermal Silicification and Fe-Tl-As-Sb-Ge-REE Enrichment in the Red Dog Zn-Pb-Ag District, Northern Alaska: Geochemistry, Origin, and Exploration Applications: Economic Geology, v. 99, p. 1481–1508, doi: 10.2113/gsecongeo.99.7.1481.

Slack, J.F., Selby, D., and Dumoulin, J.A., 2012, A hydrothermal source for metals in the metalliferous black shales fo the Brooks Range, northern Alaska: geochemical and osmium isotope evidence: Geological Society of America Abstracts with Programs, v. 44, p. 600.

Smith, D., 2017, Lithophile and chalcophile elements in sphalerite from the Anarraaq sediment-hosted Zn-Pb-Ag deposit, Red Dog district, Alaska (master's thesis): University of Alberta, Edmonton, Alberta.

Smoliar, M.I., Walker, R.J., and Morgan, J.W., 1996, Re-Os Ages of Group IIA, IIIA, IVA, and IVB Iron Meteorites: Science, v. 271, p. 1099–1102.

Smrzka, D., Kraemer, S.M., Zwicker, J., Birgel, D., Fischer, D., Kasten, S., Goedert, J.L., and Peckmann, J., 2015, Constraining silica diagenesis in methane-seep deposits: Palaeogeography, Palaeoclimatology, Palaeoecology, v. 420, p. 13–26, doi: 10.1016/j.palaeo.2014.12.007.

Snyder, G.T., Dickens, G.R., and Castellini, D.G., 2007, Labile barite contents and dissolved barium concentrations on Blake Ridge : New perspectives on barium cycling above gas hydrate systems: v. 95, p. 48–65, doi: 10.1016/j.gexplo.2007.06.001.

Suess, E., 2014, Marine cold seeps and their manifestations: geological control, biogeochemical criteria and environmental conditions: International Journal of Earth Sciences, v. 103, p. 1889–1916, doi: 10.1007/s00531-014-1010-0.

Taylor, A., Goldring, R., and Gowland, S., 2003, Analysis and application of ichnofabrics: Earth-Science Reviews, v. 60, p. 227–259, doi: 10.1016/S0012 -8252 (02) 00105-8.

Taylor, S.R., and McLennan, S.M., 1995, The geochemical evolution of the continental crust: Reviews of Geophysics, v. 33, p. 241, doi: 10.1029/95RG00262.

Teck Resources Limited, 2017, Annual Information Form:, https://www.teck.com/media/2017-Annual-Information-Form.pdf.

Torres, M.E., Bohrmann, G., Dubé, T.E., and Poole, F.G., 2003, Formation of modern and

Paleozoic stratiform barite at cold methane seeps on continental margins: Geology, v. 31, p. 897, doi: 10.1130/G19652.1.

Torres, M.E., Brumsack, H.J., Bohrmann, G., and Emeis, K.C., 1996, Barite fronts in continental margin sediments: A new look at barium remobilization in the zone of sulfate reduction and formation of heavy barites in diagenetic fronts: Chemical Geology, v. 127, p. 125–139, doi: 10.1016/0009-2541(95)00090-9.

Turchyn, A. V, and Schrag, D.P., 2006, Cenozoic evolution of the sulfur cycle : Insight from oxygen isotopes in marine sulfate: Earth and Planetary Science Letters, v. 241, p. 763–779, doi: 10.1016/j.epsl.2005.11.007.

Turekian, K.K., and Pegram, W.J., 1997, Os Isotope Record in a Cenozoic Deep-Sea Core: Its Relation to Global Tectonics and Climate, in Tectonic Uplift and Climate Change, p. 383–397, doi: 10.1007/978-1-4615-5935-1_17.

Turner, R.J.W., 1992, Formation of Phanerozoic stratiform sediment, hosted zinc-lead deposits: Evidence for the critical role of ocean anoxia: Chemical Geology, v. 99, p. 165–188, doi:10.1016 /0009 -2541 (92) 90037-6.

Veizer, J., Ala, D., Azmy, K., Bruckschen, P., Buhl, D., Bruhn, F., Garden, G.A.F., Diener, A., Ebneth, S., Godderis, Y., Jasper, T., Korte, C., Pawellek, F., Podlaha, O.G., et al., 1999, 87Sr/86Sr, δ13C and δ18O evolution of Phanerozoic seawater: Chemical Geology, v. 161, p. 59–88, doi: 10.1016/S0009-2541(99)00081-9.

Volpi, V., Camerlenghi, A., Hillenbrand, C.-D., Rebescon, M., and Ivaldiz, R., 2003, Effects of biogenic silica on sediment compaction and slope stability on the Pacificmargin of the Antarctic Peninsula: Basin Research, v. 15, p. 339–363, doi: 10.1046/j.1365-2117.2003.00210.x.

Wilkin, R.T., Barnes, H.L., and Brantley, S.L., 1996, The size distribution of framboidal pyrite in modern sediments : An indicator of redox conditions: v. 60, p. 3897–3912.

Wilkinson, J.J., Eyre, S.L., and Boyce, A.J., 2005, Ore-Forming Processes in Irish-Type Carbonate-Hosted Zn-Pb Deposits: Evidencefrom Mineralogy, Chemistry, and Isotopic Composition of Sulfides at the Lisheen Mine: Economic Geology, v. 100, p. 63–86, doi: 10.2113/100.1.0063.

Wood, S. A., 1998, Calculation of activity-activity and log fo2-pH diagrams: Techniques in hydrothermal ore deposits geology: Reviews in Economic Geology, v. 10, p. 81–96.

Worden, R.H., Smalley, P.C., and Cross, M.M., 2000, The Influence of Rock Fabric and Mineralogy on Thermochemical Sulfate Reduction: Khuff Formation, Abu Dhabi: Journal of Sedimentary Research, v. 70, p. 1210–1221.

Young, L.E., 2004, A Geologic Framework for Mineralization in the Western Brooks Range, Alaska: Economic Geology, v. 99, p. 1281–1306, doi: 10.2113/gsecongeo.99.7.1281.

Supplementary files

Supplementary material for Chapter 2 is available at http://www.geosociety.org/datareposi-tory/2015/ and is reproduced below for ease of reference. Supplementary material for Chapters 3 and 4 is archived online through Dataverse. Some of these files are reproduced below; large tables are only available online.

Index of Supplementary Files

Chapter 2: http://www.geosociety.org/datarepository/2015/2015292.pdf

- Figure DR1: Regional map of the Red Dog district
- Figure DR2: Generalized stratigraphic column of the Kuna Formation
- Figure DR3: Selected petrographic images (trace fossils in barite-rich zone)
- Figure DR4: Selected petrographic images (trace fossils in ore zones)
- Figure DR5: Schematic and examples of *Chondrites*
- Figure DR6: Schematic and examples of *Schaubcylindrichnus*
- Table DR1: Sample location details

Chapter 3: https://doi.org/10.7939/DVN/C2Q7SS

- Figure S3.1: Drill core sub-sampled for Re-Os isotopic analysis
- Table. S3.1: Whole rock analyses of Re-Os samples (online only)

Chapter 4: https://doi.org/10.7939/DVN/LJB74Z

- Table S4.1: SIMS data for pyrite, marcasite, and barite (online only)

Chapter 2 Supplementary Files: GSA Data Repository Item 2015292

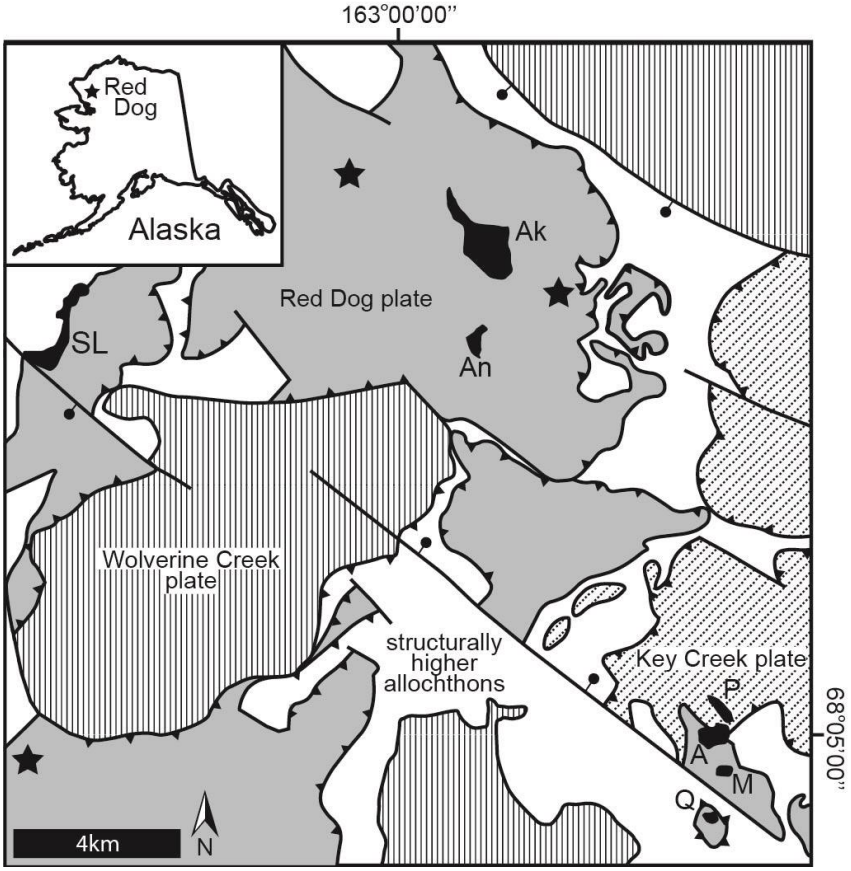

Figure DR1. Simplified map of structural plates of the Endicott Mountain allochthon. The Kuna Fm. occurs in all structural plates of the Endicott's Mountains allochthon but only hosts Zn-Pb mineralization in the Red Dog plate. The Red Dog District Mine Area includes the Main (M), Aqqaluk (A), Paalaaq (P), and Qanaiyaq (Q) deposits. Other known mineralization occurs in the Anarraaq (An), Su-Lik (SL), and Aktigiruk (Ak) deposits and in several other prospects (stars). Surface projections of deposits are delineated in solid black. The nature of some contacts are unknown. Modified after Fig. 2 in Blevings et al. (2013).

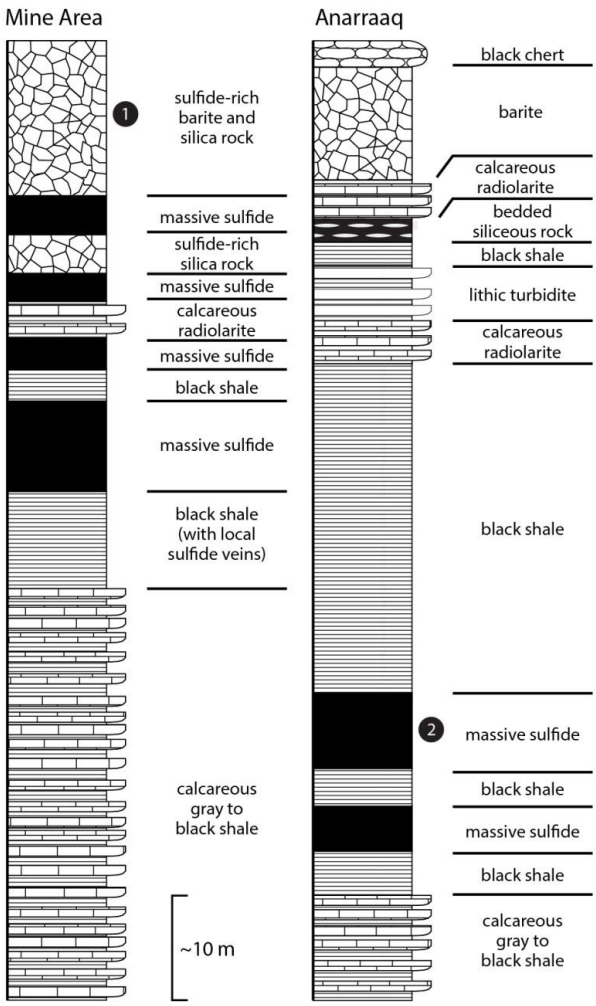

Figure DR2. Generalized stratigraphic column of the Kuna Fm. in the Mine Area deposits and Anarraaq deposit (after Fig. 3 in Slack et al., 2004). Solid black circle 1 indicates the part of the stratigraphic column represented by samples in Figs. 2A, 2B, 2C, DR3, and DR4A. Solid black circle 2 indicates samples in Figs. 2D, DR4B, and DR4C.

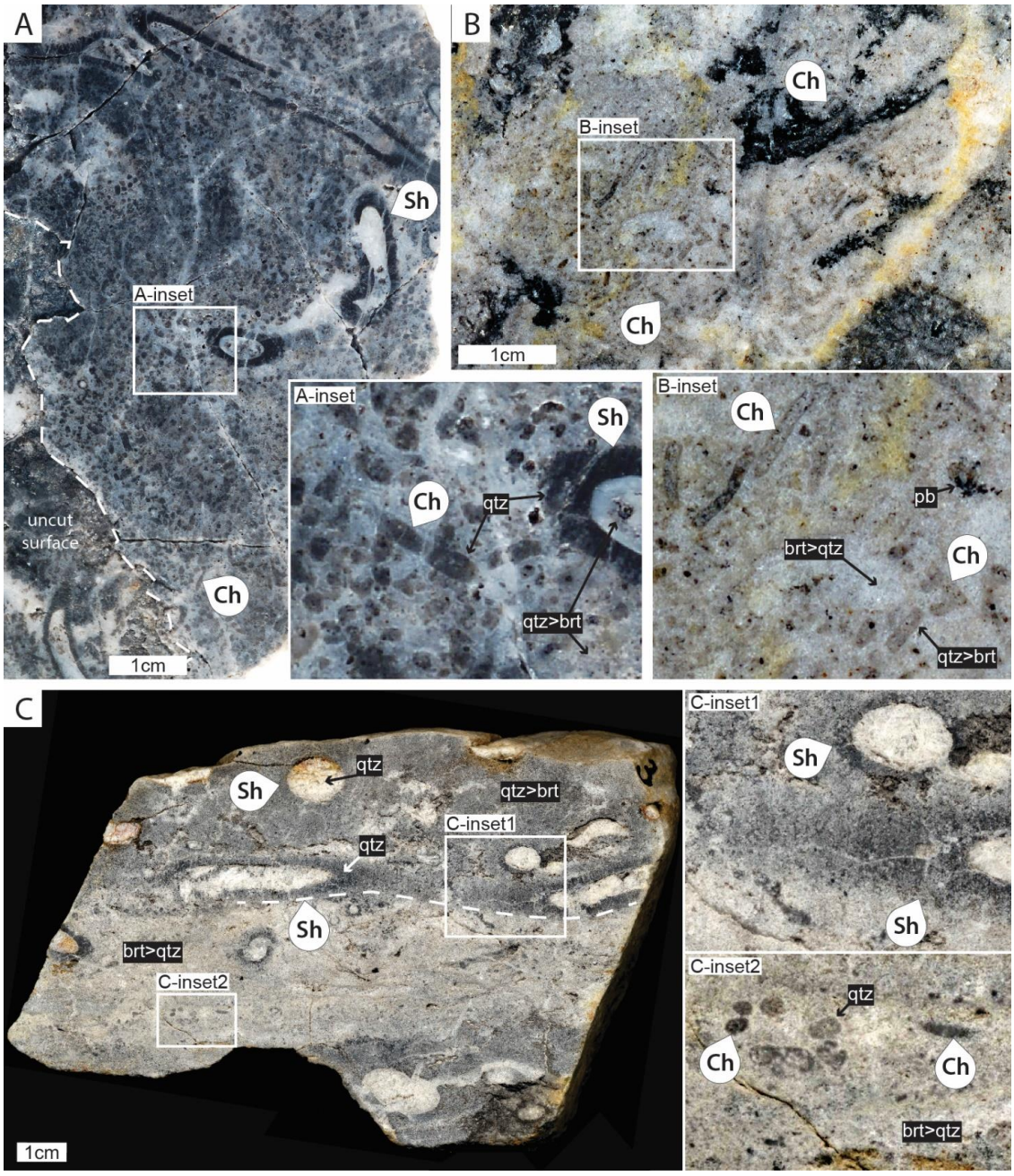

Figure DR3. Additional burrowed samples from the Qanaiyaq deposit. All samples are polished slabs of outcrop samples. **A)** Bedding-parallel sample with abundant *Schaubcylindrichnus* (Sh) and *Chondrites* (Ch). *Shaubcylindrichnus* linings are composed of dark grey quartz (qtz); infill and matrix are composed of light grey quartz > barite (qtz>brt). Note that *Schaubcylindrichnus* traces commonly crosscut bedding plane. *Chondrites* are also composed of dark grey quartz (qtz) and a branching example is highlighted in the inset. **B)** Bedding-parallel sample contains locally abundant *Chondrites* composed of quartz > barite (qtz>brt) in a matrix of barite > quartz (brt>qtz). Matrix also contains patches of pyrobitumen (pb). Inset is the same image as in Fig. 3B. Note branching *Chondrites* highlighted at right of inset. **C)** Bedding-perpendicular sample (way up unknown) shows one

Schaubcylindrichnus burrow following bedding plane for nearly the entire length of the sample. The diameter of *Schaubcylindrichnus* burrows are especially large in this sample, ranging up to approximately 1 cm. *Schaubcylindrichnus* linings and *Chondrites* burrows are composed of dark grey quartz. *Schaubcylindrichnus* infill is composed of barite and the matrix contains variable amounts of light grey quartz and barite.

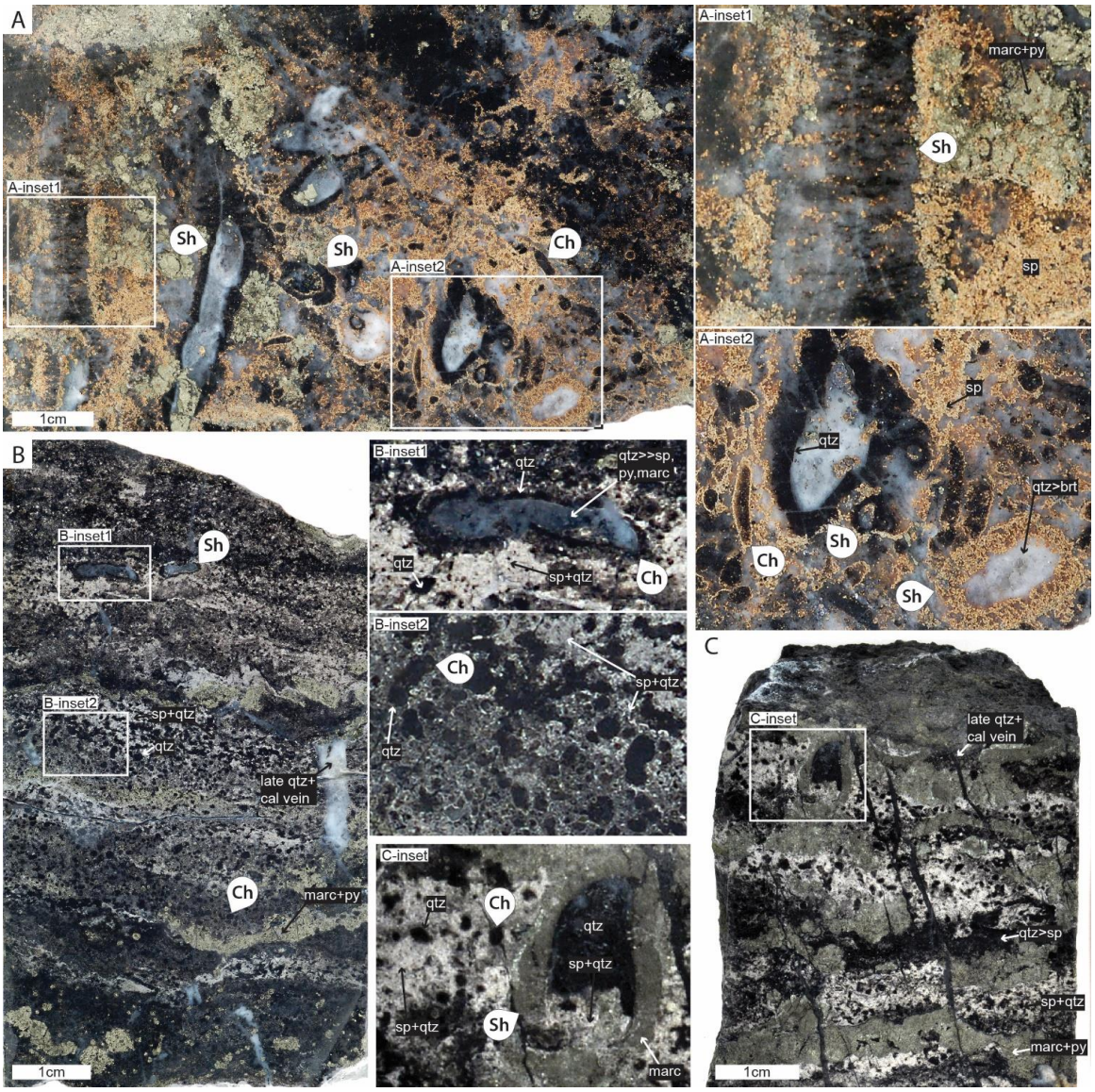

Figure DR4. Additional burrowed samples from Red Dog ore zones. All samples are polished slabs of outcrop specimens (A) and drill core (B-C) and are shown in depositional orientation unless otherwise noted. **A)** Sample of unknown orientation from the Aqqaluk deposit contains abundant *Schaubcylindrichnus* (Sh) and *Chondrites* (Ch) burrows. The upper inset shows the very edge of a *Schaubcylindrichnus* burrow intersecting sample surface in a matrix of marcasite (marc), pyrite (py), and sphalerite (sp). We tentatively interpret the lining texture to be meniscate infill, which would provide further evidence of the biogenicity of these traces. Inset A2 is the same image as Fig. 3C. *Schaubcylindrichnus* linings are composed of dark grey quartz (qtz) or sphalerite (sp) and infilled with light grey quartz > barite (qtz>brt). *Chondrites* are composed of dark grey quartz (qtz). Note that thin rims of sphalerite occur locally on both *Schaubcylindrichnus* (see highlighted burrow in middle of main image) and *Chondrites* (see highlighted burrow in inset A2). We interpret these rims to be reactive boundaries between trace and matrix, not linings. **B)** Bedding-perpendicular sample from Anarraaq ore zone. Possible *Schaubcylindrichnus* and abundant *Chondrites* are highlighted in inset

images. *Schaubcylindrichnus* linings and *Chondrites* are composed of dark grey quartz (qtz) in a matrix of intergrown sphalerite and quartz (sp+qtz). *Schaubcylindrichnis* is infilled with light grey quartz (qtz). **C)** Bedding-perpendicular sample from Anarraaq ore zone. The *Schaubcylindrichnus* lining is composed of marcasite (marc) and infilled with quartz and a zone of intergrown sphalerite and quartz, which we tentatively interpret to be geopetal. Possible *Chondrites* are composed of quartz. Matrix is composed of intercrystalline sphalerite and quartz or marcasite.

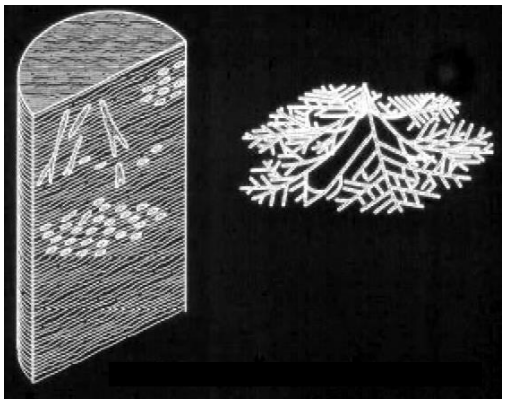

Schematic interpretation of *Chondrites*.

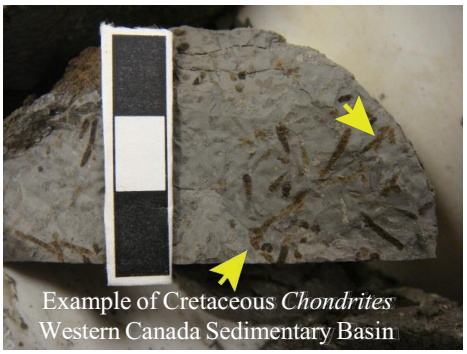

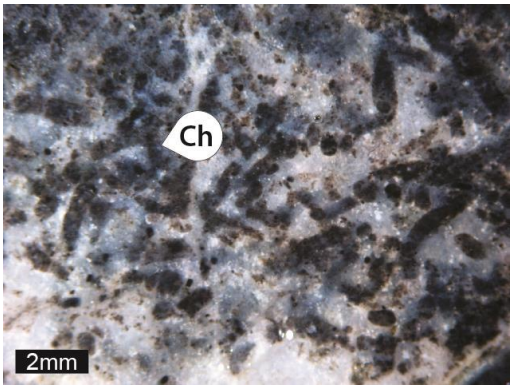

Example of *Chondrites* (Ch) this study.

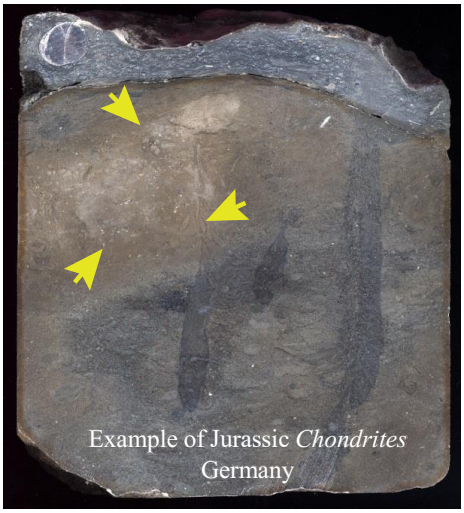

Figure DR5. Schematic and several examples of *Chondrites* in non-hydrothermally altered samples compared with Red Dog sample. **Description:** *Chondrites* is a complex root-like burrow system of regularly branching feeding tunnels of uniform diameter which never anastamose, interpenetrate, nor cut across one another (photo taxis). However, individual Chondrites can crosscut each other due to time averaging. Branching typically is in the form of side branches (up to five or six orders) angling off a higher order or main tunnel at 30 degrees to 40 degrees rather than bifurcating at Y-shaped junctions. In core, *Chondrites* commonly appears as an array of tiny elliptical dots where the vertical slice through the core truncates the numerous branching tunnels. In some instances, longitudinal sections through individual tunnels and broken portions of branches are exposed. **Interpretation:** It has been suggested that *Chondrites* represents tunnels produced by a deposit-feeding sipunculid, which worked from a fixed centre on the substrate surface and created tunnels by extending its proboscis. However, some forms of *Chondrites* penetrate so deeply into the substrate that they could have been only produced by a vermiform animal dwelling within the structure, moving bodily through the sediment in the manner of the modern polychaete *Heteromastus*.

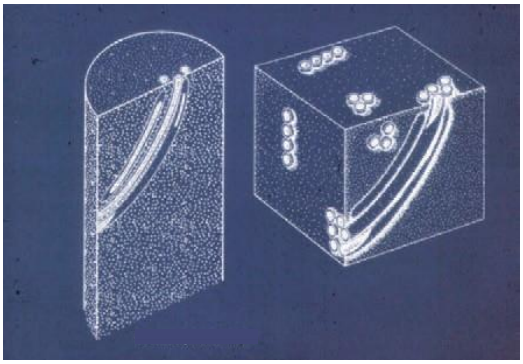

Schematic interpretation of *Schaubcylindrichnus*.

Modern agglutinated polychaete tube.

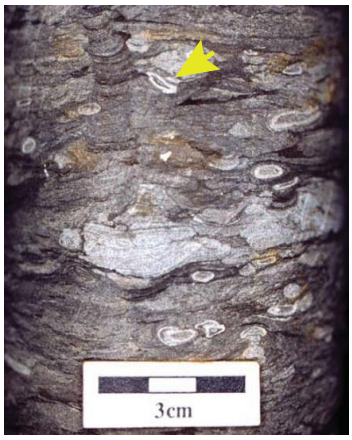

Left and above are Mesozoic examples from the Western Canadian Sedimentary Basin.

Example of *Schaubcylindrichnus* this study.

Figure DR6. Schematic, modern trace former, and several examples of *Schaubcylindrichnus* in non-hydrothermally altered samples compared with Red Dog sample. **Description**: Plural curving tubes, gently arcuate with upper ends of the tubes being vertical, whereas lower ends are approximately horizontal. Isolated sheaves or bundles of closely juxtaposed, congruent, well lined, equisize tubes that do not taper, branch, or interconnect. Number of tubes making up an individual sheaf is variable but as many as 20 per sheaf have been described. Both interior and exterior surfaces of the tubes are smooth and unornamented. Recently amended to include solitary curving tubes (formerly *Terebellina*; Miller, 1995). **Interpretation**: *Schaubcylindrichnus* is interpreted as the communal domicile of either suspension feeders or head-down tubicolous deposit feeders such as the modern maldanid polychaete *Clymenella torquata*.

Sample Name	Deposit	Type	Figure	Location
809-728.2m (2389.2ft)	Anarraaq	Diamond Drill Core	Fig. 3D, Fig. DR3B	*
923-672m (2204.6ft)	Anarraaq	Diamond Drill Core	Fig. DR3C	*
MB-01	Aqqaluk	Hand Specimen	Fig. 3C, Fig. DR4A	†
QB-002	Qanaiyaq	Hand Specimen	Fig. 3B, Fig. DR3B	UTM zone 3W 590344E, 7550422N§
QB-003	Qanaiyaq	Hand Specimen	Fig. 3A, Fig. DR3A	UTM zone 3W 590344E, 7550422N§
QB-004	Qanaiyaq	Hand Specimen	Fig. DR3C	UTM zone 3W 590344E, 7550422N§

Table DR1. Sample location details. *The location of drill holes 809 and 923 can be found on page 1578 in Kelley et al. (2004). †Sample MB-01 was taken from a set of samples belonging to the exploration geology team and is most likely from the Aqqaluk deposit, but could also be from the Main deposit. As the Main and Aqaluk deposits have been mined extensively, this is one of the few existing hand specimens accessible from those deposits. §QB samples were collected within ~100m of this GPS point.

REFERENCES

Blevings, S., Kraft, J., Stemler, J., and Krolak, T., 2013, An overview of the structure, stratigraphy, and Zn-Pb-Ag deposits of the Red Dog District, Northwestern Alaska, *in* Special Publication 17, Society of Economic Geologists, p. 361–387.

Kelley, K.D., Dumoulin, J.A., and Jennings, S., 2004, The Anarraaq Zn-Pb-Ag and barite deposit, northern Alaska: Evidence for replacement of carbonate by barite and sulfides: Economic Geology, v. 99, p. 1577–1591.

Miller, W., 1995, “Terebellina”; (= Schaubcylindrichnus freyi ichnosp. nov.) in Pleistocene outer-shelf mudrocks of northern California: Ichnos, v. 4, no. 2, p. 141–149, doi: 10.1080/10420949509380121.

Slack, J.F., Dumoulin, J.A., Schmidt, J.M., Young, L.E., and Rombach, C.S., 2004, Paleozoic sedimentary rocks in the Red Dog Zn-Pb-Ag District and vicinity, western Brooks Range, Alaska: Provenance, deposition, and metallogenic significance: Economic Geology, v. 99, p. 1385–1414.

Chapter 3 Supplementary files

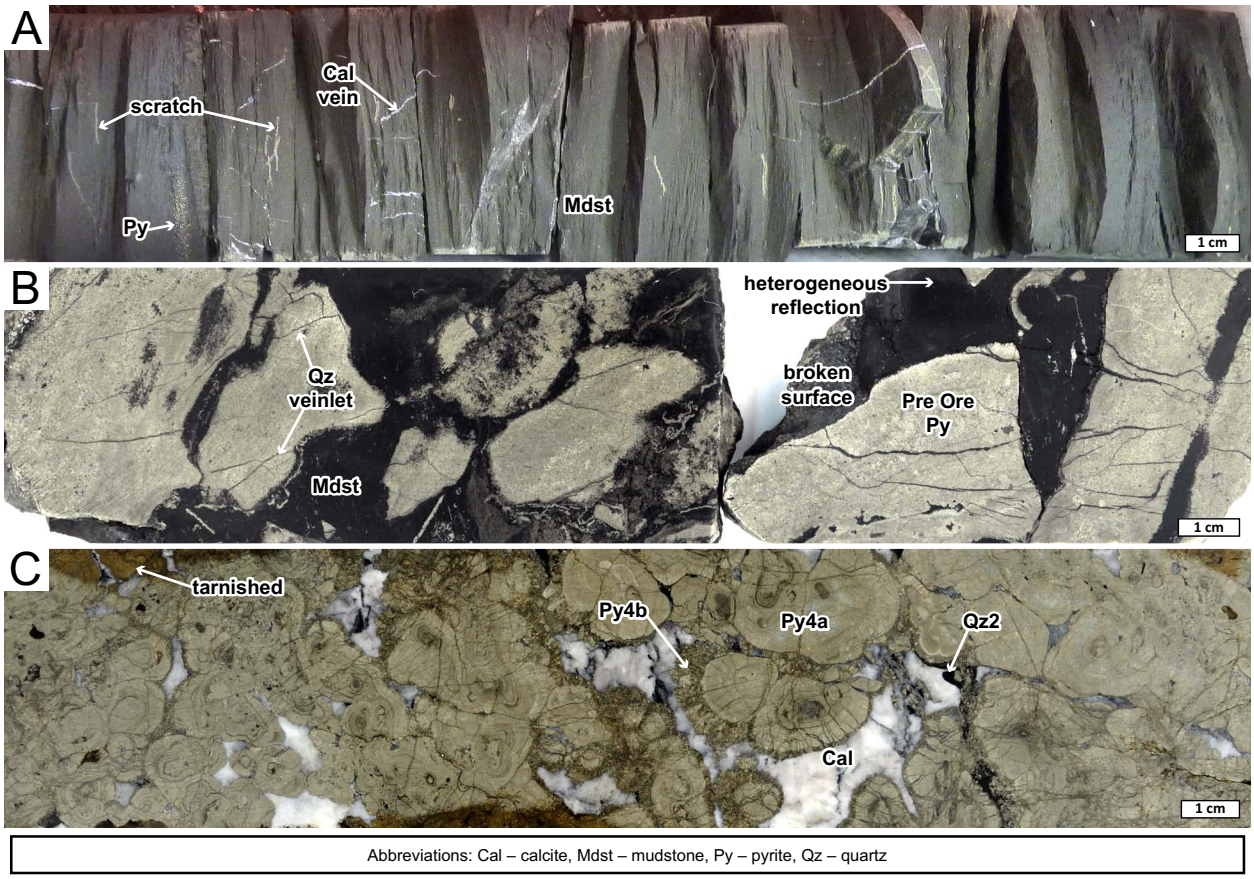

Figure S3.1: Drill core sub-sampled for Re-Os isotopic analysis. Top of core is to the left in all samples. (a) Sample 923-2123.1 – split core. Organic-rich mudstone contains minor calcite veinlets and patches of disseminated pyrite; these were avoided during sub-sampling. (b) Sample 1716-2521 – cut and wetted core. Nodular pre-ore pyrite in Ikalukrok mudstone. (c) Sample 1723-2104.9 – cut and wetted core. Ore-stage pyrite in large hydrothermal pyrite-calcite-quartz vein. Only samples of Py4a were used in isochron.